Chem Soc Rev

REVIEW ARTICLE

View Article Online
View Journal | View Issue

Cite this: *Chem. Soc. Rev.*, 2025, **54**, 5342

Integrative plasmonics: optical multi-effects and acousto-electric-thermal fusion for biosensing, energy conversion, and photonic circuits†

Hong Zhou, ‡[abcd] Dongxiao Li, ‡[ab] Qiaoya Lv ‡[ab] and Chengkuo Lee *[abc]

Surface plasmons, a unique optical phenomenon arising at the interface between metals and dielectrics, have garnered significant interest across fields such as biochemistry, materials science, energy, optics, and nanotechnology. Recently, plasmonics is evolving from a focus on "classical plasmonics," which emphasizes fundamental effects and applications, to "integrative plasmonics," which explores the integration of plasmonics with multidisciplinary technologies. This review explores this evolution, summarizing key developments in this technological shift and offering a timely discussion on the fusion mechanisms, strategies, and applications. First, we examine the integration mechanisms of plasmons within the realm of optics, detailing how fundamental plasmonic effects give rise to optical multi-effects, such as plasmon–phonon coupling, nonlinear optical effects, electromagnetically induced transparency, chirality, nanocavity resonance, and waveguides. Next, we highlight strategies for integrating plasmons with technologies beyond optics, analyzing the processes and benefits of combining plasmonics with acoustics, electronics, and thermonics, including comprehensive plasmonic-electric-acousto-thermal integration. We then review cutting-edge applications in biochemistry (molecular diagnostics), energy (harvesting and catalysis), and informatics (photonic integrated circuits). These applications involve surface-enhanced Raman scattering (SERS), surface-enhanced infrared absorption (SEIRA), surface-enhanced fluorescence (SEF), chirality, nanotweezers, photoacoustic imaging, perovskite solar cells, photocatalysis, photothermal therapy, and triboelectric nanogenerators (TENGs). Finally, we conclude with a forward-looking perspective on the challenges and future of integrative plasmonics, considering advances in mechanisms (quantum effects, spintronics, and topology), materials (Dirac semimetals and hydrogels), technologies (machine learning, edge computing, in-sensor computing, and neuroengineering), and emerging applications (5G, 6G, virtual reality, and point-of-care testing).

Received 1st September 2024

DOI: 10.1039/d4cs00427b

rsc.li/chem-soc-rev

1. Introduction

Surface plasmons are the collective oscillations of free electrons that occur at the interface between a metal (typically gold or silver) and a dielectric material upon optical excitation. To describe the coupled oscillations of electromagnetic waves and charge carriers in solids, surface plasmons are often referred to as surface plasmon polaritons (SPPs) by adding the word "polaritons". The study of surface plasmons dates back to the early 20th century, with significant milestones marking its development. The first experimental observation of plasmonic enhancement was reported by Wood in 1902,[1] who noted an anomalous decrease in light intensity reflected by a metallic grating. Over time, theoretical work and key experimental breakthroughs[2]—such as the discovery of surface-enhanced Raman scattering (SERS),[3] surface-enhanced infrared absorption (SEIRA),[4] and surface-enhanced fluorescence (SEF)[5]—established a foundation for numerous applications in sensing,[6] imaging,[7] spectroscopy, photonic devices,[8] and solar energy harvesting.[9–12] Surface plasmons continue to be a vibrant area of research, with ongoing discoveries expanding their potential applications and deepening our understanding of plasmonic phenomena.

Currently, the study of plasmons is evolving from "classical plasmonics" to "integrative plasmonics"—a transition that shifts focus from understanding only the fundamental phenomena to

[a] *Department of Electrical and Computer Engineering, National University of Singapore, Singapore 117583, Singapore. E-mail: elelc@nus.edu.sg*
[b] *Center for Intelligent Sensors and MEMS (CISM), National University of Singapore, Singapore 117583, Singapore*
[c] *NUS Graduate School-Integrative Sciences and Engineering Programme (ISEP), National University of Singapore, Singapore 119077, Singapore*
[d] *School of Mechanical Engineering, Northwestern Polytechnical University, Xi'an 710072, China*

† Electronic supplementary information (ESI) available. See DOI: https://doi.org/10.1039/d4cs00427b

‡ These authors contributed equally to this work.

exploring the rich interplay of optical multi-effects combined with electric, acoustic, and thermal technologies (Fig. 1). Classical plasmonics has provided deep insight into the properties of surface plasmons and their interactions with light; yet it faces significant challenges such as ohmic losses in metals and inherent scalability issues. These losses lead to significant energy attenuation, and while classical designs are compact, they often dissipate too much energy to be effective over practical distances. Integrative plasmonics overcomes these limitations by adopting innovative strategies. For example, by employing hybrid photonic-plasmonic structures,[13] light can travel long distances within low-loss photonic waveguides, converting to plasmons only in small, localized regions for specific tasks such as processing or sensing.

Furthermore, while classical plasmonic experiments typically address a single function—like using nanoparticles to sense local refractive index changes—integrative plasmonics allows multiple plasmonic elements to operate in concert. This facilitates the creation of complex, multifunctional devices, such as an integrated plasmonic circuit containing sources, modulators, waveguides, and detectors all on one chip. Such complexity is vital for advancing plasmonics from laboratory demonstrations to practical, high-performance devices. For instance, the combination of plasmonic near-field enhancement with the graphene bulk photovoltaic effect (BPVE) has already demonstrated zero-bias photodetection capabilities.[14] Similarly, the integration of local plasmonic heating with the photoacoustic (PA) effect enables simultaneous ultrasound imaging and imaging-guided thermal treatment of tumors, paving the way for more precise diagnostic and therapeutic solutions.[15]

Thus, we refer to this emerging interdisciplinary field as ''integrative plasmonics'', emphasizing the fusion of optical multi-effects with acousto-electrical-thermal phenomena. This integrated approach not only overcomes traditional limitations but also offers innovative methods and technological solutions for specific challenges in applications such as biosensing, energy conversion, and photonic circuits. As technological advancements continue and interdisciplinary collaborations

Hong Zhou

Hong Zhou received his BEng degree in Mechanical Engineering from Central South University, China, and his PhD degree in Instrument Science and Technology from Chongqing University, China, in 2020. From 2021 to 2025, he was a Research Fellow with the Department of Electrical and Computer Engineering at the National University of Singapore. He is currently a Professor at the School of Mechanical Engineering, Northwestern Polytechnical University, China. His research interests include plasmonics, mid-infrared metamaterials and nanophotonics for advanced sensing applications.

Dongxiao Li

Dongxiao Li received his BSc degree from the College of Artificial Intelligence, Chongqing Technology and Business University, Chongqing, China, and PhD degree in Instrument Science and Technology from Chongqing University, China, in 2022. He is now a Research Fellow at the Department of Electrical & Computer Engineering, National University of Singapore, Singapore. His research interests are focused on mid-infrared metamaterials and nanophotonics for sensing applications.

Qiaoya Lv

Qiaoya Lv is currently engaged in pursuing her PhD in Instrumentation Science and Technology at Chongqing University. Her research is centered around the design and fabrication of piezoelectric MEMS sensors, actuators, and energy harvesters. In addition, she is actively involved in the DFT calculations concerning the plasmonic nanostructures, and photocatalytic, piezoelectric, and elastic properties of materials.

Chengkuo Lee

Chengkuo Lee received his PhD degree in Precision Engineering from the University of Tokyo in 1996. Currently, he is the director of the Center for Intelligent Sensors and MEMS at the National University of Singapore, Singapore. In 2001, he cofounded Asia Pacific Microsystems, Inc., where he was the Vice President. From 2006 to 2009, he was a Senior Member of the Technical Staff at the Institute of Microelectronics, A-STAR Singapore. He has contributed to more than 516 peer-reviewed international journal articles.

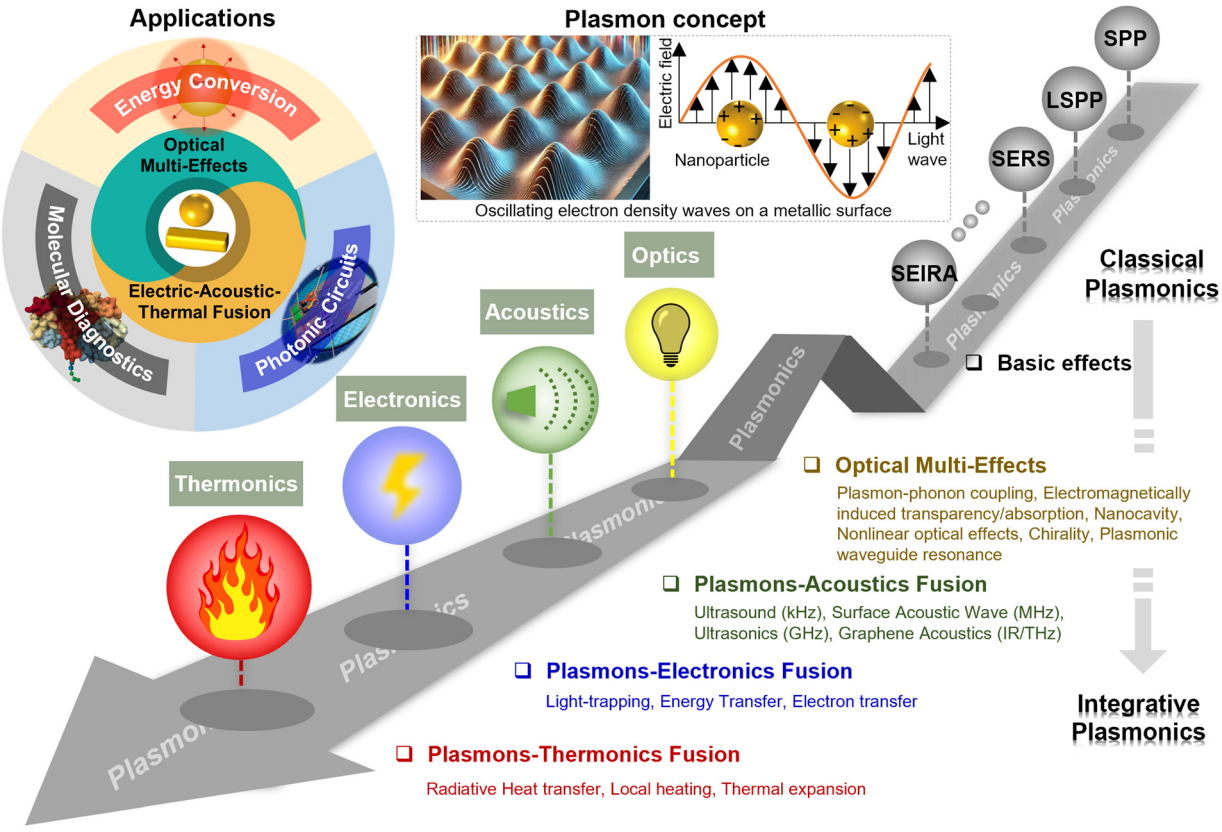

Fig. 1 Roadmap of integrative plasmonics. Since the discovery of plasmons in 1902, a diverse range of plasmonic effects have been observed, such as SPR, LSPR, SERS, and SEIRA. Currently, the study of plasmons has evolved from focusing on the basic plasmon effect to exploring optical multi-effects and the fusion with electric, acoustic, and thermal technologies, which is referred to as "integrative plasmonics". These advancements are demonstrated in cutting-edge applications across molecular diagnostics, energy conversion, and photonic integrated circuits.

deepen, the scope of plasmonic effects is set to expand further, spurring breakthrough innovations. Consequently, a systematic and comprehensive discussion of optical multi-effects and acousto-optical-thermal integration is crucial to propel the field forward. Key areas of focus include (1) the advantages of integrative plasmonics; (2) strategies for enhancing the optical multi-effects of plasmons; (3) approaches for fusing acousto-electric-thermal technologies; (4) emerging mechanisms and applications; and (5) the future development of integrative plasmonics.

In this review, we aim to address these questions by providing a comprehensive analysis of the optical multi-effects of plasmons and the fusion of plasmonic, acoustic, electric, and thermal technologies. Our objective is to offer a timely discussion and perspectives on the mechanisms, strategies, and applications of integrative plasmonics. The framework of this review is illustrated in Fig. 2. Firstly, we introduce and analyze the optical multi-effects of plasmons. This section covers various phenomena, including plasmon–phonon coupling, plasmonic nonlinear optical effects, electromagnetically induced transparency (EIT), plasmonic chirality, plasmonic nanocavity resonance, and plasmonic waveguide resonance. Through this analysis, we elucidate how basic plasmonic effects evolve into complex optical multi-effects, representing the integration of multiple effects within the realm of optics. Secondly, we analyze the multiphysical coupling of plasmons with acoustics, electronics, and thermal effects, emphasizing their comprehensive integration. This analysis highlights the strategies for combining plasmonic effects with technologies beyond optics, providing insights into how these integrations are achieved and their potential benefits. In the subsequent sections, we examine the cutting-edge and promising applications of integrative plasmonics. These applications include molecular diagnostics, energy conversion, and photonic integrated circuits (PICs). This section demonstrates the advantages of integrative plasmonics in addressing complex real-world challenges, showcasing its potential to drive innovations across various fields. Finally, we conclude with a forward-looking perspective on the future of integrative plasmonics. We offer personal views on the challenges and the potential developments in the field, emphasizing the importance of continued research and interdisciplinary collaboration for mechanism advancements, material innovations, technological breakthroughs, and application expansion, to unlock the full potential of integrative plasmonics. By following this framework, our review aims to provide a thorough understanding of the

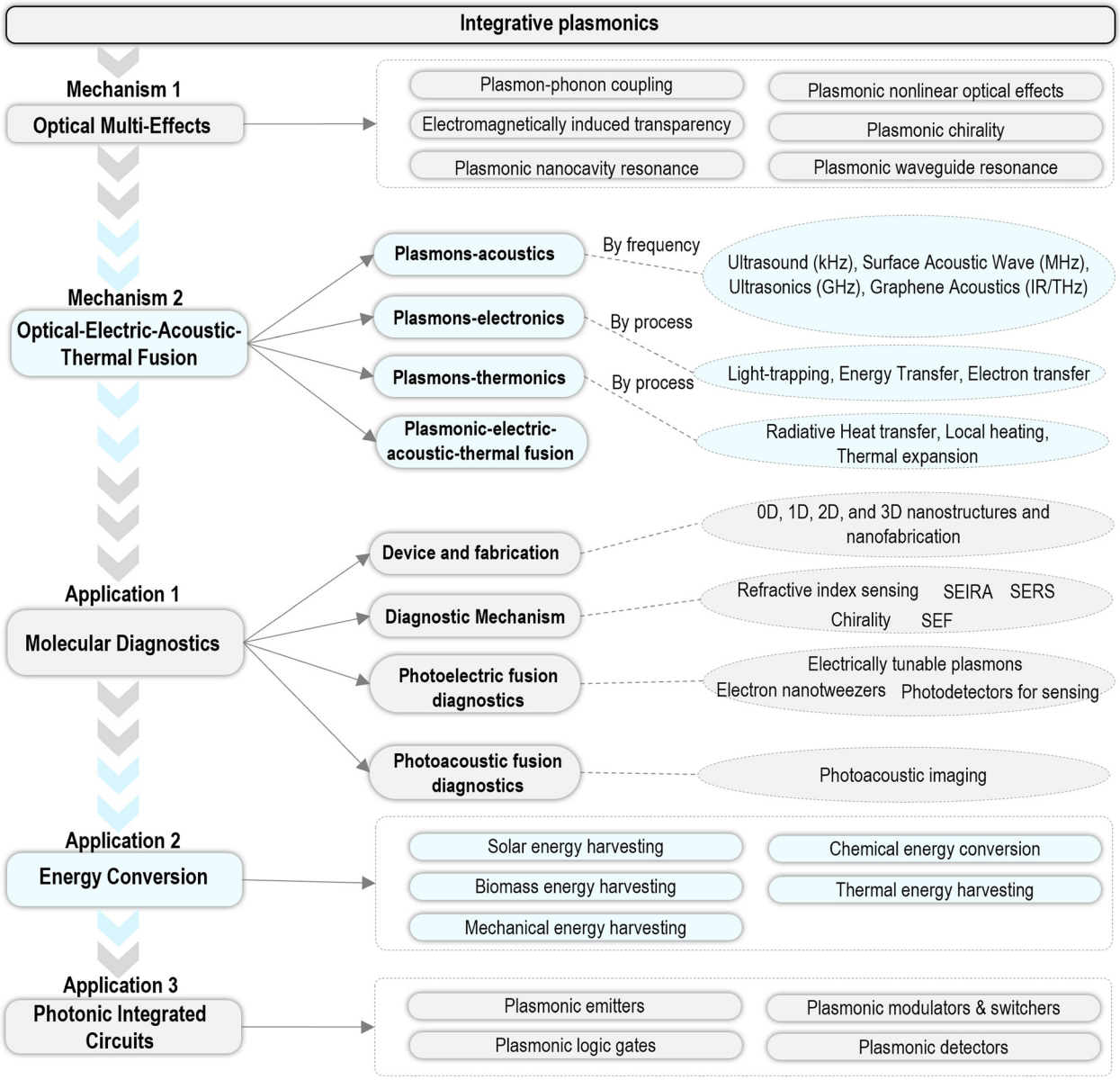

Fig. 2 Framework of this review. First, the optical multi-effects in integrative plasmonics are highlighted, followed by a discussion of the fusion of plasmons with electric, acoustic, and thermal technologies. We then review cutting-edge applications of these technologies in molecular diagnostics, energy conversion, and photonic integrated circuits. Finally, we conclude with a forward-looking perspective on the future of integrative plasmonics.

current state and future prospects of integrative plasmonics, contributing to the advancement of this rapidly evolving field.

2. Mechanics of optical multi-effects

To understand why optical multi-effects and electric-acousto-thermal fusion are pivotal features of integrative plasmonics, we first examine the excitation mechanism of plasmons, as illustrated in Fig. 3. When metal nanoparticles or nanorods interact with light, the conduction electrons in the metal are driven by the incident electric field into collective oscillations, namely localized surface plasmon polaritons (LSPPs).[16–28] The energy of the plasmon can decay both non-radiatively, resulting in absorption, and radiatively, resulting in light scattering (Fig. 3a). The non-radiative decay of the plasmon involves relaxation through electron–electron collisions or electron-lattice phonon coupling, generating hot electrons—a crucial step in the process. Hot electrons, which are not in thermal equilibrium with the atoms in the material,[29] are characterized by an elevated effective temperature described by the Fermi function.[30] They are generated *via* intraband excitations within the conduction band or through interband excitations involving transitions between other bands (*e.g.*, d bands) and the conduction band (Fig. 3b). Notably, interband excitations are less probable than intraband excitations due to the lower energy levels of the d bands.[31] The

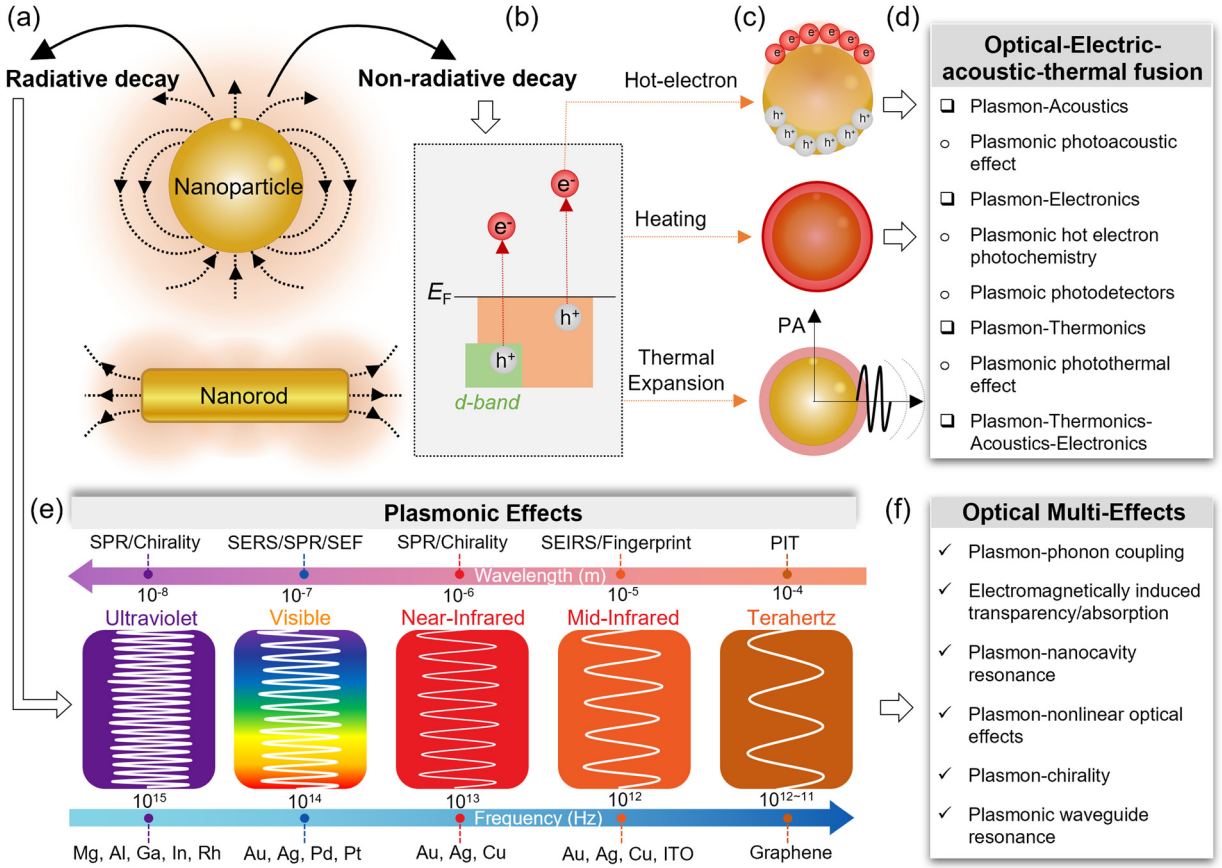

Fig. 3 Mechanics and categories of integrative plasmonics. (a) Schematic diagram of plasmonic nanoparticles and nanorods, with energy loss occurring *via* radiative and non-radiative decay. (b) Non-radiative decay involves the excitation of hot electrons. These hot electrons are generated through intraband excitations within the conduction band or interband excitations from transitions between other bands (*e.g.*, d bands) and the conduction band. (c) The excitation of hot electrons is accompanied by heating effects and thermal expansion phenomena. (d) Hot electrons correspond to electronics, heating effects correspond to thermonics, and thermal expansion can generate ultrasound, which corresponds to acoustics. Therefore, optical-electrical-acousto-thermal fusion is an important feature of integrative plasmonics. (e) Radiative decay of plasmons leads to near-field and far-field enhancements, producing different plasmonic effects with various materials across the terahertz to ultraviolet regions. (f) These plasmonic effects combine with other optical mechanisms to create optical multi-effects, such as plasmon–phonon coupling, which is another important feature of integrative plasmonics. Optical multi-effects have been shown to enable new functionalities and improve device performance in the optical field.

generation of hot electrons is accompanied by heating effects and thermal expansion phenomena (Fig. 3c). Specifically, after the initial electronic excitation, relaxation occurs on a sub-picosecond timescale *via* electron–electron scattering, leading to localized heating and a rapid increase in the metal surface temperature. This creates a significant temperature difference between the hot nanostructure surface and the cooler surrounding medium, resulting in heat exchange. During this process, thermal expansion and contraction of the surrounding medium generate ultrasonic signals. In this context, hot electrons correspond to electronic effects, heating effects correspond to thermionic effects, and thermal expansion generates ultrasound, corresponding to acoustic effects. Therefore, optical-electric-acousto-thermal fusion is a key feature of integrative plasmonics (Fig. 3d).

Regarding radiative decay, LSPPs generate strong electromagnetic fields at the surfaces of nanostructures, with local field strengths that can be several orders of magnitude greater than the incident field.[32–34] This enhancement spans various plasmonic effects from the terahertz to the UV regions (Fig. 3c). For example, in the visible light spectrum, plasmon-driven phenomena such as SERS,[35] SEF,[36] and surface plasmon resonance[37] have been experimentally observed. In the infrared region, due to molecular infrared vibration modes, the plasmon-driven SEIRA effect is widely utilized in molecular detection and imaging.[38,39] Recently, these plasmonic effects have been shown to combine with other optical mechanisms to create optical multi-effects,[40] enabling new functionalities or improving device performance. For instance, plasmon–phonon coupling has been demonstrated to achieve light–matter coupling in the ultrastrong coupling (USC) regime,[41] which holds promise for the development of novel ultrafast devices.[42] In the following sections, we will explore six optical multi-effects in detail, illustrating strategies for integrating plasmons with other effects in the field of optics. These multi-effects include plasmon–phonon coupling, plasmon-enhanced electromagnetically induced transparency/absorption, plasmonic nanocavity resonance, plasmon-enhanced nonlinear optical effects, plasmon-enhanced chirality, and plasmonic waveguide resonance.

2.1 Plasmon–phonon coupling

Surface phonon polaritons (SPhPs) arise from the interaction between polar optical phonons and long-wavelength incident fields, spanning from the mid-IR range (*e.g.*, hexagonal BN[43]) to frequencies below 10 THz (*e.g.*, GaAs[44]). These interactions occur in polar dielectric crystals between the longitudinal (LO) and transverse optic (TO) phonon frequencies, within a spectral range known as the "Reststrahlen" band.[45] Due to their excitation in polar dielectric crystals, SPhPs exhibit excellent optical properties, including lower optical losses compared to plasmonic materials, high local electromagnetic fields, and large Purcell factors. Plasmons can harness these superior optical properties by coupling with phonons.[41]

Plasmon–phonon coupling emerges when the collective oscillations of free electrons in metals or semiconductors interact with phonon modes in polar crystals. While plasmons typically reside in the visible to near-infrared range, phonon polaritons occur in the mid-infrared to terahertz regime (the Reststrahlen band). The overlap in these spectral domains enables hybrid modes that can combine the best attributes of both plasmons and phonons, leading to promising opportunities for enhanced light–matter interactions. The advantages of the hybrid modes include the following: (1) lower optical losses: polar dielectrics like h-BN (hexagonal boron nitride) exhibit lower losses in the mid-IR or terahertz regime compared to many metals at similar frequencies. Coupling plasmons to SPhPs can reduce the overall dissipation; (2) high local field enhancement: just as plasmons localize electromagnetic fields at subwavelength scales, SPhPs also confine light strongly. Their combination may further enhance this confinement, beneficial for sensing and nonlinear optical processes; and (3) tunable response: by engineering the dimensions of nanostructures or by choosing specific polar dielectrics, it becomes possible to tailor the plasmon–phonon resonant frequency, quality factor, and spatial confinement.

Plasmon–phonon coupling can be theoretically analyzed using an oscillator model consisting of three coupled harmonic oscillators subjected to an external force f, as illustrated in Fig. 4a. The two damped oscillators represent out-of-phase atomic lattice vibrations, with k-vectors aligned parallel (LO) and perpendicular (TO) to the incident field. According to the coupled harmonic oscillator theory, the coupling system can be expressed as follows:[46]

$$\ddot{p}(t) + \gamma_p \dot{p}(t) + \omega_p{}^2 p(t) = f(t) - \kappa_1 \exp(i\varphi) q_1(t) - \kappa_2 \exp(i\varphi) q_2(t) \quad (1)$$

$$\ddot{q}_1(t) + \gamma_{TO} \dot{q}_1(t) + \omega_{TO}{}^2 q_1(t) = -\kappa_1 \exp(i\varphi) p(t) \quad (2)$$

$$\ddot{q}_2(t) + \gamma_{LO} \dot{q}_2(t) + \omega_{LO}{}^2 q_2(t) = -\kappa_2 \exp(i\varphi) p(t) \quad (3)$$

where the dissipative oscillator, characterized by resonance frequencies $\omega_{LO,TO}$ and a dark-mode damping factor $\gamma_{LO,TO}$, is described by the excitation $q(t)$. The coupling strength between the plasmonic and dissipative oscillators is given by $\kappa_{1,2}$ $\exp(i\varphi)$, where φ represents the phase shift between them. γ_L denotes the bright-mode damping factor. Based on this relationship, the spectra of the plasmon–phonon coupling system can be obtained, as illustrated in Fig. 4b. In a coupled system, phonons remain fixed in the Reststrahlen band, while the plasmon resonance bifurcates into two distinct frequencies, known as the upper and lower branch frequencies. The phonon intensity varies with the coupling coefficient κ. This splitting behavior is more apparent in the dispersion curves of the plasmon–phonon coupling system (Fig. 4c). Different positions on the split correspond to varying plasmonic resonance frequencies. Since the SPhP Reststrahlen band remains fixed, altering the plasmonic resonance frequency $\Delta\omega$ results in different coupling strengths, which in turn affect the SPhP vibration intensity. For example, when the plasmonic resonance frequency shifts from ω_A to ω_B, the split moves from A to B. This redshift-induced intensity change of SPhPs can enhance identification accuracy in molecular diagnostic applications. The redshift can be caused by perturbations in the refractive index.

For instance, our group proposed a strategy to achieve phonon and plasmon coupling, as illustrated in Fig. 4d. This approach utilizes stacked trapezoidal metal (Au) antennas and phonon (silicon oxide, SiO_2) antennas, all situated on a BaF_2 substrate. The metal antennas support plasmons through the collective oscillations of free carriers, while the SiO_2 antennas support phonons through atomic displacements. The coupling of phonons and plasmons has been shown to improve identification accuracy when molecular vibrational fingerprints overlap, which is crucial for molecular diagnostic applications (Fig. 4e).[47] In one demonstration monitoring the glucose enzymatic reaction, SPhP vibrations were able to disentangle overlapping vibrational modes of glucose oxidase and water, achieving a 92% identification accuracy.

Furthermore, the coupling of phonons and plasmons can be controlled by the optical response of the nanostructure, such as polarization, ensuring that plasmon and phonon signals can be independently manipulated. This prevents mutual interference and signal masking.[46] As shown in Fig. 4f, the asymmetric design of cross-shaped nanoantennas with unequal arm lengths allows for strategic control. The plasmonic resonance frequency of the short arms is positioned away from the phonon frequency but aligns with the vibrational frequency of protein samples for vibrational imaging. Conversely, the plasmonic resonance frequency of the long arms aligns with the phononic Reststrahlen band to excite phonon modes for imaging. By manipulating the polarization direction, selective excitation of plasmonic modes in the short arms or phonon modes in the long arms is achieved. This system demonstrates increased identification accuracy, heightened sensitivity, and enhanced detection limits, down to molecule monolayers, for mid-infrared hyperspectral imaging of severe acute respiratory syndrome coronavirus (SARS-CoV).[46]

In addition to altering optical properties, plasmon–phonon interactions can influence the electron scattering mechanism and, consequently, the electrical conductivity of the material.[48] The interaction between plasmons and phonons can be tuned by adjusting parameters such as doping levels, material composition, and temperature.[49] This tunability allows for precise control of electrical properties in devices. Moreover, understanding and controlling plasmon–phonon coupling can lead

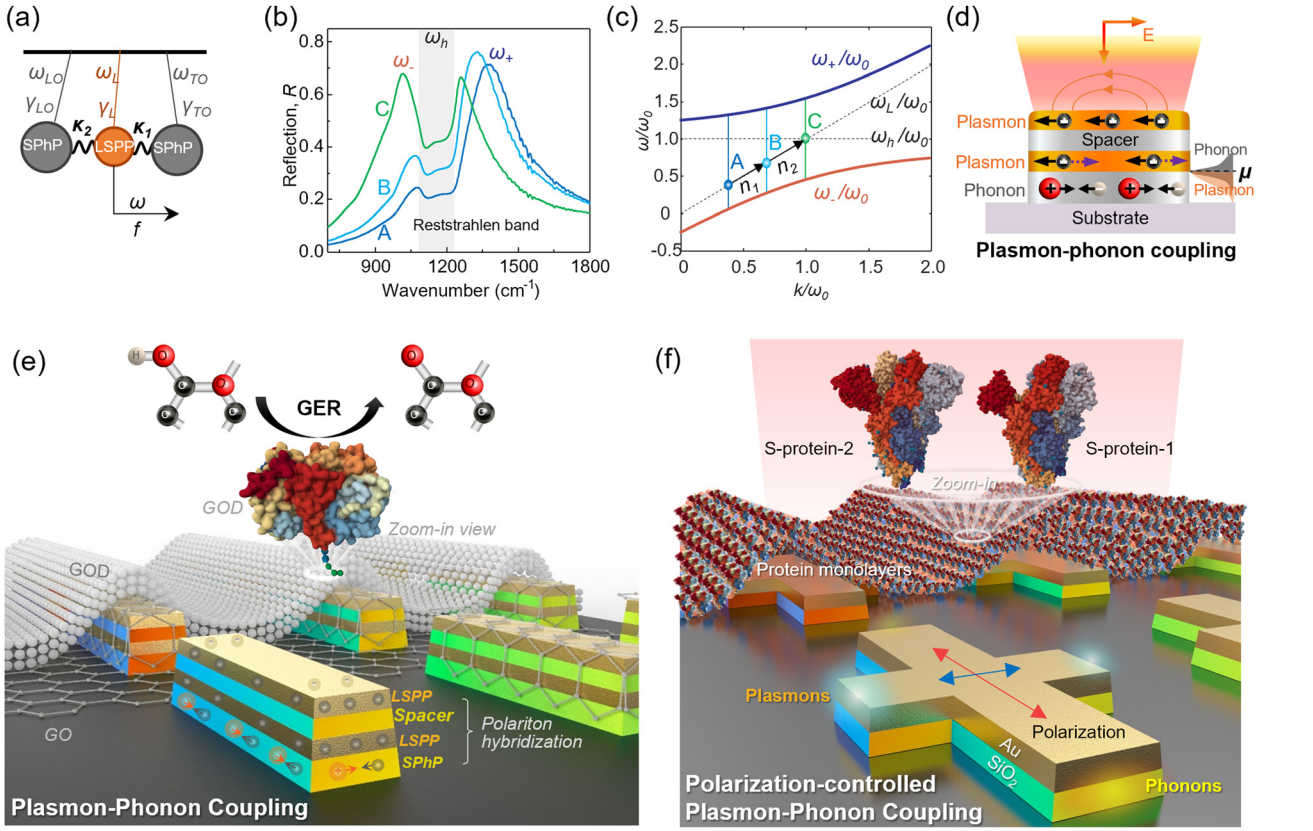

Fig. 4 Strategies for plasmon–phonon coupling. (a) Schematic view of two coupled damped oscillators with a driving force f applied to one of them. (b) Spectra of the plasmon–phonon coupling system based on the model in (a). (c) The dispersion curves of the plasmon–phonon coupling system. The curve describes how a refractive index change (from n_1 to n_2) causes a change in the resonant frequencies of plasmons ($\omega_{+,-}$). It describes the spectral change when the resonant frequencies of plasmons vary due to perturbations in the refractive index. (d) Schematic diagram of plasmon–phonon coupling. The black balls represent plasmons with the collective oscillations of free carriers in metals, and the red and white balls are phonons with atomic displacements in the form of optical phonons in polar dielectrics. (e) An example of phonon–photon coupling for the biosensing of glucose oxidase (GOD). Adapted with permission from ref. 47; Copyright 2023 Springer Nature. (f) An example of polarization-controlled phonon–photon coupling for the hyperspectral imaging application. Adapted with permission from ref. 46; Copyright 2024 Springer Nature.

to improved thermal management in electronic and photonic devices, as well as enhanced performance in thermoelectric materials.[50] For example, plasmon–phonon coupling in graphene/hBN systems can be used to flexibly modify the spectral emissivity of a thermal emitter.[51] In general, the integration of SPhPs will facilitate plasmon-based applications such as optical sensing, photodetection, and thermal management.

2.2 Electromagnetically induced transparency/absorption

Combining plasmons with quantum-like effects can improve the complexity and functionality of these phenomena. EIT is a quantum interference effect that makes an otherwise opaque medium transparent to a probe laser beam when a control laser beam is applied. EIT typically occurs in a three-level atomic system consisting of two ground states and one excited state but often requires cryogenic temperatures. Electromagnetically induced absorption (EIA), closely related to EIT, results in enhanced absorption rather than transparency.[52] In the context of EIT/EIA, surface plasmons can achieve destructive or constructive interference effects analogous to those observed in atomic EIT/EIA, creating transparency or absorption windows. It is useful to note that the phenomena of transmission, reflection, and absorption are inherently connected through the relationship $A + T + R = 1$; hence, any increase in reflection (sometimes described as electromagnetically induced reflection) or transmission can be interpreted in terms of a corresponding change in the absorption spectrum. Plasmon-driven EIT/EIA offers several advantages, including subwavelength control, versatility, integration, and room temperature operation. For example, plasmonic structures can confine light to subwavelength dimensions, leading to strong field enhancements and enabling EIT/EIA effects at the nanoscale.[53] Additionally, unlike some atomic systems that require cryogenic temperatures, plasmonic EIT/EIA can function at room temperature, making them more practical for real-world applications.

The plasmon-driven EIT/EIA can be analyzed using a coupled harmonic oscillator model (Fig. 5). According to this model, the spectral response of the plasmon system for the EIT/EIA effects can be described as[54]

$$A(\omega_0) \cong \frac{\kappa^2 \gamma_m \omega_0^2}{\mu^2 \exp(i2\varphi) + \gamma\gamma_m \omega_0^2} \quad (4)$$

where γ_m is the dark damping and φ is the phase in coupling strength $\kappa \cdot \exp(i \cdot 2\varphi)$. The term $\exp(i \cdot 2\varphi)$ significantly influences the trend of resonant absorption, which can be categorized into three groups: (1) when $0 < \varphi < \pi/4$ (Fig. 5a-I), the coupling of the dark oscillator (a mode that does not directly radiate and is not observable in the far-field) weakens the bright resonance of the plasmonic nanostructures. In this range, the real part of $\exp(i \cdot 2\varphi)$ is positive, causing a decrease in the absorption spectrum and leading to a destructive EIT signal; (2) when $\pi/4 < \varphi < \pi/2$ (Fig. 5a-III), the real part of $\exp(i \cdot 2\varphi)$ becomes negative, resulting in an increase in the absorption spectrum. Here, the dark oscillator strengthens the resonance of the bright oscillator *via* coupling $\mu \cdot \exp(i\varphi)$ (Fig. 5a-iii); (3) when $\varphi = \pi/4$ (Fig. 5a-II), the real part of $\exp(i \cdot 2\varphi)$ is zero, indicating that the movements of the two harmonic oscillators are synchronized. Therefore, the absorption change at resonance caused by the coupling of the dark oscillator is negligible (Fig. 5a-ii). Collectively, the phase shift φ between the two resonators is a crucial physical parameter for acquiring EIT and EIA signals. The phase shift φ can be tuned by controlling the wave propagation distance T (Fig. 5b and c). According to the current distribution (Fig. 5d), circulating currents only exist in the device configuration with a metal layer. The current and magnetic dipole increase as the thickness of the dielectric layer decreases. These findings provide an efficient pathway for plasmon-driven EIT/EIA transition and conversion.

The plasmon-driven EIT/EIA offers high-quality factors and low radiation losses, which are advantageous for the development of efficient photonic devices. These phenomena also enable steep linear dispersion in transparency windows, leading to an elevated group refractive index. For example, combining graphene with dielectric metasurfaces can achieve actively tunable ring-shaped EIT, where graphene plasmons can be controlled by adjusting the Fermi level through applied voltage.[55] EIT-based sensors are particularly sensitive to changes in the dielectric environment due to their high Q factor and strong local electric fields.[56] Additionally, by creating a transparency window, the group velocity of light passing through the medium can be significantly slowed down. Plasmon-driven EIT structures thus facilitate the realization of slow light devices in compact, integrated photonic circuits.[57]

2.3 Plasmonic nanocavity resonance

While individual plasmonic nanoparticles exhibit excellent light manipulation capabilities, nanocavities formed by assemblies of plasmonic particles, such as nanosphere dimers and

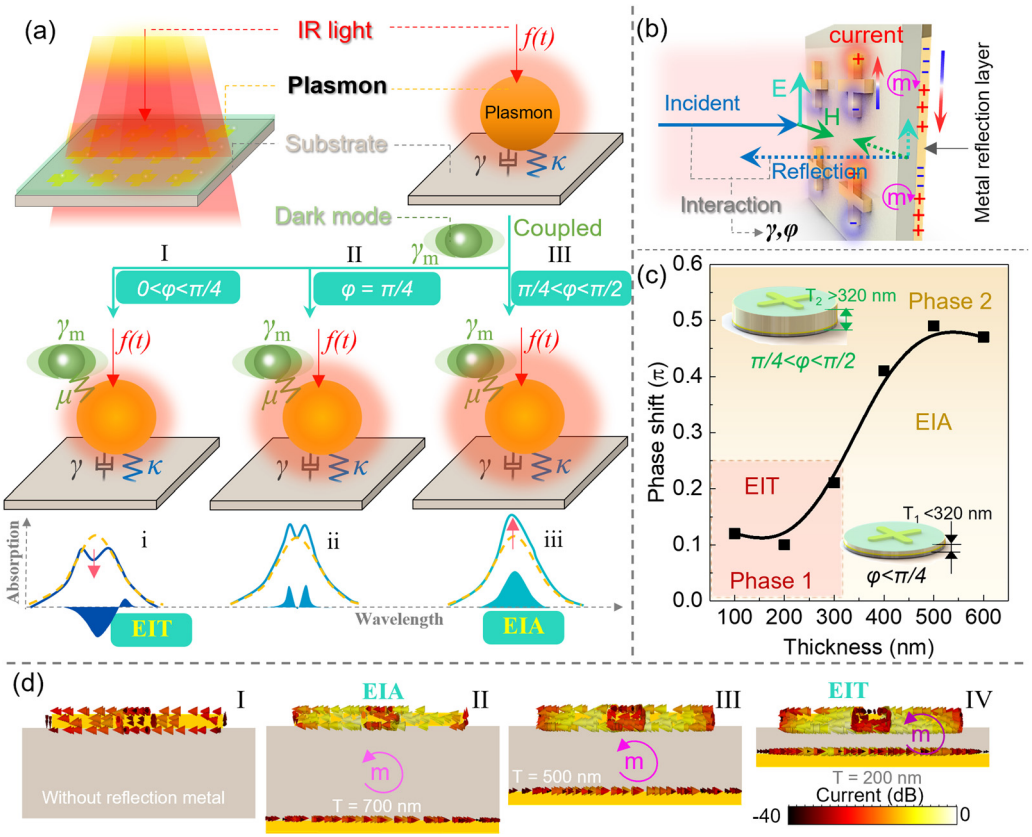

Fig. 5 Plasmon-driven electromagnetically induced transparency/absorption. (a) Schematic view of electromagnetically induced transparency/absorption (EIT/EIA) of a plasmonic device.[54] According to the coupled harmonic oscillator model, when the dark damping γ_m is coupled to the plasmonic system, its spectral response depends on the coupling strength $\kappa \cdot \exp(i \cdot 2\varphi)$, where the phase ($\varphi$) of Fano resonance is critical and has three states: (I) $0 < \varphi < \pi/4$, EIT state; (II) $\varphi = \pi/4$, critical coupling; and (III) $\pi/4 < \varphi < \pi/2$, EIA state. (b) Utilizing the reflection of a metal layer close to the plasmonic nanostructure to change the phase φ. (c) The phase φ as a function of distance T to the plasmonic nanostructure. (d) The current distribution of the plasmonic nanostructure (I) without a metal reflection layer, or with a metal reflection layer whose gap varies (II–IV). Adapted with permission from ref. 54; Copyright 2022 John Wiley and Sons.

trimers,[58–61] have garnered significant attention. These nanocavities, created by strategically assembling two or more individual nanoparticles, offer much stronger field intensities for enhanced light–matter interactions.[62] The narrow gaps between the particles enable more efficient light confinement compared to the individual constituent particles. Moreover, the plasmon coupling between constituent particles can generate a wider variety of intriguing plasmon modes, providing greater flexibility in manipulating the optical properties of the assembled nanostructures. Notable examples include bonding and anti-bonding plasmon modes in metal nanoparticle dimers,[63] super-radiant and sub-radiant plasmons in ring/disk nanocavities, and plasmonic Fano resonances in metal nanoparticle oligomers.[64–67]

Next, we introduce the nanofabrication strategies for realizing plasmonic nanocavities, specifically highlighting single nanoparticles on a film and dimers on a film. The size of the nanogap in the nanocavity is crucial as it affects the near-field coupling strength between the nanoparticles and the film.[68] There are two primary strategies for precisely controlling the nanogap size during nanofabrication. The first approach involves separating the nanoparticles from the metal film by depositing a planar dielectric film between them, with the nanogap size being adjusted by controlling the thickness of the dielectric film (Fig. 6a). The second method uses a dielectric shell coating around the metal nanoparticles to form core/shell-type nanoparticles, thereby avoiding direct contact between the metal nanoparticles and the underlying film (Fig. 6b). The nanogap size in this method is tuned by adjusting the thickness of the dielectric shell. Several methods can be employed to fabricate nanogaps, each offering distinct characteristics. The layer-by-layer (LBL) method involves depositing alternating monolayers of positively charged poly(allylamine)hydrochloride (PAH) and negatively charged polystyrene sulfonate, allowing precise control over thickness ranging from 2 to 20 nm.[69] Atomic layer deposition (ALD) achieves nanoscale-thick inorganic spacers by depositing one molecular layer per cycle, producing materials like Al_2O_3 and SiO_2 with thickness ranging from a few nanometers.[70] Self-assembled monolayers (SAMs) of amine-terminated alkanethiols create ultrathin spacers with thicknesses between 0.5 and 2 nm, controlled by the length of the alkanethiol molecules.[71] Finally, two-dimensional (2D) materials such as graphene and transition metal dichalcogenides provide natural ultrathin spacers with atomic thickness, scalable to a few nanometers using mechanical exfoliation or chemical vapor deposition.[72] These strategies enable precise control over nanogap size, which is essential for optimizing the near-field coupling strength and enhancing the performance of plasmonic nanocavities.

The impact of nanocavity on plasmonic modes can be explored by analyzing the nanogap using various theoretical analytical tools. One such method is based on the multiple scattering process,[73] as illustrated in Fig. 6a. For the incident wave S_{in}, the scattering waves include reflection of the incident

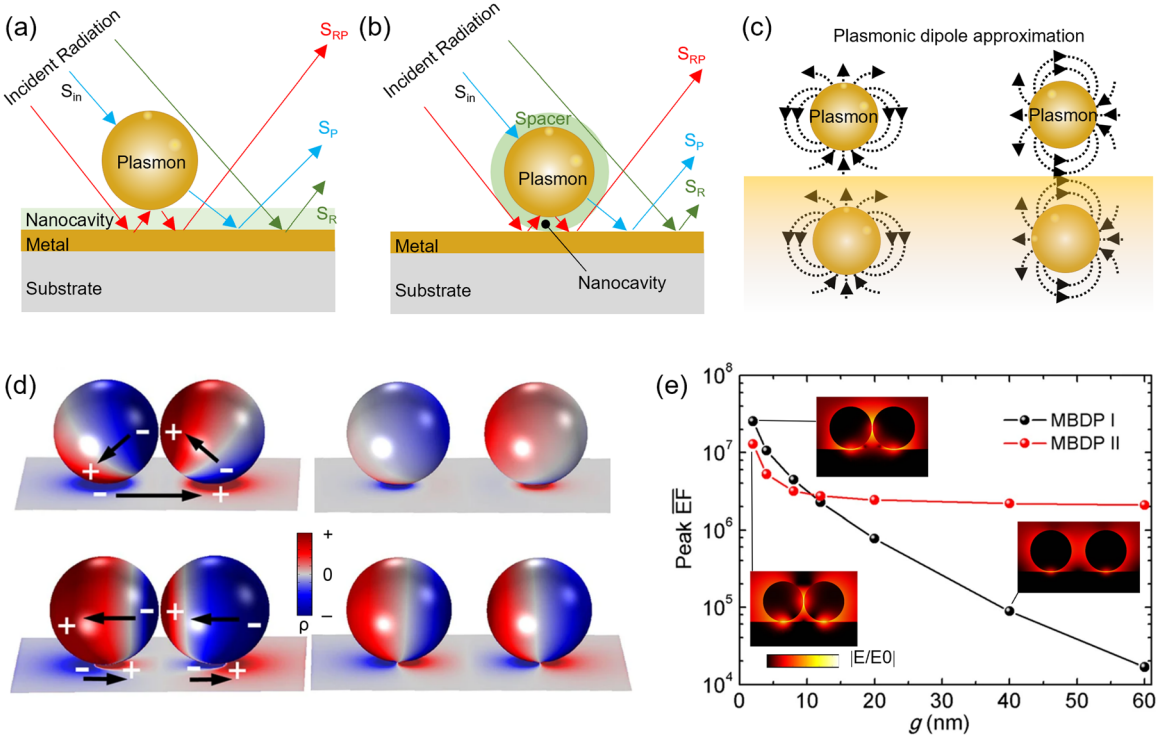

Fig. 6 Strategies for plasmonic nanocavity resonance. (a) Schematic view of a single nanoparticle-on-film construct. (b) Schematic of the core/shell type nanoparticle-on-film strategy. (c) Schematic illustration of plasmonic dipole approximation for nanoparticles-on-film configurations. (d) 3D surface charge distributions of the dimer-on-film. Upper panel: Mirror-induced bonding dipole plasmon (MBDP) mode I. Lower panel: MBDP mode II. (e) Extracted peak intensity of MBDP modes I and II as a function of the dimer gap *g*. Adapted with permission from ref. 63; Copyright 2016 Springer Nature Limited.

wave by the film without the nanoparticle S_R, reflection of the scattered wave from the nanoparticle by the metal film S_{RP}, and the scattered wave from the nanoparticle SP. Another approach is the dipole-image model within the electrostatic approximation, as depicted in Fig. 6c. For a nanostructure positioned close to a sufficiently large metal film, the plasmonic properties of the entire system are equivalent to those of a dimer consisting of the real nanostructure and its corresponding image in the metal film.[74] Additionally, an equivalent circuit model can be used to describe the nanoparticle-film gap plasmon oscillations, offering another perspective on these interactions.[75]

Consider the dimer-on-film design as an example; the simulated 3D surface charge distributions are illustrated in Fig. 6d. The results reveal a strong correlation between the surface plasmon geometry and the local electric field distributions. When two nanoparticles are in close proximity, forming a dimer, the localized charge intensities become particularly significant at the nanogap. Additionally, dual dipole modes are observed: one arising from the vertical bonding between the dimer dipole and the induced charge dipoles, and the other from the horizontal bonding. The image poles in the mirror result from the interaction with the neighboring opposite poles of the nanoparticles, where the mirror induces multiple plasmon poles. As depicted in the peak intensity plot (Fig. 6e), as the gap size g increases, the peak intensity decreases almost exponentially due to the rapid degeneration of the nanoparticles' hot-spots.

2.4 Plasmon-enhanced nonlinear optical effects

Nonlinear optical effects are crucial for modern photonic functionalities,[76–78] such as frequency control of laser light,[79] ultrashort pulse generation,[80] all-optical signal processing,[81] and ultrafast switching.[82] However, these effects are inherently weak due to the limited photon–photon interactions in materials. Integration of plasmonics with these effects can address this challenge. First, plasmons can significantly enhance these nonlinear optical effects due to the coherent oscillations of conduction electrons near noble-metal surfaces. Surface plasmons generate strong local electromagnetic fields, thereby boosting optical processes like SERS and increasing effective nonlinearities.[83–86] For example, in SERS, plasmon excitation of rough or engineered metal surfaces can enhance the inherently weak Raman process by several orders of magnitude, even enabling single-molecule detection.[87–90] Additionally, plasmonic excitations are highly sensitive to changes in dielectric properties, enabling precise control of light with light. These excitations also operate on femtosecond timescales, facilitating ultrafast optical signal processing and leading to advanced nanophotonic functionalities. For instance, this picosecond optical modulation could be used to create integrated optical components with terahertz modulation speeds.[91]

Next, three representative strategies for plasmon-enhanced nonlinear optical effects are introduced. The first is the nonlinear second-harmonic generation (SHG).[92] The suggested energy level structure and SHG pathway are exhibited in Fig. 7a. This method doubles the frequency of light through the interaction between light and nonlinear materials, which is an essential optical technology. However, due to the long interaction length between light and nonlinear materials, conventional components that achieve this function are often bulky. One solution is to embed plasmonic materials into materials with high intrinsic optical nonlinearity, which can achieve high nonlinear response at moderate powers. For instance, plasmonic gold nanorings were filled with lithium niobate (LN) using electron beam lithography and ion beam enhanced etching (Fig. 7b).[93] This configuration has been demonstrated to enhance SHG, with an EF of up to 60 (Fig. 7c). This approach offers a compact and efficient solution, making it highly suitable for practical applications in fluorescence spectroscopy and quantum communication.

The second is the four-wave mixing (FWM) effect, which is a parametric nonlinear process in which two optical electromagnetic waves that have two different frequencies interact to form another two optical waves of different frequencies, as shown in Fig. 7d. FWM has widespread applications in wavelength conversion, signal regeneration, switching, phase-sensitive amplification, nonlinear imaging and entangled photon pair generation. However, FWM processes have an extremely weak nature and suffer from very poor efficiencies. The key towards improving the efficiency of FWM is to increase the local field intensity along nonlinear materials. The enhanced electromagnetic fields of plasmonic structures can serve well to boost the nonlinear FWM process. The mechanism of the plasmon-enhanced FWM is shown in Fig. 7e. When two different frequency components ($\omega_{1,2}$) of an electromagnetic wave propagate together on the plasmon surface, a refractive index modulation at the frequency difference between the two occurs and this creates two additional frequency components ($\omega_{4wm1} = 2\omega_1 - \omega_2$, $\omega_{4wm2} = 2\omega_2 - \omega_1$).[96] For instance, Chakraborty *et al.* used a plasmonic azimuthally chirped grating (ACG) to enhance the nonlinear optical process by coupling light from the far field into localized hot spots (Fig. 7f).[94] They demonstrated significant enhancement of broadband FWM due to the interplay between localized surface plasmon resonance (LSPR) and plasmonic surface lattice resonance in the ACG.

The third is the surface-enhanced coherent anti-Stokes Raman scattering (SECARS).[97] As shown in Fig. 7g, in conventional SERS,[98–103] Stokes-Raman scattering (ω_S) is generated for the excitation of the pump (ω_P). The SERS can be further improved by combining plasmonic enhancements with coherence, that is, the pump (ω_P) and Stokes (ω_S) fields interact coherently through the high-order polarizability of the dipole-forbidden vibronic modes of a molecule, generating an anti-Stokes signal $\omega_{AS} = 2\omega_P - \omega_S$. If the input ($\omega_{P,S}$) or output ($\omega_{AS}$) frequencies are in resonance with the collective modes of the plasmonic nanostructure, the signal from molecules adsorbed onto the nanostructure will be further enhanced by the local fields of the excited plasmon modes, which is known as SECARS. For instance, Zhang *et al.* developed a quadrumer consisting of four gold nanodisks arranged to create a strong Fano resonance (Fig. 7h), thereby achieving a highly localized SECARS enhancement in a single junction at the center of the quadrumer structure (Fig. 7i).[95] The detection signal is enhanced by $\sim$11 orders of magnitude, enabling the detection of single molecules in the demonstration.

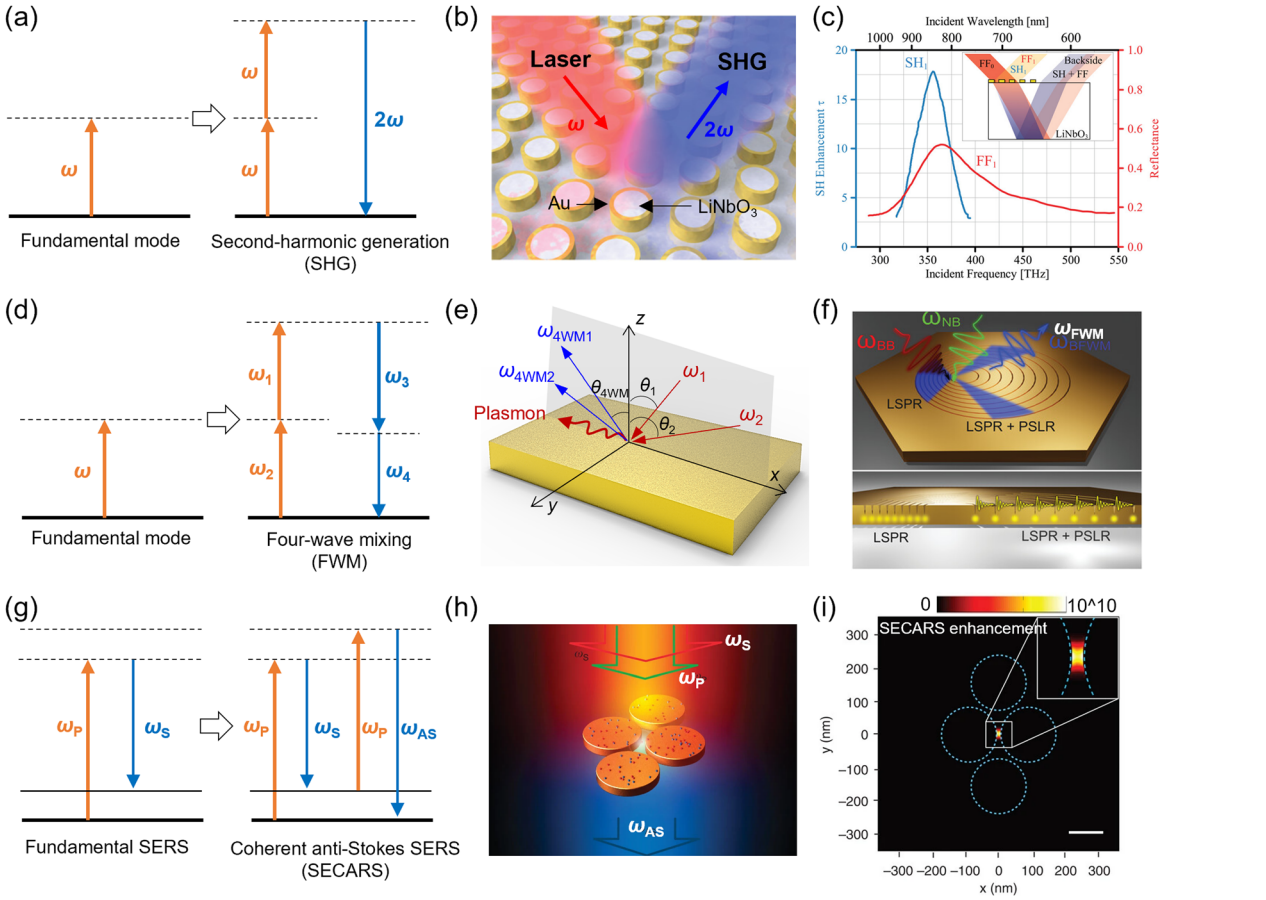

Fig. 7 Strategies for plasmon-enhanced nonlinear optical effects. (a) Photon diagrams for second-harmonic generation (SHG). The solid horizontal lines correspond to real quantum mechanical states of the material system, while the dashed lines are virtual states in which the system resides only momentarily. The orange arrows correspond to input fields that can drive the energy of the material system up or down as directed. The blue downward arrows correspond to the generated fields that return the material to its initial state. (b) Plasmon-enhanced SHG in gold nanoring resonators filled with lithium niobate. (c) Measured second-harmonic enhancement factor and linear reflection spectrum of the device in (b). Adapted with permission from ref. 93; Copyright 2015 American Chemical Society. (d) Photon diagrams for four-wave mixing (FWM). (e) Mechanism of the plasmon-enhanced FWM. (f) FWM using a gold azimuthally chirped grating. Adapted with permission from ref. 94; Copyright 2023 John Wiley and Sons. (g) Photon diagrams for surface-enhanced coherent anti-Stokes Raman scattering (SECARS). (h) SECARS configuration of two diluted molecules on a nanoquadrumer. A single-wavelength pump laser (ω_P) and a supercontinuum Stokes laser (ω_S) generate an enhanced anti-Stokes scattering (ω_S) of a molecule in the quadrumer central gap. (i) Corresponding SECARS enhancement map. Adapted with permission from ref. 95; Copyright 2014 Springer Nature.

2.5 Plasmon-enhanced chirality

A chiral object or system is defined as one whose structure and mirror image (enantiomer) are not superimposable.[104–106] Chiral structures are ubiquitous in nature, exemplified by deoxyribonucleic acid (DNA) and proteins.[107,108] While chirality is inherently a qualitative property, chiral optical systems can be quantitatively described using parameters such as optical activity (OA)/optical rotation (OR) and circular dichroism (CD)/circular conversion dichroism (CCD). OA/OR and CD/CCD quantify the rotation of the polarization plane of linearly polarized light and the differential transmittance/reflectance of left-circularly polarized (LCP) *versus* right-circularly polarized (RCP) light, respectively. Natural materials typically exhibit weak chiral optical properties due to the large mismatch between their atomic feature sizes and optical wavelengths.[109,110] Plasmonic systems, however, are promising solutions to this limitation because of their strong light–matter interactions. Consequently, methods to enhance and tailor the chiral optical response in plasmonic systems are highly valued.

Plasmonic chirality is usually categorized into intrinsic and extrinsic chirality. Intrinsic chirality arises from the geometry of the nanostructure itself, where the structure lacks any internal symmetry planes that would render it achiral. An intrinsically chiral plasmonic nano-object remains chiral irrespective of how it is illuminated because its handedness is "built into" its three-dimensional (3D) form. This intrinsic handedness cannot be altered by changing external parameters such as the incident angle or polarization of light.[111] A classic example is a spring-shaped (helical) metal nanostructure (Fig. 8a). Such a helix has a well-defined right- or left-handed geometry, ensuring a robust chiral response (*e.g.*, CD, OR) under various illumination conditions. In contrast, extrinsic chirality is not an inherent property of the structure but is induced by the specific illumination conditions. For instance, a plasmonic split ring resonator, typically an achiral object, can exhibit a chiral optical response when the incident wave vector does not lie in its symmetry plane

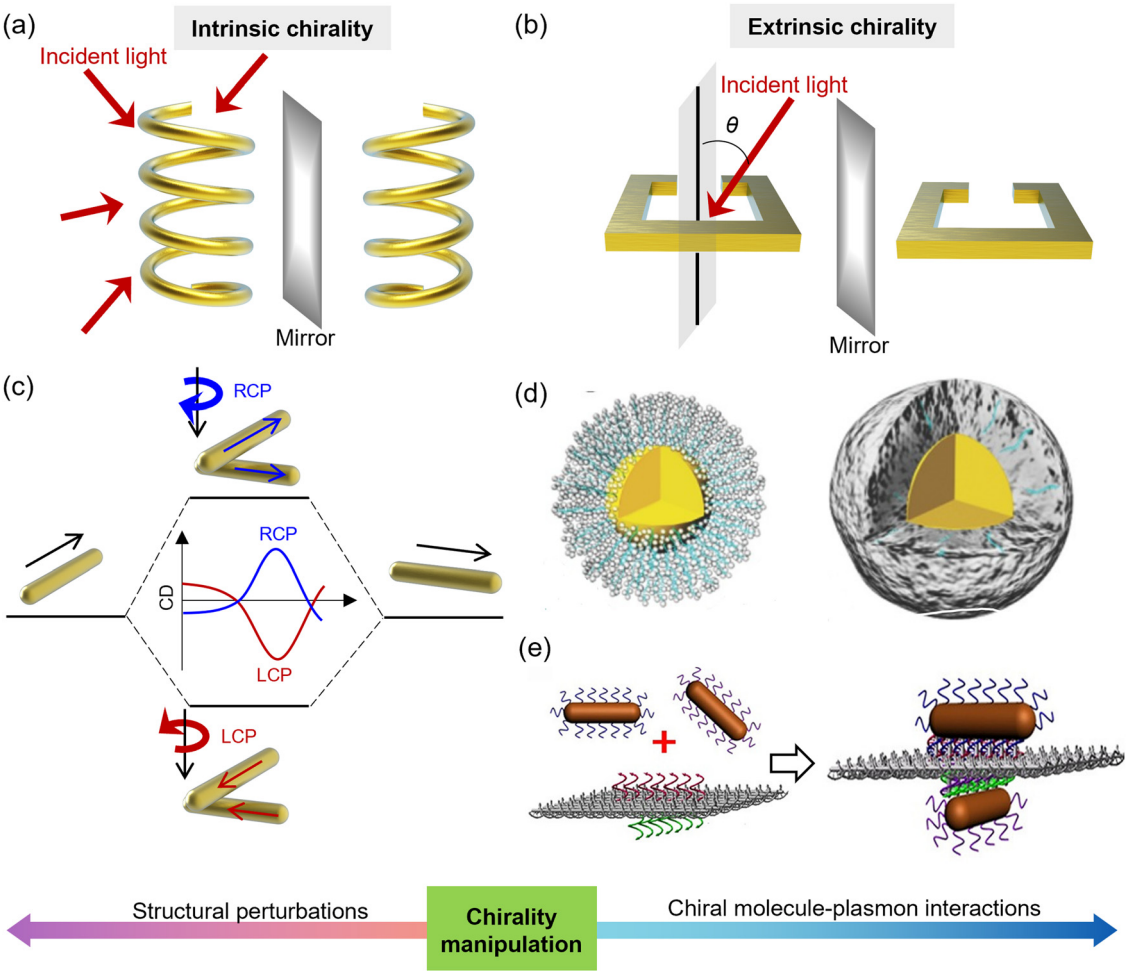

Fig. 8 Strategies for achieving plasmon-enhanced chirality. (a) Schematic view of intrinsic 3D chirality using plasmonic spring-shaped nanostructures. (b) Schematic view of extrinsic 3D chirality using a plasmonic split ring resonator. (c) Designing plasmonic chirality *via* structural perturbations. (d) Designing plasmonic chirality *via* interactions between chiral matter and plasmonic structures. Adapted with permission from ref. 113; Copyright 2014 John Wiley and Sons. (e) Fabrication of chiral nanostructures using double-sided DNA origami. Adapted with permission from ref. 114; Copyright 2013 American Chemical Society.

(Fig. 8b).[112] This phenomenon is especially useful for tunable or reconfigurable plasmonic devices. By simply rotating the sample or changing the polarization and angle of the incident beam, devices can dynamically respond to external stimuli (*e.g.*, changes in the environment, polarization switching), making them suitable for sensing applications and adaptive optics.

Next, we introduce two strategies for manipulating chirality: plasmonic structural perturbation and interaction with chiral molecules. Structural perturbation involves inducing a strong chiral optical response by altering the structure within the plasmonic system, as illustrated in Fig. 8c. In such systems, the chirality of the dimeric plasmonic nanorods is determined by the overall system's chirality rather than that of individual nanorods, because the chiral signal from the dimeric system significantly exceeds that of single nanorods. When coupled with chiral molecules, the dimeric nanorod system exhibits stronger and broader chiral responses compared to single nanorods.[115] This plasmonic chirality can be explained by plasmon hybridization theory, which provides an intuitive understanding of how plasmonic modes in coupled nanoparticles interact (Fig. 8c).[116,117] This theory explains the splitting of isolated plasmonic modes into bonding and antibonding states. However, the accuracy of this theory diminishes as the system size increases, due to its reliance on an electrostatic approach. Another method to manipulate chirality is through plasmonic interaction with chiral molecules. For achiral nanoparticles, when chiral molecules assemble on their surface, the entire system becomes chiral, effectively enhancing the weak chirality of the molecules. For instance, Wu *et al.* utilized a DNA-template growth process to create gold core-DNA-silver shell nanoparticles (Au/(DNA-Ag) core–shell NPs), as shown in Fig. 8d.[113] They used cytosine-rich single-stranded DNA to guide the growth of the silver shell around the gold core. The resulting nanoparticles exhibited intense and robust chiroptical responses at the silver plasmon band, with a high anisotropy factor.

There are two primary fabrication methods for realizing plasmonic chirality: top-down and bottom-up techniques.[118–120] Top-down techniques include electron-beam lithography (EBL), focused ion beam (FIB) milling, photolithography, reactive ion

etching (RIE), and others.[120] These methods start from a bulk structure and create nanoscale designs through lithography, etching, and deposition, making them more suitable for fabricating nanostructures with intrinsic chirality. Bottom-up techniques include chemical synthesis, ALD, and self-assembly.[120] Self-assembly is a notable approach within this category,[121] employing chiral templates, discrete DNA strands, and DNA origami templates to organize metal nanoparticles into chiral plasmonic assemblies. Chiral templates, such as biomacromolecules and polymers,[122] are powerful tools for guiding the formation of plasmonic nanostructures with strong chiral responses on a large scale. Self-assembly with discrete DNA strands leverages the highly specific interactions between complementary DNA sequences to create rationally programmable DNA nanostructures, where the distances between particles can be precisely controlled by the lengths of the DNA linkers. DNA origami templates involve the folding of a long DNA scaffold strand by using hundreds of designed short oligonucleotides. For example, Lan *et al.* used bifacial DNA origami as a template to direct the self-assembly of gold nanorods (AuNRs) into 3D nanoarchitectures (Fig. 8e).[114] They finely tuned the spatial configuration by adjusting the location of the AuNRs on the origami template, successfully creating discrete 3D nanorod dimer nanoarchitectures with tailored optical chirality.

2.6 Plasmonic waveguide resonance

Optical waveguides are essential components in fiber optic and photonic integrated circuit technologies, benefiting significantly from active photon manipulation to enhance their passive guidance mechanisms.[123–129] Emerging applications, such as PICs, demand faster nanoscale waveguide circuits that facilitate stronger light–matter interactions and lower power consumption.[130,131] However, all-dielectric waveguides face inherent limitations in miniaturization, restricted to approximately half the wavelength in the dielectric. If the waveguide's lateral dimensions fall below this threshold, light is no longer tightly confined within the waveguide and begins to leak out.

True nanoscale modal confinement can only be achieved using metals. In this configuration, photons couple with oscillating charges on the metal surface, forming surface plasmons with an effective modal area that is significantly smaller, *i.e.*, several orders of magnitude below the diffraction limit. This results in extreme confinement, albeit with substantial linear optical losses due to intrinsic electronic damping. Despite this drawback, metallic waveguides are considered revolutionary platforms capable of addressing the inherent limitations of all-dielectric nonlinear devices.

There are three classes of chip-scale plasmonic structures: plasmonic slab waveguides, plasmonic slot waveguides, and hybrid plasmonic waveguides. As shown in Fig. 9a, the plasmonic slab waveguide consists of a dielectric–metal–dielectric structure.[132] The thickness of the metal layer significantly affects the modes and propagation of SPPs. For a thick metal layer, it behaves like a semi-infinite metal/dielectric interface that supports transverse magnetic (TM) SPP modes. The penetration depth of SPPs in the metal is determined by the frequency of the incident light (upper panel of Fig. 9b). In the near-infrared range, the electric field is weakly confined transversely on the metal, with a metal penetration depth of 20–30 nm. For visible light wavelengths, the TM confinement of the electric field becomes stronger, resulting in local intensity enhancement. This weak field confinement at longer wavelengths limits the use of bulk SPP-based waveguides in applications such as PICs.[133] Therefore, significant research has been conducted to achieve field enhancement by reducing the waveguide dimensions to subwavelength sizes. At this scale, the two supported SPP modes on either side of the film can couple through their evanescent tails, generating antisymmetric and symmetric modes (lower panel of Fig. 9b), known as short-range (SR) and long-range (LR) SPPs, respectively. The responses of SR-SPPs and LR-SPPs to changes in metal thickness differ.[134] As the metal thickness increases, the loss of SR-SPPs increases and the near-field confinement becomes weaker. Conversely, for LR-SPPs, the loss decreases and the near-field confinement becomes stronger with increasing metal thickness. Metals can be as thin as a single nanowire. For instance, O'Carroll *et al.* developed a plasmonic waveguide based on nanoscale single nanowires using a melt-assisted wetting method with porous alumina templates.[135] These nanowires exhibit blue photoluminescence under ultraviolet (UV) illumination and can function as nanoscale active optical waveguides, allowing photoluminescence to propagate along the wire and out-couple at the tips.

Plasmonic slot waveguides consist of a sub-wavelength air slot flanked by two optically thick gold films, as illustrated in Fig. 9d. When the metal/air SPP modes on either surface are brought close together, they couple to form symmetric and antisymmetric modes.[137] The symmetric mode, in particular, produces sub-wavelength lateral confinement and a low group velocity. As the gap size increases, the loss of slot waveguides increases, and the near-field confinement becomes weaker. For instance, Thomaschewski *et al.* developed a plasmonic slot waveguide consisting of two gold nanostripes on lithium niobate substrates (Fig. 9e).[136] This waveguide supports two quasi-transverse electromagnetic (quasi-TEM) modes, specifically the odd and even modes, propagating along the gap. Due to the lithium niobate substrate, ultra-compact switching and modulation functionalities can be achieved by applying a voltage across the gap. This design achieves a 90% modulation depth with a 20-μm-long switch, owing to the strong overlap of slow-plasmon modes and electrostatic fields (Fig. 9f). Additionally, the waveguide exhibits a flat frequency response up to 2 GHz and a 3-dB bandwidth of 9 GHz, indicating its potential for high-speed optical communication applications.

Hybrid plasmonic waveguides, which often utilize multiple materials in intricate configurations, aim to minimize losses while maintaining nanoscale confinement. As illustrated in Fig. 9g, a typical hybrid waveguide consists of a dielectric waveguide adjacent to a metal, separated by a low-index spacer. By adjusting the spacer thickness, this design can balance the advantages of low losses and high confinement. For example, Oulton *et al.* developed a hybrid waveguide comprising a dielectric nanowire separated from a metal surface by a nanoscale dielectric gap, allowing for subwavelength optical confinement

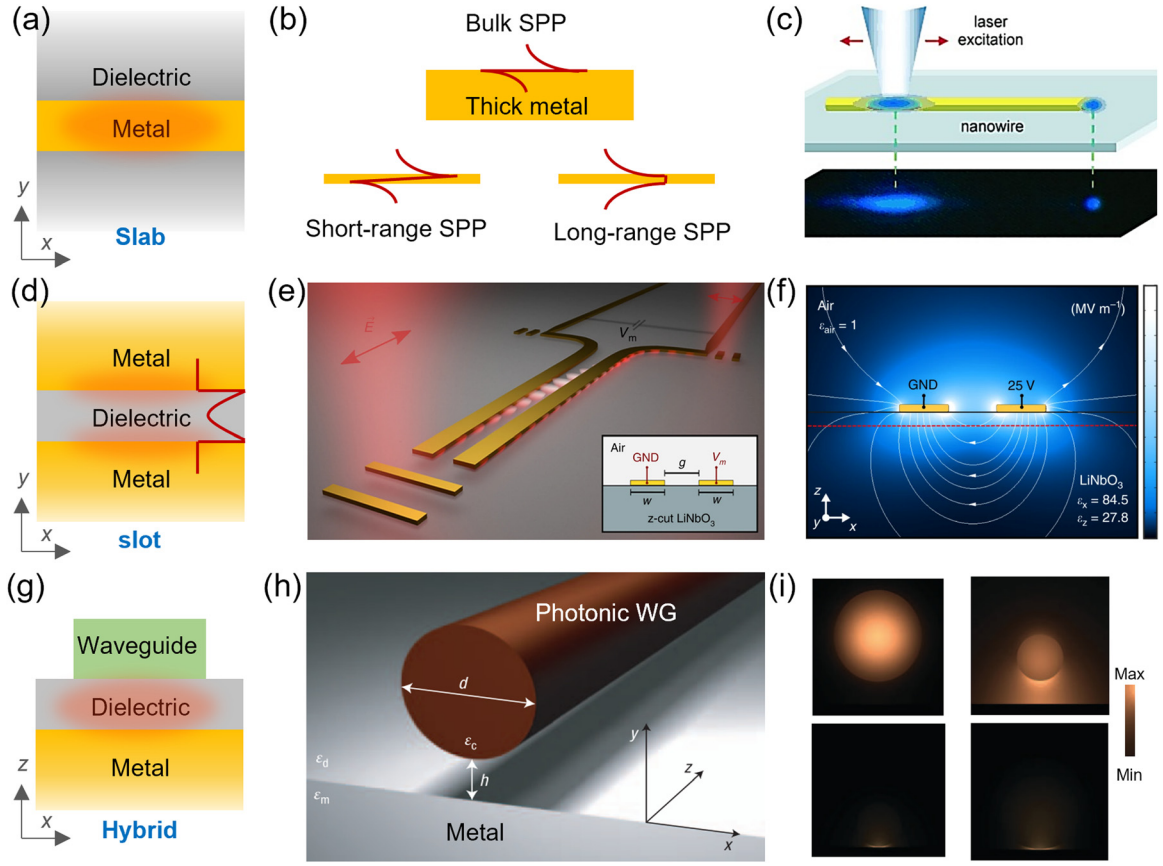

Fig. 9 Strategies for achieving plasmon-enhanced waveguides. (a) Schematic view of plasmonic slab waveguides. (b) Schematic of the bulk SPP (upper panel), short-range SPP (lower left panel), and long-range SPP (lower right panel). (c) Example of a plasmonic single-nanowire waveguide. Adapted with permission from ref. 135; Copyright 2007 John Wiley and Sons. (d) Schematic view of plasmonic slot waveguides. (e) Example of plasmonic slot waveguides. Adapted with permission from ref. 136; Copyright 2020 Springer Nature. (f) Color-coded electric field of the slot waveguides. (g) Schematic view of hybrid plasmonic waveguides. (h) Example of hybrid waveguides. Adapted with permission from ref. 13; Copyright 2008 Springer Nature. (i) Electromagnetic energy density distributions for hybrid waveguides with different gap size.

and long-range propagation (Fig. 9h).[13] This approach enables subwavelength transmission with strong mode confinement and long propagation distances, surpassing the performance of conventional plasmonic waveguides. The confined hybrid mode's size is more than 100 times smaller than the area of a diffraction-limited spot.

2.7 Section summary

In summary, this section introduces and analyzes the optical multi-effects of plasmons. We explore a range of phenomena, including plasmon–phonon coupling, plasmonic nonlinear optical effects, EIT, plasmonic chirality, plasmonic nanocavity resonance, and plasmonic waveguide resonance. Through this detailed examination, we demonstrate how fundamental plasmonic effects can evolve into complex optical multi-effects, embodying the integration of multiple optical phenomena. Nevertheless, these optical multi-effects continue to present challenges.

First, designing multi-functional nanostructures is a critical challenge in plasmonics, especially when aiming to integrate multiple optical effects and others within a single platform. The primary difficulty lies in creating nanostructures that can simultaneously support and optimize multiple plasmonic modes, each of which may have different spatial, spectral, and material requirements. Achieving this requires intricate design processes and precise material engineering, where the physical and chemical properties of the nanostructures must be finely tuned to ensure that the desired effects can coexist without unwanted interference. For instance, Ag nanoparticles and graphene nanoribbons are combined to create a multi-functional substrate capable of enhancing both SERS and SEIRAS.[138] This achieved significant EF for both SERS (up to 10^5) and SEIRAS (up to 170 times), enabling the extraction of complementary vibrational modes from molecules. Other integration strategies for multi-functional nanostructures could be layered structures, hybrid nanomaterials, tunable nanostructures, and multi-modal resonators. Specifically, for layered structures, one layer might be engineered to excite plasmons, while another is designed to excite phonons. By carefully controlling the thickness and material composition of each layer, it is possible to create a structure that supports both effects without significant cross-talk or interference.[47] Besides, tunable nanostructures are designed to

allow dynamic control over their plasmonic properties. By using materials that can change their optical characteristics in response to external stimuli (*e.g.*, electric fields, temperature, or chemical environment), these structures can be adjusted to optimize different plasmonic effects as needed. This tunability is particularly useful in applications where the conditions of measurement may vary, requiring different optical effects to be prioritized at different times. In terms of multi-modal resonators, they can support different resonant frequencies corresponding to different optical effects. The key challenge here is to design the resonator geometry in such a way that the different modes do not interfere with each other, while still providing strong field enhancement for each effect.

Second, effect synergy and optimization are also challenging. Integrating multiple optical effects in plasmonic nanostructures requires not only the individual optimization of each effect but also ensuring that these effects work synergistically when combined. Effect synergy refers to the ability of different plasmonic effects—such as SERS, SEF, and LSPR—to enhance each other's performance when integrated into a single platform. However, achieving this synergy is challenging due to the distinct and sometimes conflicting requirements of each effect. Specifically, one challenge in achieving synergy could be conflicting design requirements. Each plasmonic effect typically has specific design requirements that may conflict with those of other effects. For example, SERS often requires sharp metallic nanostructures with high curvature to generate intense localized electromagnetic fields, while SEF might require broader surfaces or different geometries to optimize fluorescence signal enhancement. Balancing these conflicting requirements in a single nanostructure is a major challenge in effect synergy. Besides, synergistic enhancement typically requires that the different effects operate within the same spectral and spatial regions. However, the resonant conditions for different effects might not naturally overlap. For instance, SERS and LSPR might occur at different wavelengths, necessitating careful tuning of the nanostructure's geometry and material properties to bring these effects into spectral alignment.

Third, balancing the spatial distribution is challenging. Field localization and distribution refers to the concentration of electromagnetic fields in a small region, often at the surface of a metallic nanostructure, where the field intensity can be orders of magnitude higher than that in the surrounding medium. This localized enhancement is crucial for amplifying weak optical signals, making it a key aspect of plasmonic devices. The challenge in field localization and enhancement lies in balancing the spatial distribution of the localized fields across the nanostructure. Different plasmonic effects often require specific spatial configurations of the enhanced fields. For instance, SERS typically benefits from "hot spots"—regions of extremely high field intensity at sharp features or junctions between nanoparticles—while other effects, such as SEF, may require a more uniform field distribution over a larger area. Achieving the right balance in the spatial distribution is challenging because it requires precise control over the nanostructure's geometry, size, and material composition.

3. Mechanics of plasmonic optical-electric-acousto-thermal fusion

3.1 Plasmonic fusion with electronics

The combination of plasmonics and electronics is achieved using hot electrons as a "bridge". The process associated with hot electrons includes plasmon generation and decay, and hot-electron generation, injection, and regeneration (Fig. 10a). The excitation and decay of plasmon have been introduced in the previous article. Plasmons are excited by incident light of a specific frequency and they dissipate their energy through radiative and non-radiative decay. The decay process is related to hot electrons, which can be traced back to 1996, when Zhao *et al.* observed the photocurrent in the TiO_2 anode by irradiating TiO_2 electrodes covered with gold or silver nanoparticles with visible light.[139] This is a surprising result because conventional TiO_2 generates photocurrent only when illuminated by UV light. The mechanism by which TiO_2 generates photocurrent under visible light irradiation is still unclear. In 2003, the mechanism was ascribed to plasmon-induced charge separation and oxidation by Ohko *et al.*[140] Subsequent studies demonstrated the three processes required to generate the photoinduced current: hot electron generation, injection, and regeneration.[141,142] Following these pioneering studies, plasmonic hot electrons have been widely used in photovoltaic and catalytic devices. Injecting and conducting away hot electrons before carrier recombination is a key factor in the fusion of plasmonics and electronics. A common injection method is to allow plasmon particles to contact a semiconductor (such as TiO_2), forming Schottky junctions to extract hot electrons.[143] The hot-electron generation and injection in TiO_2 can be completed within 50 fs.[144] The next step is hot-electron regeneration, which is to harness the energy of hot electrons before they thermalize. This can be done by transferring the energy to a different system. Carrier regeneration using liquid electrolytes or a hole-transporting material is effective. For instance, electron donor solutions containing Fe^{2+} were demonstrated to accelerate carrier regeneration.[145] To further improve the energy conversion efficiency of this process, it is crucial to optimize the donor solution or hole-transporting materials to achieve faster hot electron injection and regeneration before energy loss occurs due to electron–electron collisions.[146]

Surface plasmons are collective vibration modes of free electrons under optical excitation, which have the potential to combine electrical effects naturally. Plasmon-based electrical effects offer clear benefits in applications involving light-trapping, electron transfer, and energy transfer (Fig. 10b).[147] For instance, the enhanced light-trapping capability is advantageous for plasmon-based electrical applications, such as photodetectors, solar cells, and photocatalysis.[148–152] These applications involve energy harvesting and electron transfer.[153] Therefore, we next examine these processes in detail.

3.1.1 Light trapping. Plasmonic metal nanostructures can enhance the light absorption/trapping performance of photovoltaic absorber layers without increasing their physical thickness. Three approaches are shown in Fig. 11a. First, the light scattering effect of metal nanoparticles can be used to couple

and trap freely propagating plane waves into absorbing semiconductor films. In this case, the nanoparticles are on the semiconductor surface, and a metal reflective layer is added to increase the path of light in the film (left panel of Fig. 11a). Secondly, metal nanoparticles can be placed at the interface of different semiconductor materials (middle panel of Fig. 11a). In this configuration, the nanoparticles function as antennas, generating strong local electric fields, which enhance the efficient light absorption in the photosensitive layer. Finally, plasmonic metal nanostructures are placed on the back side of the surface in the form of periodically arranged nanoarrays (right panel of Fig. 11a). In this case, the plasmonic structures couple light into the SPP modes supported by the metal/semiconductor interface and into the guided modes in the semiconductor slab, thereby converting light into photocarriers in the semiconductor. Kim *et al.* demonstrated that the overall power conversion efficiency was increased from 3.05% to 3.69% by incorporating plasmonic Ag nanoparticles on surface modified transparent electrodes (Fig. 11b).[154] The conversion efficiency is strongly affected by the size, type, dielectric environment, and shape of the metal structure. For instance, cylindrical and hemispherical particles showed higher path length enhancements than spherical particles (Fig. 11c), with Ag particles being more effective than Au.[155]

3.1.2 Hot-electron transfer. After light is captured, hot electrons will be generated on the metal surface and transferred to adsorbed molecules *via* direct and indirect ways (Fig. 12a). In the direct transfer mechanism, these hot electrons are transferred directly from the metal nanostructure to the adsorbed molecules. This process occurs at the metal–molecule interface *via* resonant plasmon-driven electron excitation. For the transfer to be efficient, the energy of the hot electrons must match the energy levels of the unoccupied molecular orbitals of the adsorbed molecules. This energy overlap allows the hot electrons to be injected into the lowest unoccupied molecular orbital (LUMO) of the molecule. The injection of hot electrons can weaken intramolecular bonds within the adsorbed molecules, reducing the energy barrier for chemical reactions.[156] This can enhance the rate of photocatalytic reactions, making the process highly efficient for applications like solar-to-chemical energy conversion.[157] Notably, the direct transfer of hot electrons competes with other processes such as electron–phonon scattering, which can lead to the loss of hot electrons before they can be transferred to the molecules. This mechanism was experimentally demonstrated by Boerigter *et al.* by using wavelength-dependent Stokes and anti-Stokes SERS and kinetic analysis of the photocatalytic reaction in a silver nanocube–methylene blue

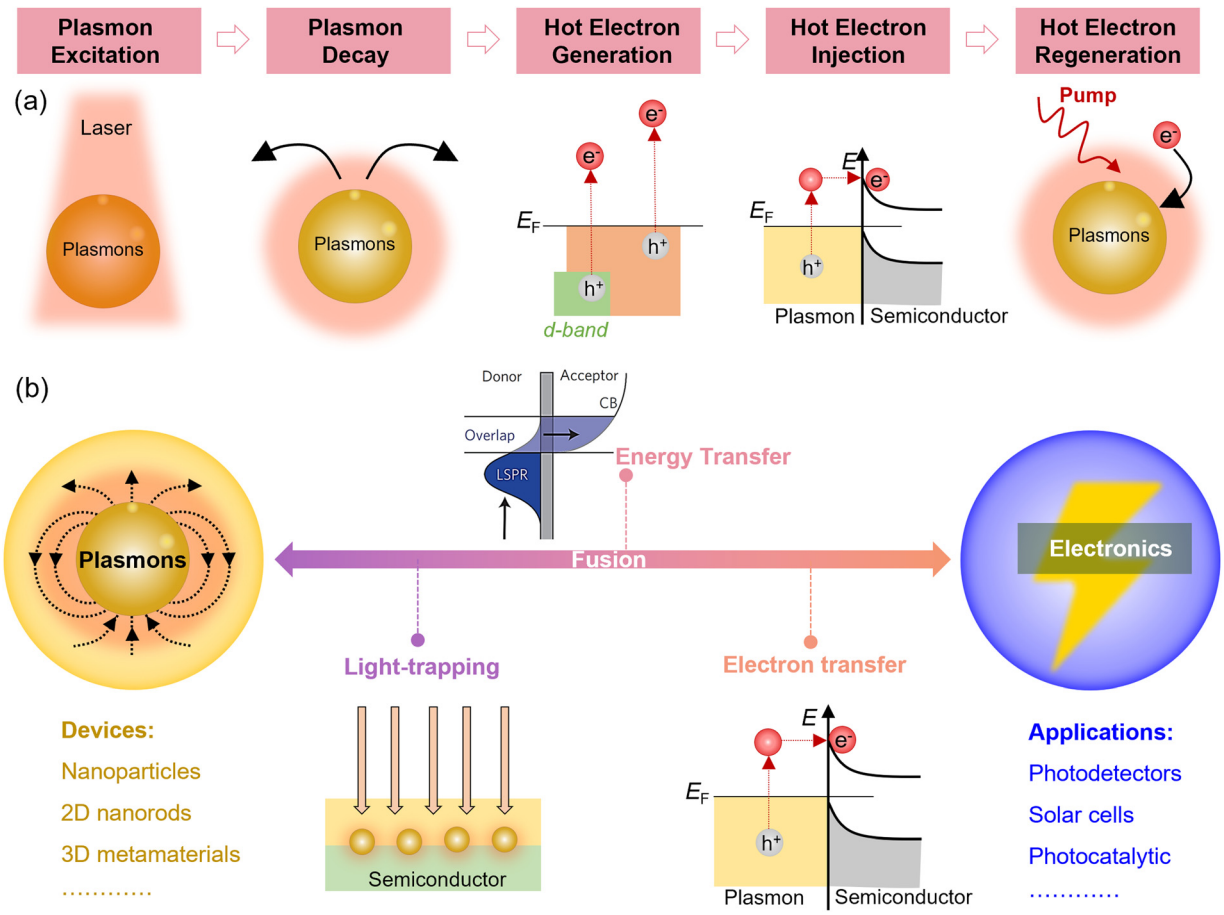

Fig. 10 Plasmonic fusion with electronics. (a) Schematic view of plasmon generation and decay, hot-electron generation, injection, and regeneration. (b) Plasmonic fusion with electronics *via* light-trapping, electron transfer, and energy transfer.

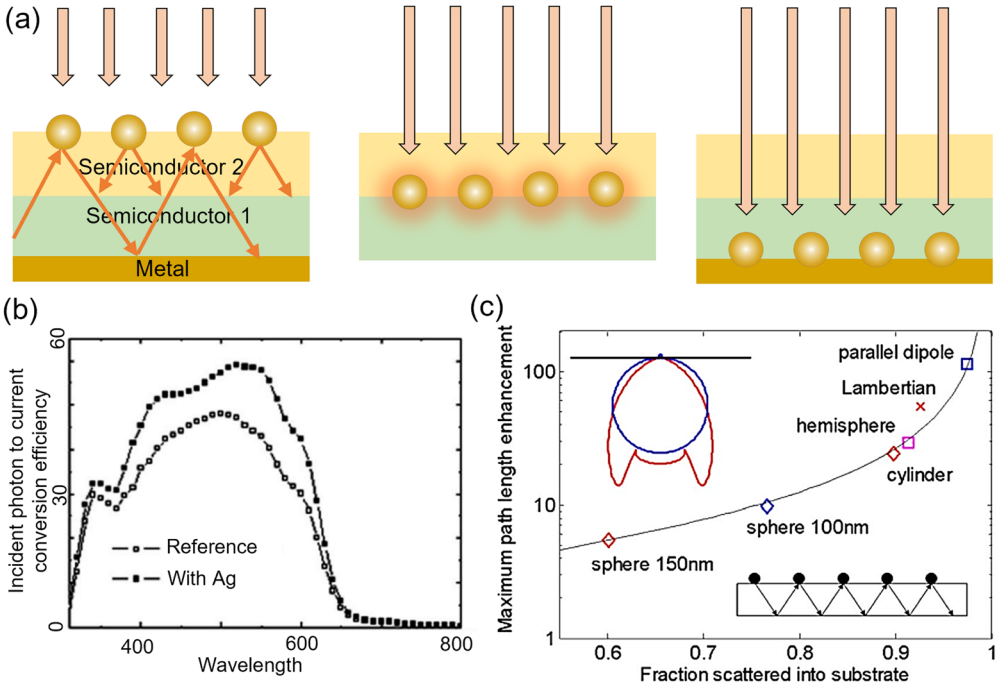

Fig. 11 Plasmonic light-trapping mechanism. (a) Schematic view of the mechanism, including the plasmonic light scattering effect (left panel), the excitation of plasmons in nanoparticles embedded in the semiconductor (middle panel), and the excitation of plasmons at the metal/semiconductor interface (right panel). (b) Performance of solar cells with/without plasmonic light-trapping. Adapted with permission from ref. 154; Copyright 2008 AIP Publishing. (c) Effect of plasmonic structure shape on light trapping. Adapted with permission from ref. 155; Copyright 2008 AIP Publishing.

system (Fig. 12b).[158] They found that the methylene blue molecule was more active at 785 nm than at 532 nm, based on the contrast of the anti-Stokes *versus* Stokes signals. Plasmon-generated hot electrons are more efficiently transferred to methylene blue molecules under irradiation with longer wavelengths, which contradicts the prediction of the conventional two-step electron transfer mechanism. Therefore, they believe that the direct charge transfer mechanism plays a significant role, leading to accelerated rates of chemical decomposition or desorption of molecules on the nanoparticle surface.

The indirect transfer of hot electrons from metal nanostructures to adsorbed molecules involves a more complex process compared to direct transfer. After the generation, hot electrons undergo a process called thermalization. This involves electron–electron scattering, which redistributes the energy among the electrons, leading to a Fermi–Dirac distribution of hot electrons and holes. In the indirect transfer mechanism, the thermalized hot electrons can spill over from the metal nanostructure into the surrounding environment. This spillover occurs when the hot electrons transiently leave the metal surface and interact with the adsorbed molecules. During the spillover, the hot electrons can transfer their energy to the adsorbed molecules. This energy transfer can destabilize the molecular bonds, facilitating chemical reactions.[160] The interaction often leads to the excitation of molecular vibrations, which can lower the activation energy for subsequent reactions. Notably, the indirect transfer process competes with other relaxation mechanisms, such as electron–phonon scattering, which can lead to the loss of hot electrons before they can interact with the adsorbed molecules. Taking the room temperature dissociation of H_2 as an example (Fig. 12c),[159] surface plasmons excited in the Au nanoparticles decay into hot electrons, which transfer into a Feshbach resonance of an H_2 molecule adsorbed on the Au surface, triggering dissociation.

3.1.3 Energy transfer *via* dipole–dipole coupling. In addition to light trapping and hot-electron transfer, the third mechanism in the plasmon enhancement process is energy transfer *via* dipole–dipole coupling, which can greatly enhance the efficiency of solar energy harvesting. In this case, the plasmonic metal absorbs sunlight and then transfers the absorbed energy from the metal to the semiconductor *via* dipole–dipole coupling, generating electron–hole pairs below and near the semiconductor band edge (Fig. 13a).[161] The energy trapped in the semiconductor can be extracted and stored *via* an external circuit. This process is denoted plasmon-induced resonant energy transfer (PIRET).[162] Notably, PIRET is a method of optical extraction rather than extending the absorption of the semiconductor *via* interfacial charge transfer. Another energy transfer mechanism in semiconductors is Förster resonance energy transfer (FRET) describing energy transfer between two light-sensitive molecules (chromophores).[163] FRET involves a donor chromophore in an excited electronic state transferring energy to an acceptor chromophore through non-radiative dipole–dipole coupling. This process is highly distance-dependent, typically effective over 1–10 nanometers. Unlike FRET, PIRET does not involve a Stokes shift and is strongly dependent on the plasmon's dephasing rate and dipole moment. PIRET can transfer energy towards shorter wavelengths (blue-shifted), whereas FRET typically involves energy transfer to

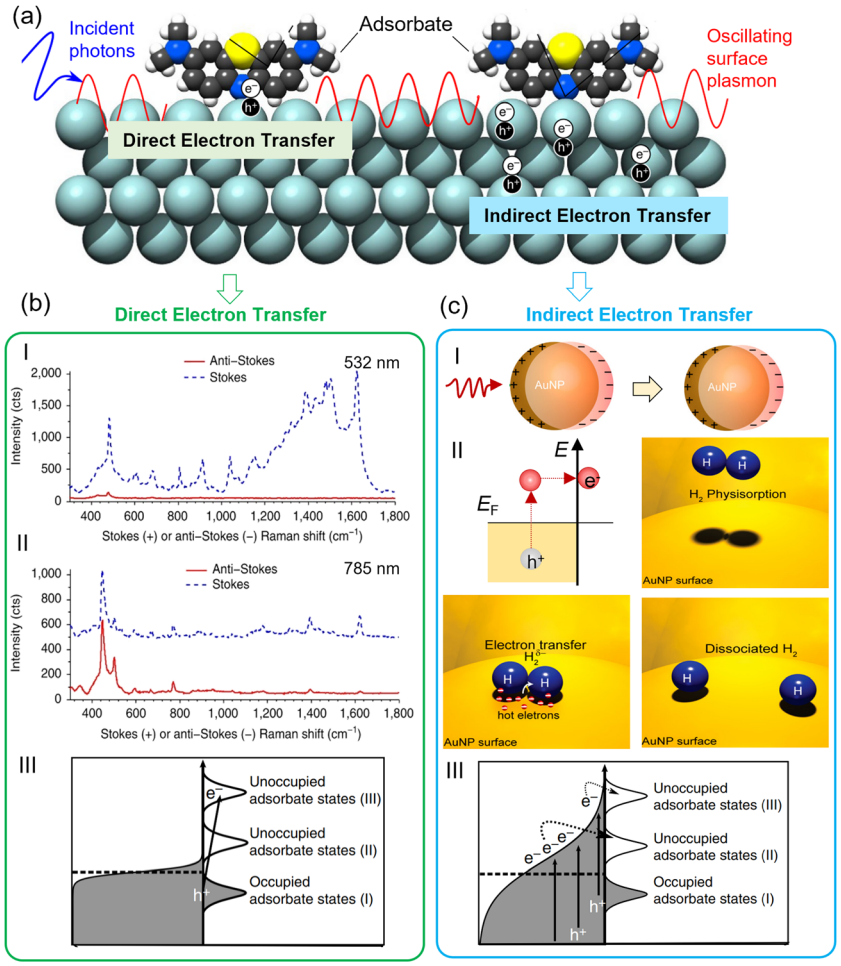

Fig. 12 Plasmonic electron transfer mechanism. (a) Schematic view of the metal/adsorbate system. (b) Direct electron transfer mechanism in metal/adsorbate systems. Adapted with permission from ref. 158; Copyright 2016 Springer Nature. (I, II)Raman spectra of methylene blue with excitation wavelengths of (I) 532 nm and (II) 785 nm. (III) Schematic diagram of the energy levels of direct electron transfer. (c) Indirect electron transfer mechanism. Adapted with permission from ref. 159; Copyright 2013 American Chemical Society. (I) Schematics of plasmon-induced hot electron generation on AuNPs. (II) Schematic diagram of H_2 dissociation on the AuNP surface. (III) Schematic diagram of the energy levels of indirect electron transfer.

longer wavelengths (red-shifted). PIRET involves non-local absorption effects, which means the energy transfer can occur over larger distances compared to FRET (Fig. 13b). PIRET for solar harvesting requires design considerations. First, PIRET is best suited for thin semiconductors to reduce recombination losses and increase absorption within the decay length of the plasmon field. Second, PIRET only occurs when spectral overlap is maintained and is best used to increase the population of carriers in spectral regions where semiconductor absorption is weak, such as near band edges. Finally, although the plasmon-metal interface has traditionally been considered only as a Schottky barrier that modifies the carrier lifetime, the relative dephasing times of the plasmon and semiconductor must be considered to achieve an efficient PIRET.[164]

PIRET involves resonant energy transfer from localized surface plasmons—typically present in metal nanoparticles—to nearby semiconductors. Dominant material systems exploiting the PIRET mechanism include metal–oxide nanostructures[29,165,166] (such as Au–TiO_2 or Ag–TiO_2 heterostructures, as well as combinations like Au–ZnO, Ag–ZnO, and Au–CeO_2 used in photocatalysis, solar cells, and sensors), metal–chalcogenide composites (for example, Au–CdS, Au–Cu_2O, and Au–ZnS systems that enable visible-light-driven photocatalysis), and alloy nanoparticle–semiconductor configurations (where alloyed plasmonic nanoparticles like Au–Ag or Au–Pd are combined with semiconductors to provide tunable plasmon resonances matching specific semiconductor band gaps, thereby potentially boosting PIRET efficiency). In contrast, FRET describes dipole–dipole coupling between two light-sensitive species, with predominant material systems including organic dye molecules[167] (classic FRET pairs like Alexa Fluor dyes, rhodamine derivatives, and cyanine dyes commonly used in bioimaging and sensing due to their high extinction coefficients and well-defined spectral overlaps), quantum dots (semiconductor nanocrystals such as CdSe/ZnS or InP/ZnS that serve as FRET donors or acceptors because of their size-tunable emission spectra and relative photostability), and perovskite nanocrystals (emerging FRET donors or acceptors in hybrid optoelectronics, where lead halide perovskite nanocrystals

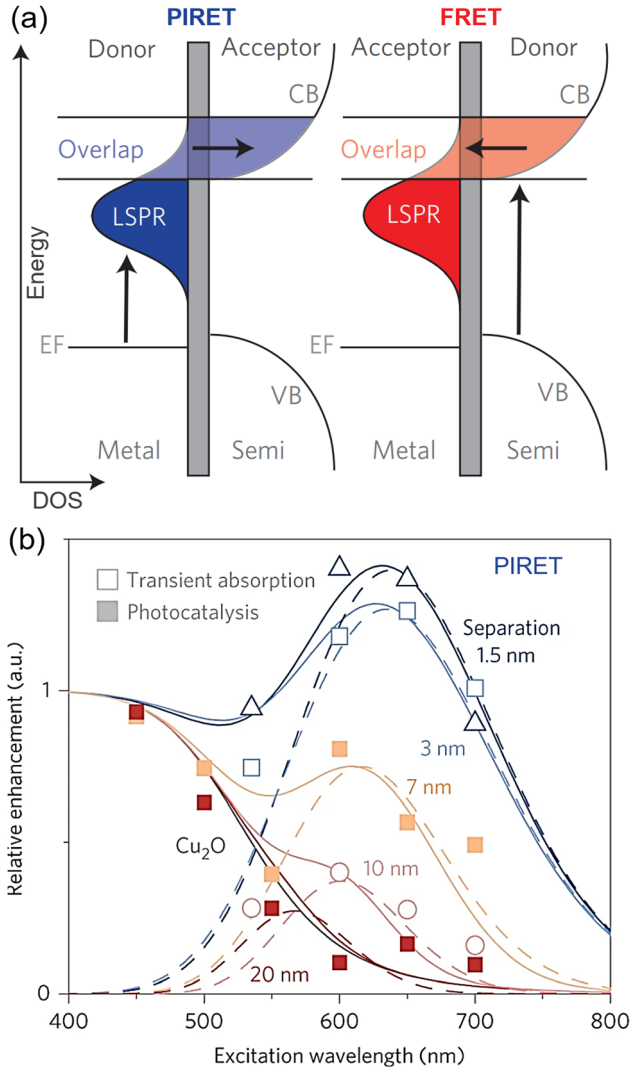

Fig. 13 Plasmonic energy transfer mechanism. (a) Comparison between plasmon-induced resonance energy transfer (PIRET) and Förster resonance energy transfer (FRET). Adapted with permission from ref. 161; Copyright 2015 Springer Nature. PIRET excites the coherent plasmon-to-semiconductor energy-transfer pathway, while FRET experiences an incoherent semiconductor-to-plasmon pathway. Both transfer energy by dipole–dipole coupling. (b) Enhancement of photoconversion by PIRET showing the distance dependence of the dipole–dipole interaction in PIRET.

like $CsPbBr_3$ exhibit bright photoluminescence along with well-defined absorption and emission overlaps for efficient energy transfer).

3.2 Plasmonic fusion with thermonics

Plasmonics, as described above, has a wide range of applications in electronics *via* hot electron enhancement in areas such as sensing and energy harvesting. In these studies, losses in the metal and the associated heat generation are often considered as side effects that must be minimized. Various strategies have been explored to reduce heat loss.[168] One approach involves material optimization, leading to the adoption of alternative plasmonic materials, such as all-dielectric materials, which exhibit lower ohmic losses compared to noble metals.[169] Structural engineering techniques, such as metal–insulator–metal configurations, have also been reported to enhance light confinement and reduce non-radiative losses by up to 50%.[53] Additionally, advanced resonator designs, including high-Q plasmonic resonators like bound states in the continuum (BIC) in continuous media, have been shown to improve energy confinement and minimize unnecessary heat generation.[170] Beyond these strategies, effective thermal management is essential to mitigate plasmonic heating. Excess thermal energy must be dissipated from plasmonic chips through conduction, convection, or radiation.[168] A recent study demonstrated a passive cooling system designed for high-performance plasmonic chips, leveraging enhanced thermal conduction and natural convection.[171] The results indicate that by integrating conventional cooling methods with well-designed thermal interfaces, self-heating can be significantly reduced, lowering the temperature of the system to a few Kelvins.

However, some studies have shown that with appropriate design, plasmon-related heat has great potential in thermal applications, which is called thermoplasmonics.[172] In 1999,[173] a seminal study utilized gold nanoparticles to generate heat and induce protein denaturation, highlighting the benefits of metal nanoparticles over traditional dyes due to their enhanced light–matter interaction at plasmonic resonance, which creates localized, high-temperature increments without thermobleaching or photobleaching. Despite its innovation, this work initially went unnoticed. Interest in nanoplasmonic heating surged with two key publications: one in 2002 introduced plasmonic photothermal imaging, combining modulated heating of nanoparticles with lock-in detection for precise positioning without photobleaching,[174] and the other in 2003 proposed plasmonic photothermal therapy for targeted cancer hyperthermia using gold nanoparticles.[175,176] These studies, alongside emerging applications like drug and gene delivery, established thermoplasmonics as a significant field, leveraging plasmonic nanoparticles as nanoscale heat sources for various innovative uses.[177–180]

Thermoplasmonics deals with the laws of heat generation and diffusion, and its core is not the propagation, interference and diffraction of light that are familiar in the field of optics. Key mechanisms in thermoplasmonics include local heating, radiative heat transfer, and thermal expansion (Fig. 14). Plasmonic nanoparticles can convert absorbed light into localized heat efficiently, which can be utilized for applications such as photothermal therapy and triggering chemical reactions.[181] Additionally, plasmons facilitate radiative heat transfer, allowing for efficient energy transfer between nanoparticles and their surroundings, enhancing thermal management in devices. Thermal expansion due to plasmonic heating can be harnessed to actuate nanoscale mechanical systems or to modify the properties of materials at the nanoscale, leading to innovative applications in nanoactuators. Next, we examine these processes in detail.

Plasmons undergo nonradiative relaxation *via* electron–electron collisions or electron-lattice phonon coupling, generating heat and increasing the surrounding temperature. The plasmonic heating process is shown in Fig. 15a.[182] When metal nanostructures are excited with resonant photons, the photoexcitation of the

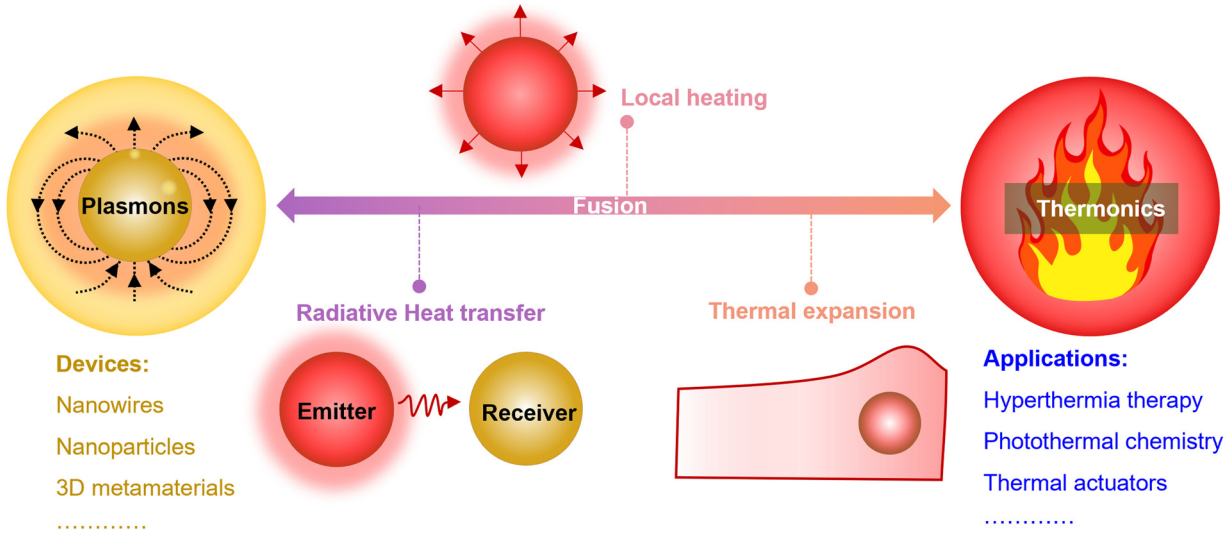

Fig. 14 Plasmonic fusion with thermionics. The plasmons enhance electronics *via* local heating, radiative heat transfer, and thermal expansion.

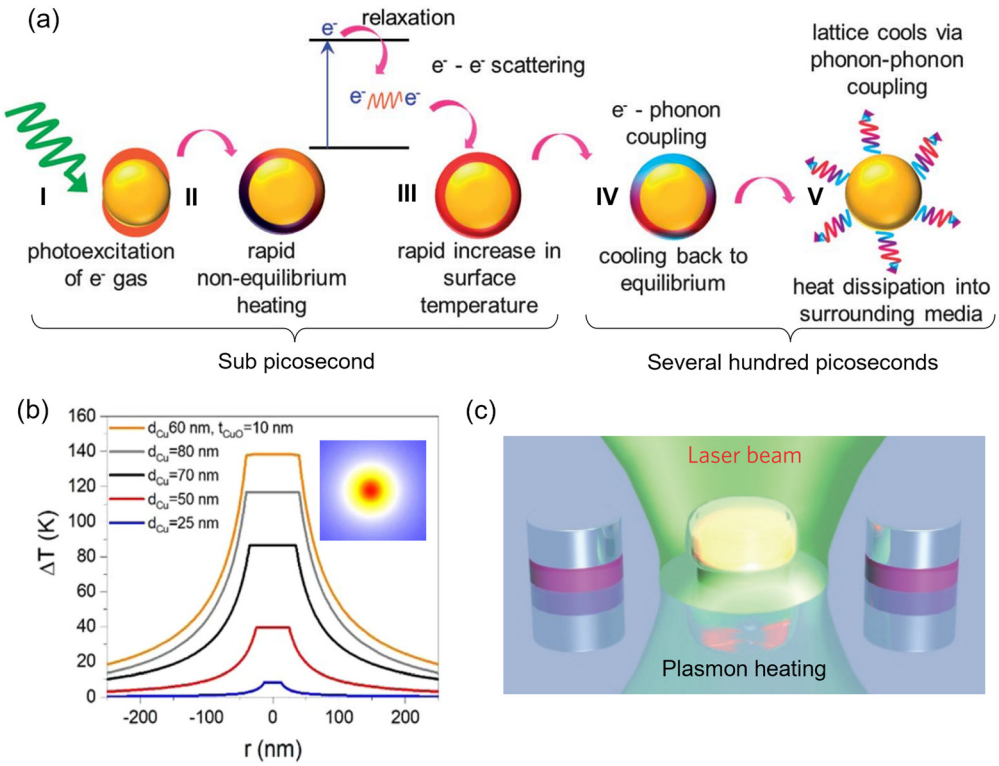

Fig. 15 Plasmonic local heating mechanism. (a) Principles of photothermal light conversion into local heat in nanoparticles. Adapted with permission from ref. 182; Copyright 2014 the Royal Society of Chemistry. The plasmonic heating process includes (I) photoexcitation of the electron gas, (II) non-equilibrium heating, (III) increase in the surface temperature, (IV) cooling to equilibrium, and (V) heat dissipation into the surrounding medium. (b) Temperature profile around 25 nm (blue), 50 nm (red), 70 nm (black), and 80 nm (grey) solid CuNPs under a constant laser power of 270 mW. Adapted with permission from ref. 185; Copyright 2020 Springer Nature. Inset: 2D heat profile of CuNPs. (c) Schematic illustration of the plasmonic heating for nanofabrication. Adapted with permission from ref. 186; Copyright 2016 Springer Nature.

electron gas results in rapid non-equilibrium heating. This process begins with the absorption of resonant light, causing collective oscillations of free electrons known as plasmons. These excited electrons quickly undergo electron–electron scattering within subpicosecond timescales, leading to a significant rise in the metal's surface temperature. Following this initial heating, the electrons transfer their energy to the lattice through electron–phonon coupling, bringing the system toward thermal equilibrium. This energy exchange happens rapidly, causing the lattice to heat up. In the subsequent hundred picoseconds, the

lattice cools down *via* phonon–phonon interactions, dissipating heat into the surrounding medium. This mechanism of localized heating and subsequent heat transfer into the environment has wide-ranging applications. In medical treatments like plasmonic photothermal therapy, the generated heat can selectively destroy cancer cells.[183] In catalysis, the localized heating can accelerate chemical reactions.[184] Moreover, this process is utilized in sensors and imaging technologies, where the heat-induced changes can produce detectable signals.

The temperature increase of plasmonic nanoparticles is affected by the laser power and the absorption cross section of nanoparticles. Fig. 15b shows the temperature profiles of three optically trapped CuNPs of different sizes under a constant laser power of 270 mW.[185] As observed, the temperature of the particle surface is the same, and the temperature rise decreases in the area away from the particle. In addition, the larger the particle, the higher its temperature. The generated local heating is not limited to being transferred to the surrounding medium, but can also be used to reshape the nanostructure itself. A representative example is plasmonic colour laser printing. As shown in Fig. 15c,[186] a laser is used to emit short, intense pulses of light onto the nanoimprinted metasurface, which generates localized heat due to the absorption of light. The localized heating causes the nanostructures to undergo thermal deformation. Depending on the laser parameters, the nanostructures can be reshaped in various ways, such as changing their size, shape, or orientation. The reshaping of the nanostructures alters their plasmonic properties, which in turn changes the way they interact with light. By precisely controlling the reshaping process, different colors can be produced. This is because the plasmonic resonances of the nanostructures determine the specific wavelengths of light they absorb and scatter. The method allows for extremely high-resolution color printing, with a resolution of up to 127 000 dots per inch (DPI). This is due to the precise control over the laser pulses and the nanoscale features of the metasurfaces.

In addition to thermal conduction, another way of heat transfer is near-field radiative heat transfer (NFRHT). This phenomenon arises when the distance between two objects is comparable to or less than their characteristic thermal wavelength, allowing energy to transfer through evanescent waves, such as frustrated modes and surface polaritons. Consequently, the heat flux in the near-field can be significantly greater than that of conventional far-field radiation. NFRHT becomes particularly pronounced when objects are separated by a vacuum gap smaller than their thermal characteristic wavelength. Research into NFRHT has uncovered intriguing effects, such as ballistic heat transport, thermal photon drag, and an unusual photon thermal Hall effect.[187] This line of study has led to innovative applications, including the development of thermophotovoltaic devices, near-field radiative cooling systems, and advanced thermal management solutions. Next, we introduce NFRHT by taking a system consisting of two monolayer bismuth selenide (Bi_2Se_3) sheets as an example, as shown in Fig. 16a.[188] The heat flux between them and their comparison with ITO and graphene are shown in Fig. 16b. For nanoscale

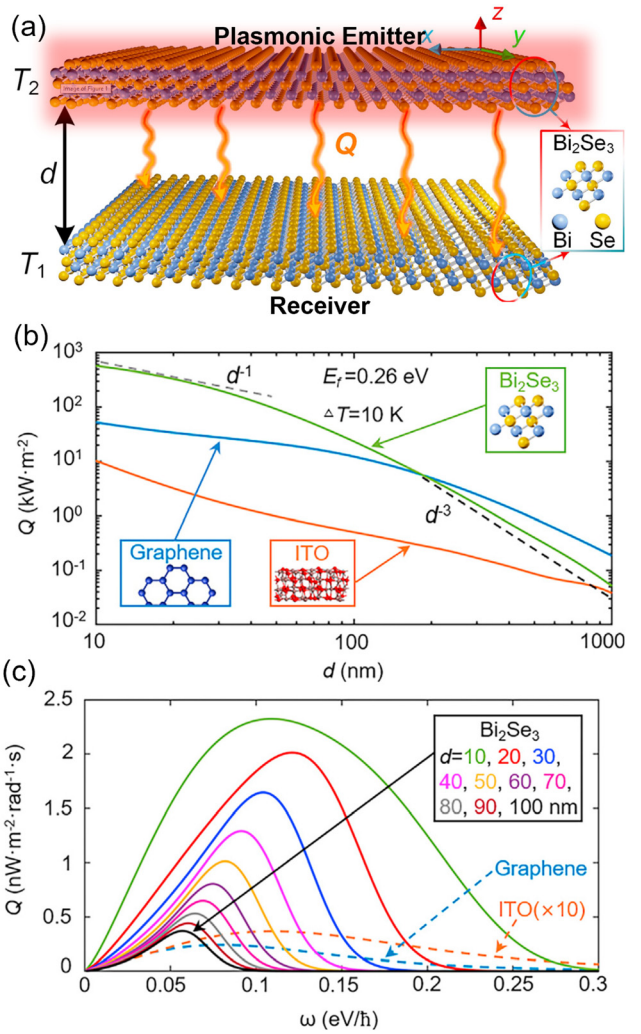

Fig. 16 Plasmonic radiative heat transfer mechanism. (a) Schematic of near-field radiative heat transfer between two sheets of bismuth selenide (Bi_2Se_3). (b) Heat flux Q of the monolayer Bi_2Se_3 sheet, monolayer graphene sheet, and bulk ITO, with different vacuum gaps. (c) Heat flux Q as a function of incident light frequency (ω) for two sheets of Bi_2Se_3 under different gaps d. Adapted with permission from ref. 188; Copyright 2021 Elsevier.

gaps, the NFRHT between two Bi_2Se_3 sheets is greatly enhanced, and its magnitude can be well above the blackbody limit. Moreover, the heat flux between Bi_2Se_3 sheets can exceed that of monolayer graphene and bulk ITO, especially at smaller gap distances. For NFRHT, the heat transfer distance is a key parameter. As the distance increases, the radiative heat flux of a single-layer Bi_2Se_3 sheet decreases monotonically due to the rapid decay of the localized density of states, and the corresponding NFRHT also decreases rapidly. In addition, the spectral radiation heat flux redshifts with increasing gaps (Fig. 16c). This redshift of the spectral radiation heat flux can be explained by the attenuation length, that is, surface polaritons located at high frequencies are more easily filtered out by larger vacuum gaps.[189]

Thermal expansion caused by uneven heating is another thermal feature. Nanostructures such as nanorods and nanowires have an uneven near-field distribution due to the lightning rod

effect, which leads to spatially distributed heat. Uneven thermal expansion is widely used in actuators. The concept of using plasmonic thermal expansion for actuation emerged due to the potential for precise and rapid control of mechanical movements at the micro- and nano-scale. Early demonstrations involved simple structures, such as cantilevers and membranes,[190] incorporating plasmonic materials that expanded upon light irradiation. In the 2010s, significant progress was made in developing plasmonic actuators.[191,192] Complex nanoscale devices that utilized plasmonic thermal expansion to achieve controlled movements were developed.[193] These actuators demonstrated high precision, fast response times, and the ability to operate at small scales. For instance, Linghu *et al.* demonstrated the plasmon-driven movement of gold nanowires on silica microfibres (Fig. 17a).[194] Specifically, plasmons are excited in metal nanowires using pulsed lasers, enhancing the heating effect and generating surface acoustic waves (SAWs). The heating causes the nanowire to expand and contract, creating a peristaltic crawling motion similar to an earthworm (Fig. 17b). The SAWs help the nanowires overcome strong surface adhesion forces, allowing precise movement along silica microfibres (Fig. 17c). This method achieves sub-nanometer positioning accuracy, low actuation power, and versatile on-chip manipulations (Fig. 17d and e).

Combining plasmonic nanoparticles with soft materials is another strategy to exploit thermal expansion. For instance, a bilayer structure combining gold nanoparticles with poly(*N*-isopropylacrylamide) and poly(acrylamide) was developed.[195] This system leverages the heating of gold nanoparticles upon exposure to their plasmon resonance wavelength, leading to differential thermal expansion between the two layers. Plasmonic resonances are particularly useful for achieving wavelength-specific responses. For example, an actuator utilizing AuNRs on polymethyl methacrylate (PMMA) was designed,[191] where careful tuning of the nanorods' dimensions allowed for sensitivity to various wavelengths in the visible and near-infrared spectra. Similarly, a wavelength-dependent actuator was developed by embedding copper nanorods in a PVA matrix.[193] In contrast, highly damped plasmonic nanostructures can be engineered for an ultrabroadband light response. This was exemplified by mechanically coupled arrays of iron nanodomes transferred onto thin polydimethylsiloxane (PDMS) layers, creating soft actuators responsive to light from UV to thermal infrared.[196] Applications of this technology include a self-regulating iris, an optical gripper, and an opto-mechanical electrical switch. Furthermore, a magnetic-plasmonic actuator consisting of hybrid Fe_3O_4/Ag nanorods within a photocurable polymer matrix was developed and modulated by altering the laser polarization.[197]

3.3 Plasmonic fusion with acoustics

The combination of plasmonics and acoustics represents a promising frontier in the field of wave-based technologies. Plasmons are renowned for their ability to manipulate light at the nanoscale, concentrating electromagnetic energy in tiny volumes. When these capabilities are harnessed alongside

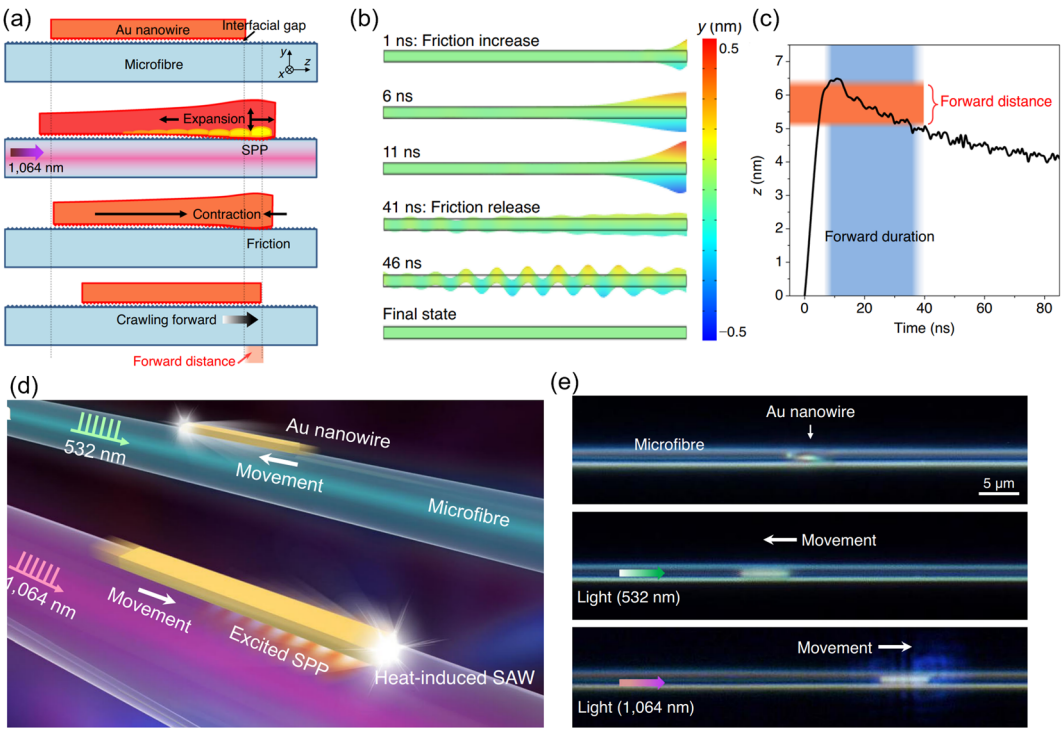

Fig. 17 Plasmonic thermal expansion. (a) Schematic diagram of the peristaltic crawling caused by thermal expansion of plasmons. Adapted with permission from ref. 194; Copyright 2021 Springer Nature. (b) Time-course changes of the nanowire in the thermal crawling. (c) Time-dependent axial expansion behavior of the nanowire front end. (d) The creeping movement of gold nanowires on silica microfibers due to thermal expansion. (e) Microscope image showing the movement of gold nanowires on suspended microfibers.

acoustic waves—mechanical vibrations that propagate through different media—the result is a powerful synergy that enhances the performance of acoustic systems across a wide range of frequencies. This integration not only addresses existing challenges in acoustics but also opens up new possibilities for applications in sensing, imaging, and fluid control. By exploring the interactions between plasmons and acoustics across different frequency ranges, we can unlock new levels of precision and efficiency in various technologies.

The combination of plasmons and acoustics covers the kHz to IR region (Fig. 18). In the kHz range, ultrasound struggles with the limited efficiency of generating and detecting ultrasound waves, particularly in applications involving the PA imaging of biological tissues *in vivo*. Plasmons, with their ability to generate local heating *via* hot electrons, significantly enhance PA effects by increasing transient thermoelastic expansion. The critical technology here involves the design of plasmonic nanostructures that resonate at the specific wavelengths used in PA applications, optimizing light absorption and conversion into ultrasound waves. Moving to the MHz range, plasmons can enhance the detection of microfluidic behavior by improving the sensitivity of sensors that interact with SAWs. This allows for more precise monitoring of fluid dynamics, while SAWs themselves are used to control the movement of these fluids.[198] This involves engineering plasmonic surfaces that can interact effectively with SAWs, enabling simultaneous detection and control within microfluidic environments. In the GHz range, a significant challenge is the excitation and detection of high-order acoustic modes, which are difficult to resolve due to their ultrafast nature. When combined with femtosecond pump–probe techniques, plasmons enable the excitation and detection of these high-order modes in thin metal films, particularly in LO acoustic modes. The plasmonic enhancement improves temporal resolution and sensitivity, making it possible to study these fast acoustic phenomena. At even higher frequencies, in the THz to infrared range, the proximity of graphene to metals can give rise to graphene acoustic plasmon resonance, which provides a novel mechanism for enhancing acoustic interactions in this spectral range. This phenomenon opens up new possibilities for acoustic manipulation and sensing in the THz to IR range. Overall, across all these frequency ranges, the integration of plasmonics with acoustics offers innovative solutions to longstanding challenges. Next, we examine these combinations in detail.

In the kHz range, plasmonic effects predominantly enhance the PA effect. Four main mechanisms for the generation of PA waves have been reported: thermal expansion or thermoelastic expansion, vaporization, optical breakdown, and photochemical processes. For biomedical applications, the thermoelastic expansion route is generally considered the mainstream strategy, induced by a slight temperature increase (usually in the millikelvin range) due to energy deposition inside biological tissues through the absorption of incident electromagnetic energy.[199] The excited PA signal is locally determined by the electromagnetic absorption and scattering properties, thermal properties (including thermal diffusivity and thermal expansion coefficient), and elastic properties of the sample. The plasmonic enhancement of the PA signal arises because plasmons can significantly increase the efficiency of light absorption and subsequent heat generation. The generation of ultrasound enhanced by plasmonic nanoparticles is shown in Fig. 19a. First, plasmons are excited by the irradiation of a pulse of light, which causes local heating. Due to the small increase in temperature caused by the absorption of heat, the plasmonic particles expand briefly. This generates a pressure transient that can be detected

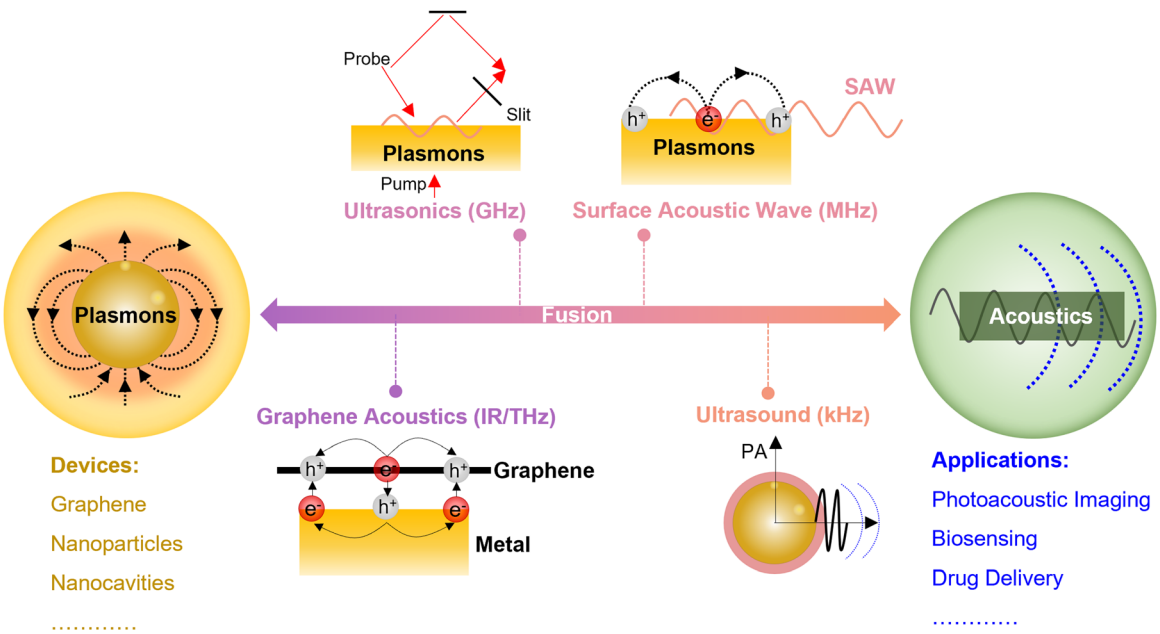

Fig. 18 Plasmonic fusion with acoustics. The combination of plasmon and acoustic devices includes ultrasound in the kHz region, SAWs in the MHz region, ultrasonics in the GHz region, and graphene acoustics in the IR/THz region.

acoustically. There is no bulk heating of the sample because the expansion is spatially and thermally confined using light pulses shorter than the thermal relaxation time of the absorber.

The resulting PA signal is a function of the optical, thermal, and elastic properties of the nanoparticle–medium system, which can be expressed by (Fig. 19b)

$$\rho_0 = \left(\frac{\beta c^2}{C_p}\right)\mu_a F = \Gamma A \quad (5)$$

where key parameters include the pressure difference (ρ_o), the thermal expansion coefficient (β) of the absorbing system, the speed of sound (c), the specific heat capacity of the absorbing system (C_p), the absorption coefficient (μ_a), and the irradiation fluence (F). Plasmons mainly affect the absorption coefficient, the thermal expansion coefficient, and the specific heat capacity of the absorber. The PA signal can be optimized by modifying the nanoparticle shape, material, and solvent. For instance, Chigrin *et al.* modeled and showed that the most promising geometries are high aspect ratio AuNRs and gold nanostars with high absorption (or μ_a) and low scattering coefficients.[201] It is therefore easy to tune changing the shape of plasmonic nanostructures. Another strategy to improve the absorption coefficient is to move plasmonics to the second near-infrared window (NIR-II, 1000–1700 nm). This is widely used in PA imaging because biological tissues have a lower background absorption in this window (Fig. 19c).[200] In particular, it provides deeper light penetration and a higher maximum permissible exposure compared to the visible spectrum and NIR-I (650–900 nm) range.

Regarding the coefficient of thermal expansion (β), it is a material property that describes how the size of an object changes with temperature and is generally challenging to alter in plasmonic nanostructures. However, β can be influenced by interfacial thermal resistance. During laser pulsing, heat is not fully confined within nanoparticles; instead, some heat diffuses into the surrounding solvent, creating a high-temperature shell-like solvent layer around the nanoparticles. This temperature rise causes thermal expansion in both the nanoparticles and the solvent. The amount of heat transferred to the solvent is determined by factors such as the laser pulse duration, the interfacial thermal resistance at the nanoparticle–solvent boundary, and the thermoelastic properties of the solvent. Thus, modifying solvent properties emerges as a viable approach to enhancing the PA signal. For instance, Shi and collaborators demonstrated through modeling and experimentation that replacing water with ethanol as the solvent for gold nanospheres increased the PA signal by a factor of 4.5.[202]

In the MHz range, there are two strategies to achieve the combination of plasmons and SAWs, depending on the way of plasmon excitation. The first approach is the interaction of SAWs with plasmons in optical waveguides with confined modes, as shown in Fig. 20a. In this configuration, SAWs can modulate the local dielectric environment and the electron density at the metal surface, leading to a periodic modulation of the plasmon resonance. This interaction can be used to dynamically tune the plasmonic response in a material, potentially allowing for the development of reconfigurable plasmonic devices. Besides, the mechanical strain and the electric fields generated by SAWs can enhance the propagation of surface plasmons along the interface, possibly leading to increased plasmonic signal strength over longer distances. For instance, Huang and co-workers integrated a semiconductor–metal–insulator–semiconductor based hybrid plasmonic waveguide with interdigital transducers for SAW generation (Fig. 20b).[203] It is demonstrated that SAWs can cause periodic refractive index variations along the direction of acoustic

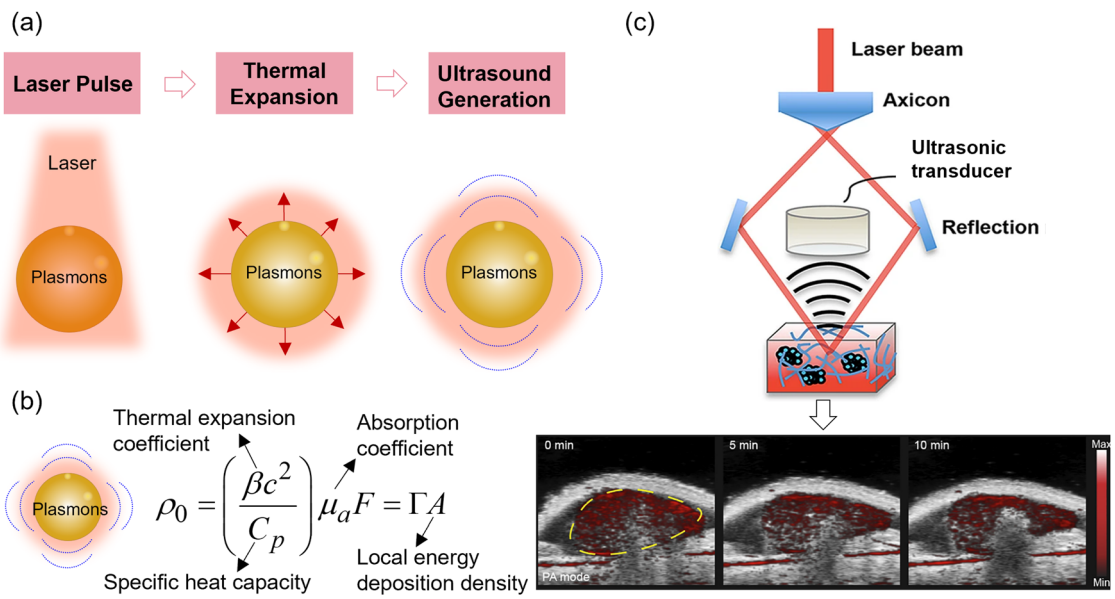

Fig. 19 Plasmon-enhanced photoacoustic effects in the kHz range. (a) Schematic diagram showing the enhancement of ultrasound generation in photoacoustic effects *via* the pressure difference induced by plasmon-enhanced thermal expansion. (b) Factors affecting pressure difference (ρ_o) in plasmon-enhanced photoacoustic effects. (c) Schematic diagram of the plasmon-enhanced photoacoustic imaging. Adapted with permission from ref. 200; Copyright 2021 American Chemical Society.

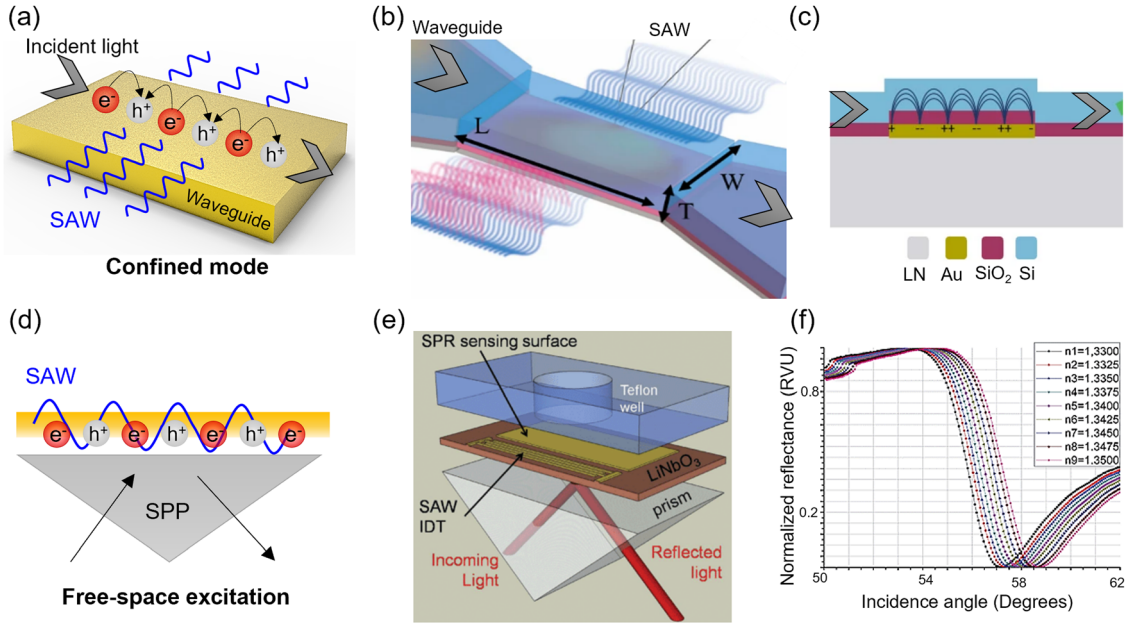

Fig. 20 Integration strategy of plasmons and surface acoustic waves (SAW) in the MHz range. (a) Schematic diagram showing the integration of plasmons and SAWs in confined modes. (b) An example illustrating the integration of SAWs with propagating SPPs *via* a plasmonic waveguide in confined modes. Adapted with permission from ref. 203; Copyright 2024 Springer Nature. (c) The cross-sectional view showing the plasmonic waveguide-SAW platform. (d) Schematic diagram showing the integration of plasmons and SAWs in free-space excitation. (e) An example illustrating the integration of SAWs and SPRs in free-space excitation. Adapted with permission from ref. 204; Copyright 2010 the Royal Society of Chemistry. (f) Refractive index-sensitive behavior of the SAW-SPR platform.

propagation (Fig. 20c). This phenomenon can be understood by considering the refractive index modulation caused by the elastic deformation induced by SAWs. Besides, the plasmonic intensity was also enhanced by the SAW, and it achieves a plasmonic intensity gain of 1.08 dB at a peak-to-peak potential swing of 3 V.

The second approach is the interaction of SAWs with plasmons in free-space excitation, as shown in Fig. 20d. In this configuration, the combination leverages the high sensitivity of plasmonic sensors to changes in the refractive index at the sensor surface, along with the ability of SAWs to manipulate and control fluids at the microscale. A specific example of this integration is the use of a common $LiNbO_3$ piezoelectric substrate, where SPR sensing is combined with SAW actuation (Fig. 20e).[204] In this setup, the $LiNbO_3$ substrate facilitates the generation of SAWs due to its piezoelectric properties. These acoustic waves can then interact with the surface plasmon waves, leading to enhanced microfluidic mixing on the sensor surface. This enhanced mixing is crucial in scenarios where rapid and uniform distribution of analytes is needed, such as in biosensing assays. Additionally, the SAW component can help reduce non-specific adsorption of molecules to the sensor surface. Non-specific adsorption often leads to false positives or reduced sensitivity in SPR sensors. By using SAWs, the surface can be actively cleaned or modulated, which helps in maintaining the specificity and accuracy of the SPR signal. This combination not only improves the sensitivity and selectivity of the sensor but also enhances the overall performance by reducing noise and improving the response time (Fig. 20f).

In the MHz range, the integration of plasmonics with ultrafast ultrasonics, particularly pico/femtosecond ultrasonics, offers significant advancements in the field by enhancing both the generation and detection of high-frequency acoustic waves. Plasmons can confine electromagnetic fields to nanoscale regions, which amplifies the interaction between light and matter. This confinement is crucial for ultrafast ultrasonics, where the ability to generate and detect acoustic waves with high spatial resolution and sensitivity is essential. The setup for ultrafast ultrasonics involves a pump–probe technique, as shown in Fig. 21a, where a short laser pulse (pump) is used to excite the material and generate acoustic waves, and a delayed pulse (probe) is used to detect the resulting changes. In the setup, the process begins with the pump beam being focused onto a gold layer from the air side, creating a localized thermal expansion that generates picosecond acoustic waves within the material. To improve the accuracy of the measurements, a portion of the probe beam is split off and used in a balanced detection scheme.

One of the primary enhancements that plasmonics brings to picosecond ultrasonics is the ability to focus energy into extremely small volumes, leading to the generation of more intense and localized acoustic waves. This is particularly useful in applications involving nanoparticles or nanostructured materials, where traditional methods might struggle to achieve sufficient excitation or detection sensitivity. In terms of detection, plasmonic enhancement can significantly improve the sensitivity to small changes in optical properties caused by acoustic waves. This is particularly important in cases where the acoustically induced changes are subtle, such as in nanoscale systems or materials with weak acoustic responses. Plasmons, by amplifying these changes, enable more precise measurements. For

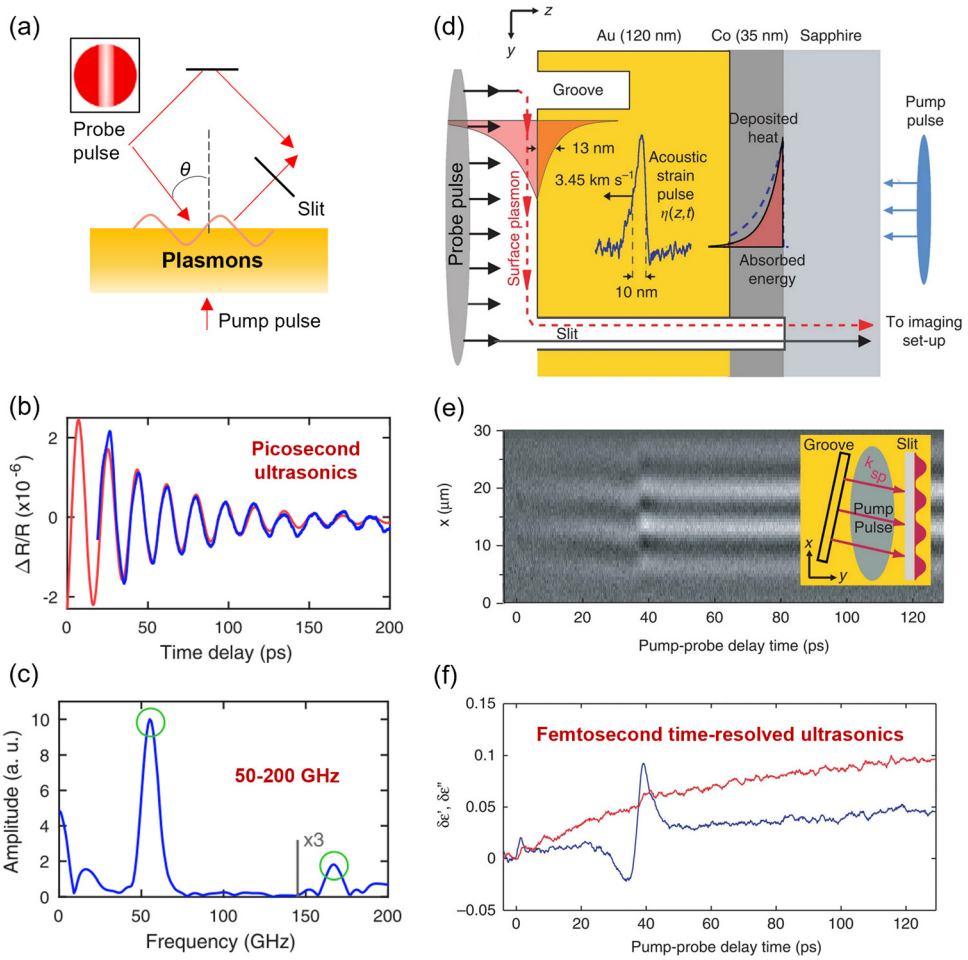

Fig. 21 Plasmon-enhanced pico/femtosecond ultrasonics in the GHz range. (a) Schematic of the pump–probe setup for GHz acoustics. (b) Time domain signal of the plasmonic ultrasonics with picosecond acoustic pulses. Adapted with permission from ref. 205; Copyright 2023 Elsevier. (c) Corresponding Fourier spectra in the frequency domain. (d) Schematic of femtosecond plasmonic ultrasonics in a hybrid gold–cobalt multilayer structure. Adapted with permission from ref. 206; Copyright 2013 Springer Nature. (e) Measured interferogram of the hybrid structure showing a shift of the interference fringes upon reflection of an ultrashort acoustic pulse. (f) Time domain signal of the hybrid structure showing femtosecond time-resolved response.

instance, Hettich and co-workers combined ultrafast pump–probe PA spectroscopy with plasmon resonance to detect LO acoustic modes in gold films.[205] The method achieved high sensitivity, detecting acoustic modes up to the 7th harmonic (~200 GHz) with sub-picometer amplitude sensing capabilities (Fig. 21b and c). It also separated the dynamics of the dielectric function and film thickness variation. To extend ultrasonics from picosecond to femtosecond, Temnov and co-workers developed a hybrid gold/cobalt bilayer structure using ultrafast surface plasmon interferometry with femtosecond time resolution (Fig. 21d).[206] They observed substantial nonlinear reshaping of acoustic pulses after propagating just 100 nm in gold (Fig. 21e and f).

In the terahertz to infrared range, a mode called acoustic graphene plasmon (AGP) with unprecedented field confinement can be excited. Its excitations can be traced back to graphene plasmons, which are collective oscillations of charge carriers in graphene, which can be excited by electromagnetic fields, particularly in the IR and THz frequency ranges. These graphene plasmons are known for their ability to confine electromagnetic energy into extremely small volumes, enabling strong light–matter interactions at the nanoscale. However, when graphene is brought close to a metal surface, with a sufficiently thin dielectric spacer in between, a different type of plasmon, known as the AGP, can be excited (Fig. 22a). The AGP arises from the interaction between the charge density oscillations in the doped graphene layer and the image charges induced in the nearby metal. This interaction effectively mirrors the oscillating charges in graphene, leading to a highly confined plasmonic mode within the narrow dielectric spacer. Unlike conventional graphene plasmons, AGPs are characterized by their ability to propagate with a much higher wavevector, allowing for extreme localization of the electromagnetic field.

One of the key properties of AGPs is their unprecedented field confinement (Fig. 22b),[207] which surpasses that of traditional graphene plasmons and other polaritonic modes in van der Waals materials. This confinement occurs primarily within the dielectric spacer, allowing the AGP to compress MIR light into extraordinarily small volumes, with a mode volume confinement

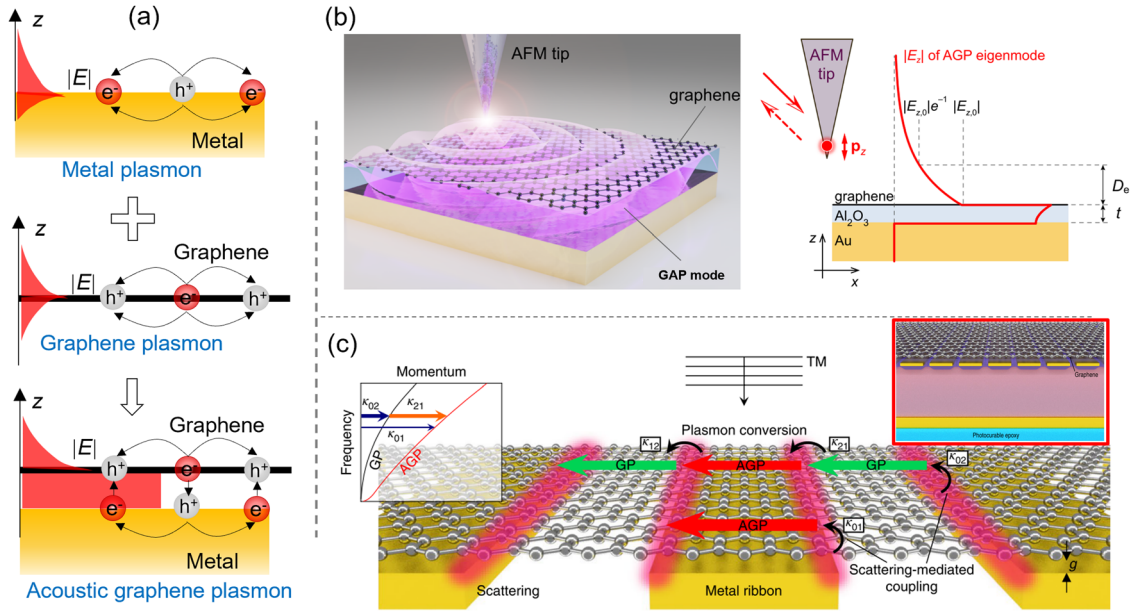

Fig. 22 Graphene acoustic plasmon in the THz to IR range. (a) Schematic diagram of the acoustic graphene plasmon. From top to bottom: Schematic diagram of the electric field decay, charge displacement, and electric field lines along the z direction of the metallic graphene plasmons and AGPs. (b) Strong light confinement in the graphene acoustic plasmon. Adapted with permission from ref. 207; Copyright 2021 Springer Nature. (c) Utilizing conventional graphene plasmons as an intermediary and integrating an optical spacer and a back reflector to excite AGPs for high absorption of incident light, ultrasensitive detection of Ångström-thick protein and dielectric films is achieved. Adapted with permission from ref. 208; Copyright 2019 Springer Nature.

factor as high as 10^{10}. Another advantage of AGPs is their reduced ohmic losses compared to graphene plasmons, as the electromagnetic energy is less concentrated in graphene itself and more within the spacer. Furthermore, AGPs do not suffer from cutoff as the spacer thickness decreases, meaning they can be sustained even when the dielectric layer is reduced to a single atomic layer, such as hexagonal boron nitride. This makes AGPs highly efficient for applications requiring strong light–matter interactions, such as molecular sensing, polaritonic dispersion engineering, and dynamic light manipulation using graphene-based metasurfaces. For instance, Oh and co-workers used a two-stage coupling scheme where free-space light couples to conventional graphene plasmons, which then couple to ultraconfined acoustic graphene plasmons (Fig. 22c).[208] They also integrated an optical spacer and a reflector to enhance the absorption. This method achieved nearly perfect absorption (94%) of incident mid-infrared light, allowing ultrasensitive detection of absorption bands and surface phonon modes in Ångström-thick protein and dielectric films. In summary, AGPs are a unique acoustic plasmonic mode with exceptional confinement capabilities and low losses, making them highly suitable for advanced photonic applications in the mid-infrared and terahertz regimes.

3.4 Plasmonic optical-electric-acousto-thermal fusion

As mentioned above, plasmonics is not isolated from optical, electrical, acoustic, and thermal technologies. In fact, plasmonics, photoelectric, acoustic, and thermal fusion is a cutting-edge concept that integrates multiple physical effects (optical, electronic, acoustic, and thermal) into a multifunctional platform to improve the efficacy and precision of plasmonics applications (Fig. 23a). Next, this fusion technology is explained using cancer diagnosis and treatment as an example. Li and co-workers developed hybrid nanoparticles (HNPs) with multiple modalities consisting of a dual-plasmonic Au@$Cu_{2-x}Se$ core–shell nanocrystal (Fig. 23b).[209] This fused platform leverages the unique properties of plasmonic nanomaterials, which can simultaneously interact with light, generate heat, catalyze chemical reactions, and produce acoustic signals. By combining these effects, plasmonic fusion enables advanced imaging, targeted therapy, and enhanced therapeutic outcomes. The first is plasmonic optical enhancement and imaging. The HNPs exhibit strong plasmonic resonance under NIR-II laser irradiation, which enhances their optical properties. This resonance allows for high-contrast NIR-II imaging, enabling real-time visualization of tumors with minimal tissue damage. The deep tissue penetration of NIR-II light, combined with reduced scattering and absorption, improves imaging quality and contrast, essential for guiding and monitoring cancer therapy. The second is the electronic catalysis. The plasmonic excitation of HNPs also generates hot carriers, which drive photocatalytic reactions in the tumor microenvironment. Specifically, the nanocrystals facilitate the Fenton-like reaction between Cu_{2+} ions and H_2O_2, producing hydroxyl radicals (–OH) that induce oxidative stress in cancer cells. This reaction is further enhanced by the NIR-II irradiation, making the treatment more effective even under hypoxic conditions where traditional therapies might fail. The third is photothermal therapy. The plasmonic resonance also induces a photothermal effect, where localized heating occurs within the tumor tissue. This effect leads to hyperthermia, which can ablate cancer cells directly. The precise control over the temperature rise, guided by real-time

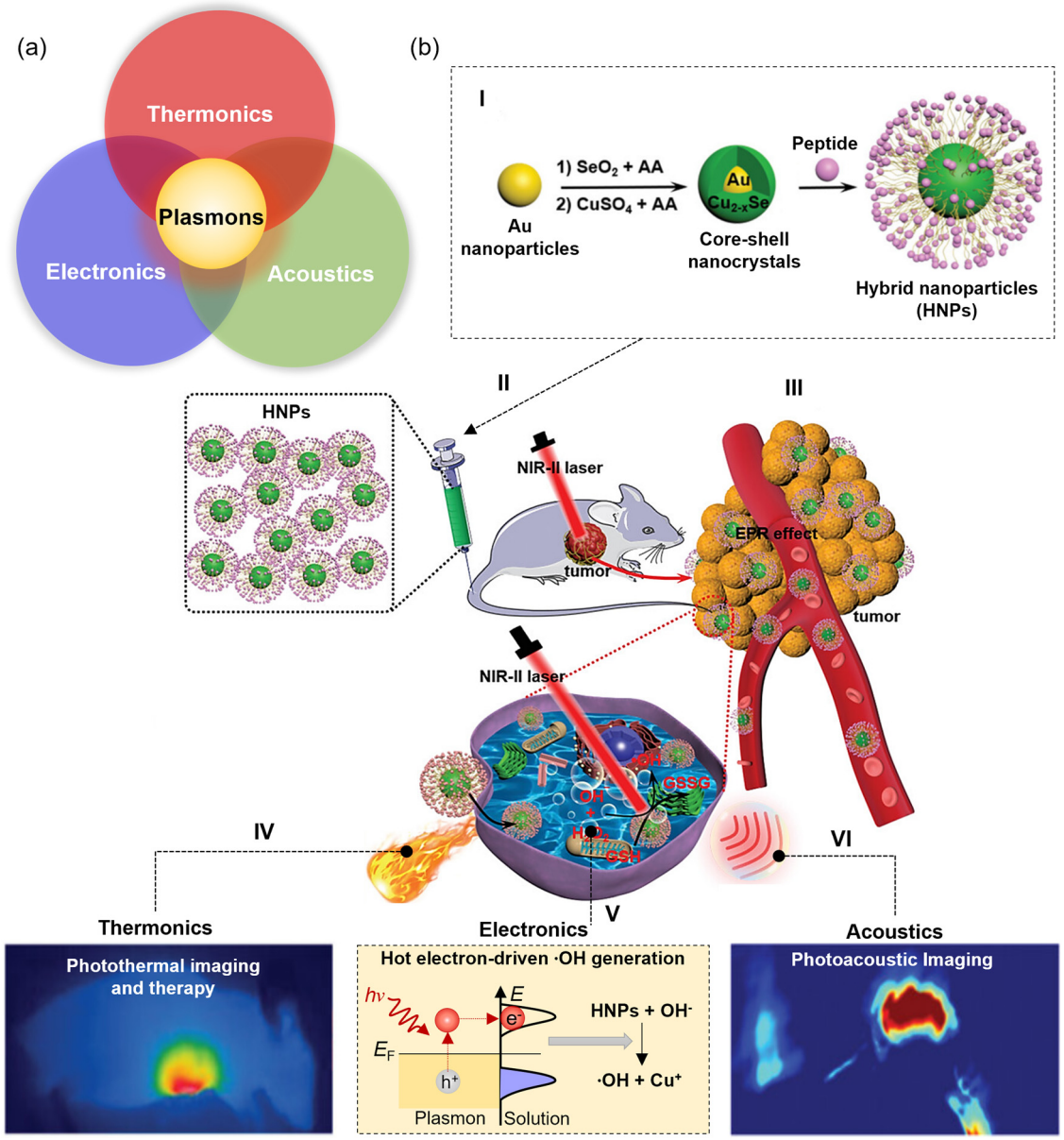

Fig. 23 Plasmonic optical-electric-acousto-thermal fusion. (a) With plasmonics as the core, electronics, thermonics, and acoustics are combined. (b) An example of the plasmonic hybrid nanoparticles (HNPs) for PA imaging and imaging-guided photothermal therapy, illustrating the fusion of optical-electric-acousto-thermal technologies. Adapted with permission from ref. 209; Copyright 2022 John Wiley and Sons. (I) Schematic illustration of the synthesis of HNPs. (II) HNPs were injected into mice. (III) Interaction between tumor tissue and HNPs. The whole process involves (IV) photothermal effect for tumor treatment, (V) hot electron-driven OH generation for Fenton reaction, and (VI) photoacoustic effect for tumor imaging.

imaging, minimizes damage to surrounding healthy tissues, enhancing the safety and efficacy of the treatment.

The plasmonic optical-electric-acousto-thermal fusion in HNPs offers several key advantages: (1) targeted and controlled therapy: the combination of imaging and therapy ensures that treatment is precisely targeted to the tumor, reducing side effects and improving outcomes; (2) hypoxia tolerance: the ability to generate OH^- radicals even in low-oxygen environments overcomes a significant barrier in cancer therapy; (3) minimized tissue damage: NIR-II light's deep penetration and the controlled photothermal effect reduce the risk of overheating and photodamage, making the treatment safer; and (4) enhanced imaging: high-contrast NIR-II and PA imaging provide detailed insights into tumor morphology and treatment efficacy, enabling better clinical decisions.

3.5 Section summary

In summary, this section introduces the fusion of plasmonic optical, electrical, acousto, and thermal effects. We analyze the multiphysical coupling of plasmons with acoustics, electronics, and thermal phenomena, emphasizing their comprehensive integration. Nevertheless, this fusion continues to present significant challenges.

One of the primary challenges in the fusion within plasmonics lies in the inherent differences between the mechanisms of optical, electric, acoustic, and thermal domains. Each of these mechanisms has unique operational characteristics and requirements. For instance, optical mechanisms often rely on precise control of light–matter interactions, while electric mechanisms focus on the efficient transport and manipulation of charge carriers. Acousto mechanisms, on the other hand, involve the propagation of mechanical waves through materials, and thermal mechanisms deal with heat generation and transfer. Plasmonics, with its ability to confine and enhance electromagnetic fields at the nanoscale, offers a potential platform to integrate these diverse mechanisms. A good example of this is the plasmonic-induced thermal effect, which can enhance both PA signals and thermal therapies, thereby creating a synergy between optical, acoustic, and thermal effects. However, designing plasmonic systems that can effectively combine these distinct mechanisms remains a significant challenge.

Another critical challenge is the lack of comprehensive theoretical frameworks that can describe the integration of optical, electric, acousto, and thermal effects within a single plasmonic system. Currently, theories in each domain are highly specialized and often do not account for the interactions between different types of energy conversion processes. For example, while there are established theories for plasmonic energy conversion and nanoparticle heating, these theories may not adequately describe how mechanical energy, converted through a nanogenerator, interacts with plasmonic excitations to produce a unified energy transfer process. The absence of such a unified theory hinders the development of integrative plasmonic technologies, as researchers lack the tools to predict and optimize cross-domain interactions. Addressing this gap requires new theoretical models that can capture the full complexity of energy interactions across optical, electric, acousto, and thermal domains within plasmonic systems.

A further challenge is finding materials that exhibit high performance across all relevant domains—optical, electric, acousto, and thermal. Most materials are optimized for one or two of these domains but may perform poorly in others. For instance, metals like gold and silver are excellent for plasmonic and electrical applications due to their superior conductivity and plasmonic resonance properties. However, these metals are not ideal for acoustic applications, where materials with better acoustic impedance matching are preferred. Similarly, materials that are thermally efficient may lack the necessary optical or electrical properties required for plasmonic applications. This scarcity of multifunctional materials complicates the design of plasmonic systems that need to excel in multiple domains simultaneously. One potential solution lies in the development of composite or hybrid materials that combine the strengths of different materials to achieve high performance across all required domains.

4. Biodiagnosis and molecular detection

Plasmonic nanostructures have the remarkable ability to confine light within sub-wavelength scales and facilitate strong light–matter interactions, paving the way for groundbreaking advancements in biomolecular detection and medical diagnostics. By leveraging their unique optical properties, these nanostructures can enhance local electromagnetic fields, thereby significantly amplifying otherwise weak molecular signals. This enables highly sensitive detection of biological, gaseous, and chemical molecules. Plasmon-enhanced spectroscopic techniques, such as refractive index (RI) sensing, SERS, SEIRA, SEF, and surface-enhanced chiral sensing, have been widely adopted in various molecular detection applications. These technologies have not only revolutionized the healthcare industry but have also had profound impacts on fields such as food safety, environmental monitoring, security, pharmaceuticals, and forensic science.

Despite the exciting potential of plasmon-enhanced molecular sensing technologies, several challenges remain. For instance, the resonant frequencies of plasmonic nanostructures often lack tunability, limiting their adaptability across different applications. Additionally, the "hotspots" generated by plasmonic nanostructures are spatially confined, which can hinder effective interaction between molecules and these hotspots, thereby affecting signal enhancement. Moreover, optical detection schemes frequently rely on large and complex instrumentation, making portable applications challenging. Furthermore, the rapid attenuation of light in biological tissues constrains the use of these techniques for *in vivo* applications. In recent years, the development of interdisciplinary approaches has led to the convergence of multiple physical fields and effects, providing novel solutions to these limitations. For example, combining plasmonics with electronics can enable dynamic tuning of the resonant frequencies of nanostructures, facilitating efficient molecular detection over a broadband range. These hybrid technologies not only improve the performance of plasmonic nanostructures but also expand their applicability in molecular diagnostics.

In this section, we will begin by categorizing plasmonic nanostructures based on their different dimensions and outlining their fundamental characteristics. We will then focus on plasmon-enhanced spectroscopic techniques and their promising applications in biochemical molecular detection. Finally, we will explore the integration of plasmonics with electronic and acoustic technologies, discussing how these combinations address current challenges in plasmonic nanostructures and offering insights into the future of these emerging technologies in molecular diagnostics (Fig. 24). Through the introduction of various plasmon-enhanced sensing, we hope to help researchers quickly understand and select the most appropriate detection technology for the field of molecular sensing. Because the topic is vast and evolving, our review will not be comprehensive. Nonetheless, we will try to describe the main research in this area and evaluate some related literature.

4.1. Plasmonic nanostructures and fabrication

4.1.1. Zero-dimensional plasmonic nanostructures. Zero-dimensional (0D) plasmonic nanostructures (Fig. 25), typically 1–100 nm in size, exhibit LSPR, generating electromagnetic hotspots that enhance sensing techniques such as SERS and SEF.[210–212] Typical examples include individual nanoparticles like nanospheres and nanocubes, which can be optimized by

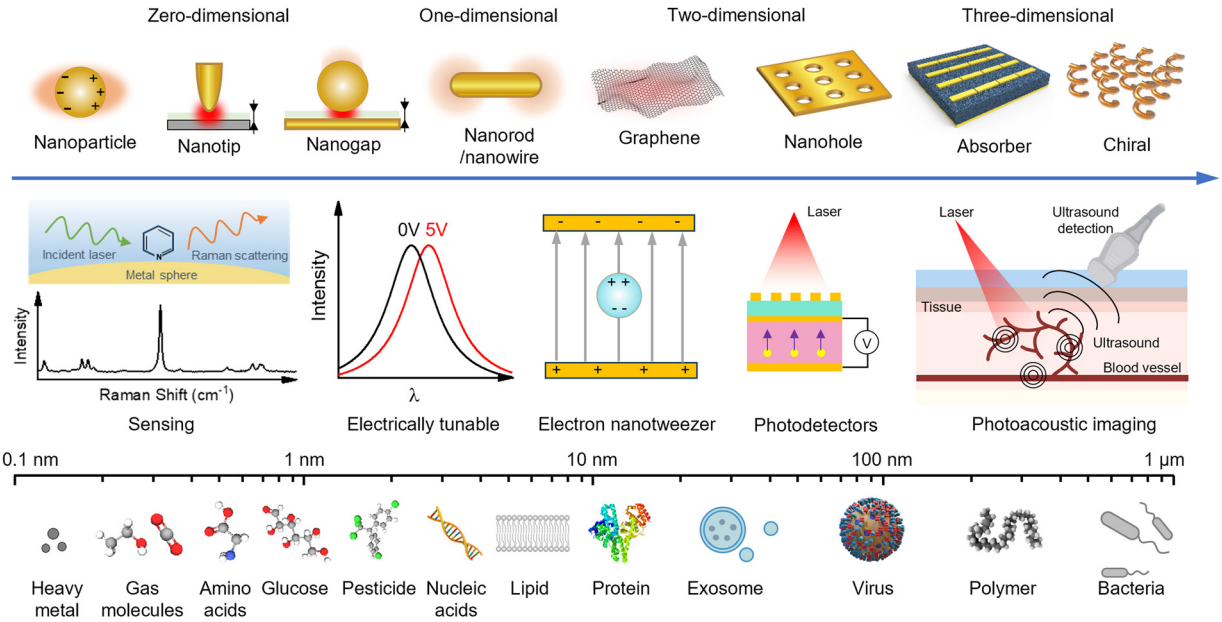

Fig. 24 Schematic diagram of integrative plasmonics for biodiagnosis and molecular detection.

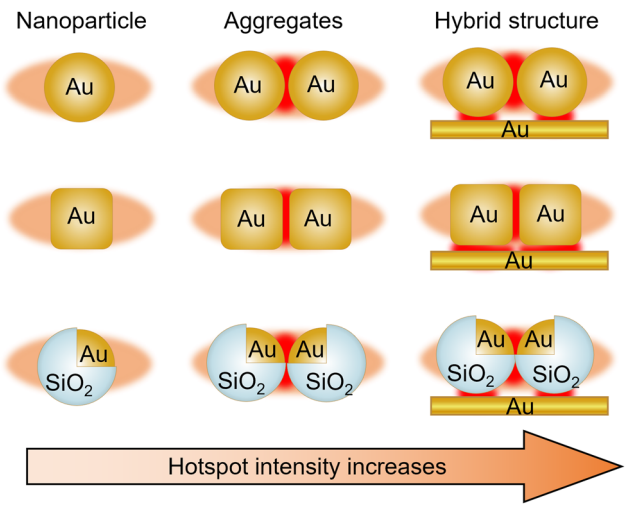

Fig. 25 Schematic diagram of a typical zero-dimensional plasmonic nanostructure.

introducing sharper edges (*e.g.*, nanostars, nanoprisms) or nanoshell structures to enhance hotspot intensity.[37,212–219] However, the electromagnetic field enhancement of individual nanoparticles rarely exceeds 10^7.[7,36] To achieve stronger hotspots, coupled nanostructures with controlled nanogaps have been developed, with nanoparticle dimers being the most common.[220–224] Due to strong electromagnetic coupling, a metal nanoparticle dimer generates highly localized fields in the nanoscale gap, enhancing SERS signals by up to 10^8.[225] The field strength increases as the gap narrows, but quantum tunneling limits enhancement when the gap is reduced below ~0.6 nm.[226] Inspired by dimer structures, researchers have designed core–shell nanoparticle dimers,[227,228] aggregates,[229,230] and multiparticle arrays with controlled nanoscale gaps.[231,232] These structures generate extremely small (~1–5 nm) yet highly effective hotspots, contributing over 50% of the sensing signal.[233,234] Therefore, precise placement of probe molecules within these hotspots is essential for effective detection.

Despite their strong localization, hotspots formed by multiparticle structures are often inaccessible on common substrate materials like silicon wafers or ceramics.[220,221] To address this, hybrid structures combining plasmonic nanostructures with target materials have been developed, generating hotspots directly on the substrate surface. A simple example is placing a single nanoparticle on a semiconductor or metal surface, where interactions between scattered and reflected electromagnetic fields create hotspots.[235–237] The intensity depends on the dielectric properties of the substrate—SERS enhancement on metal surfaces is significantly stronger than on semiconductors.[238] Additionally, the nanoparticle shape influences enhancement; for instance, nanocubes generate larger hotspot areas than nanospheres.[238] To further enhance sensitivity, nanoparticle aggregates can be used instead of single nanoparticles.[239] These structures generate hotspots both at the particle–substrate interface and within nanoscale gaps, amplifying SERS signals by two to three orders of magnitude compared to single nanoparticles.[220] Moreover, functionalizing these nanostructures enables selective molecular detection, improving specificity and sensitivity.[240–242] These advances hold great potential for applications in biosensing, environmental monitoring, and nanotechnology.

4.1.2. One-dimensional plasmonic nanostructures. One-dimensional (1D) plasmonic nanostructures, formed by extending 0D nanostructures in one direction, include nanorods, nanowires, nanoribbons, and nanotubes (Fig. 26).[243] Among these, nanorods are widely studied due to their anisotropic plasmonic properties.[244] Unlike nanospheres, nanorods exhibit two distinct plasmon modes: one along the short axis, operating in the visible

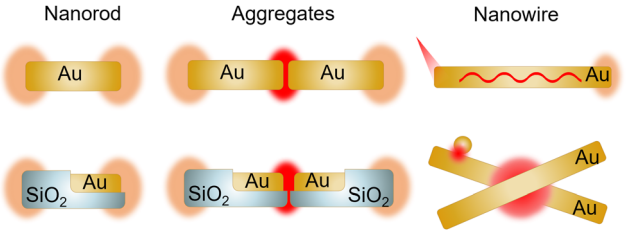

Fig. 26 Schematic diagram of a typical one-dimensional plasmonic nanostructure.

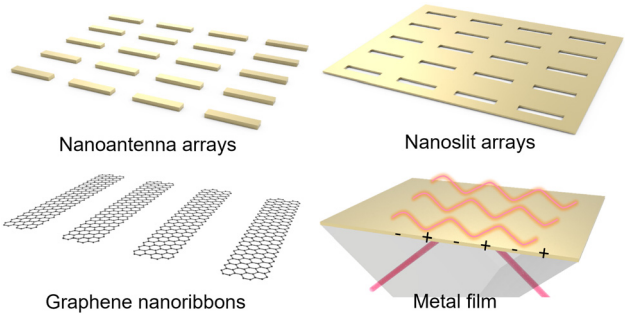

Fig. 27 Schematic diagram of a typical two-dimensional plasmonic nanostructure.

range, and another along the long axis, typically in the near-infrared range.[245] By adjusting their aspect ratio, the LSPR of nanorods can be tuned across a broad spectrum, optimizing SERS performance.[246–248] In contrast, nanospheres have a fixed and narrower plasmonic tuning range. Additionally, nanorods exhibit stronger absorption, higher quality factors, and enhanced electromagnetic fields at their tips,[249–251] making them highly sensitive to refractive index changes and well-suited for applications in biomedical imaging and photothermal therapy.[252,253]

Nanowires, with their high aspect ratio, can manipulate electrons, photons, plasmons, and phonons at the nanoscale, enabling diverse applications.[254–257] In 2000, Dickson and Lyon observed that incident light on the end of a metal nanowire could couple into surface plasmons and propagate along its length, a phenomenon known as propagating surface plasmons or SPPs.[258] Nanowires can support multiple plasmon modes, each with distinct propagation constants and polarization characteristics.[259] These properties make them ideal as plasmonic waveguides, connecting plasmonic probes to optical fibers for molecular detection.[260–262] For instance, periodic nanowire arrays have been proposed for SERS enhancement, where laser illumination excites plasmons at one end, transmitting them to the opposite end, where they enhance Raman signals.[263] However, in a remote SERS single nanowire system, the extended nanowire length restricts the excitation distance, reducing Raman signal enhancement. To overcome this, researchers have explored configurations such as nanoparticle–nanowire hybrids, crossed nanowires, and nanowire dimers, where hotspots form at junctions or crossover points, significantly improving SERS sensitivity.[264–267] Despite these advancements, Ohmic losses in metals lead to plasmonic signal decay, necessitating further research to reduce propagation losses and enhance nanowire-based plasmonic sensing.[268,269]

4.1.3. Two-dimensional plasmonic nanostructures. Unlike colloidal nanoparticles or one-dimensional nanostructures, 2D plasmonic nanostructures typically refer to periodic arrays of geometric structures (Fig. 27).[270] In the 2D realm, these nanostructure arrays are fabricated on planar substrates. Typically, coupling in a 2D array is confined to the horizontal direction, with neighboring similar nanostructures allowing the coupling of the same plasmonic modes.[271] Specifically, the collective behavior of these plasmonic modes produces coherent optical responses, resulting in stronger and narrower spectral features compared to single nanostructures.[272] Additionally, the nanostructures in 2D arrays offer more tunable dimensions, including the size, shape, material, and periodicity of the structures, providing great flexibility and tunability in plasmonic and optical properties. By customizing the size and shape of these nanostructures, plasmonic resonances can be excited across multiple bands (visible, near-infrared, mid-infrared, terahertz).[273–277] Various nanostructure patterns, such as nanorods,[278,279] nanogaps,[280] nanopores,[281,282] nanodisks,[283,284] nanorings,[285,286] and gratings,[287,288] have been reported to produce tunable plasmonic properties. The diverse designs of these nanostructures and their collective resonance behavior enable 2D arrays to support different plasmonic resonance modes, such as LSPR,[286,289] SPPs,[290] Fano resonances,[285,291,292] plasmonic whispering-gallery modes (WGM),[293,294] surface lattice resonances (SLR),[295–297] and the effective epsilon-near-zero (ENZ) effect.[41,298,299] Each plasmonic mode exhibits characteristic optical properties, unique field distributions, and distinct electromagnetic field amplitudes. By leveraging these optical properties, various molecular sensing applications can be achieved.

Graphene, a natural 2D material, possesses fascinating electronic and optical properties.[300–304] In recent years, graphene-based plasmonics has become a focal point in photonics research.[305–307] Given the practical carrier concentration in graphene, its plasmonic frequency falls within the terahertz and infrared regions.[308–312] Compared to plasmons in noble metals, graphene plasmons offer three attractive features. First, the atomic layer thickness of graphene exhibits strong confinement of the light field, providing a new platform for plasmonics and sensitive biosensing applications.[313–315] Second, graphene's high carrier mobility suggests relatively low losses when used as a plasmonic material.[301,316] Third, graphene is a tunable material and its plasmonic frequency can be easily tuned through electrostatic gating or chemical doping.[317,318] This tunability stems from the strong dependence of graphene's Dirac Fermi level on external changes, making it highly useful for achieving active plasmonic optics.[307] However, due to the significant momentum mismatch between graphene plasmons and photons, graphene plasmons cannot be directly excited by light.[312] A common method to excite localized plasmons is to pattern graphene into nanostructures.[319–321] Given their sensitivity to the surrounding environment, graphene plasmons are a highly promising platform for molecular sensing. Furthermore, exploring the coupling between graphene plasmons and molecular vibrations,[313]

as well as the coupling between graphene plasmons and phonon polaritons,[322] is of great interest.

Metallic thin films are another type of 2D plasmonic structure. Unlike LSPR supported by nanostructures and graphene, the plasmons in metal films are referred to as SPPs. In metal films, SPPs are surface electromagnetic waves that propagate along the metal–dielectric interface.[323] Unlike LSPR, SPPs require a strict momentum matching condition and cannot typically be directly excited by incident light.[324] The Kretschmann configuration is a classic example of overcoming the momentum mismatch in metal films.[325] By coupling a metal film to a high refractive index prism, an evanescent field generated by attenuated total reflection is used to excite plasmons. As long as the wavevectors match at a certain incident angle, the prism enables the horizontal wavevector component of the incident light to couple with the propagating SPP wavevector. Currently, SPP modes are widely used in label-free biomolecular sensing.[326] SPP modes have unique advantages over LSPR in sensing. For example, SPPs can propagate longer distances along the metal surface, avoiding direct exposure of high-energy lasers to the sample and thereby reducing sample damage.[327] Additionally, SPPs have a greater skin depth compared to LSPR modes.[328] This characteristic allows SPP modes to sense deeper environmental changes, making them suitable for sensing applications that require the detection of thicker samples or depth information. However, the hotspot intensity of SPP modes is generally lower than that of LSPR, resulting in lower sensing sensitivity. To enhance sensing sensitivity, researchers have proposed coupling SPP with LSPR sensing strategies,[329] such as patterning gold nanoparticle arrays or nanogratings on gold films.[330,331] This approach can create localized hotspots and enhance the near-field intensity in metal films, thereby improving the sensing performance and detection limits of SPPs.

4.1.4. Three-dimensional plasmonic nanostructures. 3D plasmonic nanostructures unlock the vertical dimension in spatial configurations (Fig. 28).[332] Specifically, in 3D nanostructure arrays, patterns are fabricated on top of other patterns or films, with a spacer layer in between. This allows 3D nanostructure arrays to exhibit additional plasmonic resonance modes arising from both horizontal and vertical coupling. Plasmonic coupling can also occur between the nanostructure patterns in the top and bottom layers. This coupling in 3D structures not only gives rise to new plasmonic modes but also displays intriguing optical phenomena. For instance, a metamaterial absorber based on a metal–insulator–metal (MIM) configuration is a typical example of a 3D plasmonic nanostructure.[333,334] In a metamaterial absorber, the bottom layer is usually a metal reflector that blocks light transmission and reflects incident light. The top metal layer typically consists of various nanostructured antennas. By tuning the thickness of the insulator and the morphology of the nanostructures, the effective permittivity, permeability, and impedance of the metamaterial absorber can be modulated. According to the impedance matching principle, reflection can be minimized when the effective impedance of the metamaterial absorber matches that of air. As the transmission spectrum is zero, absorption in the metamaterial absorber approaches unity under these conditions. Devices based on impedance matching are also known as metamaterial perfect absorbers.[333] Due to their high absorption efficiency, metamaterial perfect absorbers are used in fields such as structural color generation,[335–337] optical sensing,[338–340] solar energy harvesting,[341] and photodetection.[342–344] Furthermore, according to Kirchhoff's law, combining a metamaterial perfect absorber with a heater can create a wavelength-customizable radiation source.[345] This radiation source, which features wavelength tunability, narrow emission bandwidth, and angular independence, paves the way for compact gas sensors and spectrometers.[346,347] From a coupling perspective, the ratio of radiative to absorptive loss in a metamaterial absorber is 1, a condition referred to as critical coupling (CC).[53] In the critical coupling regime, decreasing or increasing the insulator thickness can push the metamaterial absorber into undercoupled (UC) or overcoupled (OC) modes, respectively.[54,348] When coupled with molecules, different coupling modes result in two opposite effects: EIT and EIA.

Designing multilayer resonant absorbers is another strategy for creating 3D plasmonic nanostructures.[349] Cui *et al.* proposed a conical metamaterial absorber structure composed of metal and dielectric multilayers.[350] This structure supports slow-light waveguide modes with weakly coupled resonances, mixing various resonant frequencies to achieve broadband absorption. Slow light is defined as light propagating at a group velocity much lower than the speed of light in a vacuum. Initially, the incident light propagates downward along the *z*-axis, then enters the metamaterial absorber in the form of energy flow vortices and moves upward slowly. Shorter wavelengths are trapped at the narrower top sections of the cone, while longer wavelengths are captured in the wider bottom sections. The trapped wavelengths exhibit very low reflectivity, resulting in broadband absorption by the multilayer absorber. As the multilayer structure can trap light within the dielectric layers, changing the dielectric material allows the exploration of plasmonic coupling with different materials. For example, replacing the dielectric layer with materials that support surface phonon modes, such as SiO_2 or hBN, can achieve coupling between plasmons and phonon polaritons.[351–353] Coupling

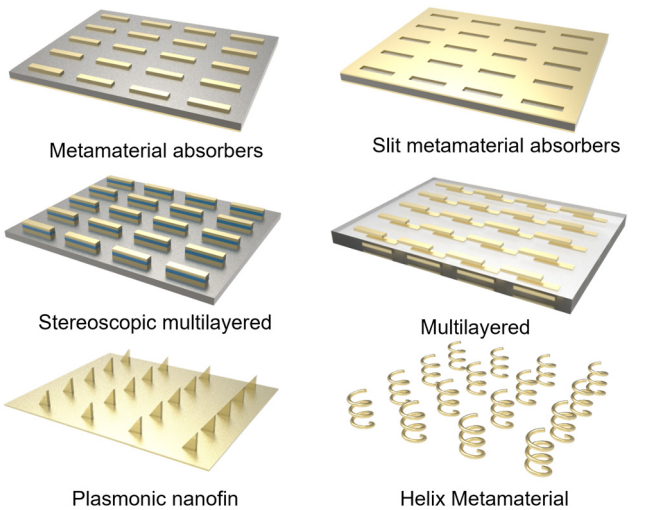

Fig. 28 Schematic diagram of a typical three-dimensional plasmonic nanostructure.

multiple modes can lead to new applications. For instance, coupling between surface plasmons and phonon polaritons can effectively address the issue of overlapping infrared vibrational fingerprints.[47] Combining a metamaterial absorber with graphene can overcome the momentum mismatch between graphene plasmons and excitation sources.[208] This approach can create a graphene plasmonic resonator with high absorption, suitable for ultra-sensitive molecular sensing.

Breaking the symmetry of nanostructured antennas can also create novel optical properties. In MIM structures, breaking the in-plane symmetry can create a quasi-bound state in the continuum (quasi-BIC) with a high quality factor.[354] The in-plane asymmetry parameters provide additional dimensions to control the system's radiative losses. By adjusting the asymmetry parameters and insulator thickness, precise control over different qBIC coupling modes (UC, CC, OC) can be achieved. Similarly, breaking the out-of-plane symmetry offers a pathway to precisely control the ratio of radiative to intrinsic losses. Plasmonic nanofins are a typical example of out-of-plane symmetry breaking.[355] By breaking the out-of-plane symmetry of nanofins in parameter space, a high-quality quasi-BIC mode can be realized under normal incidence. The radiation decay rate and access to different coupling states (UC, CC, OC) can be finely tuned by adjusting the triangular angle of the nanofins. Controlling the coupling states is crucial for maximizing the sensing performance of metasurfaces. Additionally, this spatial symmetry breaking can also induce exceptional points (EPs) in non-Hermitian systems.[356] EPs are singularities in complex frequency or wavevector space where two or more eigenvalues and their corresponding eigenstates coalesce at a specific point in parameter space.[357] For example, Park *et al.* achieved a plasmonic EP using a dual-layer plasmonic coupling with detuned resonances.[358] Studies have shown that plasmonic EPs exhibit high sensitivity when detecting low-concentration analytes. Moreover, asymmetric structural designs in parameter space can induce chiral optical responses, known as chiral metamaterials. Chiral metamaterials can produce unique optical phenomena such as CD and birefringence.[359,360] These differentiated responses arise from the chiral nature of their internal structures, allowing chiral metamaterials to exhibit varying refractive indices, absorption characteristics, and transmission properties across different electromagnetic wavebands (*e.g.*, light waves, microwaves). This selective response to polarized light holds promising applications in photonics, information technology, and biosensing.[361–363]

4.1.5. Advanced manufacturing of plasmonic nanostructures. The fabrication of plasmonic nanostructures can be categorized into two approaches: top-down and bottom-up. The bottom-up approach is a self-assembly method commonly used for creating zero-dimensional and one-dimensional plasmonic nanostructures. In recent years, DNA-based self-assembly techniques have made significant advancements.[364] These techniques leverage the properties of DNA molecules, where specific base sequences pair with each other to spontaneously form complex nanostructures.[365] DNA self-assembly offers unique advantages, such as achieving unprecedented nanoscale precision through well-controlled self-assembly processes. Additionally, this method allows for the large-scale and even batch production of plasmonic nanostructures in a highly parallel manner. Beyond static structures, DNA self-assembly can also be used to construct dynamic systems, such as nanoscale devices that respond to external stimuli like temperature, pH, or light.[366–368] Besides DNA self-assembly, other bottom-up methods, such as spontaneous nucleation and growth, solution-based self-assembly, and chemical vapor deposition (CVD), also play important roles in the fabrication of plasmonic nanostructures.[369–371] Spontaneous nucleation and growth processes utilize the natural growth mechanisms of materials to form nanostructures with specific morphologies. This method is commonly employed in the production of nanocrystals, nanowires, and nanoparticles. Solution-based self-assembly directs molecules or nanoparticles to spontaneously form ordered structures by controlling solution conditions and is often used to create polymers or nanoparticle arrays. Solution-based self-assembly also offers a unique opportunity for the fabrication of 3D plasmonic structures. In this regard, Kim *et al.* developed a 3D plasmonic nanoparticle assembly method by utilizing a femtoliter liquid meniscus to confine and guide functionalized nanoparticles.[372] This work lays the foundation for the freeform creation of 3D plasmonic structures. Furthermore, researchers have demonstrated the applications of these 3D plasmonic structures in photoluminescence enhancement and femtomolar-level virus sensing. CVD enables the precise growth of nanostructures through the decomposition and deposition of vapor-phase precursors and is typically used to manufacture nanomaterials like carbon nanotubes, graphene, and metal oxide nanowires. Currently, DNA self-assembly and other bottom-up methods have enabled the creation of a wide range of plasmonic structures with varying degrees of structural complexity and customized optical functions. However, bottom-up methods face challenges in controlling the uniformity of nanogap sizes, which can affect the reproducibility of biosensing applications.

In contrast, top-down methods primarily rely on lithography techniques to fabricate large-scale, periodically arranged 2D and 3D plasmonic nanostructures. The advantage of top-down fabrication techniques lies in their ability to produce nanostructures with various geometries, ultra-fine features, high reproducibility, and large-scale uniformity. Traditional cleanroom-based photolithography (PL) is one of the most widely used and mature manufacturing techniques in the semiconductor and microfabrication industries. However, its spatial resolution is limited by the diffraction limit of light, making it challenging for conventional photolithography to produce high-quality nanoscale dimensions and gaps. To overcome this limitation, new lithography techniques have emerged, such as electron beam lithography[373,374] and nanoimprint lithography.[375] Electron beam lithography uses a high-energy electron beam to directly pattern a resist, offering extremely high resolution and precision, enabling the fabrication of nanoscale features. Nanoimprint lithography involves imprinting a mold with nanoscale patterns onto a material, allowing high-resolution pattern transfer without being constrained by the diffraction limit of light. Despite these advances, controlling nanogaps below 5 nm and achieving atomic-level surface roughness remains challenging for emerging lithography techniques. Additionally, high fabrication costs and low

throughput are also challenges associated with lithography techniques. These factors significantly impact the performance of plasmonic nanostructures, and therefore, further improving resolution and surface precision remains a critical issue for top-down techniques in practical applications.

4.2. Plasmon-enhanced sensing technologies

4.2.1 Refractive index sensing. Surface plasmons are one of the effective ways to achieve high-sensitivity RI sensing due to the high field localization of surface plasmons. The RI sensing technology based on surface plasmons has the characteristics of high sensitivity, no need for calibration, real-time detection, non-contact operation and no damage to the sample. Combining RI sensors with appropriate biological and chemical technologies can lead to applications in biomolecule, chemical and gas sensing fields. For example, a thin film on a sensor is modified with a layer of biorecognition molecules that interact with specific molecules. When the sensor meets a specific sample, the molecules in the sample will interact with the recognition molecules on the film and bind to the film. Changes in the RI near the plasmon caused by molecular attachment lead to changes in the resonance wavelength, amplitude, or phase.[376] Therefore, the dynamic information of biological/chemical molecular interactions can be obtained based on the changes in signals, and the specificity, affinity, and dynamic characteristic parameters of molecular interactions can be analyzed from it. Here, there are two important parameters to characterize the performance of RI sensors, namely sensitivity (S_{RI}) and figure of merit (FoM). The sensitivity of the RI sensor is described as follows:[377]

$$S_{RI} = \frac{\Delta\lambda}{\Delta n} \quad (6)$$

where Δn is the change in RI and $\Delta\lambda$ is the frequency change caused by the change in RI. FoM is the RI sensitivity normalized to the width of the resonance curve, which is characterized by the full width at half maximum (FWHM), describing how accurately the sensor measures the resonance minimum. FoM is calculated as[328]

$$\mathrm{FoM} = \frac{S_{RI}}{\mathrm{FWHM}} \quad (7)$$

Typically, higher sensitivity and larger FoM indicate better performance of the refractive index sensor.

Plasmonic-based RI sensors are widely used in fields such as biological sciences and medical diagnosis due to their ease of use and low cost.[378] Compared with traditional biomedical detection methods, such as enzyme-linked immunosorbent assay (ELISA) and polymerase chain reaction (PCR), plasmonic RI sensors have the characteristics of non-invasive, real-time, label-free, and rapid detection of biomarkers. Prostate-specific antigen (PSA), as a biomarker, is commonly used in cancer diagnosis.[379] In healthy humans, the concentration range of PSA is 4.0–10 ng mL^{-1}. The risk of prostate cancer increases when serum PSA concentrations are above 10 ng mL^{-1}.[380] Therefore, quantification of PSA is crucial for early diagnosis of prostate cancer. In 2018, Khan *et al.* proposed a gold nanodisc array based on specific aptamer functionalization for the detection of PSA.[381] By customizing the size of the gold nanodisk, the localized surface plasmon resonance was tuned to occur at a wavelength of 646 nm. Aptamers are a class of single-stranded DNA/RNA molecules that have relevance and specificity for a wide range of analytes. The results showed that the DNA aptamer-functionalized gold nanodisc array achieved a sensitivity of 113 nm per RIU for PSA, with an LOD as low as 1.49 ng mL^{-1} and a detection dynamic range of 1.7–20.4 ng mL^{-1}.

In addition to protein tumor markers, plasmonic RI sensors can also be used to detect tumor-derived exosomes.[382–384] Exosomes are nanoscale extracellular vesicles (50–150 nm in diameter) that are widely found in blood, urine, saliva and breast milk.[385–389] In biological organisms, exosomes can transport molecular contents from original cells to target cells and promote communication between various cells.[390,391] Recent studies have shown that patients with malignant tumors have an abnormal increase in exosomes.[392] Therefore, exosomes are also considered as potential biomarkers in cancer diagnosis. However, the detection of exosomes usually requires extensive sample purification and labeling, which poses challenges to the miniaturization and portability of detection platforms.[393] To this end, Lm *et al.* proposed a nanoplasmonic exosome (nPLEX) assay method for quantitative analysis of exosomes.[394] Periodic nanohole arrays are used to generate strong surface plasmon resonances. The plasmon resonance signal is shifted when exosomes bind to the nanopore. Quantitative monitoring of exosomes is achieved by measuring the phase difference or intensity change caused by the offset. By customizing the array period, the electromagnetic field range overlaps with the exosome size to further improve detection sensitivity. Subsequently, Lim *et al.* proposed the amplified plasmonic exosome (APEX) technology to measure different populations of circulating amyloid beta (Aβ) protein (exosome bound *vs.* unbound) directly from blood (Fig. 29a).[395] This technology utilizes localized optical deposition and *in situ* enzymatic transformation of bilayer plasmonic nanostructures to enable sensitive multiplex population analysis. It exhibits excellent sensitivity (approximately 200 exosomes) and enables co-localization of different targets in exosomes. This technology can well reflect brain plaque burden and is used in the clinical diagnosis of Alzheimer's disease.

Plasmonic RI sensors can also be used for early diagnosis of infectious diseases.[399] In recent years, the global pandemic of COVID-19 has posed a huge health threat to the world.[400] This is despite tremendous efforts in vaccination, prevention and treatment.[401] However, shortages of health care resources pose huge challenges to low- and middle-income countries.[402] Therefore, the development of rapid, reliable testing tools remains critical to containing current and future outbreaks of SARS-CoV-2 variants and reducing hospitalization and mortality in older patients.[403,404] To date, a variety of devices based on antigen and antibody immunoassays have been studied for the detection of the COVID-19 virus.[405,406] Among them, plasmonic RI sensors have received widespread attention due to their label-free and real-time detection characteristics. Recently, some researchers have developed COVID-19 detection platforms based on plasmonic RI sensing technology.[407–409] For example, Funari *et al.* developed a gold nanospike optical microfluidic sensing platform based on the

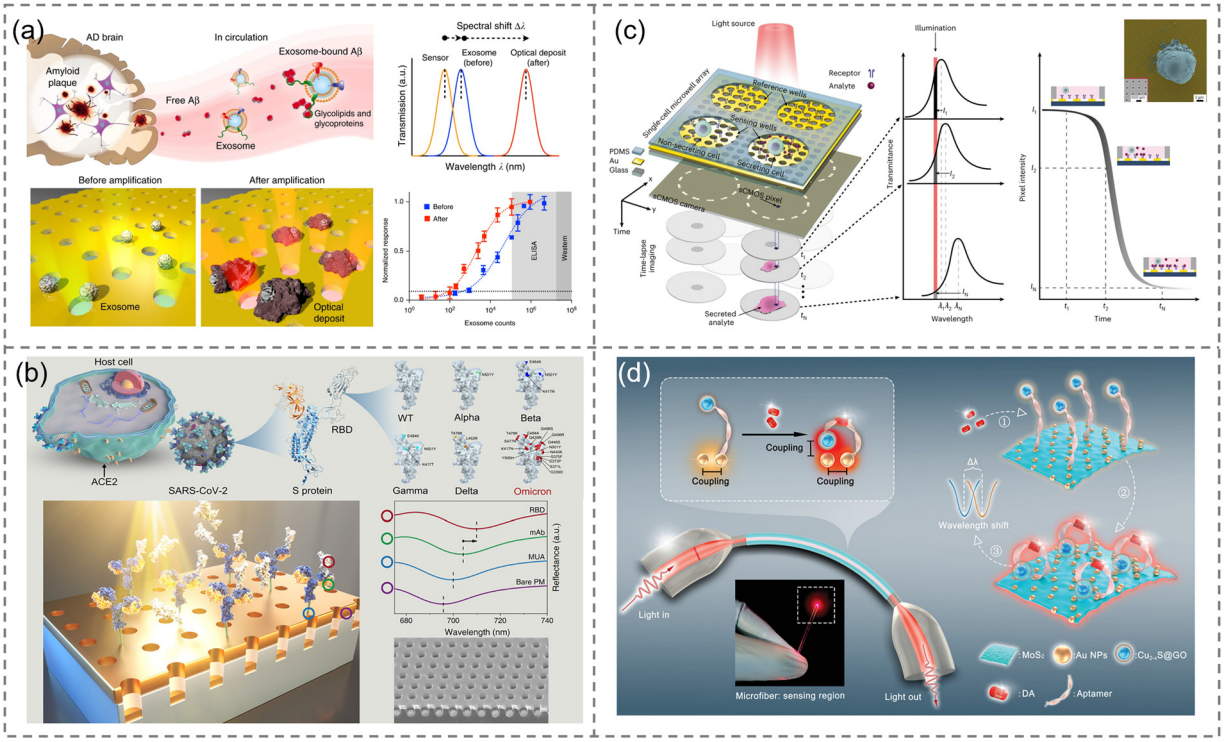

Fig. 29 RI sensing for molecular detection. (a) APEX platform for analysis of circulating exosome-bound Aβ. When exosomes localize on the nanopore, they change the refractive index near the nanopore, resulting in a red shift in the plasmon resonance frequency. Adapted with permission from ref. 395, Copyright 2019 Springer Nature. (b) mAb-functionalized plasmonic nanopores for detection of SARS-CoV-2 RBD variants. Adapted with permission from ref. 396, Copyright 2023 American Chemical Society. (c) Plasmonic nanopore arrays for spatiotemporal mapping of single-cell secretion. Adapted with permission from ref. 397, Copyright 2023 Springer Nature. (d) Plasmonic coupled optical microfiber biosensor for DA detection. Adapted with permission from ref. 398, Copyright 2023 Wiley.

principle of LSPR for detecting COVID-19 spike protein antibodies in plasmon.[410] Due to biomolecule binding events (*i.e.*, antigen–antibody binding), the RI changes around the metal structure, resulting in a red shift of the LSPR peak. Quantitative detection of COVID-19 is achieved by monitoring the red shift of the LSPR peak, with a detection limit of 0.5 pM for this sensing platform. Furthermore, Li *et al.* developed a label-free plasmonic nanopore sensor functionalized with monoclonal antibodies (mAbs) and demonstrated its binding characteristics with 12 SARS-CoV-2 spike receptor-binding domain (RBD) variants (Fig. 29b).[396] This plasmonic nanopore exhibits four vibrational modes. The binding kinetics between the 12 SARS-CoV-2 RBD variants and the mAb-functionalized plasmonic nanopores were experimentally recorded. The study shows that the fabricated plasmonic nanopores can effectively differentiate the SARS-CoV-2 Omicron BA.2 variant from other respiratory viruses. The detection limit is significantly lower than that of mainstream commercial kits, and it exhibits ultra-sensitive detection performance in both saliva and serum samples. Not only that, plasmonic RI sensors are also used for other virus detection.[411–413]

Compact and cost-effective optical devices for highly sensitive trace molecule detection are of great interest in many applications. However, when the amount of attached species is very small, highly sensitive and high-resolution spectrometers are required to record the tiny spectral shifts caused by the analyte. Such spectrometers are often bulky, expensive, and complex, which hinders the application of metasurfaces in molecular sensing and many other everyday detection scenarios. Molecular detection based on spatial multiplexing imaging has recently been developed to overcome the above difficulties.[414,415] Due to structure-dependent light scattering properties, properly designed spatially varying nanostructures have position-dependent reflectance or transmittance under narrowband light illumination and therefore exhibit intensity patterns. Adsorption or attachment of analyte molecules to the metasurface changes the intensity pattern, and changes in the intensity pattern can be captured by a camera.[378] This novel sensing method greatly simplifies the measurement equipment and demonstrates impressive sensitivity. Currently, pixelated metasurfaces (discrete changes in the geometry of nanostructured building blocks) and gradient metasurfaces (continuous changes in geometry) have been demonstrated.[288,416] In addition, this method can also be used for high-throughput parallel real-time spatial and temporal monitoring of cellular exosomes in hundreds of single cells. For example, Ansaryan *et al.* proposed a label-free nanoplasmonic imaging system capable of spatiotemporally mapping single-cell secretions in a microwell array format (Fig. 29c).[397] Gold nanohole arrays are used to support plasmon resonances. A complementary metal oxide camera is used to record spectral changes in surface plasmon resonances caused by analyte binding to receptors. The system can record intensity images of a large area in real time and simultaneously monitor

the morphology and movement of hundreds of single cells through machine learning algorithms.

Optical fibers are also effective biosensing technology in early medical diagnosis. Optical fiber technology is known to be cost-effective, flexible, compact, immune to electromagnetic interference, and suitable for remote operations.[417] However, the relatively low sensitivity severely limits the applications of optical fibers. LSPR in metal nanostructures has been proven in many works to effectively enhance the evanescent field on the surface of optical fibers, thereby improving the sensitivity of optical fiber biosensors.[418–420] Currently, plasmonic optical microfiber biosensors have been demonstrated for single-molecule detection of biomarkers or single-particle sensing with a size of 48–500 nm.[421,422] Subsequently, Huang *et al.* developed a dual-amplification nanointerface based on plasmonic coupling and conformational aptamer transition to further extend optical fiber single-molecule detection to the range of small molecules (such as dopamine (DA)) (Fig. 29d).[398] Due to the dual amplification enhancement effect, the sensor can detect single-molecule level DA molecules in biologically complex samples such as cerebrospinal fluid, whole serum, and artificial sweat, with detection limits of 1.30 am, 1.53 am, and 0.54 am, respectively. Furthermore, replacement by appropriate aptamers allows the sensor to be used to detect other target small molecules and ions at the single-molecule level.[423–426]

4.2.2 Surface-enhanced infrared absorption spectroscopy. Although RI sensors are characterized by ease of use and high sensitivity, resonant frequency shifts cannot provide more information, resulting in limitations in molecular recognition of RI sensors. Infrared absorption spectroscopy is an effective alternative to RI sensing. Infrared spectroscopy is a powerful analytical technique that provides unique information about the composition and dynamics of biochemical systems by resolving the characteristic absorption fingerprints of their constituent molecules. Based on this inherent chemical specificity and the ability for label-free, non-invasive and real-time detection, infrared spectroscopy methods have opened numerous breakthrough applications in areas such as environmental monitoring and defense, chemical analysis and medical diagnosis. However, there is a huge size mismatch between nanoscale molecules and micron-scale infrared light wavelengths, resulting in limited sensitivity when infrared spectroscopy is used to detect low molecular absorption cross-sections.[427,428] Nanoantennas with plasmonic enhancement can overcome this limitation.[429–431] This customized antenna structure can focus the incident light to the hot spot of the electromagnetic field, providing strong light–matter interaction, thereby detecting weak absorption features. The phenomenon based on plasmonic-enhanced molecular vibrations is also known as SEIRA spectroscopy. Enhancement factor (EF) is a key FOM used to quantify SEIRA sensing performance, and its expression is as follows:

$$\mathrm{EF} = \frac{I_{\mathrm{SEIRA}}}{I_{\mathrm{ref}}} \frac{N_{\mathrm{ref}}}{N_{\mathrm{SEIRA}}} \quad (8)$$

where I_{SEIRA} is the enhanced absorption vibration after plasmon coupling to the molecule and I_{ref} is the vibration intensity of the pure molecule. N_{SEIRA} is the effective number of molecules involved in SEIRA enhancement. Usually, N_{SEIRA} mainly refers to the number of molecules distributed at electromagnetic hot spots. N_{ref} represents the number of molecules in the uncoupled plasmon case.

In 1980, Hartstein *et al.* first discovered the SEIRA phenomenon through metal island films.[4] However, the randomness and non-resonant enhancement mechanism of metal island films lead to smaller EF (usually 10^1–10^2).[38,432] The emergence of metasurfaces brings new opportunities for the development of SEIRA technology.[433–437] The metasurface with a periodic structure not only overcomes the difference in randomness of the metal island film, but can also enhance its resonance by customizing the structure. In recent years, with the rapid development of micro-nano processing technology, various attractive structures have been proposed and prepared, such as asymmetric cross structures,[339,438] split resonant rings,[439] and fractal geometry.[440,441] The diverse structures provide unique opportunities to flexibly manipulate electromagnetic waves and improve SEIRA performance. These diverse structures are mostly based on artificial design. However, due to human beings' limited ability to think in extra dimensions, the structural design of metasurfaces tends to be simple geometric figures.[442] In addition, manual parameter optimization often consumes a lot of time and human resources. The rise of machine learning provides new solutions for reverse engineering metasurfaces.[443–447] The introduction of machine learning and other artificial intelligence technologies not only shortens the design cycle of metasurfaces, but is also expected to unlock new optical effects.[448,449]

Improving sensitivity is one of the important themes in SEIRA technology. Extensive research has shown that maximum SEIRA sensitivity is achieved when the plasmon resonance frequency matches the molecular vibration frequency.[450–453] In addition, increasing the near-field intensity is also the main way to improve SEIRA sensitivity.[454] A commonly used method to improve near-field strength is to prepare small gaps, including horizontal gaps[280,298,455] and vertical gaps.[456–460] For example, Dong *et al.* prepared a plasmonic bowtie nanoantenna with a horizontal gap of less than 3 nm,[455] and obtained a theoretical SEIRA EF of 10^7. Studies have shown that nanoscale gaps allow the sensing platform to detect as few as 500 4-nitrophenol molecules. On the vertical gap, using micro/nano flow channels to deliver analytes close to the antenna is an effective solution. However, as microfluidics decreases to nanometer scales, delivering analyte molecules into these gaps (*i.e.*, hot spots) becomes increasingly difficult, especially when the gap dimensions are comparable to the typical dimensions of the molecules. To this end, Miao *et al.* developed a patch-type SEIRA sensor using liquid metal.[460] This method uses liquid metal to immobilize the analyte between a plasmonic nanoantenna and the liquid metal. The height of the vertical nanogap here is close to the thickness of the analyte, which can produce a huge field enhancement, thereby significantly improving SEIRA sensitivity.

In addition to near-field enhancement, improving the spatial overlap rate between molecules and near-field (hot spots) is also critical to SEIRA sensitivity. However, part of the near-field

enhancement of the nanoantenna will enter the dielectric layer, preventing the molecules from fully overlapping with the hot spots. To solve this problem, a method of etching the dielectric layer to prepare nanopedestals was proposed.[461–463] This approach exposes hot spots to free space to increase the spatial overlap of molecules with the near field. Compared with nanoantennas on substrates, the SEIRA sensitivity of nanopedestals can be increased by 2.5–10 times.[462] In addition, the passive capture of molecules by the nanopedestal further enhances the sensitivity of SEIRA.[464] Coating the surface of plasmonic nanoantennas with molecule-enriched films or modifying probe molecules is another way to improve the spatial overlap of molecules and hot spots. Molecular enrichment films have proven effective for detecting discrete gas molecules.[465–471] For example, Zhou *et al.* used ZIF-8 as a molecular enrichment film to improve the detection sensitivity of gas molecules.[472] Subsequently, Zhou *et al.* used metal–organic framework (MOF)/polymer hybrid films to reduce the detection limit of CO_2 gas molecules to sub-ppm levels (Fig. 30a).[473] Probe molecules are often used to specifically adsorb proteins, nucleic acids, and lipids in a liquid environment.[278–280,427,474–476] Under the action of probe molecules, SEIRA technology can achieve dynamic detection of low-concentration biomolecules. Recently, new methods for improving sensitivity have emerged, such as loss optimization[54,457,477] and complex frequency wave synthesis.[478]

Improving bandwidth is another theme in SEIRA technology. Broadband spectroscopy can collect more fingerprint information, thereby enabling precise identification of molecules and fingerprint retrieval. Currently, a variety of structures have been developed for constructing broadband/multiband plasmon resonances, including fractal geometry,[440,441,480] self-similar structures,[481,482] asymmetric structures,[339] gradient metasurfaces,[483,484] and supercells.[485] Placing multiple nanoantenna structures supporting different frequencies within a single unit cell is a common method to achieve broadband/multiband.[486] However, as the density of antennas within the unit cell increases, the coupling between

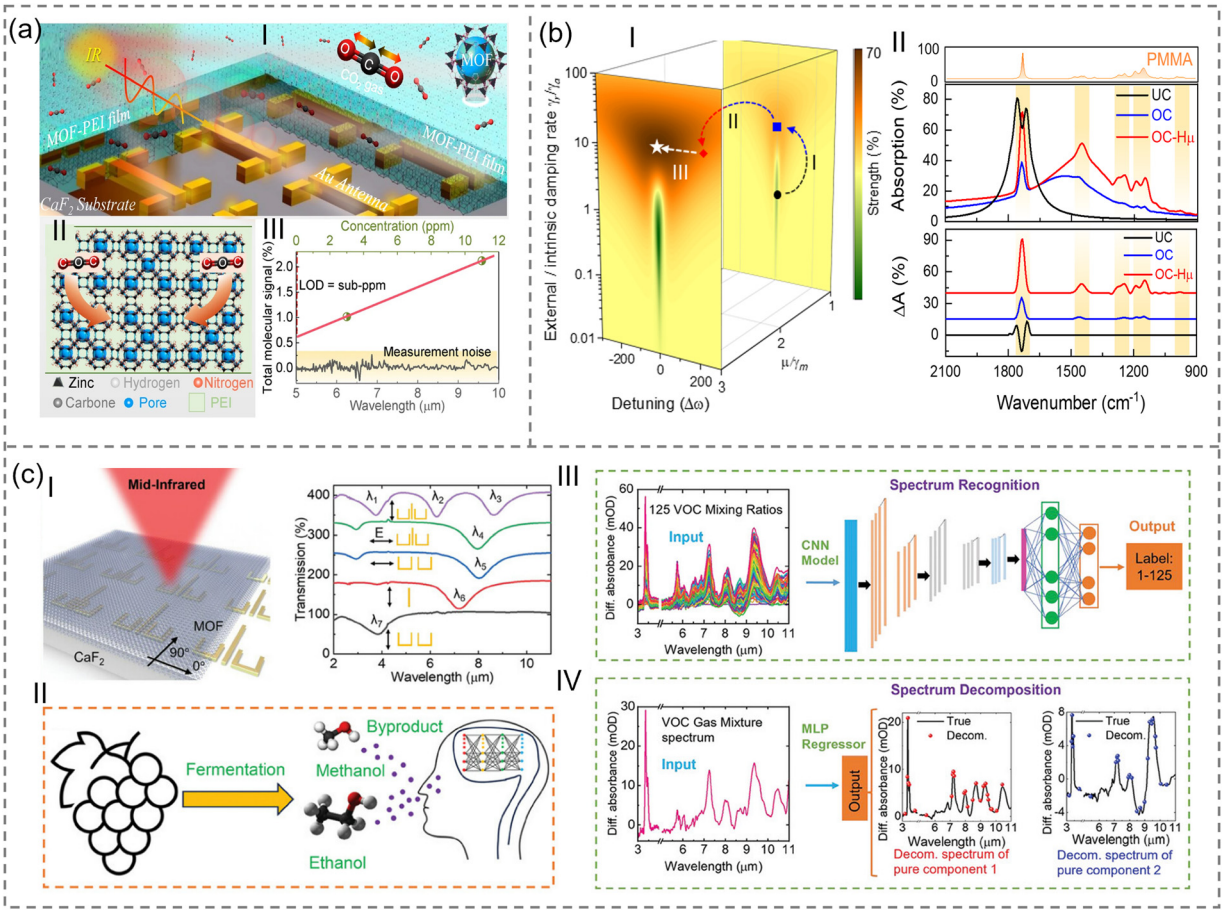

Fig. 30 SEIRA for molecular detection. (a) MOF/polymer-integrated multi-hotspot mid-infrared nanoantennas for sensitive detection of CO_2 gas. (I) Schematic diagram of the sensing platform. (II) Schematic showing the capture of CO_2 gas molecules by the porous MOF-PEI hybrid film. (III) LOD of the hybrid platform for CO_2 gas detection. Adapted with permission from ref. 473, Copyright 2022 Springer Nature. (b) Customized OC resonators for ultra-broadband and ultra-sensitive molecular detection. (I) Calculated sensitivity of plasmonic nanoantennas based on coupled-mode theory. (II) Absorption spectra and absorption difference spectra of plasmonic nanoantennas with different coupling modes after loading molecules. Adapted with permission from ref. 479, Copyright 2024 Springer Nature. (c) AI-enhanced "photonic nose" for mid-infrared spectroscopic analysis of trace VOC mixtures. (I) Schematic diagram and transmission spectrum of plasmonic nanoantennas. (II) Schematic diagram of the working mechanism of "Photonic Nose". (III) and (IV) Classification and regression models of machine learning. Adapted with permission from ref. 6, Copyright 2024 Wiley.

adjacent antennas also gradually increases. Supercells are an effective strategy to weaken the coupling of adjacent nanoantennas.[485] The supercell is composed of 16 sub-unit cells, and each sub-unit cell contains a hook-shaped nanoantenna. A broadband spectrum covering 6–9 μm is obtained by gradually changing the size of the nanoantenna. Splicing discrete spectra into continuous spectra is also a strategy to achieve broadband.[355,487–489] A typical advantage of this strategy is to establish a one-to-one mapping relationship between spectral information and spatial positions, thereby achieving spectrometer-free detection. However, this one-to-one mapping relationship results in a device with a larger area. To obtain a broadband spectrum in a smaller footprint, Li *et al.* designed an OC metamaterial absorber based on coupled mode theory.[348] This absorber has a broadband enhancement effect, and its enhancement bandwidth covers 6–14 μm. Benefiting from the broadband enhancement properties, Li *et al.* used a single array to achieve fingerprint retrieval for 13 analytes for the first time. Despite the large bandwidth of the OC metamaterial absorber, its sensitivity is relatively low. To achieve both broadband and high sensitivity in a metamaterial absorber, Li *et al.* introduced a plasmon-molecule coupling channel into the OC device (Fig. 30b).[479] The plasmon-molecule coupling channel can be modulated by adjusting the gap between adjacent nanoantennas. By reducing the gap between the nanoantennas, Li *et al.* developed a device with both bandwidth and sensitivity surpassing previous designs. Specifically, the sensitivity of the device reached 7.25% nm^{-1}.

The introduction of machine learning has further promoted the rapid development of SEIRA technology.[128,129,348,485,490,491] For example, Kavungal *et al.* developed an immunoassay-coupled nanoplasmonic infrared metasurface sensor for the specific detection of proteins associated with neurodegenerative diseases.[492] Aided by an artificial neural network, the sensor achieves unprecedented quantitative predictions of mixtures of oligomers and fibrin aggregates. SEIRA technology provides a valuable toolkit for studying dynamic reactions between molecules. However, infrared spectroscopy presents challenges in separating overlapping vibrational modes. Zhou *et al.* used stacked infrared nanoantennas to excite the coupling modes of localized surface plasmons and SPhP to solve the problem of overlapping vibration modes.[47] The research results have shown that SPhP vibration in the Reststrahlen band is particularly sensitive to molecular RI. Owing to the strong dependence of SPhP on RI, combined with deep neural network algorithms, the strongly overlapping molecular vibrations in biological reactions are dynamically unraveled. In gas sensing, Xie *et al.* introduced an artificial intelligence (AI)-enhanced "photonic nose" for trace-level volatile organic compound (VOC) gas analysis in the mid-infrared spectrum (Fig. 30c).[6] The MOF-coated plasmonic nanoantenna is designed to target VOC molecular fingerprints, achieving detection limits in the single-digit ppm range for isopropyl alcohol, ethanol, and acetone. Given the overlapping absorbance peaks among VOCs, deep learning models were employed. A convolutional neural network (CNN) model classified 125 VOC mixtures with 100% accuracy. A multilayer perceptron (MLP) model then decomposed the spectra into pure components, enabling accurate concentration predictions within an error of 10 ppm even in the presence of interferences.

4.2.3 Surface-enhanced Raman spectroscopy. Raman spectroscopy is a complementary technique to infrared spectroscopy. Although Raman spectroscopy and infrared spectroscopy both belong to molecular vibration spectroscopy, they are essentially different. For example, the infrared spectrum is an absorption spectrum, while the Raman spectrum is a scattering spectrum. Raman spectroscopy, as a form of inelastic scattering, can be used to study the vibration and rotation modes of the crystal lattice and molecules.[493,494] When laser or monochromatic light shines on a sample, the molecules in the sample will vibrate and scatter out photons of different frequencies after interacting with the incident photons. Raman spectroscopy records the frequency and intensity of scattered light. However, spontaneous Raman scattering is very weak, and the intense Rayleigh scattering often overwhelms the Raman signal, making it difficult to extract and resulting in low detection sensitivity. Raman signal intensity can be significantly enhanced through SERS.[495,496] SERS utilizes the electromagnetic enhancement effect[497] and the chemical enhancement effect[498,499] of nanostructures on the surface to improve the scattering signal of the sample. This enhancement effect is usually achieved by depositing nanoparticles on a surface such as metal or silver, forming the so-called "SERS substrate". SERS has the advantage of enabling rapid, non-invasive *in situ* detection of target molecules. The formula used to calculate SERS intensity is

$$I_{\mathrm{SERS}} \cong I_0 \left| \frac{E(\omega_{\mathrm{ext}})E(\omega_{\mathrm{det}})}{E_0(\omega_{\mathrm{ext}})E_0(\omega_{\mathrm{det}})} \right|^2 \quad (9)$$

where E and E_0 are the electric field strengths before and after plasmonic coupling with molecules respectively. ω_{ext} and ω_{det} are the excitation and detection frequencies respectively. Therefore, the EF of the Raman spectrum is

$$\mathrm{EF}_{\mathrm{SERS}} = \mathrm{EF}(\omega_{\mathrm{est}})\cdot\mathrm{EF}(\omega_{\mathrm{det}}) \quad (10)$$

SERS has received increasing attention in recent years due to its ultra-high sensitivity and selectivity in detecting extremely low concentrations of molecules. Currently, the development of SERS theory, SERS substrates, and related instruments has promoted its diverse applications in biomedical detection, nanomaterial characterization, food science, and environmental analysis.[35,500,501]

Surfaces and interfaces play crucial roles in many disciplines, including heterogeneous catalysis, electrochemistry, and photo-(electro)chemistry.[502] To fully understand surface and interfacial processes, it is necessary to obtain molecular-level information from surfaces and surface-interacting molecules. The SERS method is a powerful technique for studying surfaces and interfaces due to its ultrahigh surface sensitivity.[503] For example, Yu *et al.* developed a depth-sensitive plasmon-enhanced Raman spectroscopy method to detect the nanostructure and chemical properties of the solid electrolyte interface (SEI) on lithium anodes.[504] Dynamic molecular-level information provided by plasmon-enhanced Raman spectroscopy reveals the formation and evolution of the SEI in lithium metal batteries.

The research results are of great significance to further guide the SEI design of lithium metal batteries and improve SEI performance. With its high spatial resolution and ultra-small nanogaps, SERS can also be used for nanoscale chemical analysis of heterogeneous surfaces and to study single molecule optomechanics.[505–507]

The rich fingerprint vibration information obtained based on SERS provides a unique opportunity to develop photonic noses and photonic tongues. Inspired by the nose, Kim *et al.* proposed a SERS functionalized array to realize a powerful artificial nose sensing platform.[508] Eight SERS substrates were modified with differently functionalized SAMs. Multiple functionalized SERS substrates can embrace complex spectral information, thereby greatly improving the accuracy of biological sample identification in the absence of target-specific binding receptors. Based on a similar sensing strategy, Leong *et al.* demonstrated a SERS-based breath analyzer for rapid and non-invasive screening of individuals for COVID-19, achieving 96.2% sensitivity and 99.9% specificity. Due to the advantage that SERS technology can work in a liquid-phase environment, it also provides opportunities for the development of photonic tongues. Ling and colleagues proposed a SERS taster for multiplex analysis of wine flavor.[509] The taster captures chemical functionality within flavor molecules by employing many non-covalently interacting receptors. Ling *et al.* constructed comprehensive ''SERS superprofiles'' by combining the SERS spectra of all receptor flavors for predictive analytics using chemometrics.

There is great potential to conduct biomolecular testing directly at the point of care in a non-invasive manner.[510] However, there is a mismatch between traditional rigid SERS sensors and soft elastic organisms, which greatly limits their application in the wearable field. In this context, the development of flexible wearable SERS substrates has attracted great interest. In a recent example, Wang *et al.* proposed a wearable plasmonic metasurface sensor for non-invasive universal molecular fingerprint detection at biological interfaces (Fig. 31a).[511] This integrated platform is achieved by integrating a flexible SERS-active plasmonic metasurface as a key sensing component and a flexible electronic system capable of automatically extracting sweat and analytes from the body. Since each molecule has a unique SERS spectrum, the sensor can ''fingerprint'' targets extracted from sweat. Subsequently, Mogera *et al.* demonstrated a wearable microfluidic system based on plasmonic paper for continuous and simultaneous quantitative analysis of sweat loss, sweat rate, and metabolites in sweat.[512] An integrated flexible plasmonic wearable sensor is capable of sensitive detection and quantification of uric acid in sweat at concentrations as low as 1 μM. In the future, integrated flexible SERS sensors will show great potential in human health assessment, personalized diagnosis and treatment, and drug delivery.[513]

In addition to human health monitoring, SERS technology can also be used for plant health monitoring.[515,516] Monitoring plant health can increase plant productivity, optimize resource

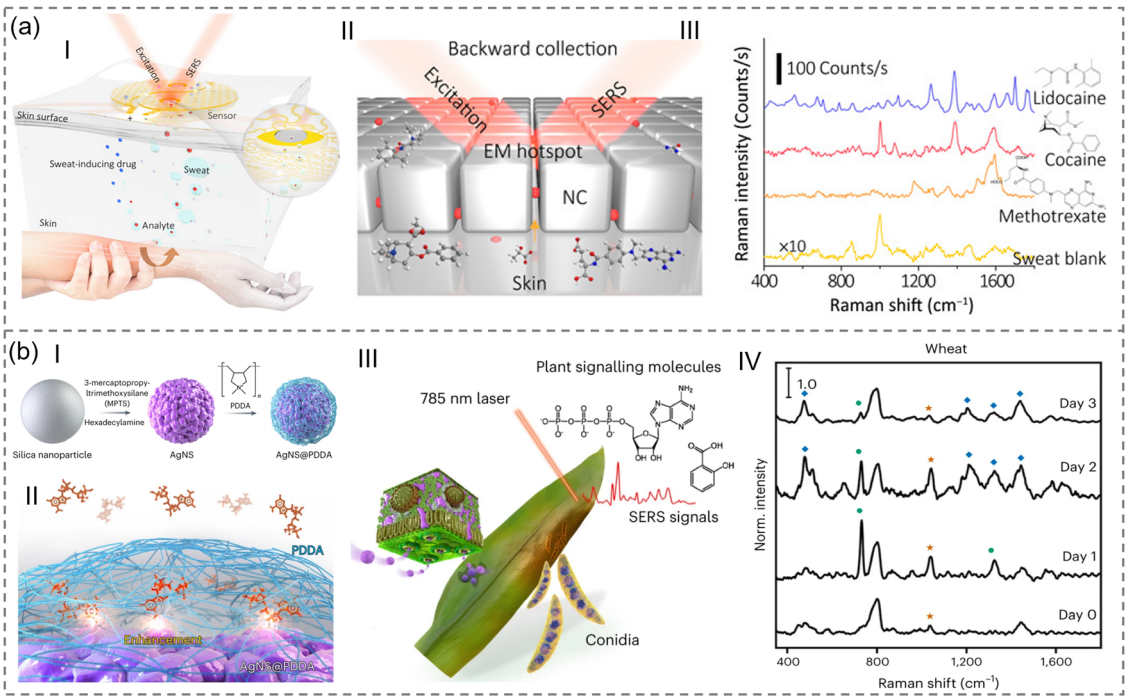

Fig. 31 SERS for molecular detection. (a) Plasmonic metamaterial-integrated wearable SERS sensing device. (I) Schematic drawing showing the working principle and design of the device. (II) Schematic illustration showing the SERS sensing principle of the nanocube metafilm. (III) SERS spectra of the human sweat samples. Adapted with permission from ref. 511, Copyright 2021 AAAS. (b) SERS nanosensor for the real-time monitoring of multiple stress signalling molecules in plants. (I) Schematic diagram of the synthesis of SERS-active nanoparticles. (II) Schematic of the enhanced Raman scattering on the surface of silver nanoshells. (III) Schematic diagram of early diagnosis of fungal diseases in crops based on SERS. (IV) Monitored SERS spectra of fungal infections in wheat. Adapted with permission from ref. 514, Copyright 2022 Springer Nature.

allocation of water and agrochemicals, and select optimal plant traits. Under stress conditions, plants release endogenous chemicals that trigger their defense mechanisms. Therefore, monitoring these endogenous signals can serve as a reliable indicator of plant health. Common endogenous signals encompass salicylic acid (SA), extracellular adenosine triphosphate (eATP), phytoalexins, and glutathione. Several studies have utilized SERS probes for detecting endogenous biomolecules or pathogens in plant extracts or isolated leaves.[517–520] Notably, a recent study by Son *et al.* presented an innovative approach for non-destructive detection of signaling molecules within living plants (Fig. 31b).[514] They introduced SERS nanoprobes into the intercellular space to monitor the transport of signaling molecules in the apoplast. These SERS nanoprobe applications successfully identified SA, eATP, cruciferous phytoalexins, and glutathione in nasturtium, common wheat, and barley under various stressors, both biotic and abiotic. Furthermore, SERS technology has found utility in detecting pesticide residues,[521,522] banned food additives,[523,524] and mycotoxins in agricultural products.[525,526] This multifaceted application of SERS underscores its potential as a versatile tool in agricultural monitoring and management.

4.2.4 Surface plasmon-enhanced chiral spectroscopy. Chiral molecules are those molecules that cannot perfectly coincide with their mirror image through rotation or translation. Therefore, they exist in two non-overlapping structures, also known as enantiomers. Chirality, as a basic attribute in nature, widely exists in nature and biomolecules. For example, there are two enantiomers of the amino acids and nucleic acids that make up proteins. Left and right hands are often used to distinguish chiral molecules. Although the elements and functional groups that make up chiral molecules are the same, their chemical properties can be quite different. Therefore, the study of chirality is very important, especially in the fields of drugs and pesticides. Often the other enantiomer of a drug or pesticide exhibits useless or harmful effects. Therefore, sensing and distinguishing chiral forms is of vital importance in the fields of analytical chemistry, biomedicine, pharmaceutical industry, and toxicology. Currently, optical rotational dispersion (ORD) and CD spectroscopy are the commonly used methods to detect molecular chirality.[527–529]

However, the intramolecular CD signal intensity is very small, usually around the 10^{-5} level. To address this limitation, leveraging chiral plasmonic structures has emerged as a promising solution.[530] In 2010, Kadodwala and colleagues pioneered the utilization of plasmonic planar chiral metamaterials for detecting chirality across various proteins (Fig. 32a).[531] Their method capitalizes on metallic gamma ion arrays on substrates, which can exist in left- or right-handed configurations. Each type of array converts incident linearly polarized light into elliptically polarized light with consistent chirality. Upon biomolecule adsorption, these metal gamma ion arrays induce resonance shifts due to the high sensitivity of surface plasmon modes to the refractive index of their surroundings. Notably, the refractive index of chiral molecules differs under left-handed and right-handed circularly polarized light, potentially leading to distinct resonance shifts in the plasmon. Thus, detecting chiral molecules involves measuring disparities in resonance shifts. Studies indicate that plasmons can enhance chiral sensitivity by up to six orders of magnitude compared to conventional CD measurements. Subsequently, the same research group introduced a shuriken-shaped metasurface, which facilitated the detection of viruses,[532] antibodies,[533] and peptide molecules.[534] This advancement leveraged enhanced chiral asymmetry and subwavelength spatial localization, further broadening the scope of chiral molecule detection in diverse applications.

Currently, commonly used CD spectra are situated in the UV, visible, and near-infrared regions, primarily because the stronger CD signals of molecules are found at shorter wavelengths. However, CD signals at these wavelengths often fail to provide detailed information about the chemical structure of the molecule, which limits their utility in distinguishing various types of chiral molecules within mixtures. In recent years, there has been a push to extend the CD spectrum into the mid-infrared region to acquire vibrational circular dichroism (VCD).[537] Unlike CD spectra, VCD offers more comprehensive molecular structure information by exploiting vibrational transitions of chiral molecules. Nonetheless, the longer wavelength VCD signal is typically 2 to 3 orders of magnitude smaller in intensity than the CD signal.[538,539] Plasmonic systems present a potential avenue for enhancing VCD signals. For instance, Chanda's team utilized an achiral plasmonic system to boost VCD detection sensitivity by 4 orders of magnitude.[540] More recently, the same team significantly enhanced the detection sensitivity of chiral molecules by fine-tuning an achiral plasmon system. Experimental findings illustrate that compared to traditional VCD spectroscopy technology, the plasmon system can elevate the detection sensitivity of chiral molecules by up to 13 orders of magnitude.[541] While numerous research efforts have demonstrated that chiral structures can amplify VCD signals, the underlying mechanism remains unclear. Addressing this, Xu *et al.* embarked on a study beginning with the fundamental relationship between planar chiral metamaterials and chiral response (Fig. 32b).[535] They theoretically hypothesized that near-field coupling strength might be a pivotal factor in far-field CD. To test this hypothesis, Xu *et al.* devised a selective exposure method to cover the nanogap of the four-resonance metamaterial, probing the correlation between the near-field coupling coefficient and the far-field CD response. Experimental results ascertain that enhanced chiral near-field plays a pivotal role in amplifying molecular signals. This critical finding paves the way for achieving ultra-small volume and label-free detection of chiral molecules. Given that the VCD spectrum contains information pertaining to the vibration of chiral molecules, it offers the feasibility of distinguishing the identity and chirality of enantiomers. Leveraging this characteristic, Xu *et al.* proposed an enhanced VCD sensing platform based on plasmonic chiral metamaterials for discerning the secondary structures of different proteins (Fig. 32c).[536] In this endeavor, Xu and colleagues demonstrate, for the first time, the potential of utilizing surface-enhanced VCD to detect chiral mixtures, thereby broadening the scope of VCD spectroscopy.

In recent years, Raman optical activity (ROA) has emerged as another valuable chiral spectroscopy technique.[542] One of its

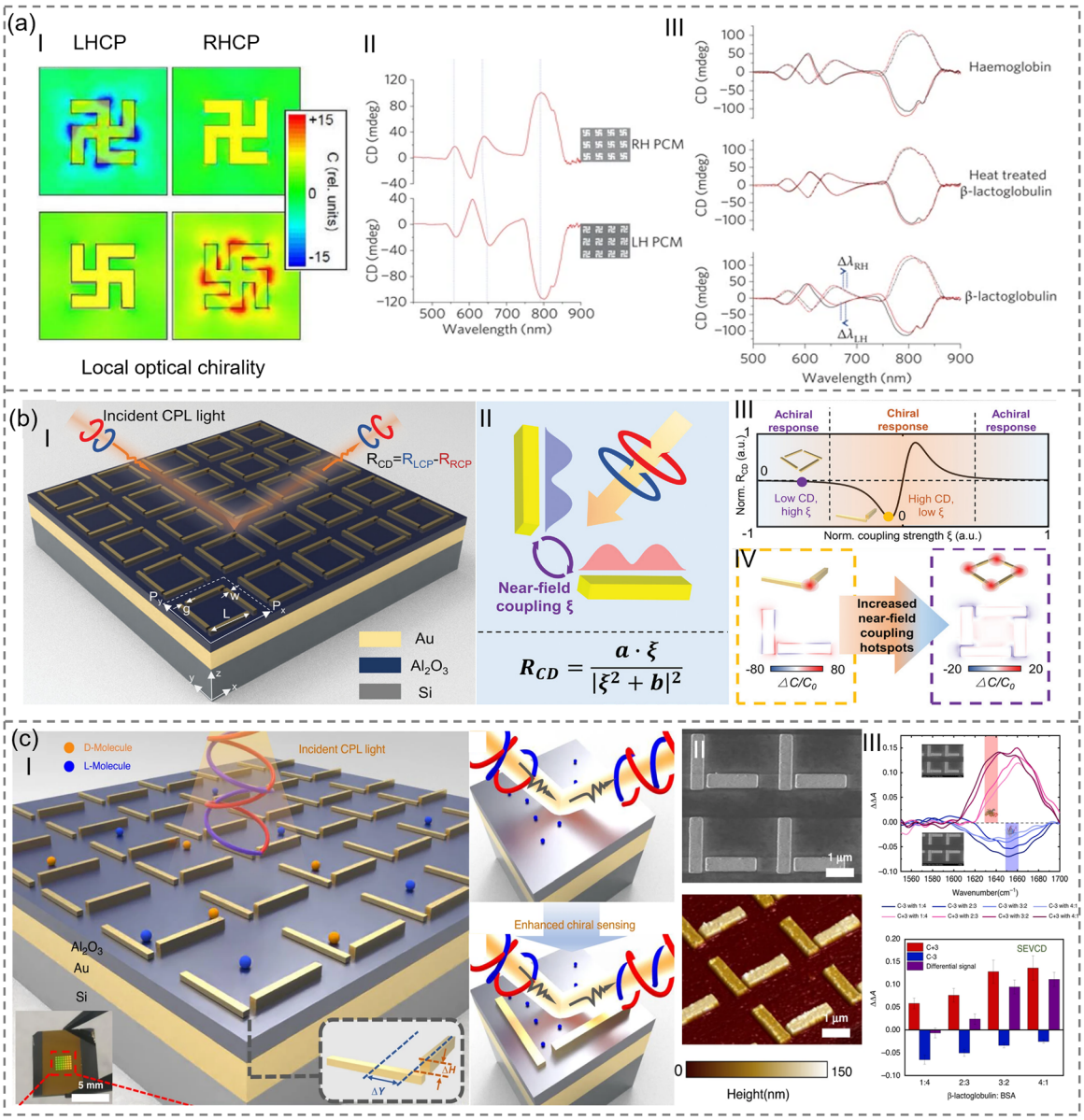

Fig. 32 Surface plasmon-enhanced chiral spectroscopy for molecular detection. (a) Ultrasensitive detection and characterization of biomolecules using superchiral fields. (I) Local optical chirality. (II) CD spectra collected from LH/RH planar chiral metamaterials immersed in distilled water. (III) Influence of the adsorbed proteins on the CD spectra of planar chiral metamaterials. Adapted with permission from ref. 531, Copyright 2010 Springer Nature. (b) Near-field induced less chiral response for chiral molecular sensors. (I) Schematic drawing of the chiral metamaterials. (II) Schematic illustration of the near-field coupling between perpendicularly positioned plasmonic resonators. (III) Calculated R_{CD} as a function of coupling strength. (IV) Simulation of the optical chiral field for both double-resonator and quadruple-resonator structures. Adapted with permission from ref. 535, Copyright 2023 Wiley. (c) Expanding chiral metamaterials for retrieving fingerprints *via* vibrational circular dichroism. (I) Schematic drawing of the surface enhanced VCD sensing platform. (II) Device characterization. (III) Experimental demonstration of chiral mixture sensing. Adapted with permission from ref. 536, Copyright 2023 Springer Nature.

primary advantages lies in its capability to analyze water dispersion samples, which may be too absorbent for VCD.[543] However, conventional ROA also faces the challenge of low signal intensity. Addressing these inherent limitations of ROA can be achieved through surface plasmon enhancement techniques. In 1983, Efrima first proposed the feasibility of surface-enhanced ROA spectroscopy in the literature.[544] Subsequently, Efrima introduced a theoretical treatment method for surface-enhanced ROA.[545] Building upon this theoretical foundation, Janesko and colleagues put forward an electromagnetic enhancement model tailored for surface-enhanced ROA spectra.[546] This model offers a concise framework that integrates the fundamental equations for unenhanced ROA with modifications to the molecular response tensor induced by substrate's electromagnetic enhancement. Presently, this model stands as the most widely adopted theoretical formulation in surface-enhanced ROA. On the experimental front, Sun and colleagues developed advanced optical technologies to detect ROA signals of molecular structures.[547]

They augmented Raman signal intensity by utilizing silver chiral nanowires as plasmonic waveguides. This technique allows for the differentiation of Raman spectra excited by left- and right-handed circularly polarized light, facilitating the determination of sample chirality and conformation. Additionally, Ostovar and his team uncovered a novel chiral transfer mechanism to enable surface-enhanced ROA.[548] This mechanism stems from the breaking of inversion symmetry in achiral nanoparticles when interacting with nearby chiral molecules, subsequently altering the symmetry of the excitation fields of left-handed circular polarization (LCP) and right-handed circular polarization (RCP). Such alterations in circularly polarized light symmetry result in asymmetric absorption in achiral probes, detectable through Raman spectroscopy.

The prospect of extending CD spectroscopy into the terahertz range is intriguing due to the ability of THz spectroscopy to capture both vibrational and rotational information of biological macromolecules. This has spurred considerable interest in realizing terahertz circular dichroism (TCD).[549] However, the absence of polarization modulation in terahertz radiation has hindered the widespread adoption of TCD. Recently, the use of nonlinear metasurfaces to generate terahertz waves with different circular polarizations has presented new opportunities for achieving TCD. For instance, Choi *et al.* employed periodic kirigami cutting to transform plasmonic sheets into tunable optical elements, enabling polarization modulation of THz radiation.[550] The herringbone pattern of microscopic metal strips facilitated a dynamic polarization rotation modulation range of over 80° across thousands of cycles. The advent of polarization modulators has paved the way for realizing TCD spectra. Subsequently, McDonnell and colleagues introduced a broadband terahertz emitter based on the Pancharatnam–Berry phase nonlinear metasurface, which exhibits unique optical functionalities.[551] Through the Pancharatnam–Berry phase nonlinear metasurface, both the polarization and phase of the terahertz wave can be precisely controlled. McDonnell *et al.* further showcased the application of PB-phase nonlinear metasurface emitters in TCD spectroscopy. TCD spectroscopy offers a distinctive tool for detecting chiral phonons in various biomolecule crystals.[552] The identification of chiral phonons not only facilitates a deeper understanding of biochemical processes but also unlocks new avenues for medical applications of terahertz photonics.[553]

4.2.5 Surface-enhanced fluorescence spectroscopy. Fluorescence detection has been widely used in life sciences and medical diagnostics due to its low detection limit and diverse fluorophore selection, which enables simultaneous measurement of multiple biomarkers. However, a key challenge limiting fluorescence detection is that the fluorescence signal can be weak at low analyte concentrations. To address this problem, complex, expensive, and bulky instrumentation is often required to maintain high detection sensitivity. For disease diagnosis, bulky instruments and large footprints often hinder their application in resource-limited settings. Recently, plasmonic metal-based nanostructures have provided a simple solution for significantly enhancing the optical properties of fluorophores. Metal nanoparticles generate plasmon resonance under the irradiation of incident light and form surface plasmons at the metal–dielectric interface. The formation of surface plasmons leads to an enhancement of the local electromagnetic field, which in turn increases the excitation rate of the fluorophore. Furthermore, the emission of the fluorophore is also enhanced due to the increased local density of states, which results in a higher probability of transition from the excited energy state to the ground energy state. Therefore, by placing fluorophores near conductive metal surfaces or particles, an increase in quantum yield and a decrease in fluorescence lifetime can be achieved. This phenomenon is called the SEF effect.[36,554]

SEF spectroscopy stands out as a remarkable tool offering ultra-high sensitivity for detection and imaging down to the single-molecule level. In the 1960s, Drexhage and colleagues made the initial observation that the decay time of molecular fluorescence correlates with the distance between the excited molecule and the metal film.[555] Subsequently, extensive research on this phenomenon has been conducted by groups led by Lakowicz and Geddes.[556–561] Early implementations of SEF commonly utilized rough silver island films as substrates.[562–564] In recent years, with advancements in nanoparticle synthesis technology, noble metal nanoparticles with diverse morphologies have gained prominence as SEF substrates.[565–568] In 2006, Kühn *et al.* demonstrated a notable advancement by employing scanning probe technology to couple a single molecule to a single spherical gold nanoparticle functioning as a nanoantenna, resulting in a fluorescence enhancement of over 20 times.[569] Nonetheless, gold nanospheres lack preferential dipole directions, and the probe does not support any resonant coupling modes, leading to limited fluorescence enhancement effects.[570] To address this limitation, the utilization of nanoshells, nanorods, nanopores, and nanobowties has been proposed to enhance local fluorescence.[571–575] Notably, Kinkhabwala and colleagues utilized electron beam lithography to fabricate gold bowties reduced to 14 nm (Fig. 33a).[571] The nanogap in these structures provides substantial field enhancement, achieving an impressive fluorescence enhancement of up to 1340-fold. This groundbreaking work significantly advances the application of SEF in small molecule detection, heralding new possibilities in the field.

Single molecule detection represents a pivotal application area within the realm of SEF spectroscopy.[578–580] In 2007, Lakowicz *et al.* achieved a significant milestone by detecting the fluorescence signal of rhodamine on a silver island membrane substrate.[581] Fluorescence emission from rhodamine increased 7-fold and the fluorescence lifetime was shortened using silver island films as substrates. Subsequently, Orrit *et al.* employed wet chemistry to synthesize a large quantity of AuNRs, providing fluorescence enhancement comparable to photolithographic components.[575] Experimental findings revealed that AuNRs yielded over 1000-fold fluorescence enhancement for nearby crystal violet molecules, with a quantum yield of 2%. More recently, there have been reports employing SEF to detect antibiotic molecules.[582–586] Beyond single molecule detection, there's significant interest in utilizing SEF to monitor reactions involving individual molecules.[587] The study of single-molecule reactions serves to deepen our understanding of chemical processes.[588,589] For instance, Li *et al.* utilized a plasmonic nanocavity substrate to

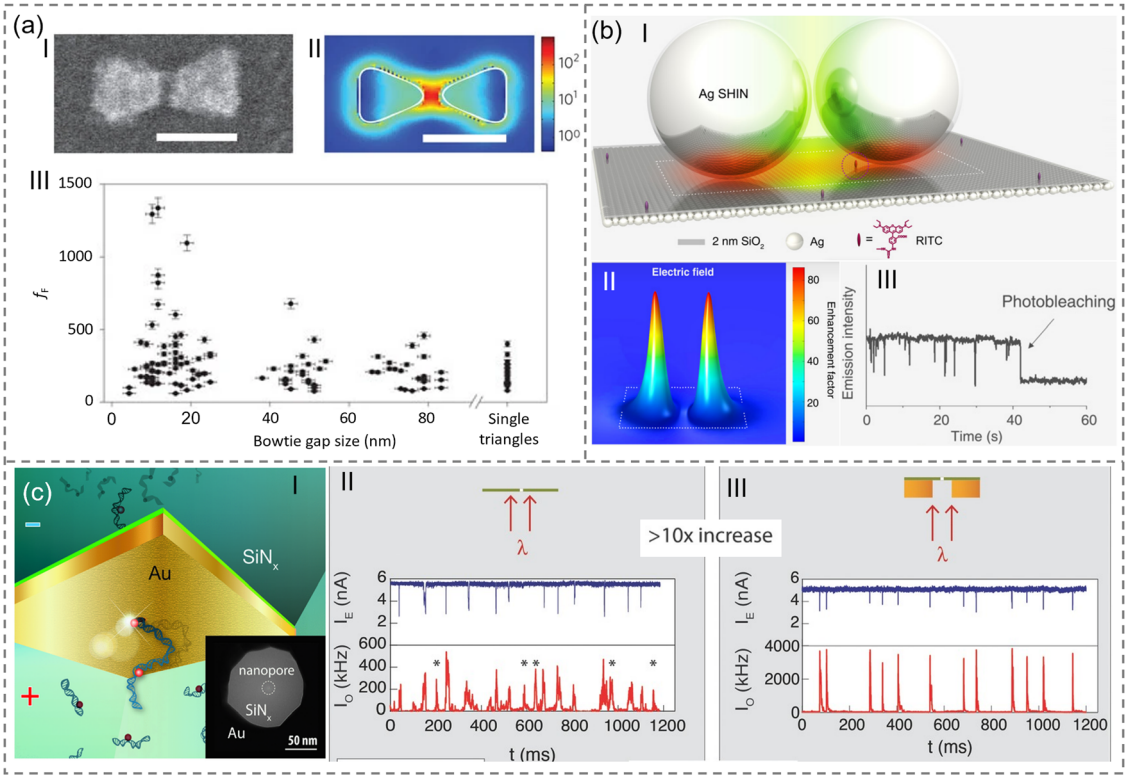

Fig. 33 SEF spectroscopy for molecular detection. (a) Large single-molecule fluorescence enhancements produced by a bowtie nanoantenna. (I) Scanning electron microscopy (SEM) image of a gold bowtie nanoantenna. (II) Finite-difference time-domain calculation of local intensity enhancement. (III) Scatter plot of fluorescence brightness enhancement of 129 fluorescent molecules as a function of bowtie gap size. Adapted with permission from ref. 571, Copyright 2009 Springer Nature. (b) Real-time detection of single-molecule reaction by plasmon-enhanced spectroscopy. (I) Schematic diagram of plasmon-enhanced single-molecule spectroscopy. (II) Simulation of the electric field distribution. (III) The characteristic emission intensity trace of a single rhodamine B isothiocyanate molecule, exhibiting blinking behavior and single-step photobleaching events. Adapted with permission from ref. 576, Copyright 2020 AAAS. (c) Light-enhancing plasmonic-nanopore biosensor for DNA detection. (I) Schematic diagram of the plasmonic nanopore device. (II) Detection signal of the non-plasmonic device. (III) Detection signal of the plasmonic nanopore device. Adapted with permission from ref. 577, Copyright 2016 Wiley.

enhance the fluorescence and Raman signals of single molecules (Fig. 33b).[576] Conformational transitions and removal of the carboxyphenyl group within the molecule induced shifts in the fluorescence emission band. Raman signals were utilized to identify reaction intermediates and unveil underlying reaction mechanisms. By correlating fluorescence spectra with Raman signatures, Li *et al.* achieved real-time monitoring of the light-induced cleavage reaction of individual rhodamine B isothiocyanate molecules.

Nucleic acids, such as DNA, are among the most important molecules in living organisms, as they carry and transmit genetic information that determines biological traits.[590] Therefore, accurate detection of nucleic acid molecules is crucial. Plasmonic nanopores have become one of the key tools for nucleic acid detection.[591] There are two main advantages to using plasmonic nanopores for nucleic acid detection. First, the potential gradient near the nanopore actively guides the nucleic acid molecules into the pore region.[592] Compared to passive diffusion, this active transport enables single-molecule detection even at low concentrations. Second, the typical nanopore diameter is designed to be slightly larger than the cross-section of the nucleic acid molecule, which restricts the movement of the molecule to a single dimension while ensuring continuous occupation of the sensing volume.[591] This restriction allows for single-molecule detection across a wide range of concentrations by increasing the residence time of the molecule. Additionally, as nucleic acid molecules pass through the nanopore, their polymer chains can be linearized, enabling continuous observation of submolecular sequences. For example, Assad *et al.* proposed a plasmon nanopore-based device for detecting individual DNA molecules (Fig. 33c).[577] In this device, a SiNx membrane faces the analyte source and the nanopore acts as a physical gate. This approach allows only one molecule to enter the nanopore at a time, reducing background noise. To characterize the sensing properties of the plasmonic nanopore, Assad *et al.* covalently labeled a 5 kbp double-stranded DNA with the fluorophore CF640R. Each DNA molecule contained seven fluorophores and was introduced into the *cis* chamber at a relatively low concentration of 0.1 nM or less. The study showed that the peak fluorescence intensity increased more than tenfold as the DNA molecule passed through the plasmonic nanopore compared to non-plasmonic devices.

Detection of amino acids and proteins using SEF holds significant promise, especially considering the crucial role amino acids play as the fundamental building blocks of various

proteins in the human body. Such detection aids in early risk assessment of chronic and malignant diseases. Lakowicz *et al.* proposed a fluorescence-enhancing substrate based on aluminum nanoparticles for label-free detection of amino acid molecules.[582] Their work demonstrated a remarkable 3500-fold fluorescence enhancement when the fluorophores were oriented perpendicular to the aluminum surface. Additionally, Lakowicz *et al.* showcased the fluorescence enhancement of tryptophan and tyrosine by aluminum nanoparticles. The pioneering work by Geddes and colleagues marked the first instance of protein detection using SEF.[593] Since then, SEF has been employed to detect various protein molecules, including erythrin, algal proteins, and recombinant proteins. In recent years, the utilization of aptamer sensors has gained popularity. Aptamers, functional single-stranded DNA or RNA molecules (10–100 nucleotides), offer unique sensitivity and specificity in binding to a variety of target molecules, such as small molecules, viruses, proteins, peptides, and even cells. Chen *et al.* proposed a novel fluorescent polarization aptasensor based on bivalent aptamers and silver nanoparticles for lactoferrin detection.[594] The bivalent aptamer was engineered to attach to the signaling molecule fluorescein isothiocyanate and the enhancer silver nanoparticles. By incorporating second-order aptamers, the distance between silver nanoparticles and fluorescent dyes could be minimized. Experimental results demonstrated that the detection sensitivity of this sensor is approximately 3 orders of magnitude higher than that of traditional aptamer-based homogeneous detection, with a detection limit of 1.25 pM. These advancements in SEF-based detection methods hold immense potential for early disease diagnosis and biomedical research, offering enhanced sensitivity and specificity in detecting amino acids and proteins.

The utilization of SEF for detecting bacteria and viruses is of utmost importance, especially in the context of public health and disease management. The pioneering work in SEF-based bacterial detection was conducted by the Lakhtakia team.[595] They employed porous metal-engraved films comprising silver, aluminum, gold, and copper as substrates to detect *E. coli* in water. Experimental findings revealed that the device exhibited approximately 20 times fluorescence enhancement compared to traditional glass substrates. Subsequently, Huang *et al.* also contributed to the detection of *E. coli* using SEF.[596] They utilized mixed thiol SAMs of PEG-thiol and COOH-thiol modified gold surfaces as substrates and leveraged long-range surface plasmons to enhance fluorescence spectroscopy. Their experimental results indicated a detection limit below 10 CFU ml^{-1}, with analyte concentrations ranging from 10 to 10^6 CFU ml^{-1}. In recent years, with the emergence of the global COVID-19 pandemic, the urgency for various sensing methods to facilitate virus detection has become paramount. Addressing this need, Hu *et al.* employed nanostructured plasmonic gold chips for multiplex assessment of antibodies against various virus variants.[597] Experimental results demonstrated that the detection limit of these chips was as low as 20 fM, more than two orders of magnitude lower than that of glass substrates. Subsequently, Zhu *et al.* introduced an in-frame gold particle nanostructure for direct assessment of the SARS-CoV-2 nucleocapsid protein.[598] By integrating gold nanostructures with a microplate reader, the sensor achieved a sensitivity of 44 fg mL^{-1} in just 3 minutes. To further enhance analytical sensitivity, Zhu *et al.* employed single-molecule counting technology, achieving a detection limit as low as 0.84 ag mL^{-1}. These advancements highlight the potential of SEF-based techniques in achieving rapid and sensitive detection of bacteria and viruses, thus playing a crucial role in disease surveillance and management efforts.

4.2.6 Nanospectroscopy *via* plasmon-induced resonant energy transfer. PIRET-based enhanced spectroscopy plays a vital role in molecular sensing. PIRET occurs through electromagnetic coupling between plasmonic nanostructures and acceptor molecules, enabling direct resonant energy transfer.[599] For instance, Liu *et al.* immobilized cytochrome *c* on a single plasmonic nanoparticle and observed quantized plasmon quenching in the resonance Rayleigh scattering spectrum.[600] Notably, the efficiency of PIRET depends on the degree of spectral overlap—the better the overlap, the higher the PIRET efficiency and the stronger the plasmonic quenching. Subsequently, Choi *et al.* utilized PIRET between conjugated metal–ligand complexes and a single gold plasmonic probe to achieve Cu^{2+} detection at concentrations as low as 1 nM.[601] By functionalizing gold nanoparticles with different ligands, this approach can be extended to the detection of other metal ions.

Beyond nanospectroscopy, PIRET also plays a significant role in molecular imaging. While fluorescence imaging has demonstrated exceptional performance in biological applications, it lacks chemical fingerprint information. Moreover, the broad absorption and emission spectra of organic fluorophores, along with their susceptibility to photobleaching and blinking effects, limit their effectiveness in long-term imaging and multiplexing.[602] In contrast, plasmonic nanoparticles based on PIRET offer a promising solution for hyperspectral imaging.[603] For example, Kim *et al.* developed a PIRET-based metasurface-driven multiplexed nanospectroscopy platform for real-time monitoring of multiple biomolecules within live cells.[604] Compared to traditional fluorescence and chemiluminescence methods, this platform leverages the stability of molecular absorption signals to overcome the constraints of photobleaching and complex preprocessing. The metasurface in their study was composed of aggregated aluminum nanodisks, which selectively modulated the scattering spectrum across the entire visible range, enabling simultaneous detection of different biomolecules. When the scattering peak of the metasurface matched the absorption frequency of a specific biomolecule, strong PIRET occurred, leading to quenching in the scattering spectrum. This approach facilitated high-spatial-resolution molecular imaging, advancing molecular sensing technologies.

4.3. Multi-effect fusion for molecular detection

4.3.1 Electrically tunable plasmons for molecular detection. The generation and maintenance of plasmons in metal nanostructures typically depend on their geometric shape, composition, and surrounding environment. However, once a metal substrate is fabricated and a specific geometric shape is obtained, the plasmon frequency of the metal is essentially

"locked", meaning it lacks external tunability. This limitation is particularly pronounced when trying to exploit multiple vibrational modes of molecules (*e.g.*, for identification) across a broad spectral range, thus restricting their practical application in SEIRA. In contrast, tunable plasmons offer greater flexibility in molecular sensing. The nanostructures used to build plasmons exhibit an open architecture in subwavelength unit cells, which facilitates the integration of materials. Therefore, incorporating functional materials such as liquid crystals,[605,606] phase-change materials,[607,608] or quantum materials enables tunable plasmons,[609,610] showcasing their extensive applications in molecular sensing.

Graphene, a single-atom-thick planar material, has unique electronic and optical properties. Importantly, the carrier density (*i.e.*, Fermi level) of graphene can be adjusted through electrostatic gating or chemical doping, allowing precise tuning of plasmonic resonances. By patterning graphene into nanoribbons, electromagnetic waves propagating in free space can directly couple to graphene and generate local plasmons. These local plasmons can significantly enhance light–matter interactions, thereby markedly increasing molecular absorption of infrared vibrational modes. Li *et al.* were the first to demonstrate the application of graphene nanoribbons in enhancing polymer film vibrational sensing.[315] Rodrigo *et al.* dynamically controlled the Fermi level of graphene nanoribbons by applying a bias voltage, achieving dynamic tuning of graphene plasmonic resonances.[313] The results showed that electrically tunable graphene could enable a single device to perform SEIRA sensing across a wide spectral range, thus enhancing the detection of specific vibrational fingerprints. Using the same approach, Hu *et al.* designed a graphene plasmonic structure for sub-monolayer molecular detection (Fig. 34a).[611] In their work, the graphene plasmonic structure was fabricated on a CaF_2 substrate to eliminate the strong plasmon–phonon hybridization in the traditional graphene plasmonic structure. Using far-field Fourier transform infrared spectroscopy, the graphene plasmonic can achieve a highly selective average enhancement of up to 20 times. Subsequently, the same research group successively designed a graphene plasmonic structure for protein detection in gas and aqueous solutions.[314,612]

Combining graphene with metal nanostructures also allows for the tuning of plasmonic resonance frequencies. Compared to traditional designs consisting only of metal nanostructures, the introduction of graphene enables easy tuning of plasmonic resonance frequencies by altering the Fermi level. Compared to plasmonic structures made solely of graphene nanoribbons, metal nanostructures provide stronger light–matter interactions, thereby enhancing the SEIRA effect. Chen *et al.* theoretically designed a broadband hybrid graphene metamaterial absorber that combines the high absorbance of metal plasmons with the electrically tunable properties of graphene, useful for molecular fingerprint retrieval (Fig. 34b).[613] Chen *et al.* optimized the sensing sensitivity of the metamaterial absorber through loss engineering. By integrating the metamaterial absorber with graphene and adjusting the Fermi level of graphene, they achieved linear modulation of the absorber's resonance frequency within the mid-infrared range. Incorporating pixelated design concepts, this hybrid resonator can serve as a potential SEIRA platform for multi-fingerprint molecular detection, quantitative analysis, and chemical identification. Experimentally, Li *et al.* designed a mid-infrared hybrid graphene metasurface biosensor for simultaneous quantitative detection and molecular identification of proteins.[614] The device features a metamaterial absorber structure with graphene positioned between a nanoribbon and a dielectric layer. By applying a bias voltage to the graphene, they were able to finely tune the plasmonic resonance

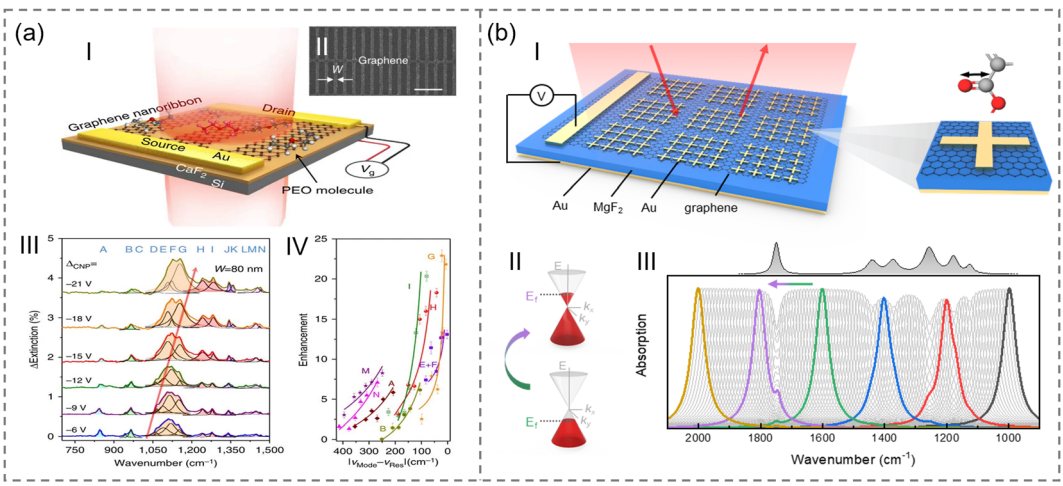

Fig. 34 Electrically tunable plasmons for molecular detection. (a) Graphene plasmon enhanced molecular fingerprint sensor. (I) Schematic of the sensor. (II) SEM image of the graphene nanoribbon pattern. (III) Highly selective detection of molecular vibrational fingerprints. (IV) Enhancement as a function of spectral detuning. Adapted with permission from ref. 611, Copyright 2016 Springer Nature. (b) A hybrid graphene metamaterial absorber for enhanced modulation and molecular fingerprint retrieval. (I) 3D schematic view of the hybrid graphene metamaterial absorber sensing platform. (II) Schematic diagram of graphene Fermi level modulation. (III) Absorption spectra of the sensing platform after loading analytes. Adapted with permission from ref. 613, Copyright 2023 Royal Society of Chemistry.

frequency (approximately 0.95 cm^{-1} V^{-1}). This precise adjustment of the plasmonic resonance frequency effectively enhances weak spectral signals, distinguishing weak fingerprint signals from device background noise. The experimental results showed that fine-tuning with graphene increased the relative absorption peak value of the protein amide I band from 5.47% to 12.84% and the relative absorption peak value of the amide II band from 4.82% to 13.82%.

4.3.2 Electron nanotweezers-plasmonics enhanced molecular detection. Various types of plasmonic nanostructures have been extensively utilized for the detection of trace substances. The key to achieving high-sensitivity trace sensing lies in precisely positioning target molecules near optical hotspots. However, ensuring that analytes are near optical hotspots remains challenging due to the free diffusion of nanoscale analytes and the localization effects of nanostructure optical hotspots. Current mainstream methods focus on improving detection sensitivity through molecular capture or concentration techniques.[279,464] Given the prevalence of biological molecules in liquid environments, there is an urgent need for novel solution-based detection strategies for efficient capture and release of target molecules.

Recently, researchers have explored methods that combine particle capture with optical detection by introducing nano-manipulators at sensing points (such as nano-antennas or nanopoints) to capture nanoscale objects.[615] Among the various nano-manipulators, electric nanotweezers have shown significant advantages, enabling real-time and repeatable manipulation of numerous particles. Dielectrophoresis (DEP) is a typical example of electric nanotweezers. The DEP force arises from differences in conductivity and dielectric constants between polarized particles and their surrounding medium. An external electric field induces net polarization at the particle–medium interface. In a spatially non-uniform field, particles are either attracted to high-field regions (positive DEP) or repelled from them (negative DEP).

Recent research has combined DEP with plasmonic sensors to concentrate molecules and enhance RI sensing. For instance, Barik *et al.* integrated large-area gold nanopore arrays with ITO electrodes to achieve efficient DEP molecule capture and real-time SPR detection (Fig. 35a).[616] The gold nanopore arrays are used for constructing surface plasmon-enhanced refractive index sensing. When molecules bind to the surface of gold nanopores, the resonant frequency shifts to longer wavelengths. Additionally, gold nanopore arrays serve as the bottom electrode for DEP, while ITO-coated glass slides act as the top electrode. By introducing the sample solution into the gap and

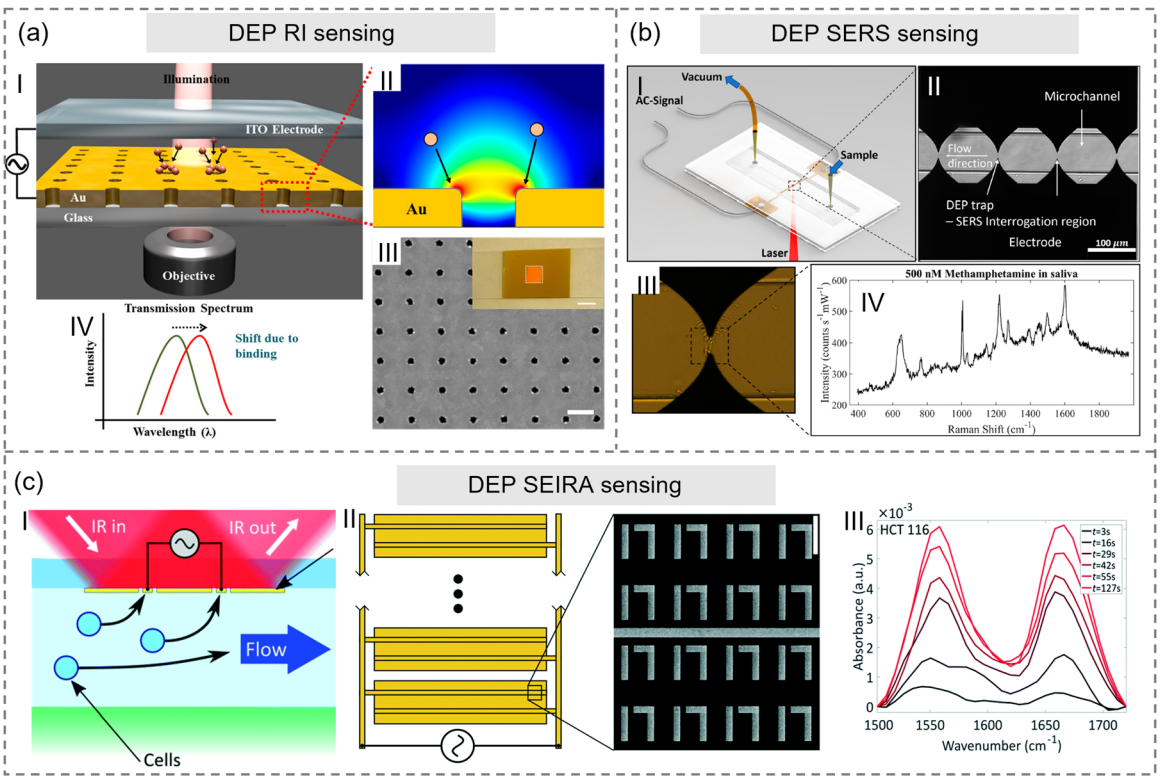

Fig. 35 Electron nanotweezers-plasmonics enhanced molecular detection. (a) DEP-enhanced plasmonic sensing with gold nanohole arrays. (I, II) Schematic of the experimental setup. (III) SEM of the nanohole array. (IV) Measured spectra. Adapted with permission from ref. 616, Copyright 2014 ACS. (b) DEP nanoparticle aggregation for on-demand SERS analysis. (I) Schematic diagram of the sensing platform. (II) SEM image of the DEP-SERS chip. (III) Close-up view of a single trap using agglomeration of nanoparticles. (IV) Typical SERS spectra acquired using the DEP-SERS chip. Adapted with permission from ref. 617, Copyright 2018 ACS. (c) Infrared spectroscopy of live cells from a flowing solution using electrically biased plasmonic metasurfaces. (I) Schematic diagram of the DEP-SEIRA platform. (II) Schematic of the metasurface pixel array. (III) SEM image of the metasurface. (IV) Measurement results. Adapted with permission from ref. 618, Copyright 2020 Royal Society of Chemistry.

applying an alternating current signal between the ITO electrode and the gold nanopore array, forces are exerted on the molecules, accelerating their movement toward the sensor surface. The results indicate that DEP technology can detect bovine serum albumin molecules at concentrations as low as 1 pM.

In addition to periodic nanopore arrays, DEP can also be integrated with other plasmonic sensors for SERS[619,620] and SEIRA detection.[618] Salemmilani *et al.* reported a microfluidic chip-based SERS platform that uses DEP technology for highly localized capture and release of SERS-active nanoparticles (Fig. 35b).[617] In this platform, SERS-active silver nanoparticles are used as capture targets. Under the influence of DEP, silver nanoparticles aggregate at specific locations, creating multiple optical hotspots that enhance Raman signals of analytes in the solution. To improve the reuse of the device, electrodes and flow channels are passivated to minimize nanoparticle contamination in the microchannels. The device has been shown to detect methamphetamine at physiologically relevant concentrations in saliva within 2 minutes. In the infrared range, Kelp *et al.* developed a DEP-SEIRA integrated microfluidic device (Fig. 35c).[618] This device incorporates DEP modules, metasurfaces, and microfluidic channels. The microfluidic channels are used to transport cells in aqueous solutions, while the plasmonic metasurfaces enhance the infrared spectra of live cells. DEP is used to attract cells to the surface of the metasurface components. With DEP, the device can acquire infrared absorption spectra of cells within one minute. When DEP is turned off, the adhered cells are released under the action of fluidic forces. This method provides a flexible approach to transporting cells to sensors, offering high throughput and usability.

4.3.3 Plasmonics-based photodetectors for molecular sensing. Photodetectors are devices that convert optical signals into electrical signals, playing a crucial role in various sensing applications. They can be broadly categorized into photon detectors and thermal detectors. Photon detectors utilize the photoelectric effect to collect and convert the charge (typically electrons) generated by incident photons into an electrical signal. Currently, there are mature photon detectors used in applications such as refractive index sensing and Raman spectroscopy. In contrast, thermal detectors work by measuring temperature changes or thermal effects to detect optical signals or radiation. They convert photon or radiation energy into heat and measure the resulting temperature changes or thermal effects. However, non-cooling photodetectors face challenges in manufacturing for the mid-infrared to far-infrared ranges due to issues like thermal noise and energy gaps. Notably, the mid-infrared spectrum contains a wealth of gas fingerprint vibration information. Therefore, mid-infrared spectral gas sensors can uniquely and sensitively identify and quantify the presence of gases.

Non-dispersive infrared (NDIR) spectroscopy is a type of mid-infrared gas sensor that analyzes gases based on the characteristic absorption wavelengths of mid-infrared radiation caused by gas molecular vibrations. Traditional NDIR gas sensors use broadband light sources and do not have pre-filters. To analyze the concentration of target gases, a bandpass filter is usually added before the detector to remove all unwanted wavelengths from the beam, allowing only the characteristic absorption wavelengths of the gas to reach the detector. To analyze several target gases in a mixture simultaneously, multiple "bandpass filter + optical detector" pairs are implemented in the NDIR gas sensor.[621,622] However, this approach significantly increases the cost, system complexity, and operating time, especially when the number of target gases is large.[623,624] This challenge stems from the lack of spectral selectivity in most commercially available mid-infrared detectors. The wavelength selectivity of plasmonic metamaterials offers a solution for narrowband mid-infrared detectors. A common approach is to integrate metamaterials with thermoelectric detectors.[343,347,625,626] For example, Tan *et al.* integrated plasmonic metamaterial absorbers on top of a pyroelectric detector to achieve infrared response at specific wavelength bands (Fig. 36a).[627] The plasmonic metamaterial absorber can absorb infrared light at specific bands and convert it into heat, thus raising the temperature at the top of the pyroelectric detector. This temperature change induces charge separation within the pyroelectric material, generating a potential difference. By measuring the magnitude of this potential difference, the intensity of the specific band of infrared light can be obtained. By adjusting the design of the metamaterial, the detection wavelength or peak absorption wavelength of the integrated absorber can be tuned to cover the entire mid-infrared spectrum. Based on this principle, Tan *et al.* developed eight narrowband detectors responsive to different wavelength bands, with detection wavelengths matching the characteristic absorption wavelengths of eight target gases: H_2S, CH_4, CO_2, CO, NO, CH_2O, NO_2, and SO_2. The detection limits for common gases such as CH_4, CO_2, and CO were found to be 63 ppm, 2 ppm, and 11 ppm, respectively. Additionally, with the aid of mathematical models, the concentration of two target gases in a mixture could be inferred from the voltage responses of two narrowband detectors.

Another approach involves integrating plasmonic metamaterials with low-dimensional materials, such as graphene, to realize mid-infrared photodetectors. The unique band structure and excellent transport properties of graphene offer unique opportunities for photodetectors. However, graphene's absorption rate in the infrared range is relatively low (about 2.3%), resulting in poor responsivity and sensing performance.[629] Therefore, an effective structure to enhance graphene's absorption is required. Research has demonstrated that periodic nanostructures can achieve extreme light confinement, thereby increasing absorption and interaction between light and matter.[630,631] Additionally, nanoantennas can serve as small metal electrodes to collect charge carriers, generating photocurrent.[632,633] Many studies have used graphene-plasmonic nanostructures to fabricate mid-infrared photodetectors, enabling the measurement of optical parameters such as wavelength, intensity, polarization, and ellipticity.[14,634–636] These measurements are critical for achieving highly integrated, high spatial resolution, and surface-enhanced sensors. For example, Xie *et al.* proposed a graphene photodetector based on nanoantennas for polarization and spectral sensing (Fig. 36b).[628] Polarization sensing is achieved through artificial near-field anisotropy realized by double L-shaped nanoantennas. The device exhibited a high responsivity of 6.3 V/W at zero bias under room

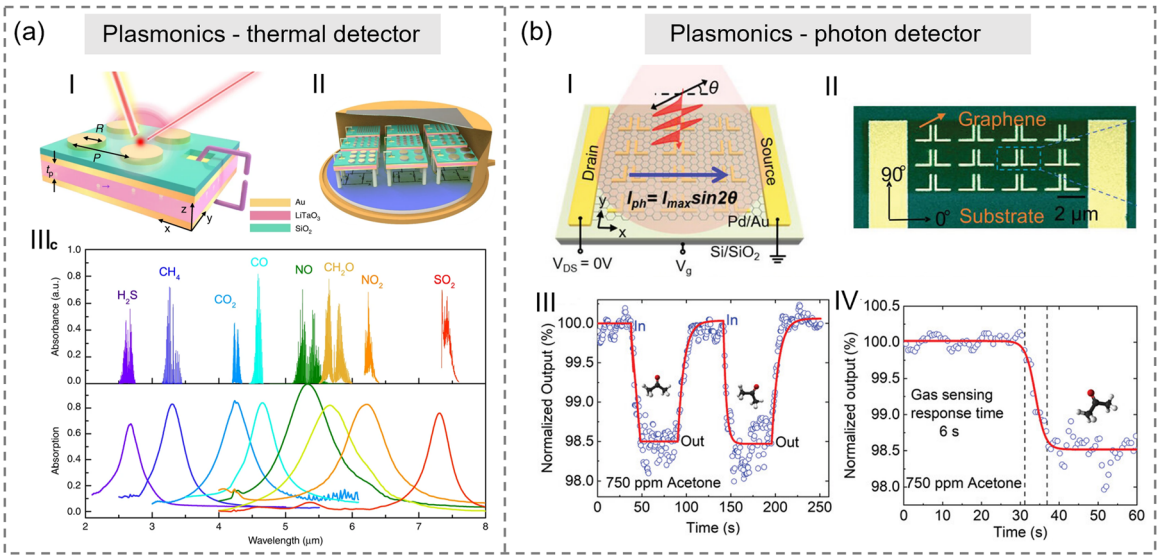

Fig. 36 Plasmonics-based photodetectors for molecular sensing. (a) NDIR multi-gas sensing *via* nanoantenna integrated narrowband detectors. (I) The device geometry of the narrowband detection element. (II) The joint package of the multiple pyroelectric elements with different detection wavelengths. (III) The measured absorption spectra of 8 fabricated MIM absorbers compared to the infrared absorption bands of eight target gases. Adapted with permission from ref. 627, Copyright 2020 Springer Nature. (b) Zero-bias long-wave infrared nanoantenna-mediated graphene photodetector for polarimetric and spectroscopic sensing. (I) Schematic diagram of nanoantenna-mediated graphene photodetectors. (II) SEM image. (III) Gas sensing response and recovery characteristic. (IV) Gas sensing response time. Adapted with permission from ref. 628, Copyright 2023 Wiley.

temperature, with a noise equivalent power as low as 1.6 nW $Hz^{-1/2}$. Finally, Xie *et al.* used acetone as an analyte for spectral sensing, demonstrating the application of the nanoantenna-graphene photodetector in molecular detection. The results showed a detection limit of 115 ppm and a dynamic gas sensing response time of 6 seconds. These results highlight the potential of graphene photodetectors in next-generation on-chip integrated photonic platforms and miniaturized spectrometers.

4.3.4 Photoacoustic fusion for molecular detection. Photoacoustic imaging (PAI) is an imaging method that combines optical and ultrasound technologies to obtain structural and functional information within biological tissues.[637] When pulsed laser light is directed onto biological tissue, the tissue absorbs the light energy, causing thermal expansion and generating ultrasound waves. These ultrasound waves can be detected by an ultrasound transducer. Since different tissues produce ultrasound waves of varying intensities, these signals can be used to reconstruct images of the tissue structure, enabling disease diagnosis and tissue assessment. As a hybrid technique, PAI leverages the advantages of traditional optical and ultrasound imaging while compensating for the limitations of each individual technique.[638] Specifically, traditional optical imaging uses the selective absorption of light by tissues or molecules at specific wavelengths to produce high-contrast images that reveal anatomical, functional, and molecular information. However, light quickly attenuates in biological tissues, limiting optical imaging to only a few millimeters of penetration depth. In contrast, ultrasound waves attenuate more slowly in tissues and can penetrate several centimeters, providing higher spatial resolution. However, traditional ultrasound imaging relies on differences in tissue acoustic impedance, resulting in lower contrast and difficulty in distinguishing tissues with similar acoustic properties. PAI addresses the limitations of optical imaging's penetration depth and ultrasound imaging's contrast by combining high-contrast optical excitation with deep-penetration ultrasound waves, thus providing richer diagnostic information than single optical or acoustic techniques.

In PAI, contrast agents play a crucial role.[639,640] They can significantly enhance the absorption of laser light by specific tissues or molecules, generating stronger PA signals and improving image contrast. Common contrast agents in PAI include endogenous chromophores (such as hemoglobin and melanin)[641,642] and exogenous agents (such as nanoparticles and polymers).[638,643] Among these, plasmonic nanoparticles are excellent PAI contrast agents due to their superior light absorption and tunable absorption peaks. Additionally, plasmonic nanoparticles exhibit outstanding photothermal conversion efficiency, good biocompatibility, and excellent physicochemical properties. By adjusting the size and shape of metal nanoparticles, their absorption cross-section can be enhanced, increasing the efficiency of photon-to-heat conversion. For example, Repenko and colleagues conducted a comparative analysis of the PA contrast of gold core–shell structures with various shapes (such as spheres, nanostars, nanorods, and nanoshells).[644] They found that melanin-coated AuNRs exhibited the most significant PA enhancement, attributed to their superior absorption rates.

In preclinical studies, PAI has led to numerous exciting discoveries and applications in small animal models. Its translational research has also attracted interest in fields such as oncology,[645,646] neuroscience,[647] and brain science.[648] For instance, Zhou *et al.* reported a NIR-II plasmonic therapeutic diagnostic system based on silica-coated self-assembled gold nanorods ($AuNCs@SiO_2$) for accurate tumor diagnosis.[649] The NIR-II "on–off" properties of

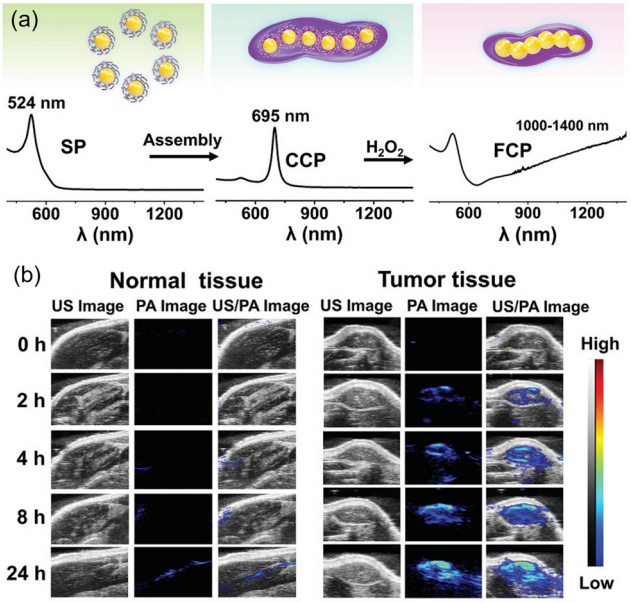

Fig. 37 Activatable NIR-II plasmonic nanotheranostics for efficient photoacoustic imaging and photothermal cancer therapy. (a) Preparation procedure of AuNCs@SiO_2 nanochains. (b) PAI of 4T1-tumor-bearing mice for tumor tissue and normal tissue as a function of post-injection time of AuNCs@SiO_2. Adapted with permission from ref. 649, Copyright 2020 Wiley.

AuNCs@SiO_2 are attributed to a typical redox reaction between the citrate ligands on the gold nanoparticles and the overexpressed H_2O_2 in the tumor microenvironment. This reaction causes the ligands to detach from the gold nanoparticles and fusion of adjacent gold nanoparticles (Fig. 37a). Fig. 37b is the angiography of AuNCs@SiO_2 on 4T1-tumor-bearing mice for tumor tissue and normal tissue. The fused AuNRs exhibit excellent NIR-II deep tissue penetration in tumor tissues, with a photothermal conversion efficiency of up to 82.2%. Moreover, the self-assembled AuNRs also demonstrate significant tumor elimination and growth inhibition effects.

Despite significant progress in PAI with metal nanoparticles, several challenges remain to be addressed for advancing its application in basic life sciences research. First, there are concerns about biocompatibility and toxicity. Although gold nanoparticles are generally considered inert, their biocompatibility heavily depends on the materials, size, shape, and synthesis methods of the nanostructures. Future research needs to thoroughly assess the biocompatibility and safety of nanoparticles *in vivo*. Additionally, metal nanoparticles may undergo non-specific aggregation in bodily fluids, which can affect their optical properties and potentially lead to vascular blockage or immune reactions. Therefore, reducing non-specific aggregation and exploring biodegradable metal nanoparticles could enhance the overall application value of PAI.

4.4 Section summary

This section provides an overview of plasmonic nanostructures and their applications in molecular detection. We begin by categorizing plasmonic nanostructures based on their dimensional properties, covering zero to 3D structures and their fabrication techniques. Next, we focus on plasmon-enhanced sensing technologies, including refractive index sensing, SEIRA spectroscopy, surface-enhanced Raman spectroscopy, and more. Finally, we discuss the integration of plasmonics with electronic and acoustic technologies, exploring how these multi-effect systems address current challenges and their potential in advancing molecular sensing capabilities.

Nevertheless, the sensing applications continue to present significant challenges. A primary challenge is achieving high sensitivity across these various techniques. For example, in SERS, the sensitivity is determined by the EF at hotspot locations,[650] which is similarly critical in SEIRAS and other surface-enhanced spectroscopy techniques. The design of substrates that can maximize these hotspots while being compatible across different detection modalities is complex. This requires the development of materials and structures that can consistently amplify weak signals from low-concentration analytes while maintaining high sensitivity across different spectral regions and types of interactions.

Another significant challenge is ensuring selectivity in complex biological environments. The molecular fingerprints provided by vibrational spectroscopy in SERS are powerful tools for identifying specific molecules, but this specificity must be maintained when integrating with other plasmonic sensing techniques. The selectivity in these applications is often compromised by background noise or interference from other biomolecules, particularly in complex samples like blood or tissue. Advanced AI-based techniques and sophisticated detection strategies are being explored to enhance selectivity.

Reproducibility is another critical issue, as consistent performance across different plasmonic techniques is essential for quantitative biosensing.[87] Variability in substrate manufacturing, environmental conditions, and sample preparation can all contribute to inconsistent results. This challenge is exacerbated in integrative approaches where multiple sensing techniques are combined, each with its own set of requirements and sensitivity. Developing robust, uniform substrates that perform reliably across different plasmonic applications is key to addressing this challenge.

The stability of plasmonic substrates is also crucial,[651] especially when applied to real-world biosensing under varying conditions of temperature, pH, and ionic strength. The durability of these substrates under different experimental conditions is essential for long-term applications, particularly in clinical diagnostics, where reliability over time is necessary.

Finally, the challenge of cost-effectiveness cannot be overlooked, particularly in the context of point-of-care testing (POCT),[652] where affordability is a key factor for widespread implementation. The development of scalable manufacturing processes that can produce high-quality plasmonic substrates at a low cost is essential for making these advanced diagnostic tools accessible in diverse healthcare settings, including remote or underserved areas.

5. Plasmon-enhanced energy conversion

The excessive reliance on non-renewable energy sources, such as coal and oil, has intensified the global energy crisis, creating

Table 1 Comparison of plasmon-enhanced energy conversion types

Energy conversion type	Working principle	Plasmon-enhanced principle	Main application areas
Solar energy	Utilizing photovoltaic or photothermal effects to convert solar energy into electrical or thermal energy	Boosting light absorption and conversion *via* plasmon-enhanced photoactivity of semiconductors	Power supply, hot water supply, *etc.*
Chemical energy	Releasing or storing energy through chemical reactions	Enhancing catalytic activity or reaction rates through plasmon-induced effects	Fuel cells, energy storage systems, *etc.*
Biomass energy	Producing energy through combustion or fermentation of biomass resources	Utilize the heat generated by LSPR to create thermo-photocatalytic conditions to promote biomass decomposition	Hydrogen production, wastewater purification, degradation of organic pollutants, *etc.*
Thermal energy	Thermal energy can be obtained through energy conversion or heat transfer	Leveraging plasmon-induced heating or energy transfer	Gas sensing, thermal emission control, biomedical applications, *etc.*
Mechanical energy	Utilizing mechanical motion or pressure to convert into other forms of energy	Utilizing plasmonic materials for enhanced friction or energy harvesting	Triboelectric nanogenerator, *etc.*

an urgent need to explore alternative methods for harnessing energy directly from the surrounding environment. Plasmon technology offers a promising solution for generating sustainable green energy. By enhancing light conversion in semiconductor materials, plasmon technology can significantly improve the efficiency of energy conversion in various applications, including solar cells,[653] solar-to-chemical energy,[654] solar-to-biomass energy,[655] and solar-to-thermal energy.[656] Moreover, it can enhance the efficiency of triboelectric nanogenerators (TENGs) by increasing the surface charge density of materials.[657] As a result, plasmon technology has found widespread use in numerous energy applications, including solar, chemical, biomass, thermal, and mechanical energy. To facilitate a more intuitive comprehension of the similarities and differences among various types of plasmon-enhanced energy conversion, Table 1 provides a systematic comparison of the primary characteristics of each energy conversion type.

5.1 Plasmon-enhanced solar energy

Solar energy conversion technology faces several challenges, including low absorption efficiency, insufficient charge separation and transfer efficiency, and a limited spectral range.[658–660] These limitations directly impact the effectiveness of converting solar energy into electricity. Excitingly, plasmon technology can enhance the collection and conversion of solar energy by increasing the photoactivity of semiconductors. The excited surface plasmons operate through five distinct mechanisms, as illustrated in Fig. 38.

5.1.1 Hot-electron injection. Hot-electron injection is the first mechanism reported for metal plasmon-enhanced photoactivity of semiconductors.[142,661] This mechanism is induced by the non-radiative decay of excited plasmons, which leads to the conversion of plasmon energy into a hot-electron–hole pair.[29] The energy of these hot electrons depends on the size and shape of metal nanoparticles, while their generation rate is determined by the non-radiative dephasing time.[662–666] When a metal and semiconductor come into contact, hot electrons can overcome the Schottky barrier at the interface (Fig. 38-I). Through hot-electron injection, plasmons can photosensitize wide-band-gap semiconductors, broadening their light absorption range.[29,141,144,165,667–673]

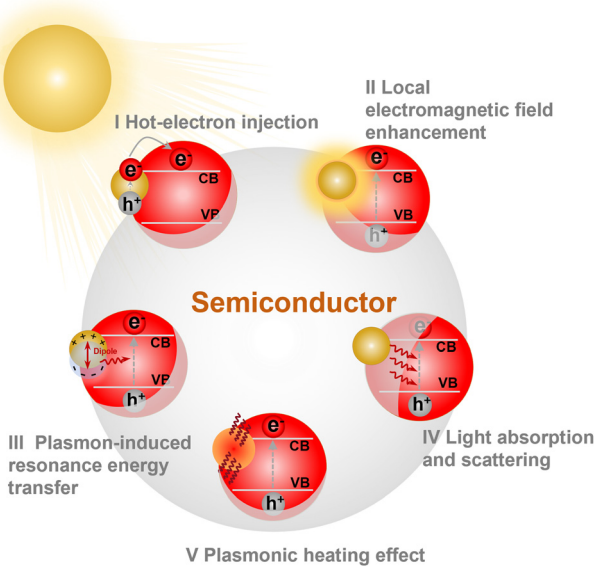

Fig. 38 Mechanisms of plasmon-enhanced photoactivity in semiconductors. (I) Hot-electron injection; (II) local electromagnetic-field enhancement; (III) plasmon-induced resonant energy transfer (PIRET); (IV) light absorption and scattering; (V) plasmonic heating effect.

5.1.2 Local electromagnetic-field enhancement. The second significant effect of metal plasmon-enhanced photoactivity is local electromagnetic-field enhancement. This effect results from the interaction of an enhanced electromagnetic field, localized near the interface of metal nanoparticles, with semiconductors (Fig. 38-II). This enhancement is highly localized and strongly depends on the shape, size, and spatial distribution of the nanostructures.[674] The electromagnetic field enhancement caused by individual NPs can be up to a factor of 10^3, and this effect is significantly amplified when multiple NPs are in close proximity. This amplified electromagnetic field can substantially improve the photon absorption rate of semiconductors in these enhanced areas.[675] Consequently, when a semiconductor is in close proximity to these NPs, the formation rate of electron–hole pairs (e^-/h^+) within the semiconductor will significantly increase, thereby enhancing photocatalytic activities.[676–678]

5.1.3 Plasmon-induced resonant energy transfer. Before a plasmon decays into hot electrons, the incident energy is stored in the polarization of the plasmon and can be transmitted through the near-field. During this process, the carrier generation efficiency is governed by the overlap integral of LSPR and the semiconductor's absorbance for dipole–dipole interactions. Hence, the near-field of plasmons can transfer energy to semiconductors in the form of resonance (Fig. 38-III).[679] For complex geometric shapes,[680] energy transfer may occur through multipole interactions.[676,681–684] Therefore, PIRET can be understood as the mechanism by which the energy of a plasmonic oscillation is transferred from a plasmonic material to a semiconductor photocatalyst *via* an electromagnetic field or dipole–dipole interaction.

5.1.4 Light absorption and scattering. The scattering of plasmons can enhance light absorption at energies above the semiconductor's bandgap.[154,685–691] The excited surface plasmon can decay radiatively through resonant scattering, which is primarily influenced by the size of the metal nanostructures (Fig. 38-IV).[692] By utilizing the large scattering cross-section of plasmons, the path length of photons can be extended through multiple reflections, increasing the likelihood of absorption. LSPR is commonly employed to induce multiple reflections, either by embedding plasmonic NPs into the active layer or by using patterned back-reflectors, which are more prevalent in solution-based and deposition-based processing methods.

5.1.5 Plasmonic heating effect. The final mechanism discussed here is the plasmonic local heating effect,[693] which occurs during the non-radiative decay of LSPR (Fig. 38-V). The interaction between photogenerated charge carriers and other electrons in the system can lead to a thermal charge-carrier distribution under incident light excitation. This distribution takes a few hundred femtoseconds to thermalize into a Fermi–Dirac distribution.[692,694,695] Following thermalization, the collision of electrons with the metal nanostructure's ions transfers energy to the lattice, inducing lattice heating. This heat then dissipates into the environment over a longer timescale, achieving thermal equilibrium between the lattice phonons and the surrounding medium, which leads to an increase in the temperature of the medium. Even a minor temperature rise (1 to 10 K) can significantly influence the reaction rate in classical catalytic systems. The plasmonic heating effect is more pronounced in smaller nanostructures, especially those below 30 nm,[696–698] and is often utilized for the thermal activation of chemical reactions.[699,700]

The primary goal of research in plasmonic solar cells is to enhance their conversion efficiency. New plasmonic nanostructures, with pre-designed sizes and shapes, have been extensively studied in various solar cells, including polymer solar cells, dye-sensitized solar cells, and heterojunction solar cells.[687,701–703] For example, Ma *et al.* developed an innovative nanostructure composed of Au nanorod–nanoparticle dimers with structural darkness (Fig. 39a), which significantly boosts the broadband light absorption of perovskite solar cells, leading to a 16% increase in efficiency (Fig. 39b and c).[704] In their study, when the concentration of Au nanorod–nanoparticle dimers coated with SiO_2 (Au dimers@SiO_2) was set at 2.8%, the average efficiency increased by 10.1% due to an improvement in the

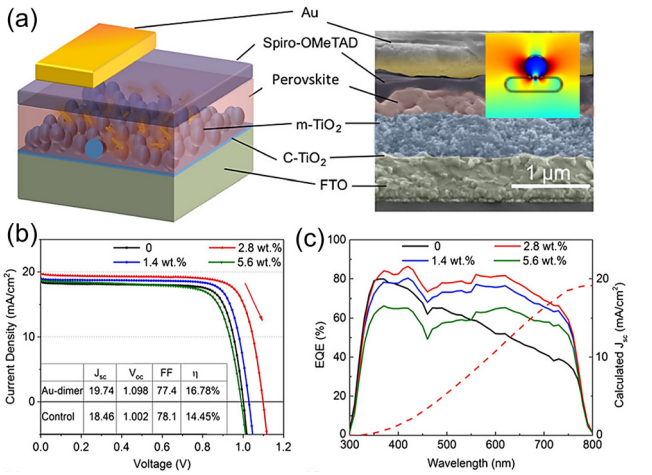

Fig. 39 Bioinspired nanostructure with Au nanorod–nanoparticle dimers for enhanced light harvesting in perovskite solar cells. (a) Schematic and SEM cross-section of the solar cell structure. Inset: 2D graph of near-field intensity improvement for an Au dimer. (b) *J*–*V* characteristics of perovskite solar cells with varying concentrations of Au dimers. (c) EQE spectra of the control sample and different additions of Au dimer@SiO_2. Adapted with permission from ref. 704; Copyright 2019 Wiley.

average short-circuit current (J_{sc}) from 17.05 to 19.35 mA cm^{-2}. This suggests that the addition of Au dimers@SiO_2 positively impacts the performance of solar cells by enhancing the short-circuit photocurrent. Furthermore, measurements indicated that increasing the amount of Au dimers led to an enhancement in external quantum efficiency (EQE) in the long wavelength region, followed by an overall decrease across all wavelengths.

In another study, Beak *et al.* developed highly efficient plasmonic organic solar cells (OSCs) by embedding Au@Ag core–shell nanocubes (Au@Ag NCs) into an anodic buffer layer, poly(3,4-ethylenedioxythiophene):polystyrene sulfonate (PEDOT:PSS) (Fig. 40a).[705] The optical gain induced by these metal nanoparticles enhanced both the EQE and absorption of the OSCs. Due to the amplified plasmonic effect of the metal nanoparticles, the plasmonic PCDTBT:PC70BM-based OSC_S with embedded Au@Ag NCs showed a 2.2-fold absorption enhancement compared to AuNPs at wavelengths between 450 and 700 nm (Fig. 40b and c). The power conversion efficiency (PCE) of PTB7-based OSCs reached 9.2%. Additionally, the shape and composition of the plasmonic nanoparticles can be adjusted to optimize charge separation and transport at the solar cell interfaces.[706]

Given the extensive literature on plasmon-assisted solar energy conversion efficiency, this discussion focuses only on representative studies. A summary of recent results is presented in Table 2.

5.2 Plasmon-enhanced chemical energy

Solar-to-chemical energy conversion is a crucial research area with significant potential for addressing current energy and environmental challenges. However, the limited optical absorption and low apparent quantum efficiency (AQE) are two major bottlenecks that constrain the efficient conversion of solar energy into chemical energy.[723] Plasmonic nanometals offer a

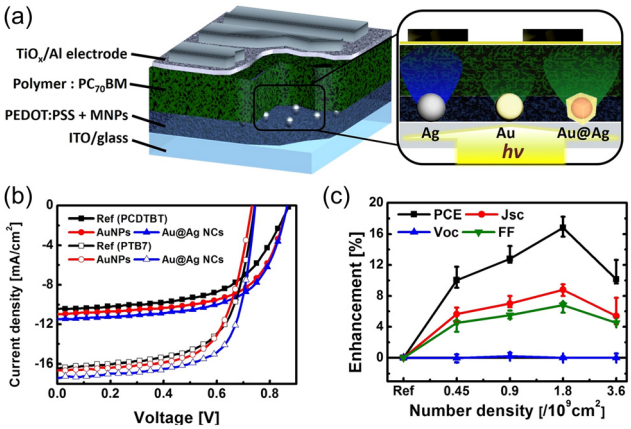

Fig. 40 High-efficiency plasmonic organic solar cells with embedded Au@Ag core–shell structures. (a) Schematic of a plasmonic organic solar cell. (b) *J*–*V* curves of the control device (black) and plasmonic OSCs with AuNPs (red) and Au@Ag NCs (blue) embedded. (c) PCE, short-circuit current density (J_{sc}), open- circuit potential (V_{oc}), and filling factor (FF) enhancements of the plasmonic OSCs with Au@Ag NCs embedded at various concentrations in a PEDOT:PSS layer. Adapted with permission from ref. 705; Copyright 2014 American Chemical Society.

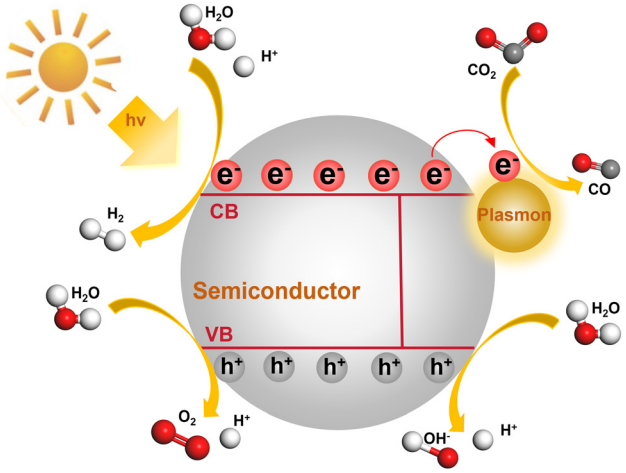

Fig. 41 The schematic diagram of the mechanisms for plasmon-enhanced chemical energy.

promising solution by combining light harvesting, hot-electron generation, heating effects, and unique catalytic functions within a single material. The surface plasmon resonance (SPR) effect has emerged as an efficient and attractive strategy for enhancing solar-to-chemical energy conversion.[724,725] These unique properties have been extensively utilized across a wide range of applications, from semiconductor photocatalysis to the rapidly developing field of surface plasmon-mediated heterogeneous catalysis. Recent advances have shown significant improvements in the efficiency of solar energy utilization across various catalytic processes.

Fig. 41 illustrates the mechanism of plasmon-enhanced chemical energy conversion. When illuminated, metal nanostructures undergo LSPR, which effectively enhances both the oxidation and reduction reactions in the valence and conduction bands of the semiconductor.[726] This section focuses on the key role of plasmonic metal nanostructures in common applications, such as carbon dioxide reduction reactions, hydrogen evolution reactions (HER), oxygen evolution reactions (OER), and oxygen reduction reactions (ORR).

5.2.1 Plasmon-enhanced carbon dioxide reduction reaction. Significant progress has been made in the photocatalytic conversion of CO_2 into solar fuels in recent years.[694,727–729] For instance, Robatjazi *et al.* reported a plasmonic Al@Cu_2O antenna-reactor heterostructure that generates charge carriers to drive the chemical transformation of CO_2 into CO (Fig. 42a).[730] This structure enhances surface reactivity and efficiently utilizes radiative LSPR damping in Al to boost carrier generation in the metal oxide shell. Their findings show that plasmon-induced reverse water–gas shift (rWGS) reactions at lower temperatures exhibit improved selectivity compared to thermally driven rWGS at higher temperatures. In this study, the rate of CO formation

Table 2 A summary of plasmon-enhanced solar energy conversion

Year	Plasmon materials	J_{sc} (mA cm^{-2})	V_{oc} (V)	PCE improvement (%)	Ref.
2019	Au nanorod–nanoparticle dimers	19.74	1.098	14.15–16.78	704
2014	Au@Ag core–shell nanocubes	17.5	0.75	7.78–9.19	705
2020	Ag back reflector	13.71	0.856	6.12–7.26	707
2019	Coupled core–shell nanoparticles	28.13	0.605	6.8–14	708
2018	Ag nanoparticles	16.46	0.87	8.04–10.6	709
2016	Au@SiO_2 core–shell nanoparticles	11.9	0.770	3.78–4.49	710
2018	Ag nanospehere, cube, cylinder, *etc.*	20.92	1.015	12.92–13.68	711
2019	Gold nanoparticles	16.66	0.65	6.29–7.58	712
2021	Au@Ag nanoparticles	17.07	0.69	2.5–3.73	713
2018	Au nanoparticles	19.36	0.57	4.04–6.0	714
2017	Au bipyramids and Au nanospheres	24.61	0.59	8.09–9.58	715
2023	Hybrid of gold nanobipyramids and nanospheres	26.53	0.84	15.46–16.62	716
2022	Au nanoparticles	41.7	0.63	14.40–19.0	717
2023	Au nanoparticles	40.78	0.64	17.90–21.39	718
2020	Au nanoparticles	22.5	0.9	8.53–10.9	719
2021	Au nanooctahedra	23.63	1.08	16.95–19.05	720
2015	Au nanoparticles	19.9	1.08	9.30–16.2	721
2023	Ag nanopyramid and nanodome	38.42	0.88	15.60 (Ag nanopyramid)–28.02 (Ag nanodome)	722

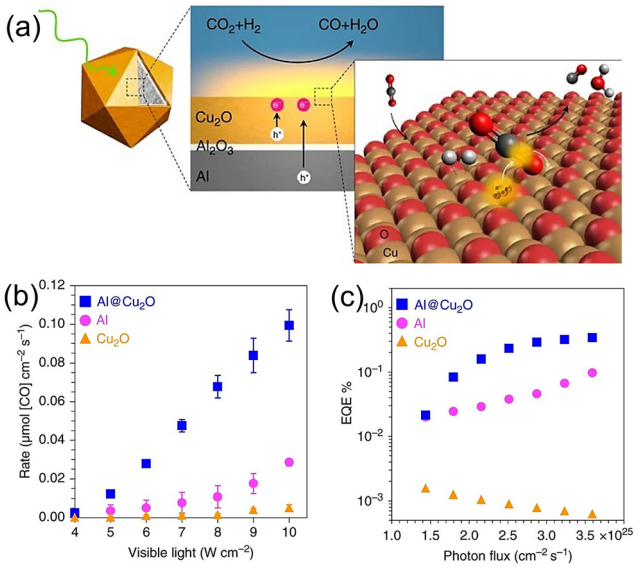

Fig. 42 Plasmon-enhanced rWGS. (a) The schematic of plasmon-induced carrier-driven rWGS on Al@Cu_2O. (b) The rate of CO formation on photocatalysts derived from Cu_2O, Al NCs, and Al@Cu_2O. (c) The apparent EQE determined from the measured reaction rate and graphed against photon flux. Adapted with permission from ref. 730; Copyright 2017 Springer Nature.

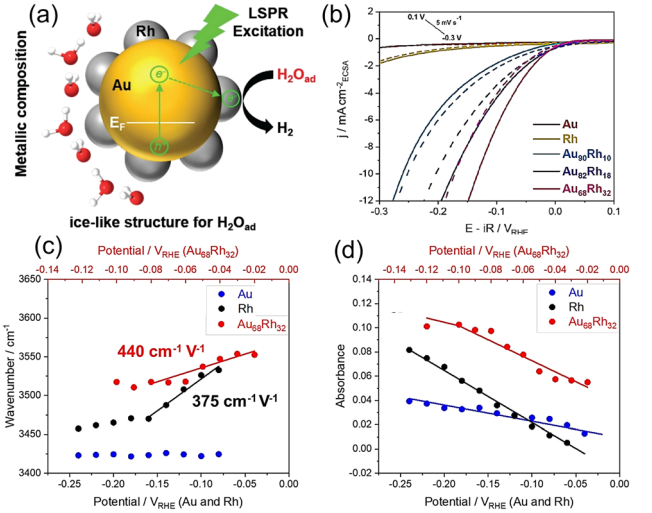

Fig. 43 Gold-rhodium nanoflowers for the plasmon-enhanced HER. (a) Schematic of electron transfer pathways for LSPR-enhanced HER. (b) Polarization curves recorded at 5 mV s^{-1} from 0.1 to −0.3 V_{RHE} for Au, Rh, and $Au_{90}Rh_{10}$, $Au_{82}Rh_{18}$, and $Au_{68}Rh_{32}$. Solid lines represent data recorded under 533 nm light excitation, whereas dashed lines correspond to experiments conducted in darkness. (c) Stark tuning plots for deconvoluted bands in the range 3400–3530 cm^{-1} for Au, Rh, and $Au_{68}Rh_{32}$. (d) Absorbance *versus* potential plots for deconvoluted bands in the range 3400–3530 cm^{-1} for Au, Rh, and $Au_{68}Rh_{32}$. Adapted with permission from ref. 738; Copyright 2021 American Chemical Society.

catalyzed by Al@Cu_2O is significantly higher than that of Cu_2O and pristine Al (Fig. 42b), with a measured EQE of approximately 0.35% for Al@Cu_2O (Fig. 42c). These results align with values reported in other scholarly studies.[731–734]

5.2.2 Plasmon-enhanced hydrogen evolution reaction (HER). Metals with large work functions, such as platinum (Pt), gold (Au), and palladium (Pd), are widely recognized as effective cocatalysts in photocatalytic HER.[735–737] Rodrigues *et al.* reported a gold–rhodium core–shell nanoflower (Au@Rh NFs) structure that enhances HER performance (Fig. 43a).[738] Their study found that HER activity increases with the Rh content in Au@Rh NFs, under both dark and illuminated conditions (Fig. 43b). $Au_{68}Rh_{32}$ NFs exhibited the highest performance in both HER and plasmon-enhanced HER (Fig. 43c and d). These results suggest that the plasmonic effects from visible light can be harnessed to boost Rh's catalytic performance by creating hybrid nanomaterials combining Rh and Au.

5.2.3 Plasmon-enhanced oxygen evolution reaction (OER). Transition metal (oxy)hydroxides, abundant in the earth, offer low cost, tunable activity, and excellent stability, making them promising candidates for electrocatalysts to enhance OER kinetics.[739,740] Hu *et al.* designed a novel electrocatalyst by decorating $Ni(OH)_2$ with Ag NPs to facilitate OER (Fig. 44a).[741] After introducing Ag NPs, the composites exhibited a distinct but broad absorption peak at ~400 nm (Fig. 44b) and significant electric field enhancement (Fig. 44c and d). The current densities for both $Ni(OH)_2$ and $Ni(OH)_2$/Ag-0.4 increased with increasing electrolyte temperatures (Fig. 44e and f). Furthermore, the activation energy (Ea) of $Ni(OH)_2$/Ag-0.4 was much lower than that of pristine $Ni(OH)_2$ (Fig. 44g), indicating a reduced energy barrier for the OER after Ag NP decoration. Consequently, the surface plasmon at the $Ni(OH)_2$/Ag interface significantly enhances OER performance by improving charge transfer and reaction kinetics.

5.2.4 Plasmon-enhanced oxygen reduction reaction (ORR). Combining plasmonic NPs with 2D electrocatalyst systems is an effective strategy to enhance electrocatalytic activity in ORR under light illumination. Ding *et al.* introduced a novel 2D "Egg Waffle"-like heterostructure, with gold nanoparticles intercalated in a palladium nanosheet (AuNP-in-PdNS), to enhance electrocatalytic activity under light exposure (Fig. 45a).[742] They found that the HER catalytic activity of $Au_{0.50}$NP-in-PdNS under light illumination (200 mW cm^{-2}) outperformed the baseline Pt/C in acidic media (Fig. 45b). These results confirm that LSPR effectively enhances the electrocatalytic HER activity of 2D AuNP-in-PdNS heterostructures. Additionally, $Au_{0.50}$NP-in-PdNS exhibited the best ORR activity, characterized by an increased half-wave potential of 0.882 V and a limiting current density of 7.5 mA cm^{-2} under light exposure, further demonstrating the plasmonic enhancement in electrocatalytic performance (Fig. 45c and d).

5.3 Plasmon-enhanced biomass energy

There is growing interest in utilizing renewable resources, such as solar energy, as a driving force and biomass-derived compounds as feedstocks for simultaneous hydrogen production. These approaches are recognized as sustainable solutions for energy generation and effective strategies against climate change. Compared to water, organic compounds interact more readily with photo-generated valence band holes, making them more suitable for valorization.[743] The process that involves the

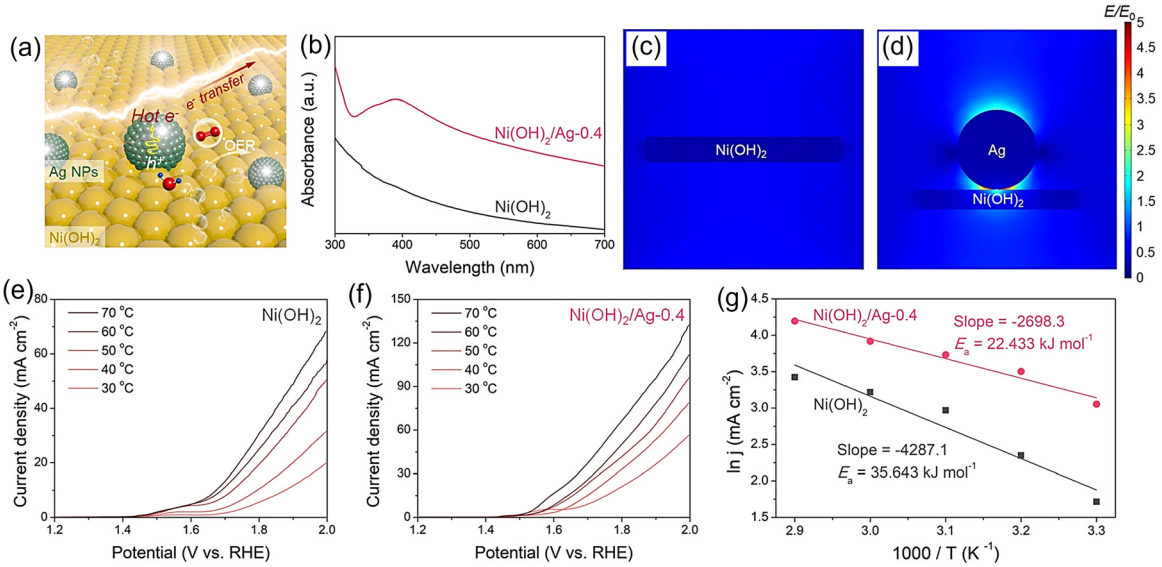

Fig. 44 Silver nanoparticles (Ag-NPs) for the plasmon-enhanced OER. (a) Schematic of mechanisms for enhanced OER activity. (b) The UV-Vis spectra of $Ni(OH)_2$ and $Ni(OH)_2$/Ag-0.4. (c) Spatial distribution of the electric field for $Ni(OH)_2$ with an excitation wavelength of 420 nm. (d) Spatial distribution of the electric field for $Ni(OH)_2$/Ag with an excitation wavelength of 420 nm. (e) LSV curves of $Ni(OH)_2$ recorded by increasing the electrolyte temperature without IR-correction. (f) LSV curves for $Ni(OH)_2$/Ag-0.4 with increasing electrolyte temperature without iR-correction. (g) Arrhenius plot of inverse temperature *versus* current density at 1.8 V (*vs.* RHE). Adapted with permission from ref. 741; Copyright 2021 Elsevier.

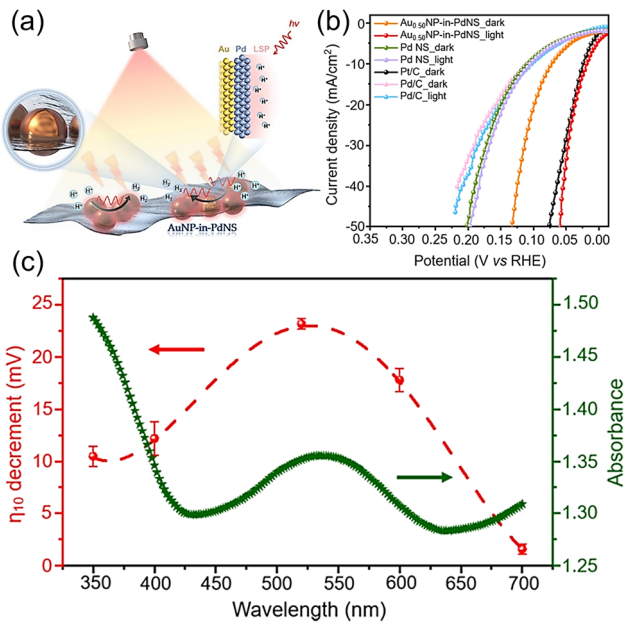

Fig. 45 AuNP-in-PdNS for enhanced electrocatalytic activity under LSPR excitation. (a) Proposed mechanism for the plasmon-enhanced ORR and HER. Plasmon-enhanced HER electrocatalysis: (b) Polarization curves collected on the $Au_{0.50}$NP-in-PdNS, Pd NS, Pt/C and Pd/C electrode at a scan rate of 10 mV s^{-1} under Xenon light illumination and dark conditions. (c) ORR polarization curves collected for $Au_{0.50}$NP-in-PdNS electrocatalysts under Xenon light illumination and dark conditions at room temperature. Plasmon-enhanced ORR electrocatalysis: (d) Polarization curves collected on the $Au_{0.50}$NP-in-PdNS, Pd NS and Pt/C electrode at a scan rate of 10 mV s^{-1} under Xenon light illumination and dark conditions. Adapted with permission from ref. 742; Copyright 2021 American Chemical Society.

degradation of organic contaminants, particularly biomass-derived ones, in wastewater under solar irradiation is known as photoreforming.[655] However, in the context of photogenerated hydrogen, the quantum efficiency of converting photon energy into hydrogen is typically suboptimal. Metal/semiconductor heterojunctions can induce LSPR, which generates a significant amount of heat in the nanoscale region, creating thermo-photocatalytic conditions without the need for additional heating systems.[166,744] Ultimately, the deployment of plasmonic nanocatalysts can substantially enhance photocatalytic activity, especially in the realm of hydrogen (H_2) evolution. Fig. 46 presents a schematic diagram of biomass photoreforming on metal/semiconductor catalysts, highlighting the role of metal plasmons as electron sinks that enhance the separation of photo-generated electron–hole pairs.

5.3.1 Photoreforming of methanol. Methanol can be readily converted to hydrogen through catalytic reactions that harness solar energy as a renewable energy resource. Naldoni *et al.* investigated the photocatalytic efficiency of Au/TiO_2 and Pt/TiO_2 in hydrogen production from methanol photoreforming (Fig. 47a).[745] Their research revealed that Pt/TiO_2 exhibits greater catalytic activity compared to both Pt/TiO_2 and pure TiO_2, resulting in enhanced hydrogen production and more efficient methanol oxidation (Fig. 47b). The superior performance of Pt/TiO_2 is attributed to Pt's greater ability, compared to Au, to act as an electron sink, effectively slowing down the recombination of photogenerated electron–hole pairs.

5.3.2 Photoreforming of ethanol. Ethanol, a biomass-derived feedstock, has the potential to act as a sacrificial electron donor, making it suitable for environmentally friendly hydrogen production. Opez *et al.* studied the influence of mono-metal (Ag, Cu, Pt)

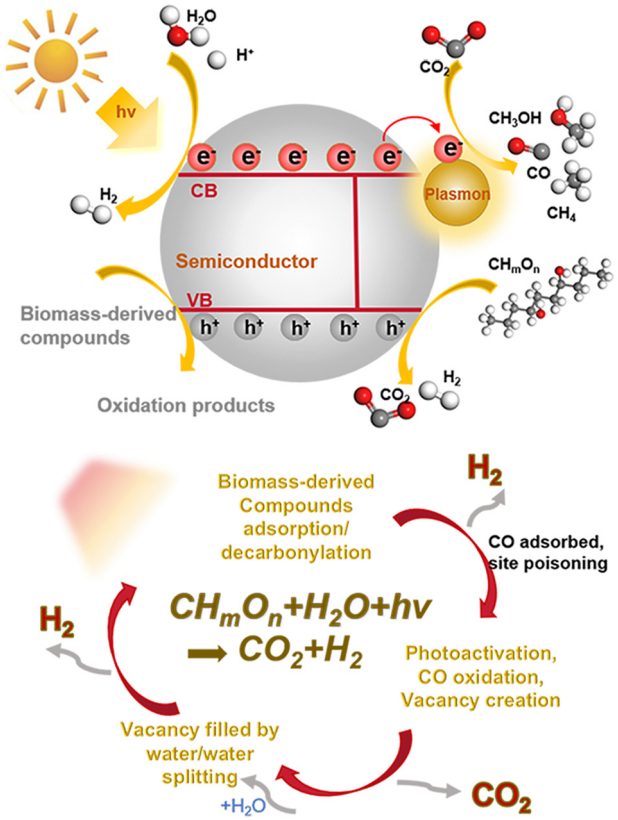

Fig. 46 Mechanisms of plasmon-enhanced biomass energy. (a) Metal as a plasmonic enhancer for separating photo-generated e^-/h^+ pairs. (b) Catalytic role of metal in the dehydrogenation of biomass-derived compounds.

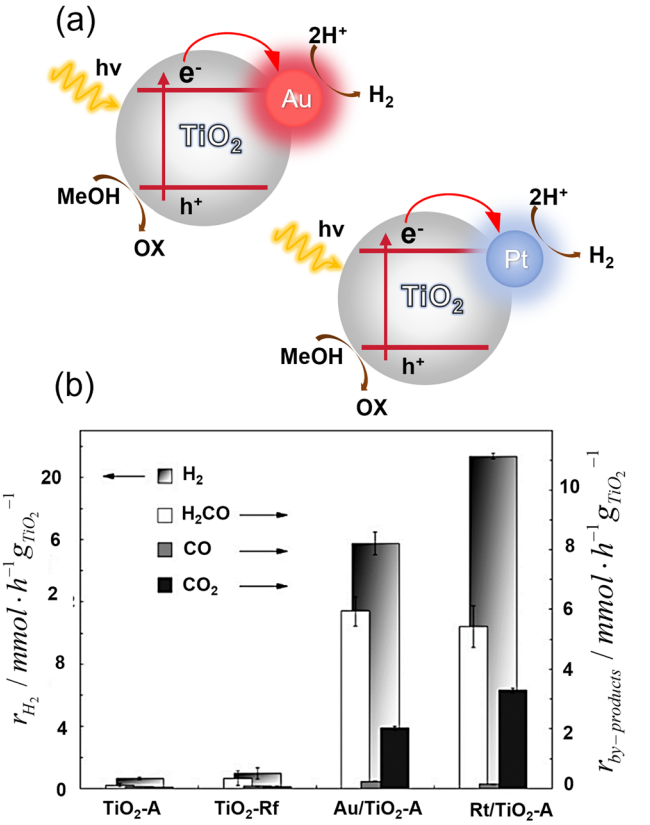

Fig. 47 Plasmon enhanced methanol photoreforming. (a) Schematic model of Pt and Au/TiO_2 photocatalysts for methanol reforming. (b) H_2, H_2CO, CO and CO_2 productivity during the photocatalytic steam reforming of methanol. Adapted with permission from ref. 745; Copyright 2013 Elsevier.

and bi-metal (Cu–Pt, Cu–Ag) loaded TiO_2 for gas-phase ethanol photoreforming.[746] In this study, Cu species demonstrated their effectiveness as a cocatalyst. TiO_2–Cu–Pt exhibited the highest H_2 productivity, with Cu helping to control the oxidation reaction, leading to a modest reduction in CO_2 formation compared to TiO_2–Pt (Fig. 48a). Moreover, the sample achieved higher H_2/CO_2 ratios due to the effect of Ag in the bimetallic TiO_2–Cu–Ag systems (Fig. 48b).

5.3.3 Photoreforming of glycerol. Glycerol, with its favorable chemical structure and a high proportion of hydrogen atoms relative to carbon and oxygen, is well-suited for photochemical transformations.[747] Tahir *et al.* reported a heterojunction catalyst of Au-loaded WO_3/TiO_2 for boosting photocatalytic H_2 evolution from glycerol photoreforming under visible light (Fig. 49a).[748] The composite samples exhibited higher visible light absorption through SPR. The maximum H_2 evolution rate achieved was 17 200 ppm h^{-1} $gcat^{-1}$ on the 0.5% Au-loaded WO_3/TiO_2 photocatalyst (Fig. 49b). This result suggests that plasmonic Au–NPs decorated on WO_3/TiO_2 heterojunctions facilitate faster charge separation and higher visible light absorption through SPR, leading to improved hydrogen production.

5.3.4 Photoreforming of glucose. Biomass photoreforming can simultaneously utilize photogenerated electrons and holes to produce gas fuels and value-added chemicals. Glucose, one of the most abundant biomass-derived compounds, has been converted into high-value chemicals.[749–751] Zhao *et al.* enhanced the efficiency and selectivity of photocatalytic glucose conversion to arabinose using gold nanoparticles decorated on three-dimensionally ordered macroporous TiO_2 (3DOM TiO_2–Au) (Fig. 50a).[752] The presence of Au NPs significantly enhances the efficiency of photogenerated electron–hole pair separation, and the LSPR endows the photocatalyst with visible-light activity. With the addition of the cocatalyst, 3DOM TiO_2–Au exhibited ~37% glucose conversion and 0.2 g L^{-1} arabinose production within 8 hours (Fig. 50b and c). These results represent a 2.8-fold and 10-fold increase in performance over traditional TiO_2. Moreover, the decoration of Au NPs notably enhanced the generation of H_2, CH_4, and CO, while the hierarchical 3DOM structure also boosted H_2 production (Fig. 50d–f).

5.3.5 Dry reforming of methane (DRM). In recent years, DRM has garnered significant scientific attention due to its ability to produce industrially valuable synthesis gas (a mixture of CO and H_2) through the conversion of CH_4 and CO_2.[753,754] Zhou *et al.* reported a plasmonic photocatalyst using Cu–Ru single-atom alloy NPs for low-temperature photocatalytic methane dry reforming, achieving high efficiency, high selectivity, and greatly suppressed coking (Fig. 51a).[755] They found that, under white light, the energy efficiency increased with light intensity, stabilizing at a peak of approximately 15% above 16 W cm^{-2} (Fig. 51b). A turnover frequency of 34 mol H_2 (mol Ru)$^{-1}$ s^{-1} and photocatalytic stability

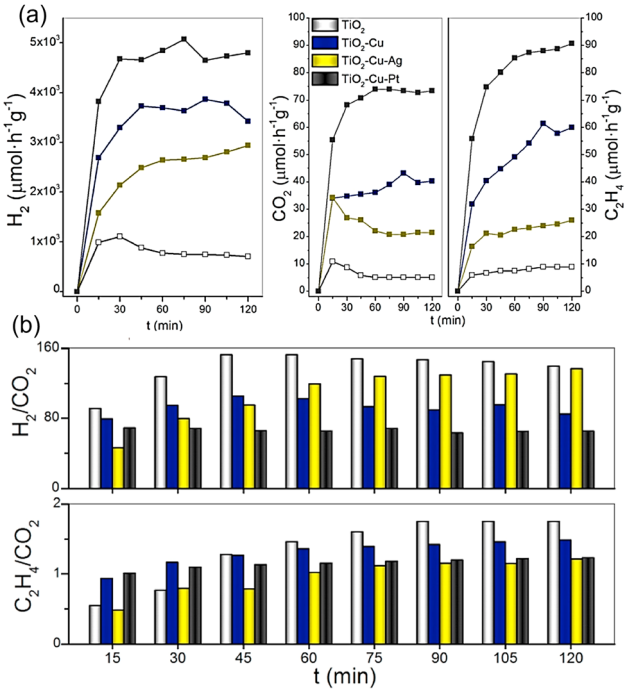

Fig. 48 Plasmon enhanced ethanol photoreforming. (a) Production rates of H_2, CO_2 and C_2H_4 with pure TiO_2 and metal-impregnated TiO_2 in a water/ethanol mixture. (b) Estimated H_2/CO_2 and C_2H_4/CO_2 ratios. Adapted with permission from ref. 746; Copyright 2018 Elsevier.

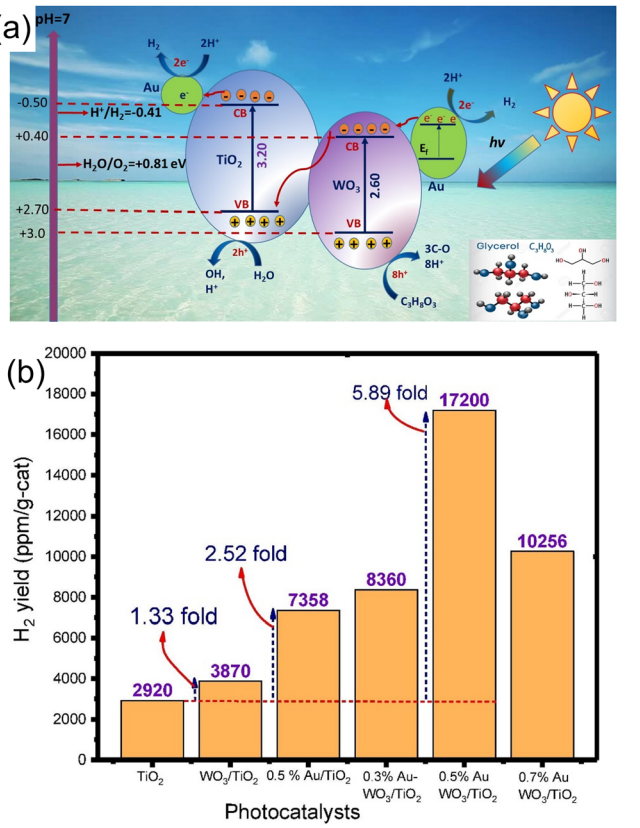

Fig. 49 Plasmon-enhanced glycerol photoreforming. (a) Mechanisms for photocatalytic H_2 production from the glycerol–water mixture over WO_3/TiO_2 with Au–NPs under visible light. (b) Photoactivity evaluation of various photocatalysts: TiO_2, WO_3/TiO_2, 0.5% Au/TiO_2, 0.3% $Au\text{-}WO_3/TiO_2$, 0.5% $Au\text{-}WO_3/TiO_2$ and 0.7% $Au\text{-}WO_3/TiO_2$. Adapted with permission from ref. 748; Copyright 2020 Elsevier.

over 50 hours were achieved under 19.2 W cm^{-2} white light illumination without the need for supplementary heating (Fig. 51c). In this study, the miniature plasmonic Cu antennas significantly enhanced light absorption, leading to efficient hot carrier generation under illumination, while single-atom Ru sites on the Cu surface contributed to the high catalytic activity.

5.4 Plasmon-enhanced thermal energy

Solar thermal energy, obtained through the conversion of solar energy to heat, has emerged as an efficient, clean, economical, and direct method for harnessing renewable energy.[756,757] However, conventional solar-thermal collection designs are plagued by significant thermal energy losses and poor thermal stability of the photothermal conversion materials used.[758] In recent years, the plasmonic heating effect of noble metal NPs has garnered significant research interest.[759–762] The dissipation of LSPPs at visible frequencies can be leveraged to create localized nanoscale heat sources. Meanwhile, noble metals typically exhibit an exceedingly low optical quantum yield, resulting in nearly 100% photothermal conversion efficiency.[763] The field of research focusing on the heating effects from plasmonic antennas is known as "thermoplasmonics".[764] To harness this heating effect, thermoplasmonics has been applied across various fields (Fig. 52), including gas sensing, thermal emission control, biomedical applications, and thermal radiation energy management.

5.4.1 Plasmon-enhanced thermal energy harvesting. Solar thermal energy, obtained through the conversion of solar energy into heat, has become a highly efficient, economical, environmentally friendly, and direct way to provide space and water heating.[757,765] Chang *et al.* reported the use of the plasmonic heating effect of noble metal NPs for efficient and facile solar-thermal energy harvesting, including solar-thermal energy conversion and thermal energy transportation (Fig. 53a).[766] Compared to conventional external photothermal conversion designs, the reported device showed a reduction in thermal resistance of more than 50% and demonstrated an over 25% improvement in solar water heating efficiency (Fig. 53b).

5.4.2 High-performance gas sensing applications. Plasmonics-based chemical sensing has proven remarkably effective for concentration-dependent gas measurements.[767,768] Karker *et al.* utilized lithographically patterned Au nanorods to collect thermal energy and applied it to gas sensing (Fig. 54a).[769] This approach eliminates the need for an external incident light source. The calibration plots of thermal and white light imaging for NO_2, H_2, and CO indicate that gas sensing results using harvested thermal energy closely match those obtained with an external incident light source (Fig. 54b–d).

5.4.3 Controlling thermal emission. Plasmon-based metasurfaces have been widely employed for customized far-field thermal emission, achieving polarized, narrowband, and directional emission.[770–772] Zhang *et al.* designed a metasurface

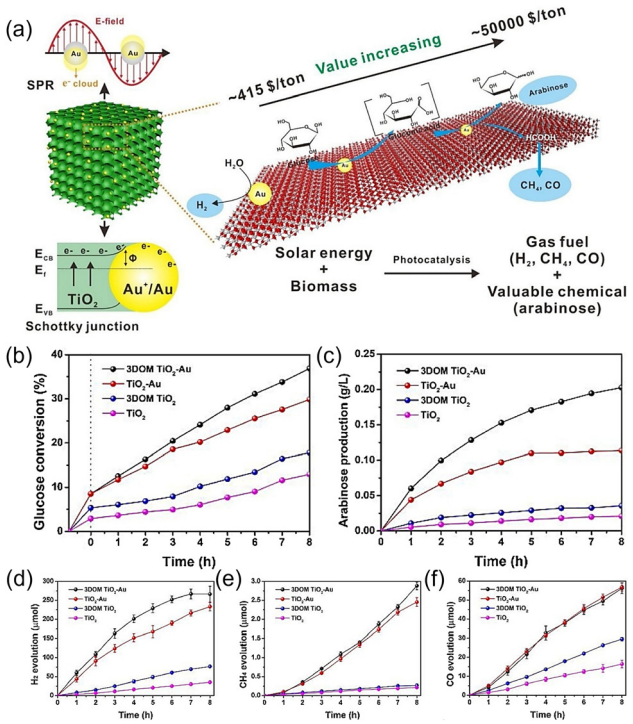

Fig. 50 Plasmon-enhanced glucose photoreforming. (a) Mechanisms for glucose photoreforming over 3DOM TiO_2-Au. (b) Glucose conversion rates. (c) Arabinose production with different photocatalysts. Gas products: (d) H_2, (e) CH_4, and (f) CO with different photocatalysts. Adapted with permission from ref. 752; Copyright 2021 Elsevier.

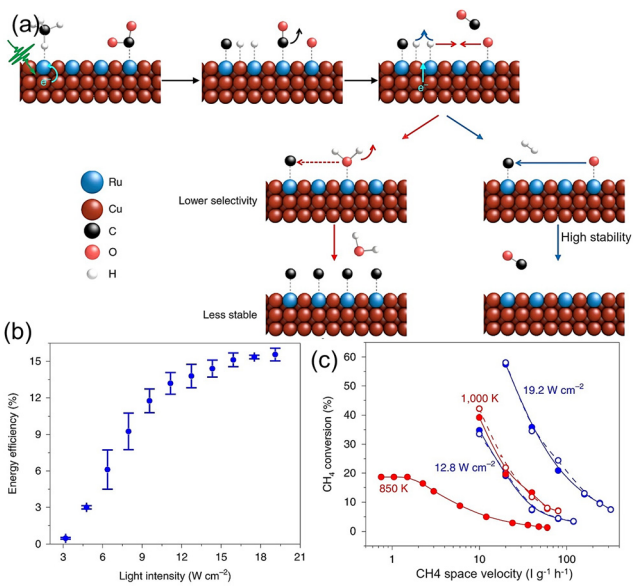

Fig. 51 Plasmon-enhanced dry reforming of methane. (a) Schematics of enhanced selectivity and stability in photocatalysis *via* the desorption induced by electronic transitions (DIET) mechanism. (b) Light-to-chemical energy efficiency of photocatalysis as a function of white light intensity. (c) Methane conversion *via* photocatalytic (blue) and thermocatalytic (red) methods as a function of space velocity. Adapted with permission from ref. 755; Copyright 2020 Springer Nature.

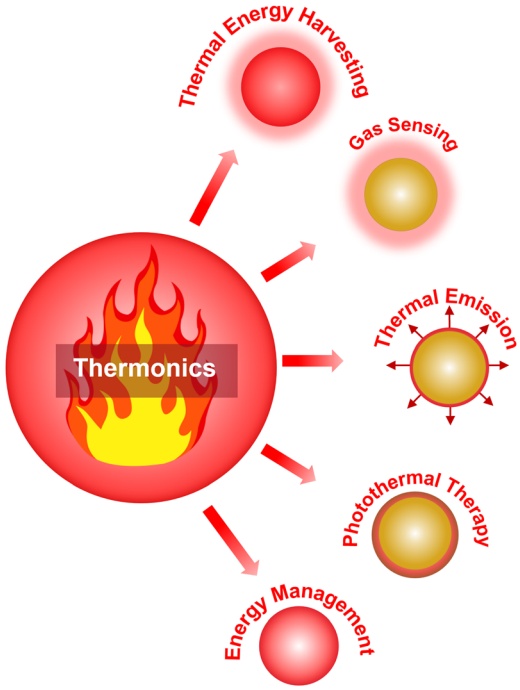

Fig. 52 Applications of thermoplasmonics.

based on nanosandwich optical absorbers (Al/SiN/Al) capable of controlling thermal emission in the infrared spectrum range (Fig. 55a).[770] The authors demonstrated that, through the intense coupling of surface lattice resonance with the magnetic resonance of the structure, unidirectional thermal emission occurs in the surface-normal direction at a wavelength of 7.1 μm (Fig. 55b). Furthermore, angular-resolved thermal emission studies revealed that the thermal emission caused by Fano resonance displayed a concentrated wavelength range and a specific directional radiation angle (Fig. 55c).

5.4.5 Photothermal therapy (PTT) applications. PTT, based on NIR light, offers a noninvasive approach for tumor ablation by inducing localized hyperthermia *via* photothermal agents.[181,773–775] Numerous experiments have adequately demonstrated the remarkable efficacy of plasmon-based PPT in tumor ablation,[776] cancer immunotherapy,[777] and anti-infection applications.[778] Zhang *et al.* synthesized 2D PtAg nanosheets with excellent photothermal and PA properties in both the NIR-I and NIR-II biowindows (Fig. 56a).[779] Due to the outstanding photothermal properties of folic acid-modified thiol-poly(SH-PEG-FA)-functionalized PtAg nanosheets in both NIR-I and NIR-II biowindows, and their accumulation at 4T1 tumor sites, the skin temperature of mice injected with PtAg nanosheets was higher after 2 minutes of irradiation with 785 and 1064 nm lasers (Fig. 56b and c). This setup enabled effective targeted ablation of tumors in mice without side effects or metastasis, guided by PAI under both NIR-I and NIR-II lasers (Fig. 56d and e).

5.4.6 Thermal radiation energy management. Surface plasmon devices and materials possess the ability to achieve directional thermal management of light energy due to their capability to manipulate light at the nanoscale.[780,781] Ma *et al.* proposed a

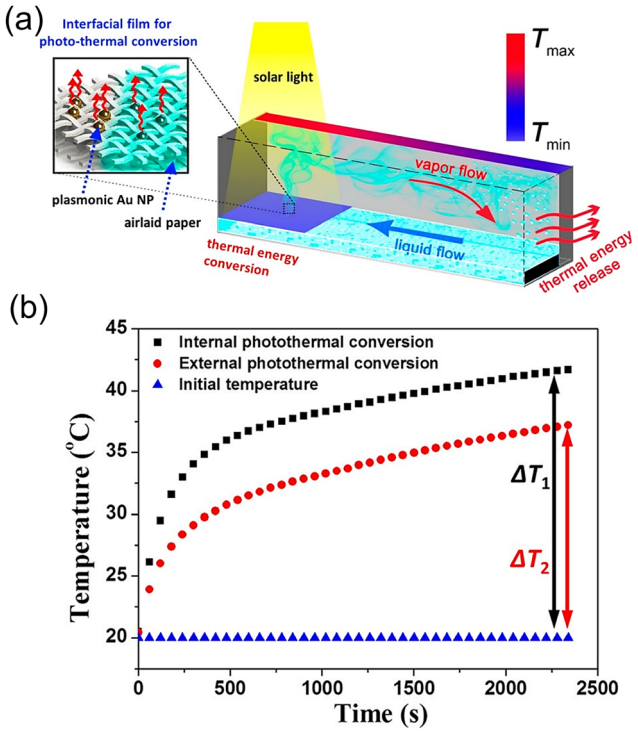

Fig. 53 Efficient solar-thermal energy harvesting *via* internal plasmonic heating. (a) Schematic of solar-thermal energy harvest driven by interfacial plasmonic heating. (b) Temperature progression profiles for solar water heating systems, comparing conventional and new solar-thermal designs. Adapted with permission from ref. 766; Copyright 2016 American Chemical Society.

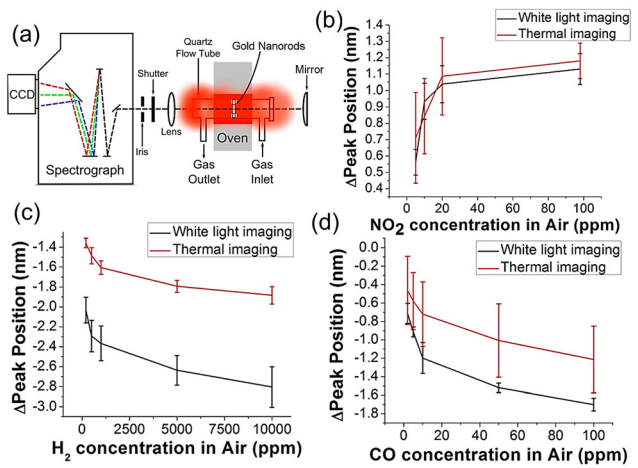

Fig. 54 Thermal energy harvesting with plasmonic-based chemical sensors. (a) Schematic of the thermal imaging setup. Calibration graphs from thermal and white light imaging for (b) NO_2, (c) H_2 and (d) CO analyte gases in an air background. Adapted with permission from ref. 769; Copyright 2014 American Chemical Society.

transparent and solar thermal metasurface based on copper nanodisks, demonstrating a maximum absorption difference of over 25% from different sides (Fig. 57a and b).[782] In this structure, LSPR is triggered around copper disks to produce absorption, while a thin silver film enhances the absorption directivity. The

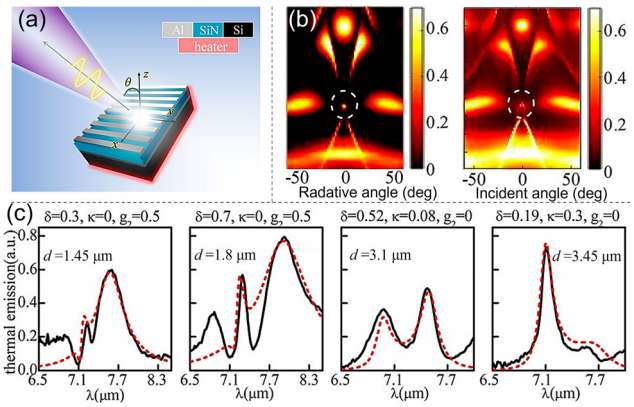

Fig. 55 Controlling thermal emission with optical absorbers in metasurfaces. (a) Schematic of the sandwich structure. (b) Measured (left) and simulated (right) angle-resolved thermal emission spectra with fixed lattice Λ = 7 μm and a varied grating width d of 3.45 μm. (c) Calculated absorptivity (red) and measured thermal emission (black) spectra *vs.* wavelength. Adapted with permission from ref. 770; Copyright 2019 American Chemical Society.

spectra show strong activity in the infrared region due to the coupling between the copper disks and the silver layer (Fig. 57c and d). Enhanced thin film preparation techniques may unlock this design's potential for managing light in architectural window applications.

5.5 Plasmon-enhanced mechanical energy

Since Professor Wang *et al.* first invented a novel arch-shaped triboelectric nanogenerator (TENG) in 2012,[783] various methods have been proposed to improve the output power of a TENG, including surface functionalization, nanoparticle doping, and chemical modification.[784–789] However, these approaches primarily alter the surface properties of triboelectric films, often resulting in low efficiency and unstable output. Surface charges are crucial in TENGs, as they not only generate current but also facilitate the conversion of mechanical energy into electrical energy. Therefore, optimizing surface charge density is essential for enhancing TENG efficiency. Recent research has shown that surface plasmon resonance and the excitation of hot electrons can form charge traps when precious metals are introduced into friction materials.[657,790] These charge traps can increase the surface charge density of TENGs through a mutual-coupling effect, significantly improving their output power.

Chen *et al.* developed a high-output-power TENG based on charge traps generated by mutual coupling effects within g-C_3N_4/MXene-Au composites (Fig. 58).[791] In this work, g-C_3N_4 absorbs light energy and generates carriers that act as charge traps. The surface plasmon resonance of Au and its excited hot electrons further contribute to the formation of charge traps. Additionally, the superior electronic transmission capability of MXene facilitates the generation of more charge traps. These charge traps enhance surface charge accumulation in the TENG through mutual coupling effects, resulting in a TENG with the output voltage, current, peak power, and power density of 510 V, 80 μA, 20 mW (4 × 4 cm), and 12.5 μW mm^{-2} at an impedance

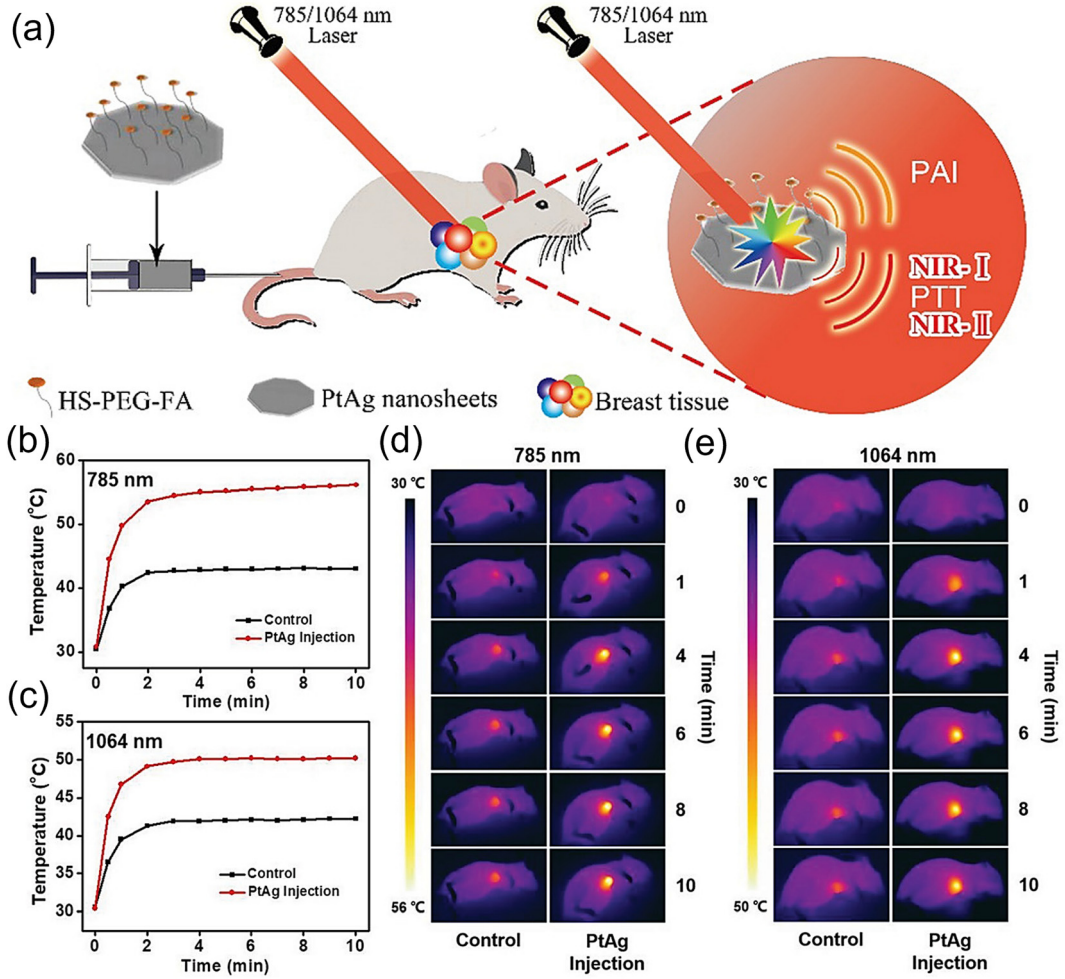

Fig. 56 Ultrathin 2D plasmonic PtAg nanosheets for broadband phototheranostics. (a) SH-PEG-FA-modified ultrathin PtAg nanosheets for 4T1 tumor-targeted PTT guided by PAI with 785 and 1064 nm lasers. (b) Photothermal heating trajectories of 4T1 tumors with a 785 nm laser. (c) Photothermal heating trajectories of 4T1 tumors with a 1064 nm laser. (d) Photothermal imaging of 4T1 tumors with a 785 nm laser. (e) Photothermal imaging of 4T1 tumors with a 1064 nm laser. Adapted with permission from ref. 779; Copyright 2021 Wiley.

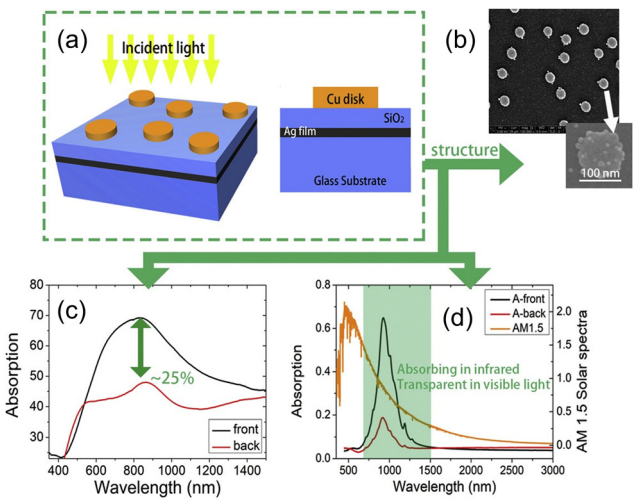

Fig. 57 Copper plasmonic metamaterial for directional thermal energy management. (a) Sketch of the operating structure. (b) SEM images of the fabricated disk. (c) Absorption spectra with front and back incidence after reduction treatment. (d) Simulated absorption spectra with front and back incidence. Adapted with permission from ref. 782; Copyright 2020 Elsevier.

of 2 MΩ, respectively. This output power was six times higher than that of a conventional TENG with PDMS.

The same research group also developed a TENG doped with Ag@SiO_2 core–shell particles (Ag@SiO_2-NPs), which exhibited high instantaneous power density under visible light illumination (Fig. 59a).[657] It was found that Ag@SiO_2-NPs alleviated the seepage effect common in conventional nanoparticles and mitigated surface charge leakage typically caused by metal nanoparticles (Fig. 59b). More importantly, the surface plasmon effect enabled the core–shell nanoparticles to further enhance the TENG's output performance (Fig. 59c–j). The peak output power reached 70 mW, the output current was 248 μA, the output power density reached up to 4.375 mW cm^{-2}, and the output voltage exceeded 1 kV when the shell thickness was 6 nm with a doping content of 0.4 wt%, far surpassing the performance of conventional TENGs.

Additionally, Gao *et al.* utilized grating-electrode-enabled surface plasmon excitation in TENGs.[790] The generation of hot electron–hole pairs from the decay of surface plasmon resonance effectively enhanced the output performance of TENGs

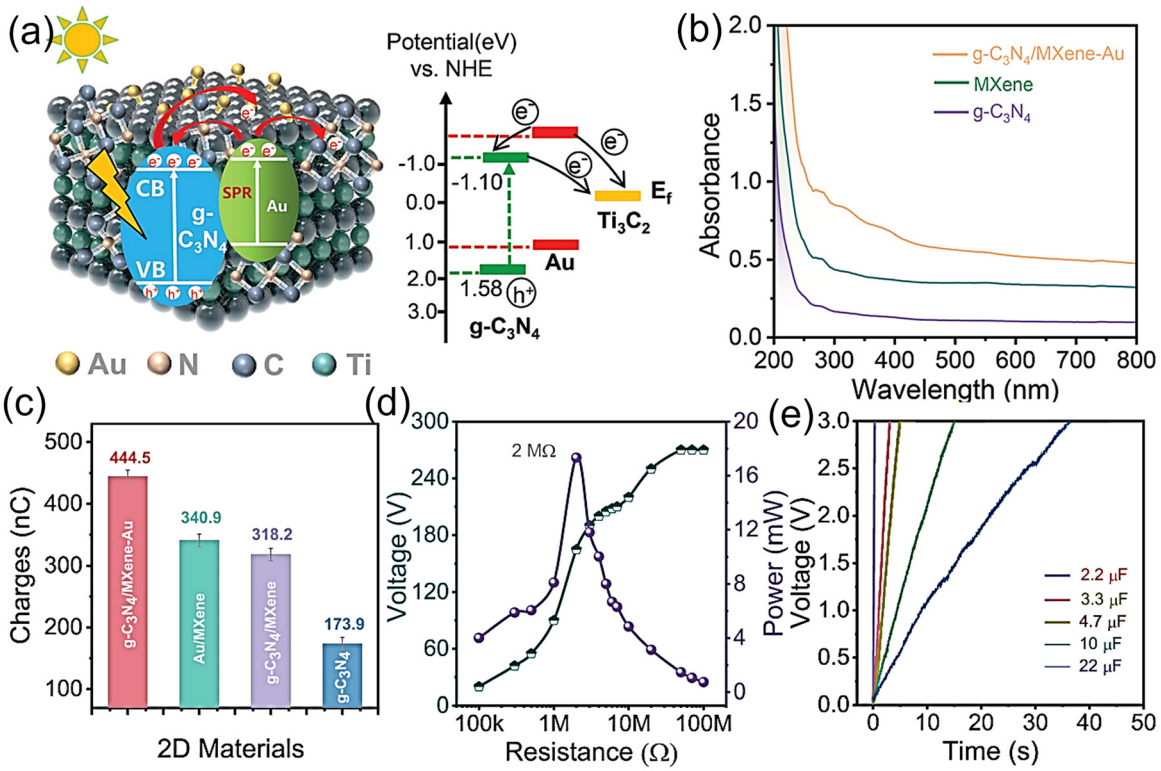

Fig. 58 Boosting TENG output performance *via* mutual coupling effects of photon-carriers and plasmon. (a) Mechanism for creating more charge traps. (b) UV-vis spectrum of g-C_3N_4, MXene, and g-C_3N_4/MXene-Au composites. (c) Charges of TENG materials under visible light. (d) Output power of the TENG with g-C_3N_4/MXene-Au composites under visible light. (e) Charge curve of the TENG with g-C_3N_4/MXene-Au composites under visible light. Adapted with permission from ref. 791; Copyright 2022 Wiley.

while reducing their output impedance (Fig. 60a–c). Using this method, a peak output power of 3.6 mW was achieved under a loading resistance of 1 MΩ, exhibiting a 4.5-fold enhancement in output power and a 75% reduction in output impedance (Fig. 60d and e).

5.6 Section summary

This section mainly examines the pivotal role of plasmons in promoting the generation and conversion of green renewable energy. Plasmons can enhance solar energy conversion by increasing the photonic activity of semiconductors, promote the conversion of solar energy into chemical energy through the SPR effect, accelerate the degradation of biomass-derived compounds and the release of hydrogen through plasmonic nanocatalysts, regulate the applications of thermal energy *via* metallic plasmonics, and increase output power by elevating the surface charge density of TENGs. In summary, plasmon technology demonstrates immense potential in advancing the development of sustainable green energy.

Plasmonics has demonstrated potent efficacy in several energy conversion processes; nonetheless, its application in several fields still faces challenges and requires further exploration by researchers. One of the primary challenges is the need to harvest energy from multiple sources. Traditional energy harvesters are often designed to capture a single type of energy, such as solar or mechanical, which limits their functionality when that energy source is unavailable. To address this limitation, integrated energy harvesters that combine multiple energy sources, such as solar cells, biomass energy, thermal energy, and mechanical energy, are essential. These hybrid systems enhance the versatility and efficiency of energy harvesting devices, allowing them to operate effectively across a broader range of scenarios. However, designing and optimizing these integrated systems to work harmoniously presents significant technical challenges.

Another challenge in conversion applications is the efficient use of the full solar spectrum. Plasmonic devices typically operate within a narrow spectral range, which limits their ability to harness energy across the entire spectrum. This restriction poses a significant obstacle for widespread energy harvesting applications. Recent advances in multifunctional plasmon materials, which can modulate electron density and temperature, offer a potential solution. By tailoring these materials to respond to different wavelength bands, it is possible to create devices that can capture energy from the entire solar spectrum. However, achieving this level of control and efficiency remains a complex challenge in material design and engineering.

As energy harvesting devices become more portable and miniaturized, maintaining efficiency and stability becomes increasingly difficult. Smaller plasmonic energy harvesters often suffer from reduced energy density, which can limit their practical applications. To overcome this challenge, researchers

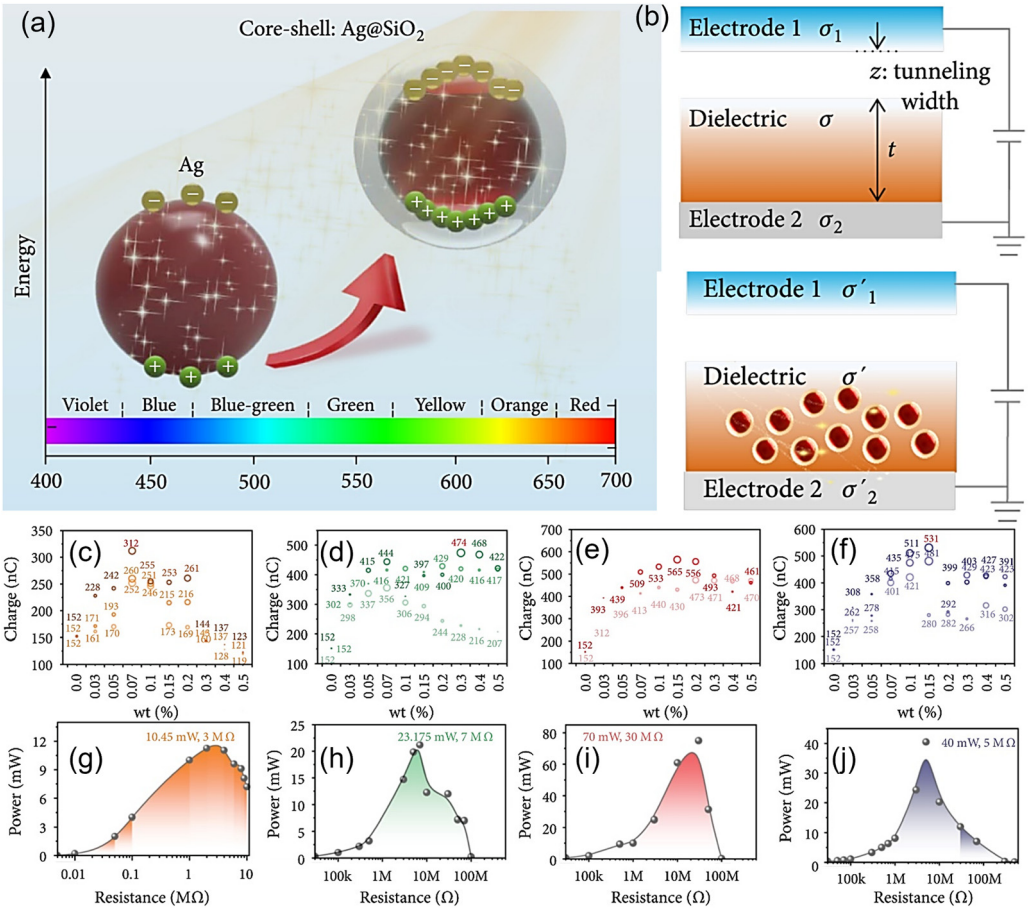

Fig. 59 Surface plasmon effect dominated high-performance TENG. (a) Superiority of Ag@SiO_2 NPs in generating the surface plasmon effect. (b) Capacitor model of a TENG, both undoped (upper) and doped with Ag@SiO_2 (lower). (c)–(f) Output voltage of Ag, Ag@SiO_2-3 nm, Ag@SiO_2-6 nm, and Ag@SiO_2-12 nm with visible light. (g)–(j) Output power of Ag, Ag@SiO_2-3 nm, Ag@SiO_2-6 nm, and Ag@SiO_2-12 nm with visible light. Adapted with permission from ref. 657; Copyright 2022 AAAS.

are exploring the use of flexible, lightweight, and highly conductive materials, along with nanotechnology, to design smaller, more efficient components.[792,793] These advancements could lead to the development of portable energy harvesters suitable for wearable technology, drones, and mobile power applications. However, balancing miniaturization with performance and reliability remains a key challenge.

6. Integrated plasmonic circuits

The rapid downsizing of electronic components to the submicron scale has brought about remarkable increases in computing power, coupled with significant cost reductions. As the microelectronics industry continues its journey towards smaller devices, it becomes increasingly plausible that both physical and economic constraints associated with top-down silicon technology will soon impose limitations on further progress. To overcome these limitations and meet the anticipated demands of future society, revolutionary breakthroughs, rather than incremental advances, are imperative. A promising avenue involves a paradigm shift from electronic signals to light. However, utilizing electromagnetic waves as information carriers in optical signal-processing devices and PICs faces a formidable challenge—the limited integration and miniaturization available.[794] This challenge is intricately linked to the diffraction limit of light in dielectric media, preventing the confinement of electromagnetic waves into nanoscale regions significantly smaller than the wavelength of light. Addressing this issue requires innovative approaches, and one captivating method involves leveraging the unique properties of plasmonic nanomaterials. Consequently, proposals for photonic components and electronic circuits based on localized plasmonic resonance have surfaced, demonstrating potential in tackling the scalability and performance challenges associated with future plasmonic integrated circuits (Fig. 61).[795] This approach holds the promise of achieving all-optical processing of optical signals, thereby enhancing the speed, bandwidth, and overall capacity of information technology. Simultaneously, it presents an opportunity to reduce costs and power consumption, aligning with the evolving needs of future communication, computing, sensing, and other fields. This section provides an overview of recent strides in integrated electronic circuits grounded in plasmonic properties, including plasmonic emitters, plasmonic

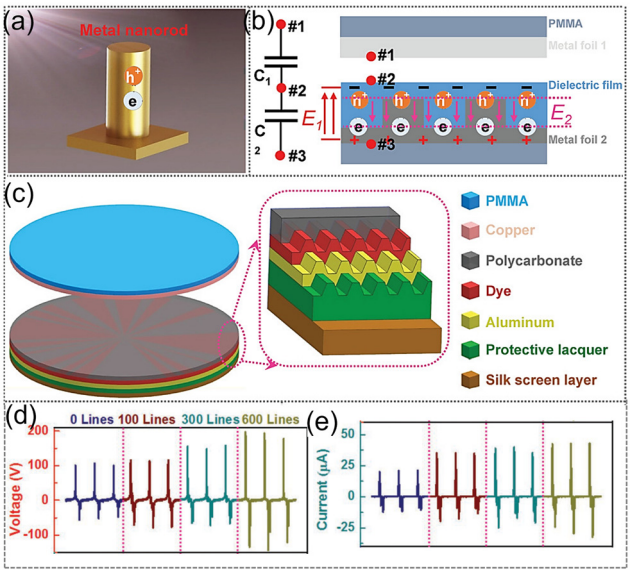

Fig. 60 Enhancing TENG performance with grating-electrode-enabled surface plasmon excitation. Theoretical model of grating-coupled surface-plasmon-enhanced TENGs: (a) Generation of hot electron–hole pairs. (b) Theoretical models of reverse electric fields from hot electron–hole pairs. (c) Schematic of the TENG with a double-layer structure based on CDs. (d) The output voltage of TENG with aluminum foil at different line densities. (e) The output current of TENG with aluminum foil at different line densities. Adapted with permission from ref. 790; Copyright 2019 Wiley.

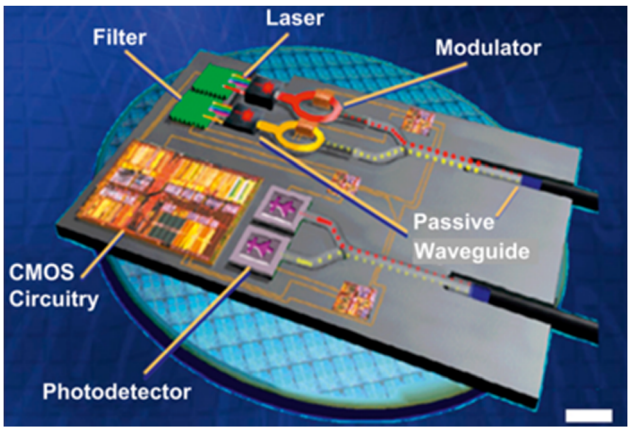

Fig. 61 Overview of plasmonic integrated circuit components featuring high functionality on small wafer footprints. Adapted with permission from ref. 795; Copyright 2012 Springer Nature.

modulators/switchers, plasmonic logic gates, and plasmonic detectors.

6.1 Plasmonic emitters

Plasmonic emitters or lasers represent a cutting-edge approach to addressing the challenges of creating highly compact plasmonic circuits. Unlike traditional lasers that amplify light, plasmonic lasers operate by amplifying surface plasmons, which are collective oscillations of electrons at the interface between a metal and a dielectric. This fundamental difference results in unique operational characteristics, particularly due to the strongly confined electromagnetic fields in a plasmonic laser cavity. One of the key features of plasmonic lasers is their ability to significantly enhance the spontaneous emission rate *via* the Purcell effect.[796] The Purcell effect, named after the physicist Edward Purcell, describes how the spontaneous emission rate of an emitter can be modified by its surrounding electromagnetic environment. In the context of plasmonic lasers, the extremely confined electromagnetic fields in the nanocavity result in a dramatically reduced effective mode volume. According to the Purcell formula $F_p \propto Q/V$, a smaller mode volume (V) and a sufficiently high quality factor (Q) lead to a larger Purcell factor (F_p), meaning the spontaneous emission rate is enhanced compared to an emitter in free space. This effect is particularly pronounced in low-dimensional plasmonic nanostructures, where the enhancement scales anomalously with frequency. The confined fields and the Purcell enhancement enable the plasmonic laser to achieve exceptionally fast response times, even at wavelengths far from the surface plasmon resonance.

The enhancement of the spontaneous emission rate is quantified by the β-factor, which represents the fraction of spontaneous emission coupled into the laser mode compared to all other modes. A high β-factor is critical because it reduces the threshold for stimulated emission, potentially allowing plasmonic lasers to operate with lower thresholds despite the inherent high losses in metal–dielectric nanostructures. However, it is important to note that while the promise of low-threshold plasmonic lasers is significant, current implementations still face considerable challenges. The high intrinsic ohmic losses in metals contribute to relatively high lasing thresholds, which is a major barrier that researchers continue to address. Despite this, the potential for plasmonic lasers to revolutionize ultra-compact photonic circuits keeps them at the forefront of nanophotonics research.

Plasmonic–luminescent hybrid emitters. The strategy to achieve high-performance plasmonic emitters involves integrating plasmonic metal structures with luminescent materials to enhance the spontaneous emission rate through plasmonic confinement. For example, Liu and colleagues introduced an innovative method to tune the lasing wavelength of a single semiconductor nanowire by leveraging the plasmon-enhanced Burstein–Moss effect (Fig. 62a).[797] The hybrid device comprises fluorescent dyes of a CdS nanowire positioned on a thin SiO_2 layer atop an Au film (Fig. 62a-I). This configuration demonstrated enhanced exciton emission intensity and recombination rates due to the efficient energy transfer from surface plasmons to CdS excitons. Moreover, the device exhibited polarization sensitivity (Fig. 62a-III), indicating its potential as a polarized light source.

Perovskite–plasmonic hybrid emitters. Another type of plasmonic emitter is the perovskite emitter. Perovskite materials are one of the exceptional candidates for light-emitting applications due to their remarkable properties, such as high photoluminescence quantum yield, tunable bandgap, and long carrier diffusion lengths.[807] In the perovskite-plasmon configuration, plasmonic nanostructures can strongly confine and enhance the local electromagnetic field around them. When a perovskite material

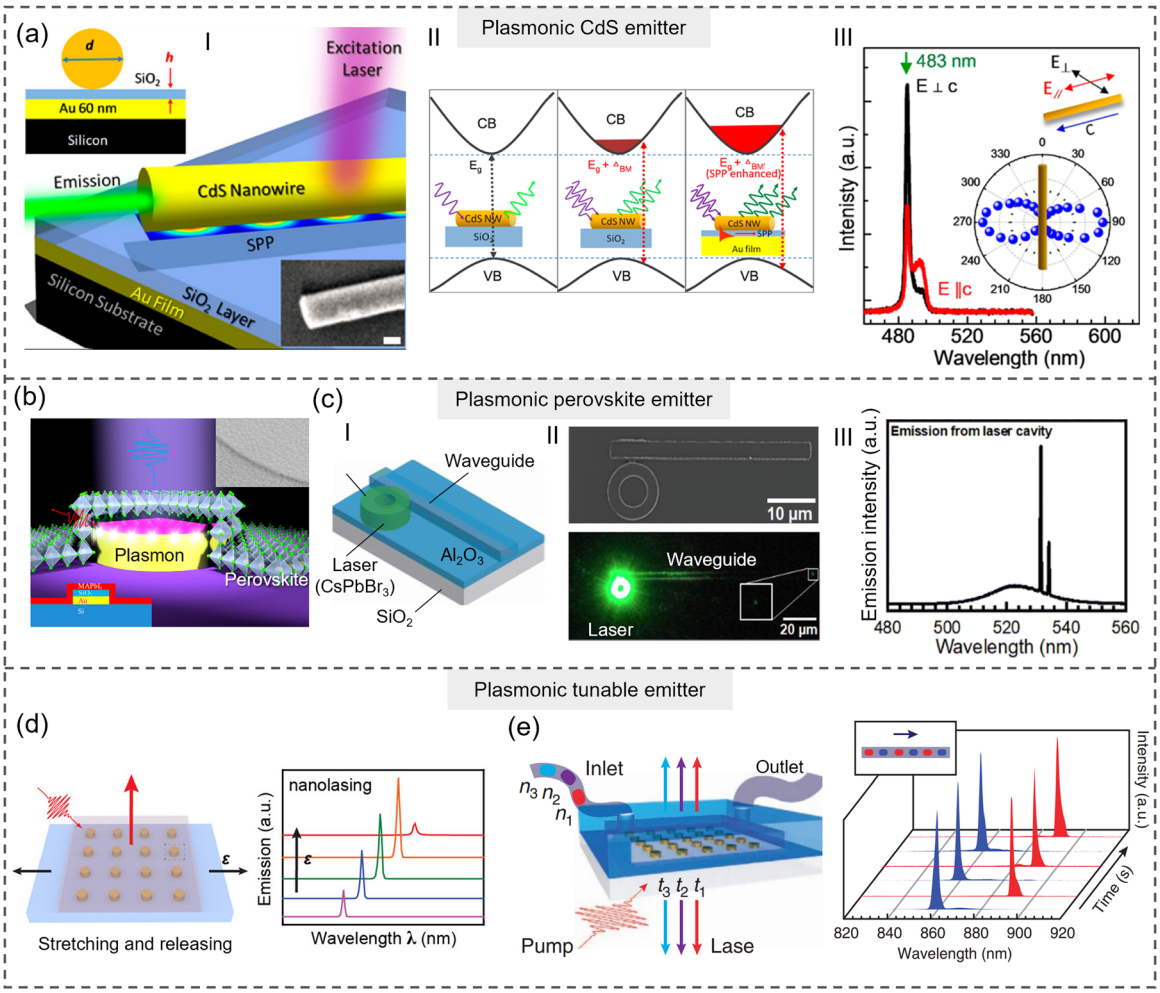

Fig. 62 Plasmonic emitters. (a) Plasmonic CdS emitter. (I) Schematic representation of the plasmonic CdS emitter. (II) Working mechanism. (III) The emission spectra and polarization-dependent behavior of the emitter. Adapted with permission from ref. 797; Copyright 2013 American Chemical Society. (b) Plasmonic perovskite emitter for free-space excitation. Adapted with permission from ref. 798; Copyright 2018 American Chemical Society. (c) Plasmonic perovskite emitter for waveguides in confined modes. (I) Schematic representation of the emitter. (II) Micro-photoluminescence image of the emitter pumped above the lasing threshold. (III) Spectra from the end of the waveguide. Adapted with permission from ref. 799; Copyright 2022 the Royal Society of Chemistry. (d) Plasmonic tunable emitter by stretching and releasing the elastomeric substrate. Adapted with permission from ref. 800–802; Copyright 2022 American Chemical Society. (e) Plasmonic tunable emitter by using liquid gain materials (IR-140 dye molecules). Optically pumped arrays of gold nanoparticles surrounded by IR-140 dye molecules are tuned as a function of the dielectric environment. Adapted with permission from ref. 803–806; Copyright 2015 Springer Nature.

is placed in proximity to such a structure, the increased field can enhance the rate of radiative recombination of excitons, leading to a stronger light emission. This effect is particularly pronounced at the plasmon resonance frequency, where the field enhancement is maximal. For instance, lead halide perovskite microplates were combined with a SiO_2–Au hybrid structure to precisely control the laser emissions in the free space by designing the plasmonic resonance (Fig. 62b).[798] Besides, the hybrid plasmonic nanostructures show significant enhancement in emission intensity due to the strong field confinement and plasmonic resonance. This enhancement is confirmed through various experiments, including the observation of sharp emission peaks and the transition from spontaneous emission to lasing action. Perovskites can also be combined with waveguides in confined modes to provide light sources for on-chip PICs. For instance, Delaunay and co-workers employed an etching-free lithographic patterning technique to fabricate the plasmonic waveguides and perovskite laser cavities (Fig. 62c).[799] The integration achieved a low lasing threshold and a propagation length over 100 μm for the waveguides (Fig. 62c-II), demonstrating effective coupling between the perovskite laser and the waveguide. This was also confirmed by the spectrum at the end of the waveguide (Fig. 62c-III). Overall, integrating perovskite materials with plasmonic nanostructures provides a powerful approach to developing efficient and compact light-emitting devices. The enhanced emission for miniaturization makes this integration a promising strategy for the next generation of optoelectronic devices. Despite the challenges such as stability and interface optimization, the synergy between perovskites and plasmonics holds significant promise for advancing light-emitting technologies.

Mechanical and chemical tunability. One of the most compelling features for plasmonic emitters is the tunability. This tunability can be achieved through various mechanisms, allowing for precise control over the emission wavelength, intensity, and polarization, which is critical for applications in sensing, imaging, and on-chip photonics.[808] The tunability of plasmonic emitters can be achieved through a variety of mechanisms, including mechanical, thermal, electrostatic, chemical, and magnetic methods. Among them, tunability *via* elastic substrates and chemical materials is highlighted as a representative method. For instance, plasmonic nanostructures are deposited on a flexible, stretchable substrate (Fig. 62d).[800] By mechanically stretching or compressing the substrate, the spacing and arrangement of the plasmonic nanostructures can be altered, leading to a change in the plasmon resonance condition. This, in turn, affects the emission wavelength and intensity of the plasmonic emitter. The significant advantages of this method are reversible tuning and a wide tuning range. The mechanical stretching and releasing of the substrate provide a reversible and dynamic method to tune the plasmonic emission, which allows for real-time control over the emitter's properties. Besides, the extent of the tuning range can be significant, depending on the elasticity of the substrate and the initial spacing of the plasmonic structures. This can enable broad wavelength tuning across a significant portion of the visible or infrared spectrum. Notably, repeated stretching and releasing of the substrate can lead to material fatigue, which may degrade the performance of the device over time. Achieving precise control over the degree of stretching and the uniformity of the strain applied across the substrate can be challenging, which may lead to non-uniform tunability.

Dynamic tunability. Another approach involves the use of liquid gain materials, such as IR-140 dye molecules, to tune the emission of plasmonic emitters (Fig. 62e).[803] In this scenario, a plasmonic structure like a gold nanoparticle array is immersed in a liquid solution containing the IR-140 dye. The dye molecules act as a gain medium that can be optically pumped, providing energy to the plasmonic system. The emission characteristics of the plasmonic emitter can be tuned by modifying the dielectric environment surrounding the gold nanoparticles, which can be achieved by changing the concentration or composition of the dye solution. The significant advantages of this method are dynamic tunability, enhanced emission, and environmental sensitivity. Notably, liquid gain materials can suffer from photobleaching or degradation over time, which may affect the long-term stability of the plasmonic emitter.

6.2 Plasmonic modulators and switches

Optical modulators are essential components in modern photonic systems, enabling the control of light signals in various applications, from telecommunications to sensing and imaging. The primary function of an optical modulator is to manipulate the properties of light—such as amplitude, phase, or polarization—by an external signal, typically electrical or optical. This modulation allows for the encoding, switching, and routing of data within photonic circuits, making optical modulators key enablers for high-speed and high-bandwidth communication systems. While traditional optical modulators have proven effective for a wide range of applications, the demand for more compact, faster, and energy-efficient devices has led to the exploration of alternative technologies. Among these, plasmonic modulators have gained significant attention due to their ability to confine light to sub-wavelength dimensions, thereby enhancing light–matter interactions far beyond the capabilities of conventional modulators.

Plasmonic modulators leverage the unique properties of surface plasmons—coherent oscillations of electrons at the interface between a metal and a dielectric. These oscillations can be strongly confined to nanoscale regions, leading to several key advantages: (1) ultra-compact size: plasmonic modulators can be much smaller than traditional optical modulators because they operate at the nanoscale, confining light to volumes much smaller than the wavelength of light. This miniaturization is critical for high-density integration in photonic circuits, allowing for more compact and scalable designs; (2) high-speed operation: the enhanced light–matter interaction in plasmonic structures enables faster modulation speeds, often in the terahertz range. This makes plasmonic modulators ideal for high-speed data transmission and processing, far surpassing the capabilities of conventional modulators; and (3) enhanced modulation depth: the strong field enhancement associated with surface plasmons allows for greater modulation depth, meaning that the degree of change in the optical signal is more pronounced. This can lead to higher signal contrast and improved performance in optical communication systems.

Electro-optic plasmonic modulators. These modulators are classified into three main types based on the mechanism used to achieve modulation: electro-optic modulators, thermo-optic modulators, and all-optical modulators. Electro-optic plasmonic modulators utilize an external electric field to alter the optical properties of a material, thereby modulating the plasmonic signal. For instance, phase change materials (PCMs) exhibit changes in electrical and/or optical properties when switching between two stable states, an amorphous phase and a crystalline phase, at high speed. Electro-optic plasmonic modulators are particularly attractive for high-speed applications due to their rapid response times. For instance, Melikyan and colleagues developed a high-speed plasmonic phase modulator (PPM) capable of encoding information in the phase of SPPs at a remarkable bit rate of 40 Gbit/s (Fig. 63a).[809]

The PPM consists of two metal tapers that facilitate the conversion between photonic and plasmonic modes, and a phase modulator section located between them. The metal taper, which narrows at an angle of 15°, acts as an interface between the silicon photonics and plasmonics, enabling efficient excitation of the plasmonic resonance by light guided through a silicon nanowire. The device is exceptionally compact, with a length of just 29 μm. It also has a flat modulation frequency response up to at least 65 GHz and maintains thermal stability up to 85 °C.

Thermo-optic and all-optical modulators. Thermo-optic plasmonic modulators rely on the temperature-dependent refractive index change in the material surrounding the plasmonic waveguide. By applying localized heating (through an electric current or optical beam), the refractive index of the

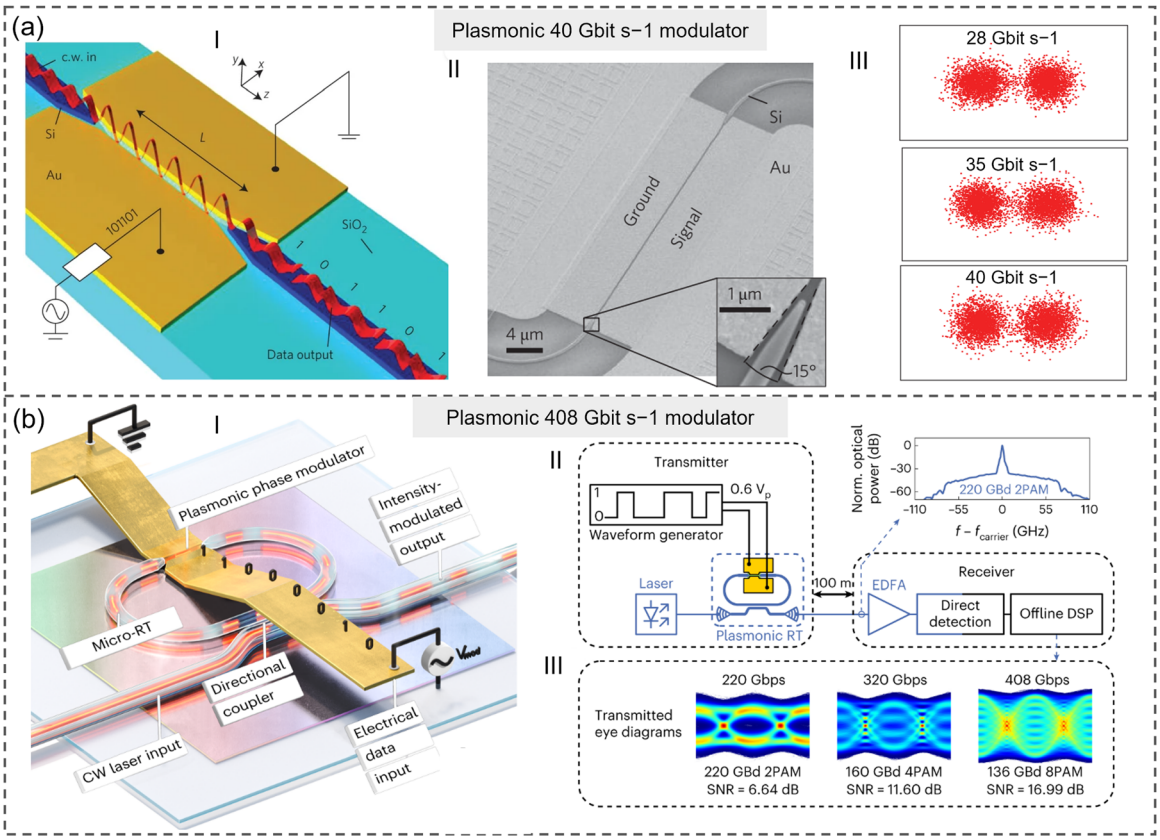

Fig. 63 Plasmonic modulators. (a) Plasmonic modulator operating at 40 Gbit/s based on electro-optic modulation in a nonlinear polymer. (I) Schematic representation of the modulator. (II) SEM image of the device. (III) Modulation experiment results. Adapted with permission from ref. 809; Copyright 2014 Springer Nature. (b) Plasmonic modulator operating at 408 Gbit/s based on thermo-optic modulation. (I) Schematic representation of the device. (II) High-speed transmission experiment. (III) Eye diagrams and signal-to-noise ratios (SNRs) for 220 Gbps, 320 Gbps, and 408 Gbps transmission. Adapted with permission from ref. 810; Copyright 2023 Springer Nature.

material changes, thus modulating the plasmonic signal. While this method offers relatively straightforward implementation, it typically results in slower modulation speeds compared to electro-optic methods. All-optical plasmonic modulators use light to modulate other light signals through nonlinear optical effects. In these devices, a control light beam interacts with the plasmonic structure, inducing a change in the refractive index of the material, which in turn modulates the signal light. All-optical modulation is particularly suited for ultra-fast applications and can be used to achieve high bandwidths. However, the nonlinear effects required for this type of modulation are often weak and require intense light fields or specially designed materials to enhance the interaction.

Micro-racetrack modulator. In addition to the established methods, recent advancements have introduced innovative approaches that significantly enhance the performance of plasmonic modulators. One such advancement is the plasmonic micro-racetrack modulator, demonstrated by Leuthold and colleagues.[810] The modulator is based on a micro-racetrack cavity that combines a plasmonic-organic-hybrid phase-shifter section with a passive photonic waveguide section (Fig. 63b). A laser input is introduced into the cavity *via* a directional coupler, and the application of voltage to the plasmonic phase shifter causes a shift in the resonance wavelength, leading to intensity modulation of the laser output. This device offers an unprecedented bandwidth of 176 GHz and operates at data rates of up to 408 Gbps with a low driving voltage of only 0.6 Vp. It demonstrates a 28-fold improvement in thermal stability over traditional silicon microring modulators (thermo-optic modulation), with continuous operation at elevated temperatures (up to 85 °C) without the need for device-level thermal control. This thermal resilience is achieved by incorporating a combination of plasmonic and photonic sections within the feedback waveguide, which allows for counterbalancing the thermo-optic effects and maintaining high-efficiency modulation.

6.3 Plasmonic logic gates

Optical logic circuits represent a significant advancement in computing technology, leveraging the properties of light for processing and transmitting information. Unlike traditional electronic logic circuits that rely on electrical signals, optical logic circuits use photons, the fundamental particles of light, to perform logical operations such as AND, OR, NOT, and XOR. This transition from electronic to optical systems is driven by several factors, including the need for higher data transmission speeds, lower power consumption, and the miniaturization of

components. Despite these advantages, optical logic circuits face challenges, including the need for continuous power to maintain operations (volatility), large device footprints due to weak interaction effects, and difficulties in achieving compact designs. Plasmonic logic circuits leverage the strong confinement of electromagnetic fields in plasmonic structures, which enhances light–matter interactions. This strong interaction allows for more efficient modulation and switching, thereby reducing the power required for operation. Additionally, plasmonic circuits excel at confining light to dimensions much smaller than the wavelength of light. The confinement occurs at the nanoscale, which allows plasmonic devices to be significantly smaller than their purely optical counterparts.

Electro-plasmonic logic circuits. Plasmonic logic circuits can be categorized into three main types based on the mechanism of signal control and processing: electro-plasmonic logic circuits, all-optical plasmonic logic circuits, and hybrid plasmonic logic circuits. The fundamental working principle of electro-plasmonic logic circuits revolves around the interaction between electrical signals and surface plasmons, with the latter being the coherent oscillations of free electrons at the interface between a metal and a dielectric. When an electric field is applied, it can modulate the properties of the plasmonic wave, such as its phase, amplitude, or polarization. This modulation is achieved through various mechanisms, including electro-optic effect, carrier injection/depletion, and electrochemical modulation. For instance, phase change materials like $Ge_2Sb_2Te_5$ exhibit significant changes in their optical and electrical properties when transitioning between their amorphous and crystalline states (Fig. 64a).[811] These properties enable the creation of non-volatile, compact, and efficient electro-plasmonic switches that do not require continuous power to maintain their state, addressing one of the main challenges faced by conventional optical logic circuits. The integration of PCMs into electro-plasmonic logic circuits allows for the development of various logic gates and memory elements, which are essential for building more complex computing architectures.

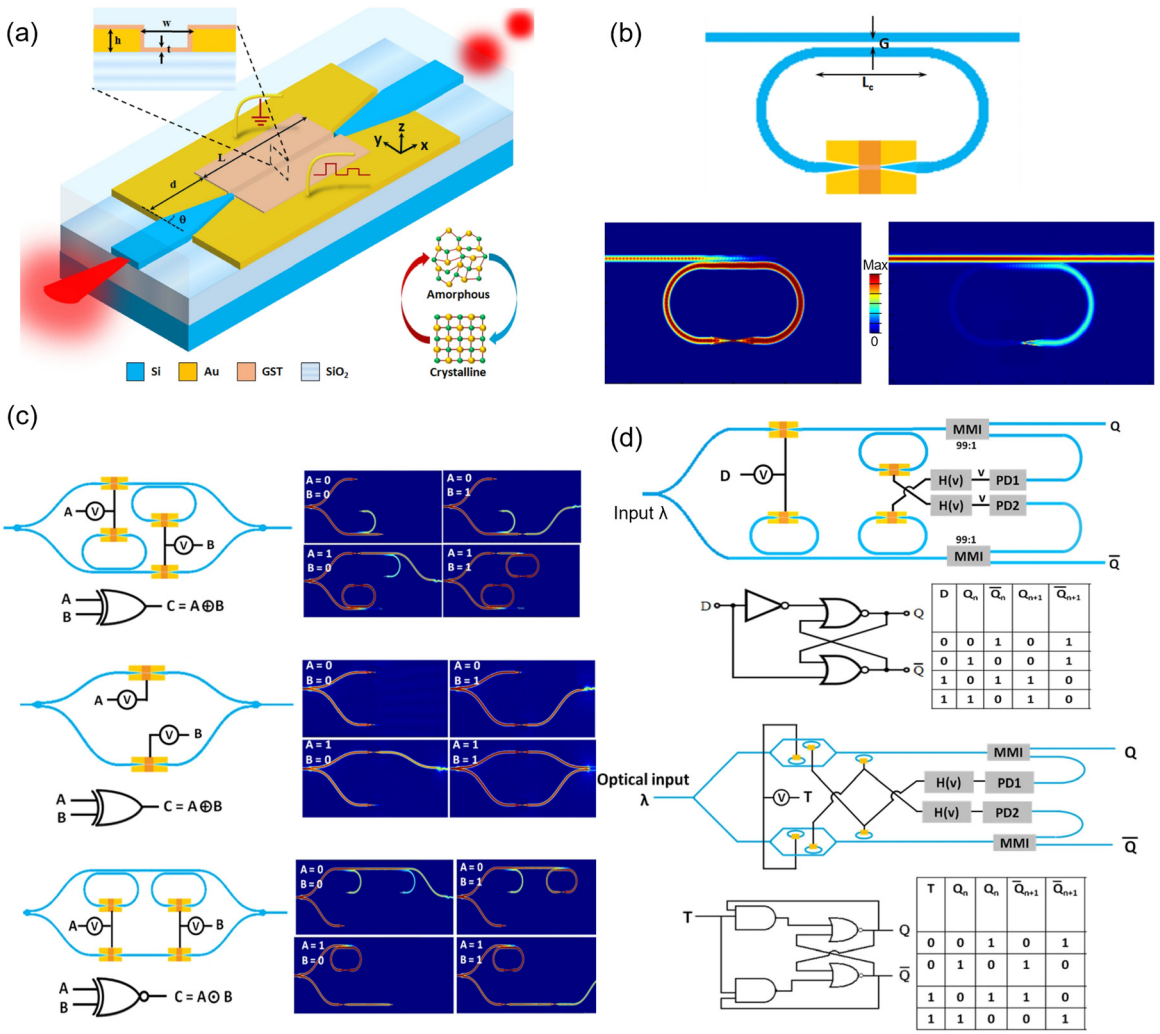

Fig. 64 Integrated electro-plasmonic logic circuits. (a) Schematic of the plasmonic slot waveguide for integrated logic circuits. The amorphous phase and crystalline phase of PCM ($Ge_2Sb_2Te_5$) are used for switching of waveguide modes. (b) Schematic diagram of waveguide mode switching and the corresponding optical electric field distribution. (c) Non-volatile fundamental EO logic operations of AND, OR, NAND, and NOR logic. (d) Sequential logic circuits. Upper panel: JK latch circuit. Lower panel: T latch circuit. Adapted with permission from ref. 811; Copyright 2021 Springer Nature.

The ability to switch the state of a PCM using either electrical or optical signals provides flexibility in circuit design. For example, the electrical threshold switching mechanism can be applied directly to the metal of a plasmonic waveguide, eliminating the need for additional electrodes or external heaters, which contributes to a more compact design (Fig. 64b). Furthermore, the use of electro-plasmonic switches in logic circuits offers the potential for implementing non-volatile sequential logic circuits, such as JK and T latches (Fig. 64c and d), which are critical for PICs.

In addition to PCMs, electro-plasmonic logic circuits also explore other materials that offer unique advantages, such as graphene, transition metal dichalcogenides (TMDs), and transparent conductive oxides (TCOs). In electro-plasmonic circuits, graphene can be used to achieve dynamic modulation of plasmonic signals. By applying a voltage, the carrier density in graphene can be modulated, leading to significant changes in its plasmonic resonance. This property makes graphene a promising candidate for developing ultrafast, tunable plasmonic devices with broad operational bandwidth. Besides, materials such as molybdenum disulfide (MoS_2) and tungsten diselenide (WSe_2) exhibit strong light–matter interactions, making them suitable for use in plasmonic circuits. TCOs, such as indium tin oxide (ITO), can be used to modulate plasmonic waves by applying an electric field, which alters the carrier concentration in the material. This change can modulate the refractive index, enabling the implementation of plasmonic logic functions with minimal optical losses.

All-optical plasmonic logic gates represent a significant advancement in the field of photonic computing, particularly in the context of free-space excitation. Unlike electro-plasmonic logic circuits, which rely on electrical signals to modulate plasmonic waves, all-optical plasmonic logic gates exclusively utilize light for both input and output operations. Plasmons in the device interact with each other to produce interference patterns, which are the basis for logical operations. The key advantages of this approach are the elimination of electrical interconnects, which can introduce delays and consume more power, and the potential for extremely high-speed operation due to the inherently fast nature of light–matter interactions.

All-optical plasmonic logic gates. One notable example of all-optical plasmonic logic gates is the use of interconnected silver nanowires to create a complete family of basic logic functions (Fig. 65a), including AND, OR, and NOT gates.[812] These logic operations are achieved by exploiting the polarization and phase-dependent interference between plasmon beams propagating through the wire network. The ability to cascade these gates is crucial for constructing more complex logic functions, such as the universal NAND and NOR gates, which are essential for implementing any logic operation. In this setup, the cascading of OR and NOT gates within a four-terminal branched silver nanowire network enables the realization of a plasmonic inverse NOR gate. Quantum dot (QD) near-field imaging is employed to trace the plasmon wave packets through the network, demonstrating precise control of optical interferences at the nanoscale.

Organic/metal nanowire heterojunctions. Another innovative approach involves the use of organic/metal nanowire heterojunctions to achieve optical modulation and logic operations. In this method, exciton polaritons in organic nanowires are coupled with surface plasmons in metal nanowires (Fig. 65b), allowing for the modulation of the output signal's intensity.[813] The organic/metal nanowire heterojunctions are selectively grown on the ends of silver nanowires, and by adjusting the polarization direction of the incident laser, the absorption coefficient of the organic nanowire is modulated. This affects the number of exciton polaritons in the organic nanowire, thereby controlling the intensity of the surface plasmons excited at the heterojunction. The scattered plasmon intensity at the output port determines the logic gate's functionality, with different input conditions yielding various Boolean logic operations, such as OR and AND gates, depending on the intensity threshold.

6.4 Plasmonic detectors

In plasmonic PICs, following the generation, routing, and modulation of surface plasmons, the data must be converted from the optical domain into the electrical domain, which is typically achieved *via* a photodetector. Integrated plasmonic detectors offer several advantages over conventional photodetectors, particularly in photonic-plasmonic hybrid circuits. These advantages include higher integration densities, low device capacitance for fast transit times leading to higher bandwidth operations, and reduced operational energy due to enhanced light–matter interactions. As detectors are scaled down in size, the response time improves, but this miniaturization often comes at the cost of reduced sensitivity and responsivity, primarily due to diminished absorption in the detector's semiconductor material. This presents a challenge, as maintaining high sensitivity and responsivity is critical for effective photodetection.

The challenge of reduced absorption in miniaturized detectors can be addressed through the use of emerging active plasmonics. Plasmonic detectors can enhance material absorption through mechanisms similar to the Purcell effect observed in plasmon nanolasers, where spontaneous emission is enhanced. Achieving strong photo-absorption involves increasing the local density of states within the absorbing semiconductor region without introducing unwanted quenching channels.

Impedance matching of photodetection. Plasmon-based photodetection in PICs can be broadly categorized into two scenarios. In the first scenario, optical data arrive in a diffraction-limited waveguide, such as those found in silicon photonics. Here, the challenge lies in impedance-mode-matching the large photonic mode to the much smaller plasmonic mode before it can be absorbed and detected. Various approaches for nanofocusing light into deep subwavelength volumes are being explored to overcome this, including the use of apertures, nanoantennas, and tapered nanometallic waveguides. Nanoantennas, in particular, are effective for light harvesting, while photodiodes or photoelectric conversion materials, such as graphene, convert the harvested light into a photocurrent.[628,636] A representative example of this is the metal antenna–graphene heterostructure (Fig. 66a), where the BPVE is utilized.[634] In this structure, non-centrosymmetric metallic nanoantennas atop graphene flakes act as meta-atoms. By modulating the doping level and Fermi level of graphene through a

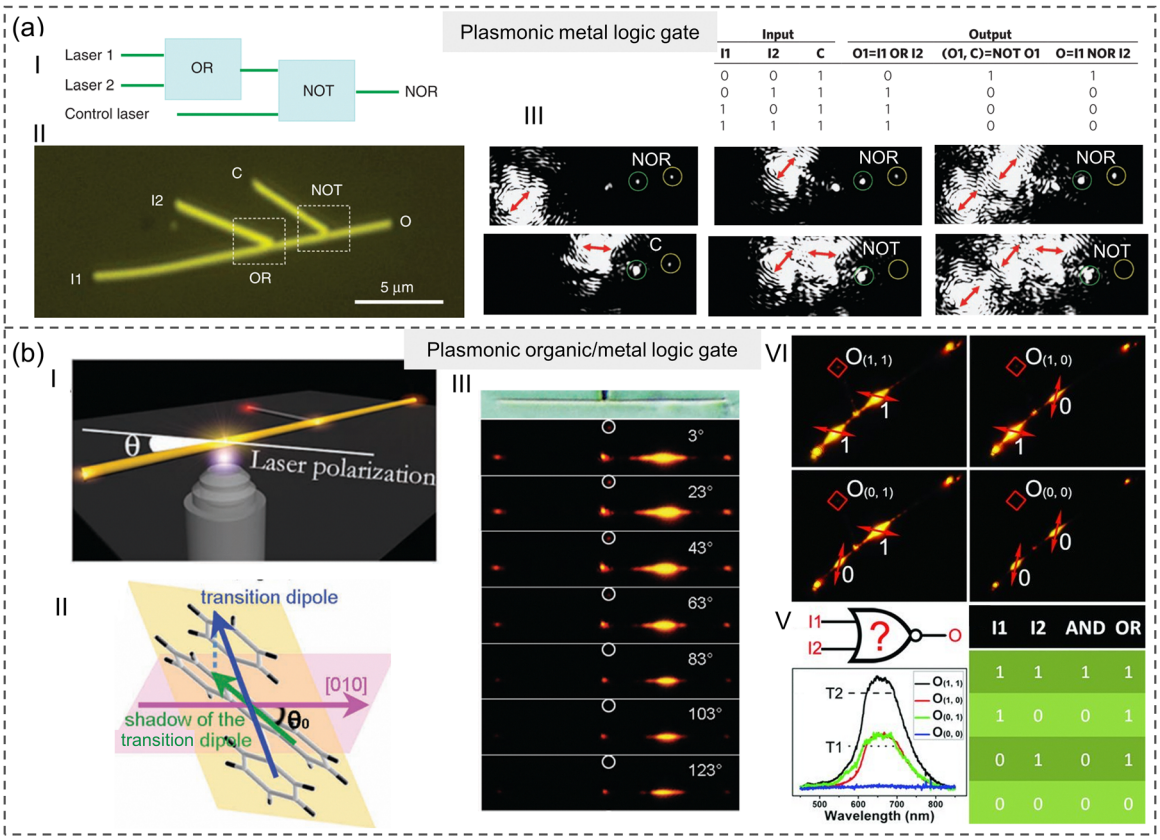

Fig. 65 All-optical plasmonic logic gates in free-space excitation. (a) Plasmonic metal logic gate. (I) Schematic illustration of the logic gate NOR. (II) Optical image of the plasmonic logic gate using the designed Ag NW structure. (III) The scattering images showing the various logic operations. Adapted with permission from ref. 812; Copyright 2011 Springer Nature. (b) Plasmonic organic/metal logic gate. (I) Schematic illustration of the organic nanowire as the logic gate. (II) Spatial relationship between transition dipole moment and preferred growth direction of organic nanowires. (III) Bright-field and photoluminescence microscopy images of the hybrid nanostructure excited at different polarization angles. (VI) Photoluminescence microscopy images of the device for logic processing. (V) Graphical symbol, scattering spectra, and truth table of the logic processing. Adapted with permission from ref. 813; Copyright 2012 John Wiley and Sons.

back gate, researchers can control the shift currents, which are influenced by the plasmonic-enhanced local field. The near-field distribution and photocurrent intensity depend on the polarization and intensity of the incident light. This approach highlights the broader concept of photodetection, where materials respond to light and convert it into electrical signals.

MIM-based photodetection. In the second scenario, the optical data carried by the waveguide mode are of a size comparable to the size of the nanoscale absorber of the detector, eliminating the need for an impedance transformer. One promising solution in this case is the integration of a metal–insulator–metal (MIM) waveguide with a nanoslit metal–semiconductor–metal (MSM) photodetector (Fig. 66b).[814] This type of detector serves both as a contact and as a coupler for plasmons, offering a very fast photoresponse and a high signal-to-noise ratio, making it suitable for high-bandwidth applications. For example, polarization-dependent and spectral measurements have shown that such detectors can achieve $e-1$ decay lengths ranging from 3.5 μm at a wavelength of 660 nm to 9.5 μm at 870 nm. Building on this concept, recent research by Nijhuis and colleagues has demonstrated the use of MIM tunnel junctions (MIM-TJs) coupled to plasmonic waveguides, achieving high-efficiency on-chip plasmon generation, manipulation, and readout (Fig. 66c).[815] These MIM-TJs, fabricated on borosilicate coverslips using UV photolithography, thermal evaporation, and EBL, have shown a plasmon–electron coupling efficiency of approximately 14%. The researchers successfully excited and detected SPPs with a propagation length of 5.2 μm for the SPPs. This study underscores the potential of direct electrical means for efficient on-chip plasmon generation and detection, which is promising for high-frequency optoelectronics and future applications in integrated plasmonic circuits.

Material choices. The choice of materials is crucial for optimizing the performance and efficiency of photodetection. Graphene is known for its high carrier mobility, broadband absorption, and tunable electrical characteristics, which make it particularly suitable for integration with plasmonic devices. Germanium (Ge) is another material that has gained significant attention for photodetection, especially in the telecommunication frequency band. Germanium offers a high absorption coefficient ($\sim 10^4$ cm^{-1}) in the near-infrared range, which is crucial for detecting light at wavelengths commonly used in fiber-optic communications. Its compatibility with silicon technology makes it an ideal candidate for integration into silicon-

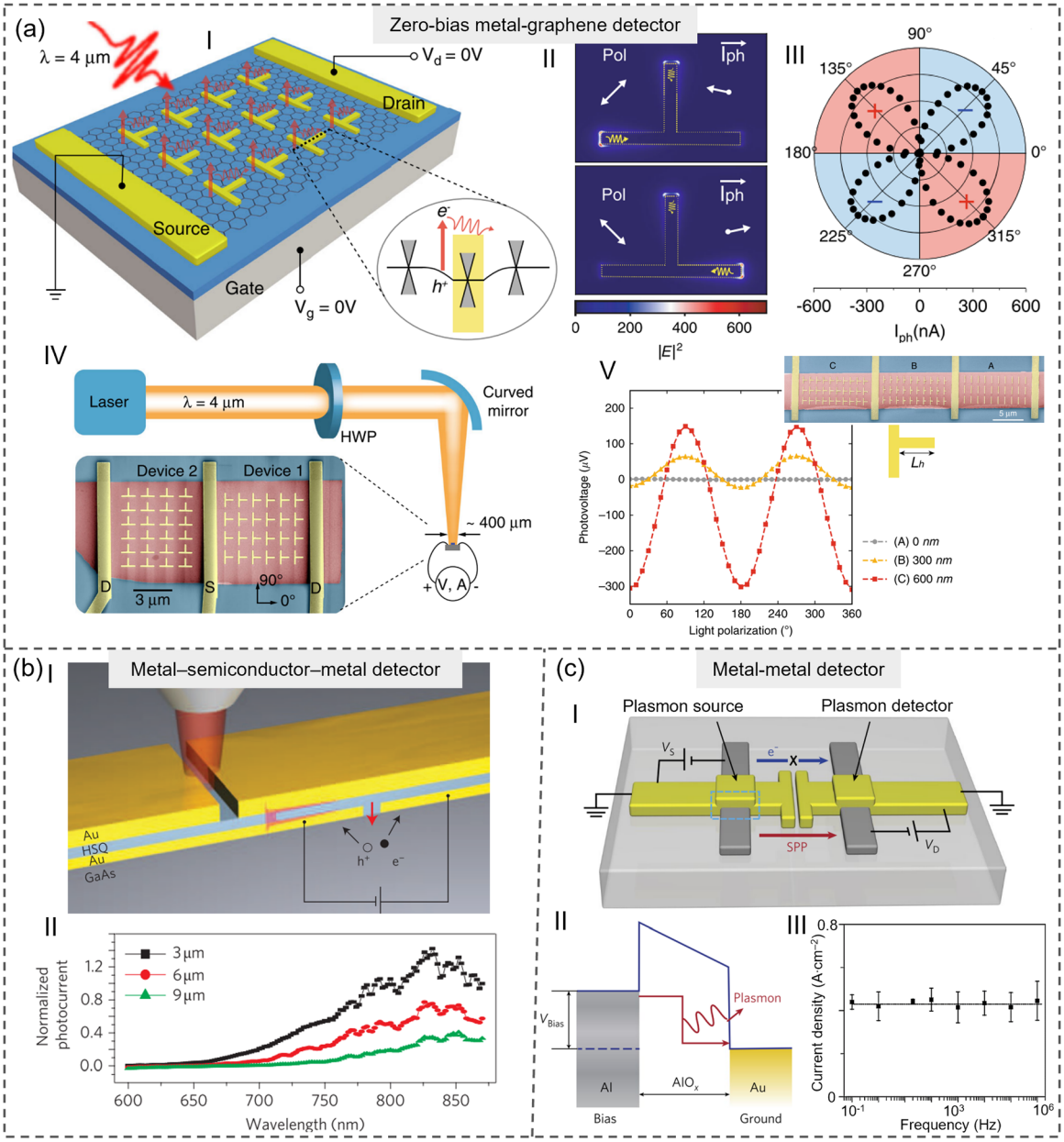

Fig. 66 Plasmonic detectors. (a) Plasmonic zero-bias metal-graphene detector. (I) Schematic illustration of the zero-bias detector. (II) Simulated near-field distribution and predicted vectorial photocurrent in a unit cell at different polarization angles of incident light (Pol). (III) Polar plot of measured photocurrents. (IV) Schematic of the experimental setup. (V) SEM images and measured photovoltage of three devices with different degrees of asymmetry. Adapted with permission from ref. 634; Copyright 2020 Springer Nature. (b) Plasmonic metal–semiconductor–metal detector. (I) Schematic illustration of the metal–semiconductor–metal detector. (II) Spectral responses of the detectors. Adapted with permission from ref. 814; Copyright 2009 Springer Nature. (c) Plasmonic metal–metal detector. (I) Schematic illustration of the metal–metal detector. (II) A simplified energy level diagram of the tunnel junction with bias showing the working mechanism. (III) Response current density of the detector in the frequency domain. Adapted with permission from ref. 815; Copyright 2017 Springer Nature.

based photonic and plasmonic circuits. In addition to graphene and Ge, III–V semiconductors such as gallium arsenide (GaAs) and indium phosphide (InP) are also commonly used in plasmonic detectors. These materials offer strong optical absorption and can be engineered to operate at specific wavelengths, making them versatile for various photonic applications. Their integration with plasmonic structures can lead to enhanced photodetection due to the strong confinement of light within the semiconductor material, which increases the interaction between light and the active region of the detector.

Overall, the development of plasmonic detectors represents a significant advancement in PICs, offering the potential for high-speed, low-power, and highly integrated optical-electrical conversion. These detectors are crucial components in the ongoing evolution of plasmonic circuits, enabling new functionalities and improving the performance of photonic systems.

6.5 Section summary

This section reviews recent advances in integrated electronic circuits leveraging plasmonic properties. It covers plasmonic emitters, modulators/switchers, logic gates, and detectors, and highlights their role in pushing the boundaries of next-generation electronics. Despite these strides, significant challenges remain in PIC applications.

One of the foremost challenges in plasmonic PICs is managing energy attenuation, a persistent issue in both electronic and plasmonic circuits. In electronic circuits, transistors modulate gate voltages and currents to process signals, while in plasmonic circuits, signal processing is reliant on the propagation of light intensity and polarization. This shift in paradigm requires the integration of repeaters and switches, with quantum dots serving as signal amplification materials. By directing excitation light onto waveguides, these repeaters can amplify signals while maintaining their original characteristics. However, the energy consumption within these integrated circuits primarily arises from scattering at junctions, thermal losses, and amplification materials for the light source. While heating losses are inevitable, they are relatively minor compared to scattering losses at junctions. Implementing total internal reflection dielectric covers at these junctions can significantly reduce energy waste. Despite these challenges, the overall energy consumption of plasmonic chips is anticipated to be considerably lower than that of electronic chips, as all operations are based on the propagation and interference of plasmons rather than electrical currents.

Another significant challenge is the fabrication of the various components on a single platform. PICs involve multiple elements, including plasmonic emitters, modulators, logic gates, switchers, and detectors, each with its own set of fabrication requirements. Achieving high levels of integration while ensuring compatibility between these diverse elements is a complex task. The fabrication process must address issues such as material compatibility, precision alignment, and minimizing losses at interfaces between different components. Additionally, the scale at which these components must be manufactured adds another layer of complexity, as even minor imperfections can lead to significant performance degradation. Overcoming these challenges is crucial for the development of fully integrated plasmonic PICs that can meet the demands of modern optical communication systems.

Heat management and loss reduction are also critical challenges in plasmonic PICs. As plasmonic circuits operate at the nanoscale, they are prone to significant heat generation, especially at junctions where scattering and material imperfections can lead to increased losses. Managing this heat is vital for maintaining the stability and performance of the circuits. Advanced materials and design techniques, such as incorporating thermal conductive layers or using materials with lower scattering losses, are being explored to mitigate these issues. However, striking a balance between reducing heat generation and maintaining efficient signal propagation remains a delicate challenge.

7. Conclusions and future perspectives

7.1 Conclusions

In summary, we present a detailed and comprehensive review of integrative plasmonics—from underlying mechanisms to device applications. It begins by exploring various optical phenomena in plasmonics, such as plasmon–phonon coupling, nonlinear optical effects, EIT, plasmonic chirality, nanocavity resonance, and waveguide resonance. The discussion then extends to advanced strategies for enhancing plasmonic responses beyond traditional single-effect phenomena. These include designing hybrid nanostructures to confine light at subwavelength scales and boost near-field interactions. Utilizing 2D materials such as graphene for dynamic tuning promotes stronger field enhancements and nonlinear processes. Then, we emphasize the synergy between plasmonic effects and other domains including acoustics, electronics, and thermal technologies. For example, plasmon-induced local heating can trigger thermoacoustic effects that generate ultrasound for high-contrast imaging or even for therapeutic interventions like tumor ablation. Collectively, these fusion strategies are paving the way for multifunctional platforms capable of simultaneous imaging, sensing, and treatment, thereby broadening applications in molecular diagnostics, energy conversion, and PICs.

Based on these discussions, several key advantages of plasmonic optical multi-effects and electric-acoustic-thermal fusion emerge.

(1) Enhanced device performance: multi-effects, such as those derived from plasmon–phonon coupling, significantly improve the overlapping of molecular fingerprint spectra in infrared spectroscopy.[47] Besides, they lead to increased sensitivity and lower detection limits in molecular diagnostics, higher conversion efficiency in energy harvesting, reduced energy consumption and extended transmission distances in photonic circuits, and more.

(2) Enabling new functionalities: integrative plasmonics allows for the realization of new functionalities that are challenging to achieve with single-field technologies. For instance, the fusion of plasmonic and BPVE facilitates zero-bias photodetection,[634] a capability that traditional approaches struggle to deliver.

(3) Expanded application range: by combining plasmonic effects with acoustic, photoelectric, and thermal technologies, integrative plasmonics enables the simultaneous execution of multiple functions, such as imaging, diagnosis, and treatment, within a single platform.[209] This multifunctionality is particularly valuable in medical diagnostics and therapy, where integrated approaches can lead to more comprehensive and effective solutions.

7.2 Challenges

While the works highlighted in this review offer promising solutions for integrative plasmonics, the field remains in its early stages due to the complexity of multiple mechanisms and interdisciplinary approaches. Currently, integrative plasmonics still faces challenges. Below are some personal insights into these challenges. It is important to note that listing these challenges is intended to foster timely discussion and progress

in the field, rather than to diminish the efforts of many colleagues or the significant advances already made.

(1) Challenges in integrating optical multi-effects on the same platform. Designing multi-functional nanostructures in plasmonics is challenging, as it requires integrating multiple optical effects while optimizing different plasmonic modes with varying spatial, spectral, and material requirements. Effect synergy and optimization pose additional difficulties, as different plasmonic effects, such as SERS, SEF, and LSPR, often have conflicting design requirements and resonant conditions, making their integration complex. Balancing the spatial distribution of localized electromagnetic fields is another critical challenge, as different effects require specific field configurations, demanding precise control over nanostructure geometry, size, and material composition to ensure optimal performance.

(2) Challenges in fusing acousto-optical-electric-thermal effects *via* plasmons. Integrating optical, electric, acoustic, and thermal mechanisms in plasmonics is challenging due to their distinct operational principles and requirements. A major difficulty lies in designing plasmonic systems that effectively combine these diverse effects while maintaining high performance. The lack of a comprehensive theoretical framework further complicates integration, as existing models are specialized and do not fully describe cross-domain interactions. Additionally, finding materials that perform well across all domains is difficult, as most are optimized for only one or two effects. Hybrid or composite materials offer a potential solution but require careful design to achieve balanced multifunctionality.

(3) Challenges in molecular diagnostics applications based on integrative plasmonics. A primary challenge in plasmonic biosensing is achieving high sensitivity across various techniques, such as SERS and SEIRAS, by optimizing hotspot enhancement. This requires developing materials and structures that amplify weak signals from low-concentration analytes while maintaining high sensitivity across different spectral regions. Ensuring selectivity in complex biological environments is another challenge, as background interference can compromise molecular specificity. Reproducibility is also critical, with variability in substrate manufacturing and environmental conditions affecting consistent performance. Stability of plasmonic substrates under fluctuating experimental conditions is essential for reliable long-term applications, especially in clinical diagnostics. Finally, cost-effectiveness remains a significant challenge, particularly in point-of-care testing, where affordable, scalable manufacturing is needed for widespread implementation.

(4) Challenges in energy conversion applications. Firstly, multifunctional and highly efficient integrated energy harvesters are capable of capturing energy from a variety of sources, but their design and optimization require further in-depth exploration to enable their application in a broader range of operational scenarios. Additionally, in the material design and engineering of plasmon-enhanced energy conversion, achieving effective utilization of the entire solar spectrum and exerting control over broadband energy capture remain a complex endeavor. Furthermore, achieving a balance between miniaturization and performance, as well as reliability, in plasmonic energy harvesters remains a pivotal challenge.

(5) Challenges in plasmonic PICs. Plasmonic PICs face challenges in managing energy attenuation, primarily due to scattering losses at junctions and thermal dissipation. Implementing repeaters with quantum dots and total internal reflection dielectric covers can help mitigate these losses. Fabrication complexity is another issue, as integrating diverse components like emitters, modulators, and detectors requires precise alignment and material compatibility. Heat management is also critical, as nanoscale plasmonic circuits generate significant thermal losses, necessitating advanced materials and design strategies to balance efficiency and stability.

7.3 Future perspectives

Looking forward to the future development of integrative plasmonics, efforts can be invested along the current development path to solve the above challenges. Additionally, based on the advances made in integrative plasmonics, some personal insights are proposed to propel the discipline toward sustained, high-quality progress in mechanism advancements, material innovations, technological breakthroughs, and application expansion, as illustrated in Fig. 67.

7.3.1 Innovative mechanisms. (1) Quantum plasmonics integration: as integrative plasmonics continues to evolve, one promising avenue is the incorporation of quantum mechanics into plasmonic systems.[816,817] Quantum plasmonics explores the interaction of plasmons with quantum states of light, such as single photons, quantum entanglement, and squeezed states. By leveraging quantum effects, integrative plasmonics can transcend classical limitations, enabling the development of ultrafast, low-power photonic devices with enhanced sensitivity.[818] This can be particularly impactful in quantum sensing and quantum communication, where the ability to manipulate and detect individual quanta is crucial. The integration of quantum effects with traditional plasmonic phenomena, such as LSPR, could lead to the discovery of new quantum-assisted mechanisms that enhance the efficiency and functionality of plasmonic devices. For example, quantum plasmonic circuits could revolutionize fields like quantum computing and quantum cryptography,[819] offering new paradigms for information processing and security.

(2) Spintronics and plasmonics: spintronics, which exploits the spin of electrons in addition to their charge, offers new possibilities for manipulating light–matter interactions in plasmonic systems. The integration of spintronic principles with plasmonics, often referred to as spin-plasmonics, has the potential to create devices that utilize the spin degree of freedom to control plasmonic excitations. This can lead to novel applications in information processing, where the combination of spintronics and plasmonics could enable the development of spin-based plasmonic transistors, spin filters, and logic gates. Recent research has shown that materials such as ferromagnetic metals and topological insulators can be used to control plasmonic modes *via* spin–orbit coupling, making spin-plasmonics a promising area for future exploration.[820]

(3) Topological plasmonics: topological photonics, which draws on concepts from topological insulators, explores the robust propagation of light along the edges of photonic

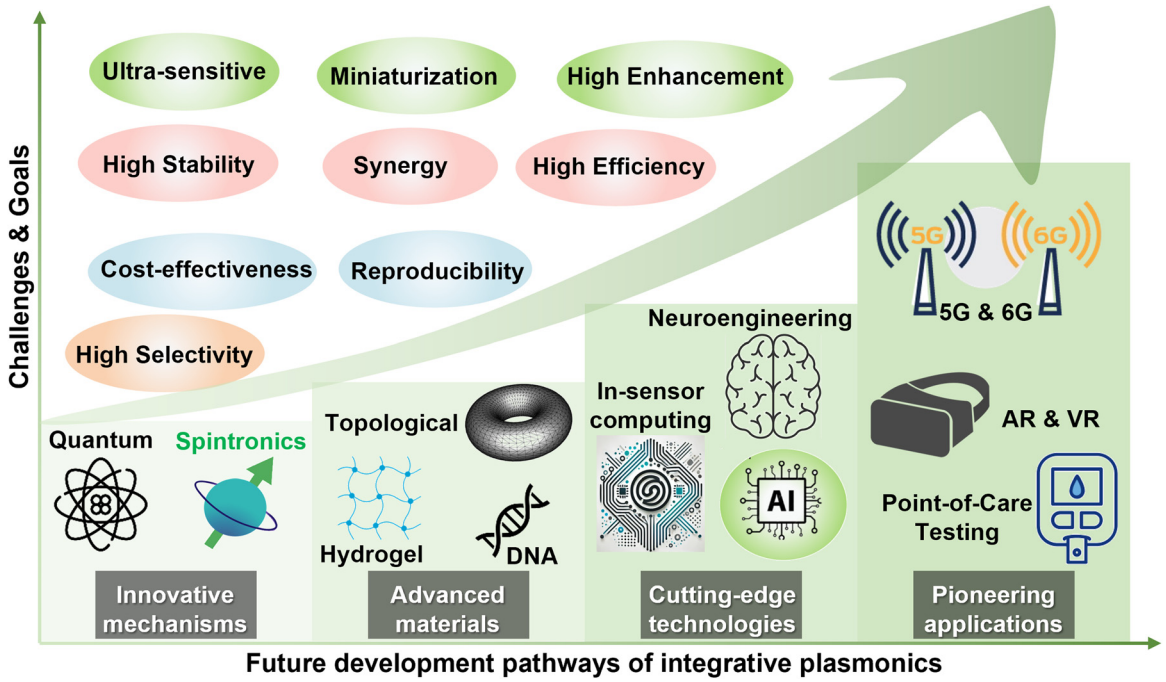

Fig. 67 Challenges, goals, and future development pathways of integrative plasmonics.

structures without backscattering.[821] When combined with plasmonics, topological plasmonics can enable the creation of plasmonic modes that are immune to defects and disorders, thus offering new routes for robust and energy-efficient photonic devices. Early research in this area has demonstrated the existence of topologically protected plasmonic edge states in certain photonic crystals and metamaterials.[822] These edge states could be utilized in applications such as robust plasmonic waveguides, sensors, and on-chip communication devices, where immunity to scattering and losses is crucial.

7.3.2 Advanced materials. (1) Topological insulators and Dirac semimetals: topological insulators (TIs) and Dirac semimetals are materials that exhibit unique electronic surface states, which are protected by time-reversal symmetry. These materials have recently attracted attention for their potential in plasmonics due to their ability to support low-loss plasmonic modes. The surface states in TIs, such as Bi_2Se_3 and Bi_2Te_3, can support spin-polarized surface plasmons that are robust against backscattering.[823] Similarly, Dirac semimetals like Cd_3As_2 and Na_3Bi exhibit linear energy dispersion and can support long-lived bulk plasmon modes.[824] The integration of these materials with conventional plasmonic structures could lead to the development of novel plasmonic devices with enhanced performance and robustness, particularly in applications requiring high efficiency and low loss, such as on-chip photonic circuits and quantum plasmonics.

(2) Biomolecule-based plasmonic nanocomposites: plasmonic materials combined with biological molecules, such as DNA, represent a cutting-edge area of research with tremendous potential, particularly in biosensing, nanomedicine, and molecular electronics.[825] These hybrid materials leverage the unique properties of both plasmonic nanoparticles and biological macromolecules, offering new functionalities that are not possible with traditional materials. Below are some of the most promising avenues for this kind of material: (I) DNA-directed assembly of plasmonic nanostructures: DNA's ability to specifically bind to complementary sequences makes it an excellent tool for directing the assembly of plasmonic nanoparticles into well-defined structures.[826] This DNA-mediated assembly allows for the precise control of nanoparticle spacing and orientation, which is crucial for tuning the plasmonic properties of the resulting nanostructures. For example, DNA can be used to create dimers, trimers, or even larger assemblies of gold or silver nanoparticles, leading to plasmonic "hot spots" where electromagnetic fields are highly concentrated.[827] These hot spots are particularly valuable in SERS and other plasmonic sensing applications, where the sensitivity of detection is greatly enhanced. (II) DNA origami and plasmonic nanostructures: DNA origami involves folding a long single-stranded DNA molecule into complex shapes with the help of short "staple" strands.[828] This method allows for the creation of nanoscale structures with precise geometries. When combined with plasmonic nanoparticles, DNA origami can be used to position these nanoparticles with nanometer precision, creating custom-designed plasmonic structures with tailored optical properties. (III) Plasmonic nanoswitches based on DNA conformation changes: DNA molecules can undergo significant conformational changes in response to various stimuli, such as changes in ionic strength, temperature, or the binding of specific ligands.[829] These conformational changes can be exploited to create plasmonic nanoswitches, where the optical properties of plasmonic nanoparticles are modulated by the state of the attached DNA molecules.

(3) Plasmon–hydrogel hybrids: plasmonic materials combined with hydrogels represent an exciting and rapidly

developing area of research.[830] The combination of these two materials results in a versatile platform with a wide range of potential applications, particularly in biosensing, drug delivery, and smart materials. Below are some of the most promising avenues for this kind of material: (I) stimuli-responsive plasmonic hydrogels: hydrogels can respond to various external stimuli, such as pH, temperature, light, and the presence of specific chemicals or biomolecules.[831] When plasmonic nanoparticles (*e.g.*, gold or silver nanoparticles) are embedded within a hydrogel matrix, the hybrid material can exhibit significant changes in its optical properties in response to these stimuli. This change is primarily due to the alteration of the interparticle distance within the hydrogel, which affects the plasmonic coupling between the nanoparticles. (II) Plasmonic hydrogels for controlled drug delivery: one of the most promising applications of plasmon–hydrogel hybrids is in controlled drug delivery.[832] The hydrogel matrix can encapsulate drugs, while the plasmonic nanoparticles enable remote control over the release of these drugs through light-induced heating. When exposed to specific wavelengths of light, the plasmonic nanoparticles generate localized heat (*via* the photothermal effect), which can induce the hydrogel to undergo a phase transition (*e.g.*, from a swollen to a collapsed state), releasing the encapsulated drugs in a controlled manner. (III) Optomechanical actuators: plasmon–hydrogel composites can also be used to create optomechanical actuators.[833] These are devices that convert optical energy into mechanical motion. When plasmonic nanoparticles embedded in a hydrogel absorb light, the localized heating can cause the hydrogel to swell or shrink, resulting in mechanical movement. This optomechanical response can be finely tuned by adjusting the composition of the hydrogel and the size, shape, and concentration of the plasmonic nanoparticles.

7.3.3 Cutting-edge technologies. (1) Machine learning and artificial intelligence: artificial intelligence methods dominated by machine learning have been widely used in fields such as science, materials, and engineering.[834–838] The fusion of integrative plasmonics with ML and AI represents a transformative approach to optimizing plasmonic systems. ML algorithms can be employed to design and predict the behavior of plasmonic structures, identifying optimal configurations that maximize performance for specific applications. For example, AI-driven design tools can rapidly explore the vast parameter space of plasmonic nanostructures, accelerating the discovery of new materials and configurations that enhance multi-effect plasmonic responses.[447] Furthermore, AI can aid in the real-time processing of data from plasmonic sensors, enabling more accurate and rapid detection of biological and chemical analytes.[485] In addition to AI-assisted design and data processing, a critical and transformative aspect of integrating AI with plasmonics lies in the AI-driven decision-making process. This step involves utilizing AI algorithms to make informed and adaptive decisions based on the processed data, enabling plasmonic systems to respond dynamically to changing conditions or specific tasks.[839] Additionally, the synergy between AI and integrative plasmonics can also extend to adaptive photonic circuits, where AI algorithms dynamically adjust circuit parameters to optimize performance, thus paving the way for smart photonic systems with self-learning capabilities.

(2) Edge computing and in-sensor computing: edge computing involves processing data closer to the data source, minimizing latency and reducing the need for data to be sent to centralized servers. Plasmonic sensors can be integrated into edge computing systems to provide real-time, on-site data processing with high sensitivity and specificity. The strong LSPR of plasmonic nanostructures enables the detection of minute changes in the local environment, making them ideal for applications where rapid and precise measurements are critical.[840] In-sensor computing takes the concept of edge computing further by embedding computational capabilities directly within the sensor itself. This approach allows for the immediate processing of data at the point of capture, reducing the need for data transmission and enabling even faster decision-making.[841] Key advantages include reduced latency, high energy efficiency, reduced data bottlenecks, and autonomous decision-making.

(3) Integrating plasmonics with optogenetics and neuroengineering: optogenetics traditionally uses light to control neurons and other cells that have been genetically modified to express light-sensitive ion channels. By combining plasmonic nanostructures with optogenetic tools, researchers can enhance the spatial and temporal resolution of light delivery, as well as introduce new functionalities that were previously unattainable. For instance, in the absence of NIR-activated opsins, upconversion nanoparticles can be used as light-emitting transducers for nanoparticle-mediated optogenetics.[842] In neuroengineering, plasmonics can improve neural interface performance.[843] By using plasmonic nanoparticles to enhance the delivery and localization of light, more precise control of neuronal activity can be achieved. This enhanced precision is crucial for mapping neural circuits and understanding brain function. Moreover, plasmonic nanoparticles can generate localized heat through thermoplasmonic effects, which can be used to modulate neural activity in a controlled manner. For example, AuNRs can be used to activate temperature-sensitive ion channels in neurons, allowing for precise neuromodulation using NIR light.[844] This approach reduces the need for invasive procedures, as NIR light can penetrate deeper into tissues compared to visible light.

7.3.4 Pioneering applications. (1) 5G and 6G Telecommunications: the transition from 5G to 6G in telecommunications demands significant advancements in data transmission rates, latency reduction, and reliability enhancement.[845] Plasmonics, with its unique ability to confine and manipulate light at subwavelength scales, offers a promising solution to overcome these challenges. Plasmonic devices, such as plasmonic modulators and waveguides, can operate at terahertz frequencies, providing the ultra-fast signal processing required for 6G networks.[846] Additionally, the compact size and high-speed capabilities of plasmonic components make them ideal for integration into photonic circuits, which are essential for next-generation telecommunications infrastructure. The future potential of plasmonics in 6G lies in its ability to enable higher data density and faster data transfer rates, thus supporting the massive connectivity and enhanced mobile broadband needed for 6G applications.

(2) Augmented reality (AR) and virtual reality (VR): the demand for more immersive AR and VR experiences is driving the need for advanced optical components that can deliver high-resolution, real-time visual processing.[847–849] Plasmonics can significantly enhance AR/VR technologies by enabling the development of miniaturized, high-performance optical devices such as lenses, waveguides, and holographic displays.[850] Plasmonic metasurfaces, for example, can manipulate light with sub-wavelength precision, enabling the creation of ultra-thin, flat optical elements that can be seamlessly integrated into AR glasses or VR headsets.[851] These plasmonic components can improve image quality, reduce latency, and enhance the overall user experience by providing faster and more accurate visual processing.

(3) Point-of-care testing (POCT): POCT represents a paradigm shift in medical diagnostics by enabling rapid, on-site testing at the patient's location, such as in a doctor's office, clinic, or even at home.[852,853] The incorporation of plasmonic technologies into POCT platforms offers several advantages. Plasmonic-based POCT devices can provide real-time results with high accuracy and sensitivity, which are crucial for the timely diagnosis and management of diseases. These devices can be miniaturized and designed for ease of use, allowing non-specialists to perform complex diagnostic tests quickly and accurately. For instance, plasmonic-enhanced lateral flow assays, which are widely used in POCT, can offer improved sensitivity for detecting biomarkers related to infectious diseases, cancer, and cardiovascular conditions.[88]

Data availability

No primary research results, software or code have been included and no new data were generated or analysed as part of this review.

Conflicts of interest

There are no conflicts to declare.

Acknowledgements

This work was supported by the Ministry of Education (MOE) of the Singapore under the research grant R-263-000-F18-112/A-0009520-01-00; Manufacturing, Trade, and Connectivity (MTC) Industry Alignment Fund – Pre-Positioning (IAF-PP) program (Grant No. M23M5a0069), A-8002184-00-00; Manufacturing, Trade, and Connectivity (MTC) White Space Fund (Grant No. M24W1NS005), A-8002323-00-00; and National Research Foundation (NRF) under the Mid-sized grant project (Grant No. NRF-MSG-2023-0002).

References

1 R. W. Wood, *London, Edinburgh Dublin Philos. Mag. J. Sci.*, 2009, **4**, 396–402.
2 J. C. Maxwell-Garnett, *Philos. Trans. R. Soc., A*, 1904, **203**, 385–420.
3 M. Fleischmann, P. J. Hendra and A. J. McQuillan, *Chem. Phys. Lett.*, 1974, **26**, 163–166.
4 A. Hartstein, J. R. Kirtley and J. C. Tsang, *Phys. Rev. Lett.*, 1980, **45**, 201–204.
5 M. Moradi, M. Jäger, G. R. Newkome and U. S. Schubert, *J. Mater. Chem. C*, 2023, **11**, 1610–1647.
6 J. Xie, Z. Ren, H. Zhou, J. Zhou, W. Liu and C. Lee, *Adv. Opt. Mater.*, 2024, 2401582.
7 J. S. Lin, X. D. Tian, G. Li, F. L. Zhang, Y. Wang and J. F. Li, *Chem. Soc. Rev.*, 2022, **51**, 9445–9468.
8 Y. Kitajima, H. Sakamoto and K. Ueno, *Nanoscale*, 2021, **13**, 5187–5201.
9 A. V. Kabashin, V. G. Kravets and A. N. Grigorenko, *Chem. Soc. Rev.*, 2023, **52**, 6554–6585.
10 D. You, R. Wang, J. Xie, L. Liu, K. Li, X. Han, T. Guo and C. Xu, *J. Mater. Chem. A*, 2022, **10**, 14078–14089.
11 P. Pienpinijtham, Y. Kitahama and Y. Ozaki, *Nanoscale*, 2022, **14**, 5265–5288.
12 S.-L. Peng, G.-Y. Chen and S.-W. Hsu, *J. Mater. Chem. C*, 2022, **10**, 16573–16582.
13 R. F. Oulton, V. J. Sorger, D. A. Genov, D. F. P. Pile and X. Zhang, *Nat. Photonics*, 2008, **2**, 496–500.
14 J. Wei, C. Xu, B. Dong, C.-W. Qiu and C. Lee, *Nat. Photonics*, 2021, **15**, 614–621.
15 T. Yan, M. Su, Z. Wang and J. Zhang, *Small*, 2023, **19**, e2300539.
16 Y.-K. Liao, Y.-S. Lai, F. Pan and Y.-H. Su, *J. Mater. Chem. A*, 2023, **11**, 11187–11201.
17 W. Jiang, D. Sun, C. Cai and H. Zhang, *Analyst*, 2023, **148**, 3791–3797.
18 N. Hildebrandt, M. Lim, N. Kim, D. Y. Choi and J. M. Nam, *Chem. Commun.*, 2023, **59**, 2352–2380.
19 J. Dey, A. Virdi and M. Chandra, *Nanoscale*, 2023, **15**, 17879–17888.
20 X. Zhuo, S. Li, N. Li, X. Cheng, Y. Lai and J. Wang, *Nanoscale*, 2022, **14**, 8362–8373.
21 B. Zhang, T. Kong, C. Zhang, X. Mi, H. Chen, X. Guo, X. Zhou, M. Ji, Z. Fu, Z. Zhang and H. Zheng, *Nanoscale*, 2022, **14**, 16314–16320.
22 F. O. Yevtushenko, S. V. Dukhopelnykov, Y. G. Rapoport, T. L. Zinenko and A. I. Nosich, *RSC Adv.*, 2022, **12**, 4589–4594.
23 M. Wang, Y. Yu, S. Prucnal, Y. Berencen, M. S. Shaikh, L. Rebohle, M. B. Khan, V. Zviagin, R. Hubner, A. Pashkin, A. Erbe, Y. M. Georgiev, M. Grundmann, M. Helm, R. Kirchner and S. Zhou, *Nanoscale*, 2022, **14**, 2826–2836.
24 M. Wagner, A. Seifert and L. M. Liz-Marzan, *Nanoscale Horiz.*, 2022, **7**, 1259–1278.
25 F. Pan, C. C. Wu, Y. L. Chen, P. Y. Kung and Y. H. Su, *Nanoscale*, 2022, **14**, 13532–13541.
26 A. Lishchuk, E. Csanyi, B. Darroch, C. Wilson, A. Nabok and G. J. Leggett, *Chem. Sci.*, 2022, **13**, 2405–2417.
27 C. W. Moon, M. J. Choi, J. K. Hyun and H. W. Jang, *Nanoscale Adv.*, 2021, **3**, 5981–6006.
28 F. M. Balci, S. Sarisozen, N. Polat, C. M. Guvenc, U. Karadeniz, A. Tertemiz and S. Balci, *Nanoscale Adv.*, 2021, **3**, 1674–1681.
29 C. Clavero, *Nat. Photonics*, 2014, **8**, 95–103.
30 A. D. Semenov, G. N. Goltsman and R. Sobolewski, *Supercond. Sci. Technol.*, 2002, **15**, R1–R16.

31 T. P. White and K. R. Catchpole, *Appl. Phys. Lett.*, 2012, **101**, 073905.
32 M. Kumar, J. Dey, M. S. Verma and M. Chandra, *Nanoscale*, 2020, **12**, 11612–11618.
33 J. A. Jackman, A. Rahim Ferhan and N. J. Cho, *Chem. Soc. Rev.*, 2017, **46**, 3615–3660.
34 L. Wang and G. Arrabito, *Analyst*, 2015, **140**, 5821–5848.
35 A. Campion and P. Kambhampati, *Chem. Soc. Rev.*, 1998, **27**, 241–250.
36 J. F. Li, C. Y. Li and R. F. Aroca, *Chem. Soc. Rev.*, 2017, **46**, 3962–3979.
37 L. J. Sherry, S. H. Chang, G. C. Schatz, R. P. Van Duyne, B. J. Wiley and Y. N. Xia, *Nano Lett.*, 2005, **5**, 2034–2038.
38 K. Ataka and J. Heberle, *Anal. Bioanal. Chem.*, 2007, **388**, 47–54.
39 S. Y. Zhang, C. L. Wong, S. W. Zeng, R. Z. Bi, K. Tai, K. Dholakia and M. Olivo, *Nanophotonics*, 2021, **10**, 259–293.
40 P. A. D. Goncalves and F. J. Garcia de Abajo, *Nanoscale*, 2023, **15**, 11852–11859.
41 D. Yoo, F. de León-Pérez, M. Pelton, I.-H. Lee, D. A. Mohr, M. B. Raschke, J. D. Caldwell, L. Martín-Moreno and S.-H. Oh, *Nat. Photonics*, 2020, **15**, 125–130.
42 A. Frisk Kockum, A. Miranowicz, S. De Liberato, S. Savasta and F. Nori, *Nat. Rev. Phys.*, 2019, **1**, 19–40.
43 E. Yoxall, M. Schnell, A. Y. Nikitin, O. Txoperena, A. Woessner, M. B. Lundeberg, F. Casanova, L. E. Hueso, F. H. L. Koppens and R. Hillenbrand, *Nat. Photonics*, 2015, **9**, 674–678.
44 H. Chang, Z. Li, W. Lou, Q. Yao, J. M. Lai, B. Liu, H. Ni, Z. Niu, K. Chang and J. Zhang, *Nanoscale*, 2022, **14**, 13046–13052.
45 J. D. Caldwell, L. Lindsay, V. Giannini, I. Vurgaftman, T. L. Reinecke, S. A. Maier and O. J. Glembocki, *Nanophotonics*, 2015, **4**, 44–68.
46 H. Zhou, D. Li, Z. Ren, C. Xu, L.-F. Wang and C. Lee, *Sci. Adv.*, 2024, **10**, eado3179.
47 H. Zhou, Z. Ren, D. Li, C. Xu, X. Mu and C. Lee, *Nat. Commun.*, 2023, **14**, 7316.
48 B. A. Sanborn, *Phys. Rev. B:Condens. Matter Mater. Phys.*, 1995, **51**, 14256–14264.
49 M. Janipour, I. B. Misirlioglu and K. Sendur, *Sci. Rep.*, 2016, **6**, 34071.
50 J. Cunha, T. L. Guo, G. Della Valle, A. N. Koya, R. Proietti Zaccaria and A. Alabastri, *Adv. Opt. Mater.*, 2020, **8**, 2001225.
51 J. Huang, F. Deng, F. Ye, H. Y. Fu, S. Zhang and Q. Li, *Carbon*, 2023, **213**, 118210.
52 S. Y. Li, Z. Tang, D. D. Zhu and H. F. Zhang, *Phys. Chem. Chem. Phys.*, 2023, **25**, 19666–19683.
53 R. Adato, A. Artar, S. Erramilli and H. Altug, *Nano Lett.*, 2013, **13**, 2584–2591.
54 H. Zhou, D. Li, Z. Ren, X. Mu and C. Lee, *InfoMat*, 2022, **4**, e12349.
55 G. Sun, S. Peng, X. Zhang and Y. Zhu, *Nanomaterials*, 2020, **10**, 1064.
56 M. Yang, L. Liang, Z. Zhang, Y. Xin, D. Wei, X. Song, H. Zhang, Y. Lu, M. Wang, M. Zhang, T. Wang and J. Yao, *Opt. Express*, 2019, **27**, 19520–19529.
57 F. Lopez-Rayon, M. L. Arroyo Carrasco, R. I. Rodriguez-Beltran, R. Salas-Montiel and R. Tellez-Limon, *Nanomaterials*, 2022, **12**, 1701.
58 J. H. Mokkath, *Phys. Chem. Chem. Phys.*, 2024, **26**, 14796–14807.
59 C. Guo, S. Xia, Y. Tian, F. Li, G. Xu, F. Wu and W. Niu, *Phys. Chem. Chem. Phys.*, 2024, **26**, 5773–5777.
60 S. K. Pal, D. Bardhan, D. Sen, H. Chatterjee and S. K. Ghosh, *Nanoscale Adv.*, 2023, **5**, 1943–1955.
61 R. S. Nithyananda Kumar, M. Eerdekens, Y. de Coene, V. S. Nagaraja, S. Ahadzadeh, M. Van Landeghem, T. Verbiest and W. Deferme, *Nanoscale Adv.*, 2023, **5**, 1750–1759.
62 W. Peng, J. W. Zhou, M. L. Li, L. Sun, Y. J. Zhang and J. F. Li, *Chem. Sci.*, 2024, **15**, 2697–2711.
63 Y. Huang, L. Ma, M. Hou, J. Li, Z. Xie and Z. Zhang, *Sci. Rep.*, 2016, **6**, 30011.
64 X. Luo, W. Yue, S. Zhang, H. Liu, Z. Chen, L. Qiao, C. Wu, P. Li and Y. He, *Lab Chip*, 2023, **23**, 388–399.
65 K. A. Dahan, Y. Li, J. Xu and C. Kan, *Phys. Chem. Chem. Phys.*, 2023, **25**, 18545–18576.
66 H. Zhang, H. Chen, T. Zhang, X. Mi, Z. Jiang, Z. Zhou, L. Guo, M. Zhang, Z. Zhang, N. Liu and H. Xu, *Nanoscale Adv.*, 2022, **4**, 1145–1150.
67 Q. Wang, L. Hou, C. Li, H. Zhou, X. Gan, K. Liu, F. Xiao and J. Zhao, *Nanoscale*, 2022, **14**, 10773–10779.
68 L. Zhang, X. Wang, H. Chen, C. Liu and S. Deng, *Nanoscale*, 2022, **14**, 12257–12264.
69 J. J. Mock, R. T. Hill, A. Degiron, S. Zauscher, A. Chilkoti and D. R. Smith, *Nano Lett.*, 2008, **8**, 2245–2252.
70 L. Zhang, J. H. Prosser, G. Feng and D. Lee, *Nanoscale*, 2012, **4**, 6543–6552.
71 R. T. Hill, J. J. Mock, A. Hucknall, S. D. Wolter, N. M. Jokerst, D. R. Smith and A. Chilkoti, *ACS Nano*, 2012, **6**, 9237–9246.
72 G. M. Akselrod, T. Ming, C. Argyropoulos, T. B. Hoang, Y. Lin, X. Ling, D. R. Smith, J. Kong and M. H. Mikkelsen, *Nano Lett.*, 2015, **15**, 3578–3584.
73 C.-Z. Huang, M.-J. Wu and S.-Y. Chen, *J. Phys. Chem. C*, 2015, **119**, 13799–13806.
74 G.-C. Li, Q. Zhang, S. A. Maier and D. Lei, *Nanophotonics*, 2018, **7**, 1865–1889.
75 F. Benz, B. de Nijs, C. Tserkezis, R. Chikkaraddy, D. O. Sigle, L. Pukenas, S. D. Evans, J. Aizpurua and J. J. Baumberg, *Opt. Express*, 2015, **23**, 33255–33269.
76 M. Kauranen and A. V. Zayats, *Nat. Photonics*, 2012, **6**, 737–748.
77 S. Jiang, Z. Li, J. Tang, W. Huang, Z. Tan, D. Pan, X. Chen and G. Nie, *Phys. Chem. Chem. Phys.*, 2024, **26**, 2058–2065.
78 T. P. Rasmussen, A. Rodriguez Echarri, F. J. Garcia de Abajo and J. D. Cox, *Nanoscale*, 2023, **15**, 3150–3158.
79 L. Agiotis and M. Meunier, *Laser Photonics Rev.*, 2022, **16**, 2200076.
80 I.-Y. Park, S. Kim, J. Choi, D.-H. Lee, Y.-J. Kim, M. F. Kling, M. I. Stockman and S.-W. Kim, *Nat. Photonics*, 2011, **5**, 677–681.
81 H. Wang, Z. Hu, J. Deng, X. Zhang, J. Chen, K. Li and G. Li, *Sci. Adv.*, 2024, **10**, eadk3882.

82 G. Ni, L. Wang, M. Goldflam, M. Wagner, Z. Fei, A. McLeod, M. Liu, F. Keilmann, B. Özyilmaz and A. Castro Neto, *Nat. Photonics*, 2016, **10**, 244–247.
83 I. W. Un, Y. Dubi and Y. Sivan, *Nanoscale*, 2022, **14**, 5022–5032.
84 M. E. King, M. V. Fonseca Guzman and M. B. Ross, *Nanoscale*, 2022, **14**, 602–611.
85 M. Hu, Z. Huang, R. Liu, N. Zhou, H. Tang and G. Meng, *Nanoscale Adv.*, 2022, **4**, 4730–4738.
86 R. Wu, Q. Jin, C. Storey, J. Collins, G. Gomard, U. Lemmer, L. Canham, R. Kling and A. Kaplan, *Nanoscale Horiz.*, 2021, **6**, 781–790.
87 Y. Zhao, A. Kumar and Y. Yang, *Chem. Soc. Rev.*, 2024, **53**, 1004–1057.
88 S. Lee, H. Dang, J. I. Moon, K. Kim, Y. Joung, S. Park, Q. Yu, J. Chen, M. Lu, L. Chen, S. W. Joo and J. Choo, *Chem. Soc. Rev.*, 2024, **53**, 5394–5427.
89 H. D. Trinh, S. Kim, J. Park and S. Yoon, *Nanoscale*, 2022, **14**, 17003–17012.
90 A. Olshtrem, O. Guselnikova, P. Postnikov, A. Trelin, M. Yusubov, Y. Kalachyova, L. Lapcak, M. Cieslar, P. Ulbrich, V. Svorcik and O. Lyutakov, *Nanoscale*, 2020, **12**, 14581–14588.
91 M. Guizzardi, S. Bonfadini, L. Moscardi, I. Kriegel, F. Scotognella and L. Criante, *Phys. Chem. Chem. Phys.*, 2020, **22**, 6881–6887.
92 C. C. Zhang, J. Y. Zhang, J. R. Feng, S. T. Liu, S. J. Ding, L. Ma and Q. Q. Wang, *Nanoscale*, 2024, **16**, 5960–5975.
93 D. Lehr, J. Reinhold, I. Thiele, H. Hartung, K. Dietrich, C. Menzel, T. Pertsch, E. B. Kley and A. Tunnermann, *Nano Lett.*, 2015, **15**, 1025–1030.
94 A. Chakraborty, P. Barman, A. K. Singh, X. Wu, D. A. Akimov, T. Meyer-Zedler, S. Nolte, C. Ronning, M. Schmitt, J. Popp and J. S. Huang, *Laser Photonics Rev.*, 2023, **17**, 2200958.
95 Y. Zhang, Y.-R. Zhen, O. Neumann, J. K. Day, P. Nordlander and N. J. Halas, *Nat. Commun.*, 2014, **5**, 4424.
96 J. Renger, R. Quidant, N. van Hulst and L. Novotny, *Phys. Rev. Lett.*, 2010, **104**, 046803.
97 Y. Feng, Y. Wang, F. Shao, L. Meng and M. Sun, *Phys. Chem. Chem. Phys.*, 2022, **24**, 13911–13921.
98 X. Zheng, Z. Ye, Z. Akmal, C. He, J. Zhang and L. Wang, *Chem. Soc. Rev.*, 2024, **53**, 656–683.
99 Z. Wei, A. Vandergriff, C. H. Liu, M. Liaqat, M. P. Nieh, Y. Lei and J. He, *Nanoscale*, 2024, **16**, 708–718.
100 Y. Wang, R. Liu, Z. Zhong, J. Liu, X. Feng, L. Liu and F. Jiang, *Chem. Commun.*, 2024, **60**, 9046–9049.
101 S. Duan, G. Tian and Y. Luo, *Chem. Soc. Rev.*, 2024, **53**, 5083–5117.
102 Y. X. Zhao, Z. X. Zheng, L. S. Zhang, J. R. Feng, L. Ma and S. J. Ding, *Phys. Chem. Chem. Phys.*, 2023, **25**, 15209–15218.
103 C. Deriu, S. Thakur, O. Tammaro and L. Fabris, *Nanoscale Adv.*, 2023, **5**, 2132–2166.
104 Y. Chen and M. Sun, *Nanoscale*, 2023, **15**, 11834–11851.
105 V. Yadav and S. Siddhanta, *Mater. Adv.*, 2022, **3**, 1825–1833.
106 W. Wu and M. Pauly, *Mater. Adv.*, 2022, **3**, 186–215.
107 P. Peluso and B. Chankvetadze, *Chem. Rev.*, 2022, **122**, 13235–13400.
108 M. Zhang, G. Qing and T. Sun, *Chem. Soc. Rev.*, 2012, **41**, 1972–1984.
109 G. Yang, L. Sun and Q. Zhang, *Nanoscale Adv.*, 2024, **6**, 318–336.
110 N. S. S. Nizar, M. Sujith, K. Swathi, C. Sissa, A. Painelli and K. G. Thomas, *Chem. Soc. Rev.*, 2021, **50**, 11208–11226.
111 H. Li, Y. Ren, M. He and H. Qi, *Phys. Chem. Chem. Phys.*, 2024, **26**, 17860–17868.
112 J. Mun, M. Kim, Y. Yang, T. Badloe, J. Ni, Y. Chen, C.-W. Qiu and J. Rho, *Light: Sci. Appl.*, 2020, **9**, 139.
113 X. Wu, L. Xu, W. Ma, L. Liu, H. Kuang, W. Yan, L. Wang and C. Xu, *Adv. Funct. Mater.*, 2014, **25**, 850–854.
114 X. Lan, Z. Chen, G. Dai, X. Lu, W. Ni and Q. Wang, *J. Am. Chem. Soc.*, 2013, **135**, 11441–11444.
115 Q. Zhang, T. Hernandez, K. W. Smith, S. A. Hosseini Jebeli, A. X. Dai, L. Warning, R. Baiyasi, L. A. McCarthy, H. Guo, D. H. Chen, J. A. Dionne, C. F. Landes and S. Link, *Science*, 2019, **365**, 1475–1478.
116 E. Prodan, C. Radloff, N. J. Halas and P. Nordlander, *Science*, 2003, **302**, 419–422.
117 X. Yin, M. Schäferling, B. Metzger and H. Giessen, *Nano Lett.*, 2013, **13**, 6238–6243.
118 L. A. Warning, A. R. Miandashti, L. A. McCarthy, Q. Zhang, C. F. Landes and S. Link, *ACS Nano*, 2021, **15**, 15538–15566.
119 A. Lininger, G. Palermo, A. Guglielmelli, G. Nicoletta, M. Goel, M. Hinczewski and G. Strangi, *Adv. Mater.*, 2023, **35**, 2107325.
120 H. S. Khaliq, A. Nauman, J. W. Lee and H. R. Kim, *Adv. Opt. Mater.*, 2023, **11**, 2300644.
121 M. J. Urban, C. Shen, X.-T. Kong, C. Zhu, A. O. Govorov, Q. Wang, M. Hentschel and N. Liu, *Annu. Rev. Phys. Chem.*, 2019, **70**, 275–299.
122 S. Lee, D. Jeong, S. Kk, S. Chen, F. Westerlund, B. Kang, K.-H. Kim, M. P. Jonsson and E. S. H. Kang, *J. Mater. Chem. A*, 2023, **11**, 21569–21576.
123 S. Xu, Z. Ren, B. Dong, J. Zhou, W. Liu and C. Lee, *Adv. Opt. Mater.*, 2022, **11**, 2202228.
124 X. Liu, Q. Qiao, B. Dong, W. Liu, C. Xu, S. Xu and G. Zhou, *Int. J. Optomechatronics*, 2022, **16**, 42–57.
125 Q. Qiao, X. Liu, Z. Ren, B. Dong, J. Xia, H. Sun, C. Lee and G. Zhou, *ACS Photonics*, 2022, **9**, 2367–2377.
126 W. Liu, Y. Ma, X. Liu, J. Zhou, C. Xu, B. Dong and C. Lee, *Nano Lett.*, 2022, **22**, 6112–6120.
127 W. Liu, Y. Ma, Y. Chang, B. Dong, J. Wei, Z. Ren and C. Lee, *Nanophotonics*, 2021, **10**, 1861–1870.
128 J. Zhou, X. Liu, H. Zhou, S. Xu, J. Xie, C. Xu, W. Liu, Z. Zhang and C. Lee, *Laser Photonics Rev.*, 2025, 2400754.
129 J. Zhou, Z. Zhang, B. Dong, Z. Ren, W. Liu and C. Lee, *ACS Nano*, 2022, **17**, 711–724.
130 Z. Xiao, W. Liu, S. Xu, J. Zhou, Z. Ren and C. Lee, *Adv. Opt. Mater.*, 2023, **11**, 2301028.
131 X. Liu, W. Liu, Z. Ren, Y. Ma, B. Dong, G. Zhou and C. Lee, *Int. J. Optomechatronics*, 2021, **15**, 120–159.
132 D. Barshilia, A. C. Komaram, P. C. Chen, L. K. Chau and G. E. Chang, *Analyst*, 2022, **147**, 4417–4425.
133 Y. Su, Y. He, X. Guo, W. Xie, X. Ji, H. Wang, X. Cai, L. Tong and S. Yu, *ACS Photonics*, 2023, **10**, 2020–2030.
134 A. Tuniz, *Riv. Nuovo Cimento*, 2021, **44**, 193–249.

135 D. O'Carroll, I. Lieberwirth and G. Redmond, *Small*, 2007, **3**, 1178–1183.
136 M. Thomaschewski, V. A. Zenin, C. Wolff and S. I. Bozhevolnyi, *Nat. Commun.*, 2020, **11**, 748.
137 J. Wei and C. Lee, *Opt. Lett.*, 2019, **44**, 6041–6044.
138 J. Nong, L. Tang, G. Lan, P. Luo, Z. Li, D. Huang, J. Shen and W. Wei, *Small*, 2021, **17**, 2004640.
139 G. Zhao, H. Kozuka and T. Yoko, *Thin Solid Films*, 1996, **277**, 147–154.
140 Y. Ohko, T. Tatsuma, T. Fujii, K. Naoi, C. Niwa, Y. Kubota and A. Fujishima, *Nat. Mater.*, 2003, **2**, 29–31.
141 Y. T. Tian, *J. Am. Chem. Soc.*, 2005, **127**, 7632–7637.
142 Y. Tian and T. Tatsuma, *Chem. Commun.*, 2004, 1810–1811.
143 M. Berdakin, G. Soldano, F. P. Bonafe, V. Liubov, B. Aradi, T. Frauenheim and C. G. Sanchez, *Nanoscale*, 2022, **14**, 2816–2825.
144 A. D. Furube, L. Hara, K. Katoh and R. Tachiya, *J. Am. Chem. Soc.*, 2007, **129**, 14852–14853.
145 Y. Tian, X. Wang, D. Zhang, X. Shi and S. Wang, *J. Photochem. Photobiol., A*, 2008, **199**, 224–229.
146 J. H. Mokkath, *Phys. Chem. Chem. Phys.*, 2023, **25**, 28750–28760.
147 W. R. Erwin, H. F. Zarick, E. M. Talbert and R. Bardhan, *Energy Environ. Sci.*, 2016, **9**, 1577–1601.
148 S. Zhang, D. Fan, Q. Yan, Y. Lu, D. Wu, B. Fu and M. Zhao, *J. Mater. Chem. A*, 2024, **12**, 19627–19662.
149 A. Phengdaam, S. Phetsang, S. Jonai, K. Shinbo, K. Kato and A. Baba, *Nanoscale Adv.*, 2024, **6**, 3494–3512.
150 T. Kong, A. Liao, Y. Xu, X. Qiao, H. Zhang, L. Zhang and C. Zhang, *RSC Adv.*, 2024, **14**, 17041–17050.
151 J. Zhu, J. Dai, Y. Xu, X. Liu, Z. Wang, H. Liu and G. Li, *Nanoscale Adv.*, 2023, **5**, 6819–6829.
152 K. An, J. Hu and J. Wang, *Phys. Chem. Chem. Phys.*, 2023, **25**, 19358–19370.
153 L. Wen and B. Liu, *Phys. Chem. Chem. Phys.*, 2024, **26**, 11113–11125.
154 S.-S. Kim, S.-I. Na, J. Jo, D.-Y. Kim and Y.-C. Nah, *Appl. Phys. Lett.*, 2008, **93**, 073307.
155 K. R. Catchpole and A. Polman, *Appl. Phys. Lett.*, 2008, **93**, 191113.
156 B. M. Weight, X. Li and Y. Zhang, *Phys. Chem. Chem. Phys.*, 2023, **25**, 31554–31577.
157 Q. Zhang, Z. Zuo and D. Ma, *Chem. Commun.*, 2023, **59**, 7704–7716.
158 C. Boerigter, R. Campana, M. Morabito and S. Linic, *Nat. Commun.*, 2016, **7**, 10545.
159 S. Mukherjee, F. Libisch, N. Large, O. Neumann, L. V. Brown, J. Cheng, J. B. Lassiter, E. A. Carter, P. Nordlander and N. J. Halas, *Nano Lett.*, 2013, **13**, 240–247.
160 D. Zabelin, A. Tulupova, A. Zabelina, A. Tosovska, R. Valiev, R. Ramazanov, D. Mares, V. Jerabek, V. Burtsev, M. Erzina, A. Michalcová, A. Skvortsova, V. Svorcik and O. Lyutakov, *J. Mater. Chem. A*, 2024, **12**, 21310–21320.
161 X. Yan, L. Liang, J. Yang, W. Liu, X. Ding, D. Xu, Y. Zhang, T. Cui and J. Yao, *Opt. Express*, 2015, **23**, 29128–29137.
162 J. Li, S. K. Cushing, F. Meng, T. R. Senty, A. D. Bristow and N. Wu, *Nat. Photonics*, 2015, **9**, 601–607.
163 H. Sahoo, *J. Photochem. Photobiol., C*, 2011, **12**, 20–30.
164 X. Wang, S. Gao and J. Ma, *Nanoscale*, 2023, **15**, 1754–1762.
165 S. Mubeen, G. Hernandez-Sosa, D. Moses, J. Lee and M. Moskovits, *Nano Lett.*, 2011, **11**, 5548–5552.
166 S. K. Cushing, J. Li, F. Meng, T. R. Senty, S. Suri, M. Zhi, M. Li, A. D. Bristow and N. Wu, *J. Am. Chem. Soc.*, 2012, **134**, 15033–15041.
167 I. L. Medintz, A. R. Clapp, H. Mattoussi, E. R. Goldman, B. Fisher and J. M. Mauro, *Nat. Mater.*, 2003, **2**, 630–638.
168 S. V. Boriskina, T. A. Cooper, L. Zeng, G. Ni, J. K. Tong, Y. Tsurimaki, Y. Huang, L. Meroueh, G. Mahan and G. Chen, *Adv. Opt. Photonics*, 2017, **9**, 775–827.
169 J. Xu, Y. Wu, P. Zhang, Y. Wu, R. A. Vallée, S. Wu and X. Liu, *Adv. Opt. Mater.*, 2021, **9**, 2100112.
170 S. Yang, C. Hong, Y. Jiang and J. C. Ndukaife, *ACS Photonics*, 2021, **8**, 1961–1971.
171 A. A. Vyshnevyy and D. Y. Fedyanin, *ACS Photonics*, 2016, **3**, 51–57.
172 T. Kong, B. Kang, W. Wang, T. Deckert-Gaudig, Z. Zhang and V. Deckert, *Nanoscale*, 2024, **16**, 10745–10750.
173 G. Huttmann and R. Birngruber, *IEEE J. Sel. Top. Quantum Electron.*, 1999, **5**, 954–962.
174 D. Boyer, P. Tamarat, A. Maali, B. Lounis and M. Orrit, *Science*, 2002, **1073765**, 297.
175 L. R. Hirsch, R. J. Stafford, J. A. Bankson, S. R. Sershen, B. Rivera, R. E. Price, J. D. Hazle, N. J. Halas and J. L. West, *Proc. Natl. Acad. Sci. U. S. A.*, 2003, **100**, 13549–13554.
176 A. L. Siegel, L. Polo-Parada and G. A. Baker, *Chem. Commun.*, 2022, **58**, 13119–13122.
177 H. Zhang, T. Wang, H. Liu, F. Ren, W. Qiu, Q. Sun, F. Yan, H. Zheng, Z. Li and M. Gao, *Nanoscale*, 2019, **11**, 7600–7608.
178 M. I. Stockman, K. Kneipp, S. I. Bozhevolnyi, S. Saha, A. Dutta, J. Ndukaife, N. Kinsey, H. Reddy, U. Guler, V. M. Shalaev, A. Boltasseva, B. Gholipour, H. N. S. Krishnamoorthy, K. F. MacDonald, C. Soci, N. I. Zheludev, V. Savinov, R. Singh, P. Groß, C. Lienau, M. Vadai, M. L. Solomon, D. R. Barton, M. Lawrence, J. A. Dionne, S. V. Boriskina, R. Esteban, J. Aizpurua, X. Zhang, S. Yang, D. Wang, W. Wang, T. W. Odom, N. Accanto, P. M. de Roque, I. M. Hancu, L. Piatkowski, N. F. van Hulst and M. F. Kling, *J. Opt.*, 2018, **20**, 043001.
179 F. Chen, J. Yao, X. Wang, S. Wang, Z. Liu and T. Ding, *Nanoscale*, 2023, **15**, 476–482.
180 S. Anuthum, F. Hasegawa, C. Lertvachirapaiboon, K. Shinbo, K. Kato, K. Ounnunkad and A. Baba, *Phys. Chem. Chem. Phys.*, 2022, **24**, 7060–7067.
181 A. Amirjani, P. Shokrani, S. A. Sharif, H. Moheb, H. Ahmadi, Z. S. Ahmadiani and M. S. Paroushi, *J. Mater. Chem. B*, 2023, **11**, 3537–3566.
182 J. A. Webb and R. Bardhan, *Nanoscale*, 2014, **6**, 2502–2530.
183 P. Gao, Y. Wei, Q. Xu and Y. Jiang, *New J. Chem.*, 2022, **46**, 16359–16369.
184 D. Mateo, J. L. Cerrillo, S. Durini and J. Gascon, *Chem. Soc. Rev.*, 2021, **50**, 2173–2210.
185 P. Purohit, A. Samadi, P. M. Bendix, J. J. Laserna and L. B. Oddershede, *Sci. Rep.*, 2020, **10**, 1198.

186 X. Zhu, C. Vannahme, E. Hojlund-Nielsen, N. A. Mortensen and A. Kristensen, *Nat. Nanotechnol.*, 2016, **11**, 325–329.
187 J. Song, Q. Cheng, B. Zhang, L. Lu, X. Zhou, Z. Luo and R. Hu, *Rep. Prog. Phys.*, 2021, **84**, 036501.
188 R. Liu, L. Ge, B. Wu, Z. Cui and X. Wu, *iScience*, 2021, **24**, 103408.
189 X. Liu and Z. Zhang, *ACS Photonics*, 2015, **2**, 1320–1326.
190 C.-N. Chen, J. Y. Chyan, C. Max Hsieh and J. Andrew Yeh, *J. Opt. A: Pure Appl. Opt.*, 2008, **10**, 044007.
191 B. Han, Y. L. Zhang, L. Zhu, Y. Li, Z. C. Ma, Y. Q. Liu, X. L. Zhang, X. W. Cao, Q. D. Chen, C. W. Qiu and H. B. Sun, *Adv. Mater.*, 2019, **31**, e1806386.
192 F. Pujol-Vila, P. Güell-Grau, J. Nogués, M. Alvarez and B. Sepúlveda, *Adv. Funct. Mater.*, 2023, **33**, 2213109.
193 J. Chen, J. Feng, F. Yang, R. Aleisa, Q. Zhang and Y. Yin, *Angew. Chem., Int. Ed.*, 2019, **58**, 9275–9281.
194 S. Linghu, Z. Gu, J. Lu, W. Fang, Z. Yang, H. Yu, Z. Li, R. Zhu, J. Peng, Q. Zhan, S. Zhuang, M. Gu and F. Gu, *Nat. Commun.*, 2021, **12**, 385.
195 Q. Shi, H. Xia, P. Li, Y. S. Wang, L. Wang, S. X. Li, G. Wang, C. Lv, L. G. Niu and H. B. Sun, *Adv. Opt. Mater.*, 2017, **5**, 1700442.
196 P. Güell-Grau, F. Pi, R. Villa, J. Nogués, M. Alvarez and B. Sepúlveda, *Appl. Mater. Today*, 2021, **23**, 101052.
197 Z. Li, Z. Ye, L. Han, Q. Fan, C. Wu, D. Ding, H. L. Xin, N. V. Myung and Y. Yin, *Adv. Mater.*, 2021, **33**, e2006367.
198 P. Vachon, S. Merugu, J. Sharma, A. Lal, E. J. Ng, Y. Koh, J. E. Lee and C. Lee, *Microsyst. Nanoeng.*, 2024, **10**, 33.
199 M. Xu and L. V. Wang, *Rev. Sci. Instrum.*, 2006, **77**, 041101.
200 W. Yim, J. Zhou, Y. Mantri, M. N. Creyer, C. A. Moore and J. V. Jokerst, *ACS Appl. Mater. Interfaces*, 2021, **13**, 14974–14984.
201 R. García-Álvarez, L. Chen, A. Nedilko, A. Sánchez-Iglesias, A. Rix, W. Lederle, V. Pathak, T. Lammers, G. von Plessen, K. Kostarelos, L. M. Liz-Marzán, A. J. C. Kuehne and D. N. Chigrin, *ACS Photonics*, 2020, **7**, 646–652.
202 Y. Shi, H. Qin, S. Yang and D. Xing, *Nano Res.*, 2016, **9**, 3644–3655.
203 R. Gupta, K. Barman, L. Y. Lee, A. Chauhan and J. J. Huang, *Discover Nano*, 2024, **19**, 10.
204 A. Renaudin, V. Chabot, E. Grondin, V. Aimez and P. G. Charette, *Lab Chip*, 2010, **10**, 111–115.
205 F. Noll, N. Krauss, V. Gusev, T. Dekorsy and M. Hettich, *Photoacoustics*, 2023, **30**, 100464.
206 V. V. Temnov, C. Klieber, K. A. Nelson, T. Thomay, V. Knittel, A. Leitenstorfer, D. Makarov, M. Albrecht and R. Bratschitsch, *Nat. Commun.*, 2013, **4**, 1468.
207 S. G. Menabde, I. H. Lee, S. Lee, H. Ha, J. T. Heiden, D. Yoo, T. T. Kim, T. Low, Y. H. Lee, S. H. Oh and M. S. Jang, *Nat. Commun.*, 2021, **12**, 938.
208 I. H. Lee, D. Yoo, P. Avouris, T. Low and S. H. Oh, *Nat. Nanotechnol.*, 2019, **14**, 313–319.
209 B. Shan, H. Liu, L. Li, Y. Lu and M. Li, *Small*, 2022, **18**, e2105638.
210 J. X. Fang, S. Y. Du, S. Lebedkin, Z. Y. Li, R. Kruk, M. Kappes and H. Hahn, *Nano Lett.*, 2010, **10**, 5006–5013.
211 Y. J. Zhang, P. M. Radjenovic, X. S. Zhou, H. Zhang, J. L. Yao and J. F. Li, *Adv. Mater.*, 2021, **33**, e2005900.
212 J. F. Li, Y. J. Zhang, S. Y. Ding, R. Panneerselvam and Z. Q. Tian, *Chem. Rev.*, 2017, **117**, 5002–5069.
213 A. O. Govorov and H. H. Richardson, *Nano Today*, 2007, **2**, 30–38.
214 M. D. Sonntag, J. M. Klingsporn, A. B. Zrimsek, B. Sharma, L. K. Ruvuna and R. P. Van Duyne, *Chem. Soc. Rev.*, 2014, **43**, 1230–1247.
215 M. J. Mulvihill, X. Y. Ling, J. Henzie and P. D. Yang, *J. Am. Chem. Soc.*, 2010, **132**, 268–274.
216 C. E. Talley, J. B. Jackson, C. Oubre, N. K. Grady, C. W. Hollars, S. M. Lane, T. R. Huser, P. Nordlander and N. J. Halas, *Nano Lett.*, 2005, **5**, 1569–1574.
217 C. Radloff and N. J. Halas, *Nano Lett.*, 2004, **4**, 1323–1327.
218 N. M. Ngo, H. V. Tran and T. R. Lee, *ACS Appl. Nano Mater.*, 2022, **5**, 14051–14091.
219 J. Otsuki, K. Sugawa and S. Jin, *Mater. Adv.*, 2021, **2**, 32–46.
220 S. Y. Ding, J. Yi, J. F. Li, B. Ren, D. Y. Wu, R. Panneerselvam and Z. Q. Tian, *Nat. Rev. Mater.*, 2016, **1**, 1–16.
221 S. Y. Ding, E. M. You, Z. Q. Tian and M. Moskovits, *Chem. Soc. Rev.*, 2017, **46**, 4042–4076.
222 W. Y. Li, P. H. C. Camargo, X. M. Lu and Y. N. Xia, *Nano Lett.*, 2009, **9**, 485–490.
223 D. K. Lim, K. S. Jeon, H. M. Kim, J. M. Nam and Y. D. Suh, *Nat. Mater.*, 2010, **9**, 60–67.
224 G. Chen, Y. Wang, L. H. Tan, M. X. Yang, L. S. Tan, Y. Chen and H. Y. Chen, *J. Am. Chem. Soc.*, 2009, **131**, 4218–4219.
225 J. M. McMahon, S. Z. Li, L. K. Ausman and G. C. Schatz, *J. Phys. Chem. C*, 2012, **116**, 1627–1637.
226 W. Q. Zhu and K. B. Crozier, *Nat. Commun.*, 2014, **5**, 5228.
227 Z. Q. Tian, B. Ren, J. F. Li and Z. L. Yang, *Chem. Commun.*, 2007, 3514–3534, DOI: **10.1039/b616986d**.
228 C. P. Byers, H. Zhang, D. F. Swearer, M. Yorulmaz, B. S. Hoener, D. Huang, A. Hoggard, W. S. Chang, P. Mulvaney, E. Ringe, N. J. Halas, P. Nordlander, S. Link and C. F. Landes, *Sci. Adv.*, 2015, **1**, e1500988.
229 L. B. Yang, P. Li, H. L. Liu, X. H. Tang and J. H. Liu, *Chem. Soc. Rev.*, 2015, **44**, 2837–2848.
230 K. L. Wustholz, A. I. Henry, J. M. McMahon, R. G. Freeman, N. Valley, M. E. Piotti, M. J. Natan, G. C. Schatz and R. P. Van Duyne, *J. Am. Chem. Soc.*, 2010, **132**, 10903–10910.
231 M. P. Cecchini, V. A. Turek, J. Paget, A. A. Kornyshev and J. B. Edel, *Nat. Mater.*, 2013, **12**, 165–171.
232 B. Peng, G. Y. Li, D. H. Li, S. Dodson, Q. Zhang, J. Zhang, Y. H. Lee, H. V. Demir, X. Y. Ling and Q. H. Xiong, *ACS Nano*, 2013, **7**, 5993–6000.
233 Y. Fang, N. H. Seong and D. D. Dlott, *Science*, 2008, **321**, 388–392.
234 M. J. Banholzer, J. E. Millstone, L. D. Qin and C. A. Mirkin, *Chem. Soc. Rev.*, 2008, **37**, 885–897.
235 S. Y. Chen, J. J. Mock, R. T. Hill, A. Chilkoti, D. R. Smith and A. A. Lazarides, *ACS Nano*, 2010, **4**, 6535–6546.
236 C. Ciracì, R. T. Hill, J. J. Mock, Y. Urzhumov, A. I. Fernández-Domínguez, S. A. Maier, J. B. Pendry, A. Chilkoti and D. R. Smith, *Science*, 2012, **337**, 1072–1074.
237 S. P. Zhang, K. Bao, N. J. Halas, H. X. Xu and P. Nordlander, *Nano Lett.*, 2011, **11**, 1657–1663.

238 M. Rycenga, X. H. Xia, C. H. Moran, F. Zhou, D. Qin, Z. Y. Li and Y. A. Xia, *Angew. Chem., Int. Ed.*, 2011, **50**, 5473–5477.
239 S. Chen, L. Y. Meng, H. Y. Shan, J. F. Li, L. H. Qian, C. T. Williams, Z. L. Yang and Z. Q. Tian, *ACS Nano*, 2016, **10**, 581–587.
240 R. P. Vanduyne and J. P. Haushalter, *J. Phys. Chem.*, 1983, **87**, 2999–3003.
241 A. K. Kuhlman and A. T. Zayak, *J. Phys. Chem. Lett.*, 2014, **5**, 964–968.
242 J. J. Xu, W. W. Zhao, S. P. Song, C. H. Fan and H. Y. Chen, *Chem. Soc. Rev.*, 2014, **43**, 1601–1611.
243 L. Jiang, Y. H. Sun, F. W. Huo, H. Zhang, L. D. Qin, S. Z. Li and X. D. Chen, *Nanoscale*, 2012, **4**, 66–75.
244 J. P. Zheng, X. Z. Cheng, H. Zhang, X. P. Bai, R. Q. Ai, L. Shao and J. F. Wang, *Chem. Rev.*, 2021, **121**, 13342–13453.
245 H. J. Chen, L. Shao, Q. Li and J. F. Wang, *Chem. Soc. Rev.*, 2013, **42**, 2679–2724.
246 A. L. Schmucker, N. Harris, M. J. Banholzer, M. G. Blaber, K. D. Osberg, G. C. Schatz and C. A. Mirkin, *ACS Nano*, 2010, **4**, 5453–5463.
247 J. Zuloaga, E. Prodan and P. Nordlander, *ACS Nano*, 2010, **4**, 5269–5276.
248 B. K. Sahu, A. Dwivedi, K. K. Pal, R. Pandian, S. Dhara and A. Das, *Appl. Surf. Sci.*, 2021, **537**, 147615.
249 X. H. Huang, S. Neretina and M. A. El-Sayed, *Adv. Mater.*, 2009, **21**, 4880–4910.
250 M. Hu, C. Novo, A. Funston, H. N. Wang, H. Staleva, S. L. Zou, P. Mulvaney, Y. N. Xia and G. V. Hartland, *J. Mater. Chem.*, 2008, **18**, 1949–1960.
251 P. K. Jain, K. S. Lee, I. H. El-Sayed and M. A. El-Sayed, *J. Phys. Chem. B*, 2006, **110**, 7238–7248.
252 O. Henrotte, E. Y. Santiago, A. Movsesyan, L. Mascaretti, M. Afshar, A. Minguzzi, A. Vertova, Z. M. Wang, R. Zboril, S. Kment, A. O. Govorov and A. Naldoni, *ACS Nano*, 2023, **17**, 11427–11438.
253 J. Yguerabide and E. E. Yguerabide, *Anal. Biochem.*, 1998, **262**, 157–176.
254 X. Guo, Y. B. Ying and L. M. Tong, *Acc. Chem. Res.*, 2014, **47**, 656–666.
255 R. X. Yan, D. Gargas and P. D. Yang, *Nat. Photonics*, 2009, **3**, 569–576.
256 S. Lal, J. H. Hafner, N. J. Halas, S. Link and P. Nordlander, *Acc. Chem. Res.*, 2012, **45**, 1887–1895.
257 L. N. Quan, J. Kang, C. Z. Ning and P. D. Yang, *Chem. Rev.*, 2019, **119**, 9153–9169.
258 R. M. Dickson and L. A. Lyon, *J. Phys. Chem. B*, 2000, **104**, 6095–6098.
259 H. Wei, D. Pan, S. P. Zhang, Z. P. Li, Q. Li, N. Liu, W. H. Wang and H. X. Xu, *Chem. Rev.*, 2018, **118**, 2882–2926.
260 X. Guo, Y. G. Ma, Y. P. Wang and L. M. Tong, *Laser Photonics Rev.*, 2013, **7**, 855–881.
261 X. Xiong, C. L. Zou, X. F. Ren, A. P. Liu, Y. X. Ye, F. W. Sun and G. C. Guo, *Laser Photonics Rev.*, 2013, **7**, 901–919.
262 Y. Z. Huang, Y. R. Fang, Z. L. Zhang, L. Zhu and M. T. Sun, *Light:Sci. Appl.*, 2014, **3**, e199.
263 S. J. Lee and M. Moskovits, *J. Am. Chem. Soc.*, 2012, **134**, 11384–11387.
264 H. Wei, F. Hao, Y. Z. Huang, W. Z. Wang, P. Nordlander and H. X. Xu, *Nano Lett.*, 2008, **8**, 2497–2502.
265 M. W. Knight, N. K. Grady, R. Bardhan, F. Hao, P. Nordlander and N. J. Halas, *Nano Lett.*, 2007, **7**, 2346–2350.
266 W. G. Chen, H. Y. Shi, F. Wan, P. Y. Wang, Z. L. Gu, W. H. Li, L. A. Ke and Y. Z. Huang, *J. Mater. Chem. C*, 2017, **5**, 7028–7034.
267 R. Chikkaraddy, D. Singh and G. V. P. Kumar, *Appl. Phys. Lett.*, 2012, **100**, 043108.
268 W. H. Wang, W. J. Zhou, T. Fu, F. Wu, N. Zhang, Q. F. Li, Z. F. Xu and W. H. Liu, *Nano Energy*, 2018, **48**, 197–201.
269 N. Zhang, T. Fu, H. X. Xu and W. H. Wang, *Nano Energy*, 2020, **68**, 104322.
270 W. J. Wang, M. Ramezani, A. I. Väkeväinen, P. Törmä, J. G. Rivas and T. W. Odom, *Mater. Today*, 2018, **21**, 303–314.
271 S. Kasani, K. Curtin and N. Q. Wu, *Nanophotonics*, 2019, **8**, 2065–2089.
272 F. J. G. de Abajo, *Rev. Mod. Phys.*, 2007, **79**, 1267–1290.
273 D. Sell, J. Yang, S. Doshay, K. Zhang and J. A. Fan, *ACS Photonics*, 2016, **3**, 1919–1925.
274 A. Sobhani, M. W. Knight, Y. Wang, B. Zheng, N. S. King, L. V. Brown, Z. Fang, P. Nordlander and N. J. Halas, *Nat. Commun.*, 2013, **4**, 1643.
275 I. Morichika, K. Murata, A. Sakurai, K. Ishii and S. Ashihara, *Nat. Commun.*, 2019, **10**, 3893.
276 M. Gupta, V. Savinov, N. Xu, L. Cong, G. Dayal, S. Wang, W. Zhang, N. I. Zheludev and R. Singh, *Adv. Mater.*, 2016, **28**, 8206–8211.
277 C. Huang, L. Liang, P. Chang, H. Yao, X. Yan, Y. Zhang and Y. Xie, *Adv. Mater.*, 2023, e2310493, DOI: **10.1002/adma.202310493**.
278 D. Rodrigo, A. Tittl, N. Ait-Bouziad, A. John-Herpin, O. Limaj, C. Kelly, D. Yoo, N. J. Wittenberg, S. H. Oh, H. A. Lashuel and H. Altug, *Nat. Commun.*, 2018, **9**, 2160.
279 D. Etezadi, J. B. Warner, H. A. Lashuel and H. Altug, *ACS Sens.*, 2018, **3**, 1109–1117.
280 A. John-Herpin, A. Tittl and H. Altug, *ACS Photonics*, 2018, **5**, 4117–4124.
281 X. K. Li, M. Soler, C. I. Ozdemir, A. Belushkin, F. Yesilkoy and H. Altug, *Lab Chip*, 2017, **17**, 2208–2217.
282 A. E. Cetin, D. Etezadi, B. C. Galarreta, M. P. Busson, Y. Eksioglu and H. Altug, *ACS Photonics*, 2015, **2**, 1167–1174.
283 M.-N. Su, P. D. Dongare, D. Chakraborty, Y. Zhang, C. Yi, F. Wen, W.-S. Chang, P. Nordlander, J. E. Sader, N. J. Halas and S. Link, *Nano Lett.*, 2017, **17**, 2575–2583.
284 I. Staude, A. E. Miroshnichenko, M. Decker, N. T. Fofang, S. Liu, E. Gonzales, J. Dominguez, T. S. Luk, D. N. Neshev, I. Brener and Y. Kivshar, *ACS Nano*, 2013, **7**, 7824–7832.
285 H. Liu, E. S. P. Leong, Z. Wang, G. Si, L. Zheng, Y. J. Liu and C. Soci, *Adv. Opt. Mater.*, 2013, **1**, 978–983.
286 E. M. Larsson, J. Alegret, M. Kall and D. S. Sutherland, *Nano Lett.*, 2007, **7**, 1256–1263.
287 M. Kraft, A. Braun, Y. Luo, S. A. Maier and J. B. Pendry, *ACS Photonics*, 2016, **3**, 764–769.

288 M. X. Wu, G. H. Li, X. Y. Ye, B. Zhou, J. H. Zhou and J. X. Cai, *Adv. Sci.*, 2022, **9**, e2201682.
289 W. Withayachumnankul, C. M. Shah, C. Fumeaux, K. Kaltenecker, M. Walther, B. M. Fischer, D. Abbott, M. Bhaskaran and S. Sriram, *Adv. Opt. Mater.*, 2013, **1**, 443–448.
290 W. A. Murray, S. Astilean and W. L. Barnes, *Phys. Rev. B:Condens. Matter Mater. Phys.*, 2004, **69**, 165407.
291 A. E. Miroshnichenko, S. Flach and Y. S. Kivshar, *Rev. Mod. Phys.*, 2010, **82**, 2257–2298.
292 C. Wu, A. B. Khanikaev, R. Adato, N. Arju, A. A. Yanik, H. Altug and G. Shvets, *Nat. Mater.*, 2011, **11**, 69–75.
293 C. G. Biris and N. C. Panoiu, *Phys. Rev. Lett.*, 2013, **111**, 203903.
294 M. R. Foreman, J. D. Swaim and F. Vollmer, *Adv. Opt. Photonics*, 2015, **7**, 168–240.
295 T. Dang, J. Yang, C. Zang, S. Ma, Y. Ding, H. Yoda, H. Tabata and H. Matsui, *Sens. Actuators, B*, 2024, **417**, 136230.
296 Z. Li, S. Butun and K. Aydin, *ACS Nano*, 2014, **8**, 8242–8248.
297 V. G. Kravets, A. V. Kabashin, W. L. Barnes and A. N. Grigorenko, *Chem. Rev.*, 2018, **118**, 5912–5951.
298 D. Yoo, F. Vidal-Codina, C. Ciraci, N. C. Nguyen, D. R. Smith, J. Peraire and S. H. Oh, *Nat. Commun.*, 2019, **10**, 4476.
299 M. Z. Alam, S. A. Schulz, J. Upham, I. De Leon and R. W. Boyd, *Nat. Photonics*, 2018, **12**, 79–83.
300 K. S. Novoselov, A. K. Geim, S. V. Morozov, D. Jiang, M. I. Katsnelson, I. V. Grigorieva, S. V. Dubonos and A. A. Firsov, *Nature*, 2005, **438**, 197–200.
301 F. J. G. de Abajo, *ACS Photonics*, 2014, **1**, 135–152.
302 D. Ansell, I. P. Radko, Z. Han, F. J. Rodriguez, S. I. Bozhevolnyi and A. N. Grigorenko, *Nat. Commun.*, 2015, **6**, 8846.
303 A. K. Geim, *Science*, 2009, **324**, 1530–1534.
304 A. K. Geim and K. S. Novoselov, *Nat. Mater.*, 2007, **6**, 183–191.
305 Q. L. Bao and K. P. Loh, *ACS Nano*, 2012, **6**, 3677–3694.
306 Q. S. Guo, C. Li, B. C. Deng, S. F. Yuan, F. Guinea and F. N. Xia, *ACS Photonics*, 2017, **4**, 2989–2999.
307 A. N. Grigorenko, M. Polini and K. S. Novoselov, *Nat. Photonics*, 2012, **6**, 749–758.
308 S. Thongrattanasiri, F. H. L. Koppens and F. J. G. de Abajo, *Phys. Rev. Lett.*, 2012, **108**, 047401.
309 P. A. Huidobro, M. Kraft, S. A. Maier and J. B. Pendry, *ACS Nano*, 2016, **10**, 5499–5506.
310 T. T. Kim, H. Kim, M. Kenney, H. S. Park, H. D. Kim, B. Min and S. Zhang, *Adv. Opt. Mater.*, 2018, **6**, 1700507.
311 S. H. Mousavi, I. Kholmanov, K. B. Alici, D. Purtseladze, N. Arju, K. Tatar, D. Y. Fozdar, J. W. Suk, Y. F. Hao, A. B. Khanikaev, R. S. Ruoff and G. Shvets, *Nano Lett.*, 2013, **13**, 1111–1117.
312 T. Low and P. Avouris, *ACS Nano*, 2014, **8**, 1086–1101.
313 D. Rodrigo, O. Limaj, D. Janner, D. Etezadi, F. Javier Garcia de Abajo, V. Pruneri and H. Altug, *Science*, 2015, **349**, 165–168.
314 H. Hu, X. Yang, X. Guo, K. Khaliji, S. R. Biswas, F. J. Garcia de Abajo, T. Low, Z. Sun and Q. Dai, *Nat. Commun.*, 2019, **10**, 1131.
315 Y. Li, H. Yan, D. B. Farmer, X. Meng, W. Zhu, R. M. Osgood, T. F. Heinz and P. Avouris, *Nano Lett.*, 2014, **14**, 1573–1577.
316 A. Woessner, M. B. Lundeberg, Y. Gao, A. Principi, P. Alonso-González, M. Carrega, K. Watanabe, T. Taniguchi, G. Vignale, M. Polini, J. Hone, R. Hillenbrand and F. H. L. Koppens, *Nat. Mater.*, 2015, **14**, 421–425.
317 F. Wang, Y. B. Zhang, C. S. Tian, C. Girit, A. Zettl, M. Crommie and Y. R. Shen, *Science*, 2008, **320**, 206–209.
318 M. Liu, X. B. Yin, E. Ulin-Avila, B. S. Geng, T. Zentgraf, L. Ju, F. Wang and X. Zhang, *Nature*, 2011, **474**, 64–67.
319 L. Ju, B. S. Geng, J. Horng, C. Girit, M. Martin, Z. Hao, H. A. Bechtel, X. G. Liang, A. Zettl, Y. R. Shen and F. Wang, *Nat. Nanotechnol.*, 2011, **6**, 630–634.
320 H. G. Yan, X. S. Li, B. Chandra, G. Tulevski, Y. Q. Wu, M. Freitag, W. J. Zhu, P. Avouris and F. N. Xia, *Nat. Nanotechnol.*, 2012, **7**, 330–334.
321 H. G. Yan, T. Low, W. J. Zhu, Y. Q. Wu, M. Freitag, X. S. Li, F. Guinea, P. Avouris and F. N. Xia, *Nat. Photonics*, 2013, **7**, 394–399.
322 V. W. Brar, M. S. Jang, M. Sherrott, S. Kim, J. J. Lopez, L. B. Kim, M. Choi and H. Atwater, *Nano Lett.*, 2014, **14**, 3876–3880.
323 J. A. Polo and A. Lakhtakia, *Laser Photonics Rev.*, 2011, **5**, 234–246.
324 P. Törmä and W. L. Barnes, *Rep. Prog. Phys.*, 2015, **78**, 013901.
325 E. Kretschm and H. Raether, *Z. Naturforsch., A:Phys. Sci.*, 1968, **23**, 2135–2136.
326 Y. Xu, P. Bai, X. D. Zhou, Y. Akimov, C. E. Png, L. K. Ang, W. Knoll and L. Wu, *Adv. Opt. Mater.*, 2019, **7**, 1801433.
327 L. Li, *Manipulation of near field propagation and far field radiation of surface plasmon polariton*, Springer, 2017.
328 M. A. Otte, B. Sepúlveda, W. H. Ni, J. P. Juste, L. M. Liz-Marzán and L. M. Lechuga, *ACS Nano*, 2010, **4**, 349–357.
329 Y. Z. Chu, M. G. Banaee and K. B. Crozier, *ACS Nano*, 2010, **4**, 2804–2810.
330 L. P. Du, X. J. Zhang, T. Mei and X. C. Yuan, *Opt. Express*, 2010, **18**, 1959–1965.
331 A. Dhawan, M. Canva and T. Vo-Dinh, *Opt. Express*, 2011, **19**, 787–813.
332 C. M. Soukoulis and M. Wegener, *Nat. Photonics*, 2011, **5**, 523–530.
333 H. Tao, A. C. Strikwerda, M. Liu, J. P. Mondia, E. Ekmekci, K. Fan, D. L. Kaplan, W. J. Padilla, X. Zhang, R. D. Averitt and F. G. Omenetto, *Appl. Phys. Lett.*, 2010, **97**, 261909.
334 N. I. Landy, S. Sajuyigbe, J. J. Mock, D. R. Smith and W. J. Padilla, *Phys. Rev. Lett.*, 2008, **100**, 207402.
335 S. D. Rezaei, R. J. H. Ng, Z. G. Dong, J. F. Ho, E. H. H. Koay, S. Ramakrishna and J. K. W. Yang, *ACS Nano*, 2019, **13**, 3580–3588.
336 K. Kumar, H. G. Duan, R. S. Hegde, S. C. W. Koh, J. N. Wei and J. K. W. Yang, *Nat. Nanotechnol.*, 2012, **7**, 557–561.
337 X. M. Goh, Y. H. Zheng, S. J. Tan, L. Zhang, K. Kumar, C. W. Qiu and J. K. W. Yang, *Nat. Commun.*, 2014, **5**, 5361.
338 N. Liu, M. Mesch, T. Weiss, M. Hentschel and H. Giessen, *Nano Lett.*, 2010, **10**, 2342–2348.

339 K. Chen, R. Adato and H. Altug, *ACS Nano*, 2012, **6**, 7998–8006.
340 K. Chen, T. D. Dao, S. Ishii, M. Aono and T. Nagao, *Adv. Funct. Mater.*, 2015, **25**, 6637–6643.
341 C. F. Liu, G. H. Duan, B. Zhang, Y. J. Liu, Y. Shuai and Z. L. Wang, *Appl. Energy*, 2024, **372**, 123807.
342 W. Li, Z. J. Coppens, L. V. Besteiro, W. Y. Wang, A. O. Govorov and J. Valentine, *Nat. Commun.*, 2015, **6**, 8379.
343 T. D. Dao, S. Ishii, T. Yokoyama, T. Sawada, R. P. Sugavaneshwar, K. Chen, Y. Wada, T. Nabatame and T. Nagao, *ACS Photonics*, 2016, **3**, 1271–1278.
344 M. J. Dai, C. W. Wang, B. Qiang, F. K. Wang, M. Ye, S. Han, Y. Luo and Q. J. Wang, *Nat. Commun.*, 2022, **13**, 4560.
345 A. Lochbaum, Y. Fedoryshyn, A. Dorodnyy, U. Koch, C. Hafner and J. Leuthold, *ACS Photonics*, 2017, **4**, 1371–1380.
346 A. Livingood, J. R. Nolen, T. G. Folland, L. Potechin, G. Lu, S. Criswell, J.-P. Maria, C. T. Shelton, E. Sachet and J. D. Caldwell, *ACS Photonics*, 2021, **8**, 472–480.
347 A. Lochbaum, A. Dorodnyy, U. Koch, S. M. Koepfli, S. Volk, Y. Fedoryshyn, V. Wood and J. Leuthold, *Nano Lett.*, 2020, **20**, 4169–4176.
348 D. Li, H. Zhou, Z. Chen, Z. Ren, C. Xu, X. He, T. Liu, X. Chen, H. Huang, C. Lee and X. Mu, *Adv. Mater.*, 2023, **35**, e2301787.
349 Z. L. Shen, S. N. Li, Y. F. Xu, W. Yin, L. Y. Zhang and X. F. Chen, *Phys. Rev. Appl.*, 2021, **16**, 014066.
350 Y. Cui, K. H. Fung, J. Xu, H. Ma, Y. Jin, S. He and N. X. Fang, *Nano Lett.*, 2012, **12**, 1443–1447.
351 A. Y. Nikitin, R. Hillenbrand, A. Bylinkin, F. Calavalle, M. Barra-Burillo, R. V. Kirtaev, E. Nikulina, E. Modin, E. Janzen, J. H. Edgar, F. Casanova, L. E. Hueso, V. S. Volkov, P. Vavassori, I. Aharonovich and P. Alonso-Gonzalez, *Nano Lett.*, 2023, **23**, 3985–3993.
352 C. Huck, J. Vogt, T. Neuman, T. Nagao, R. Hillenbrand, J. Aizpurua, A. Pucci and F. Neubrech, *Opt. Express*, 2016, **24**, 25528–25539.
353 D. Ray, T. V. Raziman, C. Santschi, D. Etezadi, H. Altug and O. J. F. Martin, *Nano Lett.*, 2020, **20**, 8752–8759.
354 J. Wang, T. Weber, A. Aigner, S. A. Maier and A. Tittl, *Laser Photonics Rev.*, 2023, 2300294, DOI: 10.1002/lpor.202300294.
355 A. Aigner, A. Tittl, J. Wang, T. Weber, Y. Kivshar, S. A. Maier and H. Ren, *Sci. Adv.*, 2022, **8**, eadd4816.
356 A. D. Li, H. Wei, M. Cotrufo, W. J. Chen, S. Mann, X. Ni, B. C. Xu, J. F. Chen, J. Wang, S. H. Fan, C. W. Qiu, A. Alú and L. Chen, *Nat. Nanotechnol.*, 2023, **18**, 706–720.
357 S. K. Ozdemir, S. Rotter, F. Nori and L. Yang, *Nat. Mater.*, 2019, **18**, 783–798.
358 J.-H. Park, A. Ndao, W. Cai, L. Hsu, A. Kodigala, T. Lepetit, Y.-H. Lo and B. Kanté, *Nat. Phys.*, 2020, **16**, 462–468.
359 Y. Zhao, M. A. Belkin and A. Alù, *Nat. Commun.*, 2012, **3**, 870.
360 J. K. Gansel, M. Thiel, M. S. Rill, M. Decker, K. Bade, V. Saile, G. von Freymann, S. Linden and M. Wegener, *Science*, 2009, **325**, 1513–1515.
361 S. Yoo and Q. H. Park, *Nanophotonics*, 2019, **8**, 249–261.
362 W. L. Gao, M. Lawrence, B. A. Yang, F. Liu, F. Z. Fang, B. Béri, J. S. Li and S. Zhang, *Phys. Rev. Lett.*, 2015, **114**, 037402.
363 Y. Chen, J. Gao and X. D. Yang, *Nano Lett.*, 2018, **18**, 520–527.
364 N. Liu and T. Liedl, *Chem. Rev.*, 2018, **118**, 3032–3053.
365 N. C. Seeman, *Nano Lett.*, 2010, **10**, 1971–1978.
366 K. Vogele, J. List, G. Pardatscher, N. B. Holland, F. C. Simmel and T. Pirzer, *ACS Nano*, 2016, **10**, 11377–11384.
367 A. Kuzyk, M. J. Urban, A. Idili, F. Ricci and N. Liu, *Sci. Adv.*, 2017, **3**, e1602803.
368 S. Simoncelli, E. M. Roller, P. Urban, R. Schreiber, A. J. Turberfield, T. Liedl and T. Lohmüller, *ACS Nano*, 2016, **10**, 9809–9815.
369 G. A. Vinnacombe-Willson, Y. Conti, S. J. Jonas, P. S. Weiss, A. Mihi and L. Scarabelli, *Adv. Mater.*, 2022, **34**, e2205330.
370 A. Klinkova, H. Thérien-Aubin, A. Ahmed, D. Nykypanchuk, R. M. Choueiri, B. Gagnon, A. Muntyanu, O. Gale, G. C. Walker and E. Kumacheva, *Nano Lett.*, 2014, **14**, 6314–6321.
371 M. Rycenga, C. M. Cobley, J. Zeng, W. Y. Li, C. H. Moran, Q. Zhang, D. Qin and Y. N. Xia, *Chem. Rev.*, 2011, **111**, 3669–3712.
372 W.-G. Kim, J.-M. Lee, Y. Yang, H. Kim, V. Devaraj, M. Kim, H. Jeong, E.-J. Choi, J. Yang and Y. Jang, *Nano Lett.*, 2022, **22**, 4702–4711.
373 A. A. Tseng, K. Chen, C. D. Chen and K. J. Ma, *IEEE Trans. Electron. Packag. Manuf.*, 2003, **26**, 141–149.
374 M. Altissimo, *Biomicrofluidics*, 2010, **4**, 026503.
375 S. Y. Chou, P. R. Krauss and P. Renstrom, *Appl. Phys. Lett.*, 1995, **67**, 3114–3116.
376 Y. M. Yang, I. I. Kravchenko, D. P. Briggs and J. Valentine, *Nat. Commun.*, 2014, **5**, 5753.
377 B. Spacková, P. Wrobel, M. Bocková and J. Homola, *Proc. IEEE*, 2016, **104**, 2380–2408.
378 S. A. Khan, N. Z. Khan, Y. N. Xie, M. T. Abbas, M. Rauf, I. Mehmood, M. Runowski, S. Agathopoulos and J. F. Zhu, *Adv. Opt. Mater.*, 2022, **10**, 2200500.
379 C. Fernández-Sánchez, C. J. McNeil, K. Rawson, O. Nilsson, H. Y. Leung and V. Gnanapragasam, *J. Immunol. Methods*, 2005, **307**, 1–12.
380 S. D. Mikolajczyk, W. J. Catalona, C. L. Evans, H. J. Linton, L. S. Millar, K. M. Marker, D. Katir, A. Amirkhan and H. G. Rittenhouse, *Clin. Chem.*, 2004, **50**, 1017–1025.
381 Y. Khan, A. Li, L. Chang, L. Li and L. Guo, *Sens. Actuators, B*, 2018, **255**, 1298–1307.
382 C. Y. Wang, C. H. Huang, Z. Q. Gao, J. L. Shen, J. C. He, A. MacLachlan, C. Ma, Y. Chang, W. Yang, Y. X. Cai, Y. Lou, S. Y. Dai, W. Q. Chen, F. Li and P. Y. Chen, *ACS Sens.*, 2021, **6**, 3308–3319.
383 H. T. Feng, S. Y. Min, Y. Q. Huang, Z. F. Gan, C. W. Liang, W. D. Li and Y. Chen, *Sens. Actuators, B*, 2024, **400**, 134899.
384 Y. D. Wang, Z. H. Mao, Q. Chen, K. Koh, X. J. Hu and H. X. Chen, *Biosens. Bioelectron.*, 2022, **201**, 113954.
385 C. Théry, M. Ostrowski and E. Segura, *Nat. Rev. Immunol.*, 2009, **9**, 581–593.
386 M. Colombo, G. Raposo and C. Théry, in *Annual Review of Cell and Developmental Biology*, ed. R. Schekman and R. Lehmann, 2014, vol. 30, pp. 255–289.

387 R. J. Simpson, J. W. E. Lim, R. L. Moritz and S. Mathivanan, *Expert Rev. Proteomics*, 2009, **6**, 267–283.
388 H. L. Shao, H. Im, C. M. Castro, X. Breakefield, R. Weissleder and H. H. Lee, *Chem. Rev.*, 2018, **118**, 1917–1950.
389 S. El Andaloussi, I. Maeger, X. O. Breakefield and M. J. A. Wood, *Nat. Rev. Drug Discovery*, 2013, **12**, 348–358.
390 H. Peinado, M. Aleckovic, S. Lavotshkin, I. Matei, B. Costa-Silva, G. Moreno-Bueno, M. Hergueta-Redondo, C. Williams, G. García-Santos, C. M. Ghajar, A. Nitadori-Hoshino, C. Hoffman, K. Badal, B. A. Garcia, M. K. Callahan, J. D. Yuan, V. R. Martins, J. Skog, R. N. Kaplan, M. S. Brady, J. D. Wolchok, P. B. Chapman, Y. B. Kang, J. Bromberg and D. Lyden, *Nat. Med.*, 2012, **18**, 883–891.
391 F. Pucci, C. Garris, C. P. Lai, A. Newton, C. Pfirschke, C. Engblom, D. Alvarez, M. Sprachman, C. Evavold, A. Magnuson, U. H. von Andrian, K. Glatz, X. O. Breakefield, T. R. Mempel, R. Weissleder and M. J. Pittet, *Science*, 2016, **352**, 242–246.
392 M. Boyiadzis and T. L. Whiteside, *Leukemia*, 2017, **31**, 1259–1268.
393 C. Théry, S. Amigorena, G. Raposo and A. Clayton, *Curr. Protoc. Cell Biol.*, 2006, **30**, 3–22.
394 H. Im, H. Shao, Y. I. Park, V. M. Peterson, C. M. Castro, R. Weissleder and H. Lee, *Nat. Biotechnol.*, 2014, **32**, 490.
395 C. Z. J. Lim, Y. Zhang, Y. Chen, H. T. Zhao, M. C. Stephenson, N. R. Y. Ho, Y. Chen, J. Chung, A. Reilhac, T. P. Loh, C. L. H. Chen and H. L. Shao, *Nat. Commun.*, 2019, **10**, 11.
396 F. J. Li, J. P. Hong, C. H. Guan, K. Y. Chen, Y. N. Xie, Q. Wu, J. J. Chen, B. C. Deng, J. Q. Shen, X. Y. Liu, R. S. Hu, Y. L. Zhang, Y. X. Chen and J. F. Zhu, *ACS Nano*, 2023, **17**, 3383–3393.
397 S. Ansaryan, Y. C. Liu, X. Li, A. M. Economou, C. S. Eberhardt, C. Jandus and H. Altug, *Nat. Biomed. Eng.*, 2023, **7**, 943–958.
398 Y. Y. Huang, P. W. Chen, L. Y. Zhou, J. Y. Zheng, H. T. Wu, J. X. Liang, A. X. Xiao, J. Li and B. O. Guan, *Adv. Mater.*, 2023, **35**, e2304116.
399 Z. H. Li, L. Leustean, F. Inci, M. Zheng, U. Demirci and S. Q. Wang, *Biotechnol. Adv.*, 2019, **37**, 107440.
400 L. Liu, S. Iketani, Y. Guo, J. F. Chan, M. Wang, L. Liu, Y. Luo, H. Chu, Y. Huang, M. S. Nair, J. Yu, K. K. Chik, T. T. Yuen, C. Yoon, K. K. To, H. Chen, M. T. Yin, M. E. Sobieszczyk, Y. Huang, H. H. Wang, Z. Sheng, K. Y. Yuen and D. D. Ho, *Nature*, 2022, **602**, 676–681.
401 F. C. Zhu, C. L. Zhuang, K. Chu, L. Zhang, H. Zhao, S. J. Huang, Y. Y. Su, H. Y. Lin, C. L. Yang, H. M. Jiang, X. Zang, D. L. Liu, H. X. Pan, Y. M. Hu, X. H. Liu, Q. Chen, Q. Q. Song, J. L. Quan, Z. H. Huang, G. H. Zhong, J. Y. Chen, J. L. Han, H. Sun, L. B. Cui, J. X. Li, Y. X. Chen, T. Y. Zhang, X. Z. Ye, C. G. Li, T. Wu, J. Zhang and N. S. Xia, *Lancet Respir. Med.*, 2022, **10**, 749–760.
402 A. Asghari, C. Wang, K. M. Yoo, A. Rostamian, X. C. Xu, J. D. Shin, H. Dalir and R. T. Chen, *Appl. Phys. Rev.*, 2021, **8**, 031313.
403 J. Cheong, H. Yu, C. Y. Lee, J. U. Lee, H. J. Choi, J. H. Lee, H. Lee and J. Cheon, *Nat. Biomed. Eng.*, 2020, **4**, 1159–1167.
404 L. Q. Wang, X. J. Wang, Y. G. Wu, M. Q. Guo, C. J. Gu, C. H. Dai, D. R. Kong, Y. Wang, C. Zhang, D. Qu, C. H. Fan, Y. H. Xie, Z. Q. Zhu, Y. Q. Liu and D. C. Wei, *Nat. Biomed. Eng.*, 2022, **6**, 276–285.
405 X. T. Tan, M. Krel, E. Dolgov, S. Park, X. Z. Li, W. S. Wu, Y. L. Sun, J. Zhang, M. K. K. Oo, D. S. Perlin and X. D. Fan, *Biosens. Bioelectron.*, 2020, **169**, 112572.
406 A. F. Ogata, A. M. Maley, C. Wu, T. Gilboa, M. Norman, R. Lazarovits, C. P. Mao, G. Newton, M. Chang, K. Nguyen, M. Kamkaew, Q. Zhu, T. E. Gibson, E. T. Ryan, R. C. Charles, W. A. Marasco and D. R. Walt, *Clin. Chem.*, 2020, **66**, 1562–1572.
407 Y. J. Yang, J. Murray, J. Haverstick, R. A. Tripp and Y. P. Zhao, *Sens. Actuators, B*, 2022, **359**, 131604.
408 R. Funari, H. Fukuyama and A. Q. Shen, *Biosens. Bioelectron.*, 2022, **208**, 114193.
409 L. P. Huang, L. F. Ding, J. Zhou, S. L. Chen, F. Chen, C. Zhao, J. Q. Xu, W. J. Hu, J. S. Ji, H. Xu and G. L. Liu, *Biosens. Bioelectron.*, 2021, **171**, 112685.
410 R. Funari, K. Y. Chu and A. Q. Shen, *Biosens. Bioelectron.*, 2020, **169**, 112578.
411 H. Y. Lin, C. H. Huang, S. H. Lu, I. T. Kuo and L. K. Chau, *Biosens. Bioelectron.*, 2014, **51**, 371–378.
412 S. Zheng, D. K. Kim, T. J. Park, S. J. Lee and S. Y. Lee, *Talanta*, 2010, **82**, 803–809.
413 A. A. Yanik, M. Huang, O. Kamohara, A. Artar, T. W. Geisbert, J. H. Connor and H. Altug, *Nano Lett.*, 2010, **10**, 4962–4969.
414 F. Yesilkoy, E. R. Arvelo, Y. Jahani, M. Liu, A. Tittl, V. Cevher, Y. Kivshar and H. Altug, *Nat. Photonics*, 2019, **13**, 390–396.
415 Y. Jahani, E. R. Arvelo, F. Yesilkoy, K. Koshelev, C. Cianciaruso, M. De Palma, Y. Kivshar and H. Altug, *Nat. Commun.*, 2021, **12**, 3246.
416 S. Min, S. Li, Z. Zhu, Y. Liu, C. Liang, J. Cai, F. Han, Y. Li, W. Cai, X. Cheng and W. D. Li, *Adv. Mater.*, 2021, **33**, e2100270.
417 P. F. Wang, L. Bo, Y. Semenova, G. Farrell and G. Brambilla, *Biosensors*, 2015, **5**, 471–499.
418 A. M. Shrivastav, S. K. Mishra and B. D. Gupta, *Sens. Actuators, B*, 2015, **212**, 404–410.
419 W. C. Zhou, K. W. Li, Y. L. Wei, P. Hao, M. B. Chi, Y. S. Liu and Y. H. Wu, *Biosens. Bioelectron.*, 2018, **106**, 99–104.
420 Y. Y. Huang, P. W. Chen, H. Liang, A. X. Xiao, S. K. Zeng and B. O. Guan, *Biosens. Bioelectron.*, 2020, **156**, 112147.
421 P. W. Chen, Y. Y. Huang, Y. Bo, H. Liang, A. X. Xiao and B. O. Guan, *Chem. Eng. J.*, 2021, **407**, 127143.
422 H. T. Li, Y. Y. Huang, G. H. Hou, A. X. Xiao, P. W. Chen, H. Liang, Y. G. Huang, X. T. Zhao, L. L. Liang, X. H. Feng and B. O. Guan, *Sci. Adv.*, 2019, **5**, eaax4659.
423 R. Raghunandhan, L. H. Chen, H. Y. Long, L. L. Leam, P. L. So, X. Ning and C. C. Chan, *Sens. Actuators, B*, 2016, **233**, 31–38.
424 S. Mariani, L. M. Strambini and G. Barillaro, *ACS Sens.*, 2018, **3**, 595–605.
425 K. J. Kim, P. Lu, J. T. Culp and P. R. Ohodnicki, *ACS Sens.*, 2018, **3**, 386–394.

426 C. Ribaut, V. Voisin, V. Malachovská, V. Dubois, P. Mégret, R. Wattiez and C. Caucheteur, *Biosens. Bioelectron.*, 2016, **77**, 315–322.
427 R. Adato and H. Altug, *Nat. Commun.*, 2013, **4**, 2154.
428 K. Ataka, T. Kottke and J. Heberle, *Angew. Chem., Int. Ed.*, 2010, **49**, 5416–5424.
429 F. Neubrech, C. Huck, K. Weber, A. Pucci and H. Giessen, *Chem. Rev.*, 2017, **117**, 5110–5145.
430 H. Zhou, D. X. Li, X. D. Hui and X. J. Mu, *Int. J. Optomechatronics*, 2021, **15**, 97–119.
431 D. X. Li, C. Xu, J. S. Xie and C. Lee, *Nanomaterials*, 2023, **13**, 2377.
432 R. F. Aroca, D. J. Ross and C. Domingo, *Appl. Spectrosc.*, 2004, **58**, 324A–338A.
433 N. I. Zheludev, *Science*, 2010, **328**, 582–583.
434 N. J. Halas, S. Lal, W. S. Chang, S. Link and P. Nordlander, *Chem. Rev.*, 2011, **111**, 3913–3961.
435 A. G. Brolo, *Nat. Photonics*, 2012, **6**, 709–713.
436 X. X. Yang, Z. P. Sun, T. Low, H. Hu, X. D. Guo, F. J. G. de Abajo, P. Avouris and Q. Dai, *Adv. Mater.*, 2018, **30**, 1704896.
437 K. Yang, X. Yao, B. W. Liu and B. Ren, *Adv. Mater.*, 2021, 2007988.
438 B. Cerjan, X. Yang, P. Nordlander and N. J. Halas, *ACS Photonics*, 2016, **3**, 354–360.
439 E. Cubukcu, S. Zhang, Y.-S. Park, G. Bartal and X. Zhang, *Appl. Phys. Lett.*, 2009, **95**, 043113.
440 S. Gottheim, H. Zhang, A. O. Govorov and N. J. Halas, *ACS Nano*, 2015, **9**, 3284–3292.
441 E. Aslan, E. Aslan, R. Wang, M. K. Hong, S. Erramilli, M. Turkmen, O. G. Saracoglu and L. Dal Negro, *ACS Photonics*, 2016, **3**, 2102–2111.
442 Z. A. Kudyshev, A. V. Kildishev, V. M. Shalaev and A. Boltasseva, *Appl. Phys. Rev.*, 2020, **7**, 021407.
443 I. Malkiel, M. Mrejen, A. Nagler, U. Arieli, L. Wolf and H. Suchowski, *Light: Sci. Appl.*, 2018, **7**, 60.
444 S. Jafar-Zanjani, S. Inampudi and H. Mosallaei, *Sci. Rep.*, 2018, **8**, 11040.
445 Z. H. Jiang, S. Yun, F. Toor, D. H. Werner and T. S. Mayer, *ACS Nano*, 2011, **5**, 4641–4647.
446 C. Yeung, J.-M. Tsai, B. King, B. Pham, D. Ho, J. Liang, M. W. Knight and A. P. Raman, *Nanophotonics*, 2021, **10**, 1133–1143.
447 D. Li, H. Zhou, X. Hui, X. He and X. Mu, *Anal. Chem.*, 2021, **93**, 9437–9444.
448 W. Ma, Z. Liu, Z. A. Kudyshev, A. Boltasseva, W. Cai and Y. Liu, *Nat. Photonics*, 2020, **15**, 77–90.
449 J. Q. Jiang, M. K. Chen and J. A. Fan, *Nat. Rev. Mater.*, 2021, **6**, 679–700.
450 F. Neubrech, A. Pucci, T. W. Cornelius, S. Karim, A. Garcia-Etxarri and J. Aizpurua, *Phys. Rev. Lett.*, 2008, **101**, 157403.
451 P. Alonso-Gonzalez, P. Albella, F. Neubrech, C. Huck, J. Chen, F. Golmar, F. Casanova, L. E. Hueso, A. Pucci, J. Aizpurua and R. Hillenbrand, *Phys. Rev. Lett.*, 2013, **110**, 203902.
452 J. Vogt, C. Huck, F. Neubrech, A. Toma, D. Gerbert and A. Pucci, *Phys. Chem. Chem. Phys.*, 2015, **17**, 21169–21175.
453 X. Hui, C. Yang, D. Li, X. He, H. Huang, H. Zhou, M. Chen, C. Lee and X. Mu, *Adv. Sci.*, 2021, **8**, 2100583.
454 D. Dregely, F. Neubrech, H. Duan, R. Vogelgesang and H. Giessen, *Nat. Commun.*, 2013, **4**, 2237.
455 L. Dong, X. Yang, C. Zhang, B. Cerjan, L. Zhou, M. L. Tseng, Y. Zhang, A. Alabastri, P. Nordlander and N. J. Halas, *Nano Lett.*, 2017, **17**, 5768–5774.
456 I. Hwang, M. Kim, J. Yu, J. Lee, J. H. Choi, S. A. Park, W. S. Chang, J. Lee and J. Y. Jung, *Small Methods*, 2021, **5**, e2100277.
457 J. Xu, Z. Ren, B. Dong, X. Liu, C. Wang, Y. Tian and C. Lee, *ACS Nano*, 2020, **14**, 12159–12172.
458 T. H. H. Le and T. Tanaka, *ACS Nano*, 2017, **11**, 9780–9788.
459 T. H. H. Le, A. Morita, K. Mawatari, T. Kitamori and T. Tanaka, *ACS Photonics*, 2018, **5**, 3179–3188.
460 X. L. Miao, T. S. Luk and P. Q. Liu, *Adv. Mater.*, 2022, **34**, 2107950.
461 I. Hwang, J. Yu, J. Lee, J. H. Choi, D. G. Choi, S. Jeon, J. Lee and J. Y. Jung, *ACS Photonics*, 2018, **5**, 3492–3498.
462 A. E. Cetin, D. Etezadi and H. Altug, *Adv. Opt. Mater.*, 2014, **2**, 866–872.
463 Y. Jung, I. Hwang, J. Yu, J. Lee, J. H. Choi, J. H. Jeong, J. Y. Jung and J. Lee, *Sci. Rep.*, 2019, **9**, 7834.
464 X. Miao, L. Yan, Y. Wu and P. Q. Liu, *Light: Sci. Appl.*, 2021, **10**, 5.
465 Y. Chang, D. Hasan, B. Dong, J. Wei, Y. Ma, G. Zhou, K. W. Ang and C. Lee, *ACS Appl. Mater. Interfaces*, 2018, **10**, 38272–38279.
466 X. Y. Chong, Y. J. Zhang, E. W. Li, K. J. Kim, P. R. Ohodnicki, C. H. Chang and A. X. Wang, *ACS Sens.*, 2018, **3**, 230–238.
467 D. Hasan and C. Lee, *Adv. Sci.*, 2018, **5**, 1700581.
468 N. Bareza, K. K. Gopalan, R. Alani, B. Paulillo and V. Pruneri, *ACS Photonics*, 2020, **7**, 879–884.
469 N. Bareza, Jr., B. Paulillo, T. M. Slipchenko, M. Autore, I. Dolado, S. Liu, J. H. Edgar, S. Vélez, L. Martín-Moreno, R. Hillenbrand and V. Pruneri, *ACS Photonics*, 2022, **9**, 34–42.
470 D. Li, H. Zhou, Z. Ren and C. Lee, *Small Sci.*, 2024, 2400250.
471 D. Li, A. Yadav, H. Zhou, K. Roy, P. Thanasekaran and C. Lee, *Global Chall.*, 2024, **8**, 2300244.
472 H. Zhou, X. Hui, D. Li, D. Hu, X. Chen, X. He, L. Gao, H. Huang, C. Lee and X. Mu, *Adv. Sci.*, 2020, **7**, 2001173.
473 H. Zhou, Z. Ren, C. Xu, L. Xu and C. Lee, *Nano-Micro Lett.*, 2022, **14**, 207.
474 Q. Guo, H. Zhu, F. Liu, A. Y. Zhu, J. C. Reed, F. Yi and E. Cubukcu, *ACS Photonics*, 2014, **1**, 221–227.
475 D. Etezadi, J. B. Warner, F. S. Ruggeri, G. Dietler, H. A. Lashuel and H. Altug, *Light: Sci. Appl.*, 2017, **6**, e17029.
476 X. Hui, C. Yang, D. Li, X. He, H. Huang, H. Zhou, M. Chen, C. Lee and X. Mu, *Adv. Sci.*, 2021, **8**, e2100583.
477 J. Wei, Y. Li, Y. Chang, D. M. N. Hasan, B. Dong, Y. Ma, C. W. Qiu and C. Lee, *ACS Appl. Mater. Interfaces*, 2019, **11**, 47270–47278.
478 K. Zeng, C. Wu, X. Guo, F. Guan, Y. Duan, L. L. Zhang, X. Yang, N. Liu, Q. Dai and S. Zhang, *eLight*, 2024, **4**, 1.

479 D. Li, H. Zhou, Z. Ren, C. Xu and C. Lee, *Nano-Micro Lett.*, 2024, **17**, 1–19.
480 D. Hasan, C. P. Ho and C. Lee, *ACS Omega*, 2016, **1**, 818–831.
481 D. X. Li, H. Zhou, X. D. Hui, X. M. He, H. Huang, J. J. Zhang, X. J. Mu, C. K. Lee and Y. Yang, *Adv. Sci.*, 2021, **8**, 12.
482 D. Rodrigo, A. Tittl, A. John-Herpin, O. Limaj and H. Altug, *ACS Photonics*, 2018, **5**, 4903–4911.
483 F. U. Richter, I. Sinev, S. Zhou, A. Leitis, S. H. Oh, M. L. Tseng, Y. Kivshar and H. Altug, *Adv. Mater.*, 2024, e2314279, DOI: **10.1002/adma.202314279**.
484 P. Jangid, F. U. Richter, M. L. Tseng, I. Sinev, S. Kruk, H. Altug and Y. Kivshar, *Adv. Mater.*, 2024, **36**, e2307494.
485 Z. Ren, Z. Zhang, J. Wei, B. Dong and C. Lee, *Nat. Commun.*, 2022, **13**, 3859.
486 S. D. Liu, E. S. Leong, G. C. Li, Y. Hou, J. Deng, J. H. Teng, H. C. Ong and D. Y. Lei, *ACS Nano*, 2016, **10**, 1442–1453.
487 A. Tittl, A. Leitis, M. Liu, F. Yesilkoy, D. Y. Choi, D. N. Neshev, Y. S. Kivshar and H. Altug, *Science*, 2018, **360**, 1105–1109.
488 A. Leitis, A. Tittl, M. Liu, B. H. Lee, M. B. Gu, Y. S. Kivshar and H. Altug, *Sci. Adv.*, 2019, **5**, eaaw2871.
489 M. Najem, F. Carcenac, T. Taliercio and F. Gonzalez-Posada, *Adv. Opt. Mater.*, 2022, **10**, 2201025.
490 A. John-Herpin, D. Kavungal, L. von Mucke and H. Altug, *Adv. Mater.*, 2021, 2006054, DOI: **10.1002/adma.202006054**.
491 X. Liu, Z. Zhang, J. Zhou, W. Liu, G. Zhou and C. Lee, *Small*, 2024, 2400035.
492 D. Kavungal, P. Magalhães, S. T. Kumar, R. Kolla, H. A. Lashuel and H. J. S. A. Altug, *Sci. Adv.*, 2023, **9**, eadg9644.
493 J. R. Baena and B. Lendl, *Curr. Opin. Chem. Biol.*, 2004, **8**, 534–539.
494 E. Smith and G. Dent, *Modern Raman spectroscopy: a practical approach*, John Wiley & Sons, 2019.
495 X. Wang, S. C. Huang, S. Hu, S. Yan and B. Ren, *Nat. Rev. Phys.*, 2020, **2**, 253–271.
496 C. Zong, M. X. Xu, L. J. Xu, T. Wei, X. Ma, X. S. Zheng, R. Hu and B. Ren, *Chem. Rev.*, 2018, **118**, 4946–4980.
497 G. C. Schatz, M. A. Young and R. P. Van Duyne, in *Surface-Enhanced Raman Scattering: Physics and Applications*, ed. K. Kneipp, M. Moskovits and H. Kneipp, 2006, vol. 103, pp. 19–45.
498 L. Jensen, C. M. Aikens and G. C. Schatz, *Chem. Soc. Rev.*, 2008, **37**, 1061–1073.
499 L. L. Zhao, L. Jensen and G. C. Schatz, *J. Am. Chem. Soc.*, 2006, **128**, 2911–2919.
500 J. Langer, D. J. de Aberasturi, J. Aizpurua, R. A. Alvarez-Puebla, B. Auguie, J. J. Baumberg, G. C. Bazan, S. E. J. Bell, A. Boisen, A. G. Brolo, J. Choo, D. Cialla-May, V. Deckert, L. Fabris, K. Faulds, F. J. G. de Abajo, R. Goodacre, D. Graham, A. J. Haes, C. L. Haynes, C. Huck, T. Itoh, M. Ka, J. Kneipp, N. A. Kotov, H. Kuang, E. C. Le Ru, H. K. Lee, J. F. Li, X. Y. Ling, S. A. Maier, T. Mayerhofer, M. Moskovits, K. Murakoshi, J. M. Nam, S. Nie, Y. Ozaki, I. Pastoriza-Santos, J. Perez-Juste, J. Popp, A. Pucci, S. Reich, B. Ren, G. C. Schatz, T. Shegai, S. Schlucker, L. L. Tay, K. G. Thomas, Z. Q. Tian, R. P. Van Duyne, T. Vo-Dinh, Y. Wang, K. A. Willets, C. Xu, H. Xu, Y. Xu, Y. S. Yamamoto, B. Zhao and L. M. Liz-Marzan, *ACS Nano*, 2020, **14**, 28–117.
501 W. E. Smith, *Chem. Soc. Rev.*, 2008, **37**, 955–964.
502 C. L. Xie, Z. Q. Niu, D. Kim, M. F. Li and P. D. Yang, *Chem. Rev.*, 2020, **120**, 1184–1249.
503 Y. K. Xu, Y. R. Zhang, C. C. Li, Z. W. Ye and S. E. J. Bell, *Acc. Chem. Res.*, 2023, **56**, 2072–2083.
504 Y. Gu, E. M. You, J. D. Lin, J. H. Wang, S. H. Luo, R. Y. Zhou, C. J. Zhang, J. L. Yao, H. Y. Li, G. Li, W. W. Wang, Y. Qiao, J. W. Yan, D. Y. Wu, G. K. Liu, L. Zhang, J. F. Li, R. Xu, Z. Q. Tian, Y. Cui and B. W. Mao, *Nat. Commun.*, 2023, **14**, 3536.
505 S. Zaleski, A. J. Wilson, M. Mattei, X. Chen, G. Goubert, M. F. Cardinal, K. A. Willets and R. P. Van Duyne, *Acc. Chem. Res.*, 2016, **49**, 2023–2030.
506 R. Esteban, J. J. Baumberg and J. Aizpurua, *Acc. Chem. Res.*, 2022, **55**, 1889–1899.
507 J. Kneipp, H. Kneipp and K. Kneipp, *Chem. Soc. Rev.*, 2008, **37**, 1052–1060.
508 N. Kim, M. R. Thomas, M. S. Bergholt, I. J. Pence, H. Seong, P. Charchar, N. Todorova, A. Nagelkerke, A. Belessiotis-Richards, D. J. Payne, A. Gelmi, I. Yarovsky and M. M. Stevens, *Nat. Commun.*, 2020, **11**, 207.
509 Y. X. Leong, Y. H. Lee, C. S. L. Koh, G. C. Phan-Quang, X. Han, I. Y. Phang and X. Y. Ling, *Nano Lett.*, 2021, **21**, 2642–2649.
510 P. B. Luppa, C. Müller, A. Schlichtiger and H. Schlebusch, *TrAC, Trends Anal. Chem.*, 2011, **30**, 887–898.
511 Y. L. Wang, C. Zhao, J. J. Wang, X. Luo, L. J. Xie, S. J. Zhan, J. M. Kim, X. Z. Wang, X. J. Liu and Y. B. Ying, *Sci. Adv.*, 2021, **7**, eabe4553.
512 U. Mogera, H. Guo, M. Namkoong, M. S. Rahman, T. Nguyen and L. M. Tian, *Sci. Adv.*, 2022, **8**, eabn1736.
513 L. P. Song, J. Chen, B. B. Xu and Y. J. Huang, *ACS Nano*, 2021, **15**, 18822–18847.
514 W. K. Son, Y. S. Choi, Y. W. Han, D. W. Shin, K. Y. H. Min, J. Shin, M. J. Lee, H. Son, D. H. Jeong and S. Y. Kwak, *Nat. Nanotechnol.*, 2023, **18**, 205–216.
515 C. Farber, M. Mahnke, L. Sanchez and D. Kurouski, *TrAC, Trends Anal. Chem.*, 2019, **118**, 43–49.
516 S. Mahanty, S. Majumder, R. Paul, R. Boroujerdi, E. Valsami-Jones and C. Laforsch, *Sci. Total Environ.*, 2024, **950**, 174252.
517 Y. Y. Zhang, L. Z. Li, H. Zhang, J. J. Shang, C. Li, S. Naqvi, Z. Birech and J. D. Hu, *Anal. Bioanal. Chem.*, 2022, **414**, 2757–2766.
518 M. David, A. Serban, C. Radulescu, A. F. Danet and M. Florescu, *Bioelectrochemistry*, 2019, **129**, 124–134.
519 C. H. Huang, G. P. Singh, S. H. Park, N. H. Chua, R. J. Ram and B. S. Park, *Front. Plant Sci.*, 2020, **11**, 663.
520 N. Altangerel, G. O. Ariunbold, C. Gorman, M. H. Alkahtani, E. J. Borrego, D. Bohlmeyer, P. Hemmer, M. V. Kolomiets, J. S. Yuan and M. O. Scully, *Proc. Natl. Acad. Sci. U. S. A.*, 2017, **114**, 3393–3396.

521 T. Wang, S. P. Wang, Z. H. Cheng, J. C. Wei, L. L. Yang, Z. F. Zhong, H. Hu, Y. T. Wang, B. P. Zhou and P. Li, *Chem. Eng. J.*, 2021, **424**, 130323.
522 M. L. Xu, Y. Gao, X. X. Han and B. Zhao, *J. Agric. Food Chem.*, 2017, **65**, 6719–6726.
523 D. R. Zhang, H. B. Pu, L. J. Huang and D. W. Sun, *Trends Food Sci. Technol.*, 2021, **109**, 690–701.
524 L. Jiang, M. M. Hassan, S. Ali, H. H. Li, R. Sheng and Q. S. Chen, *Trends Food Sci. Technol.*, 2021, **112**, 225–240.
525 N. Logan, C. Cao, S. Freitag, S. A. Haughey, R. Krska and C. T. Elliott, *Adv. Mater.*, 2024, **36**, e2309625.
526 Z. H. Wu, H. B. Pu and D. W. Sun, *Trends Food Sci. Technol.*, 2021, **110**, 393–404.
527 N. Purdie and K. A. Swallows, *Anal. Chem.*, 1989, **61**, 77A–89A.
528 W. P. Zhou, Y. P. Ruan, H. D. Wu, H. Zhang, J. S. Tang, Z. D. Xie, L. Tang, Y. Wang, Y. E. Ji, K. P. Jia, C. W. Qiu, Y. Q. Lu and K. Y. Xia, *Elight*, 2024, **4**, 12.
529 S. Beaulieu, A. Comby, D. Descamps, B. Fabre, G. A. Garcia, R. Géneaux, A. G. Harvey, F. Légaré, Z. Masin, L. Nahon, A. F. Ordonez, S. Petit, B. Pons, Y. Mairesse, O. Smirnova and V. Blanchet, *Nat. Phys.*, 2018, **14**, 484–489.
530 R. M. Kim, J. H. Han, S. M. Lee, H. Kim, Y. C. Lim, H. E. Lee, H. Y. Ahn, Y. H. Lee, I. H. Ha and K. T. Nam, *J. Chem. Phys.*, 2024, **160**, 061001.
531 E. Hendry, T. Carpy, J. Johnston, M. Popland, R. V. Mikhaylovskiy, A. J. Lapthorn, S. M. Kelly, L. D. Barron, N. Gadegaard and M. Kadodwala, *Nat. Nanotechnol.*, 2010, **5**, 783–787.
532 T. Kakkar, C. Keijzer, M. Rodier, T. Bukharova, M. Taliansky, A. J. Love, J. J. Milner, A. S. Karimullah, L. D. Barron, N. Gadegaard, A. J. Lapthorn and M. Kadodwala, *Light: Sci. Appl.*, 2020, **9**, 195.
533 M. Hajji, M. Cariello, C. Gilroy, M. Kartau, C. D. Syme, A. Karimullah, N. Gadegaard, A. Malfait, P. Woisel, G. Cooke, W. J. Peveler and M. Kadodwala, *ACS Nano*, 2021, **15**, 19905–19916.
534 V. Tabouillot, R. Kumar, P. L. Lalaguna, M. Hajji, R. Clarke, A. S. Karimullah, A. R. Thomson, A. Sutherland, N. Gadegaard, S. Hashiyada and M. Kadodwala, *ACS Photonics*, 2022, **9**, 3617–3624.
535 C. Xu, Z. Ren, H. Zhou, J. Zhou, D. Li and C. Lee, *Adv. Funct. Mater.*, 2023, 2314482, DOI: **10.1002/adfm.202314482**.
536 C. Xu, Z. Ren, H. Zhou, J. Zhou, C. P. Ho, N. Wang and C. Lee, *Light: Sci. Appl.*, 2023, **12**, 154.
537 T. A. Keiderling, *Curr. Opin. Chem. Biol.*, 2002, **6**, 682–688.
538 V. Baumruk and T. A. Keiderling, *J. Am. Chem. Soc.*, 1993, **115**, 6939–6942.
539 P. K. Bose and P. L. Polavarapu, *Carbohydr. Res.*, 1999, **319**, 172–183.
540 A. Vázquez-Guardado and D. Chanda, *Phys. Rev. Lett.*, 2018, **120**, 137601.
541 A. Biswas, P. Cencillo-Abad, M. W. Shabbir, M. Karmakar and D. Chanda, *Sci. Adv.*, 2024, **10**, eadk2560.
542 S. Abdali and E. W. Blanch, *Chem. Soc. Rev.*, 2008, **37**, 980–992.
543 D. Kurouski, *Anal. Chim. Acta*, 2017, **990**, 54–66.
544 S. Efrima, *Chem. Phys. Lett.*, 1983, **102**, 79–82.
545 S. Efrima, *J. Chem. Phys.*, 1985, **83**, 1356–1362.
546 B. G. Janesko and G. E. Scuseria, *J. Chem. Phys.*, 2006, **125**, 124704.
547 M. T. Sun, Z. L. Zhang, P. J. Wang, Q. Li, F. C. Ma and H. X. Xu, *Light:Sci. Appl.*, 2013, **2**, e112.
548 S. O. Pour, L. Rocks, K. Faulds, D. Graham, V. Parchansky, P. Bour and E. W. Blanch, *Nat. Chem.*, 2015, **7**, 591–596.
549 W. J. Choi, S. H. Lee, B. C. Park and N. A. Kotov, *J. Am. Chem. Soc.*, 2022, **144**, 22789–22804.
550 W. J. Choi, G. Cheng, Z. Y. Huang, S. Zhang, T. B. Norris and N. A. Kotov, *Nat. Mater.*, 2019, **18**, 820–826.
551 C. McDonnell, J. H. Deng, S. Sideris, T. Ellenbogen and G. X. Li, *Nat. Commun.*, 2021, **12**, 30.
552 W. J. Choi, K. Yano, M. Cha, F. M. Colombari, J. Y. Kim, Y. C. Wang, S. H. Lee, K. Sun, J. M. Kruger, A. F. De Moura and N. A. Kotov, *Nat. Photonics*, 2022, **16**, 366–373.
553 M. Kim and V. V. Tsukruk, *Nat. Photonics*, 2022, **16**, 337–338.
554 Y. Jeong, Y. M. Kook, K. Lee and W. G. Koh, *Biosens. Bioelectron.*, 2018, **111**, 102–116.
555 K. Drexhage, H. Kuhn and F. Schäfer, *Ber. Bunsenges. Phys. Chem.*, 1968, **72**, 329.
556 J. R. Lakowicz, *Anal. Biochem.*, 2001, **298**, 1–24.
557 C. D. Geddes, I. Gryczynski, J. Malicka, Z. Gryczynski and J. R. Lakowicz, *Comb. Chem. High Throughput Screening*, 2003, **6**, 109–117.
558 K. Aslan, J. R. Lakowicz, H. Szmacinski and C. D. Geddes, *J. Fluoresc.*, 2004, **14**, 677–679.
559 K. Aslan, I. Gryczynski, J. Malicka, E. Matveeva, J. R. Lakowicz and C. D. Geddes, *Curr. Opin. Biotechnol*, 2005, **16**, 55–62.
560 J. R. Lakowicz, C. D. Geddes, I. Gryczynski, J. Malicka, Z. Gryczynski, K. Aslan, J. Lukomska, E. Matveeva, J. A. Zhang, R. Badugu and J. Huang, *J. Fluoresc.*, 2004, **14**, 425–441.
561 K. Aslan, J. R. Lakowicz and C. D. Geddes, *Anal. Bioanal. Chem.*, 2005, **382**, 926–933.
562 T. Schalkhammer, F. R. Aussenegg, A. Leitner, H. Brunner, G. Hawa, C. Lobmaier and F. Pittner, *San Jose*, Ca, 1997.
563 J. R. Lakowicz, B. Shen, Z. Gryczynski, S. D'Auria and I. Gryczynski, *Biochem. Biophys. Res. Commun.*, 2001, **286**, 875–879.
564 E. G. Matveeva, Z. Gryczynski and J. R. Lakowicz, *J. Immunol. Methods*, 2005, **302**, 26–35.
565 L. M. Liz-Marzán, *Langmuir*, 2006, **22**, 32–41.
566 Y. N. Xia, Y. J. Xiong, B. Lim and S. E. Skrabalak, *Angew. Chem., Int. Ed.*, 2009, **48**, 60–103.
567 F. Tang, F. He, H. C. Cheng and L. D. Li, *Langmuir*, 2010, **26**, 11774–11778.
568 H. Li, W. B. Qiang, M. Vuki, D. K. Xu and H. Y. Chen, *Anal. Chem.*, 2011, **83**, 8945–8952.
569 S. Kühn, U. Håkanson, L. Rogobete and V. Sandoghdar, *Phys. Rev. Lett.*, 2006, **97**, 017402.
570 T. H. Taminiau, F. D. Stefani, F. B. Segerink and N. F. Van Hulst, *Nat. Photonics*, 2008, **2**, 234–237.
571 A. Kinkhabwala, Z. F. Yu, S. H. Fan, Y. Avlasevich, K. Müllen and W. E. Moerner, *Nat. Photonics*, 2009, **3**, 654–657.

572 D. P. Fromm, A. Sundaramurthy, P. J. Schuck, G. Kino and W. E. Moerner, *Nano Lett.*, 2004, **4**, 957–961.
573 D. Punj, M. Mivelle, S. B. Moparthi, T. S. van Zanten, H. Rigneault, N. F. van Hulst, M. F. García-Parajó and J. Wenger, *Nat. Nanotechnol.*, 2013, **8**, 512–516.
574 R. Bardhan, N. K. Grady, J. R. Cole, A. Joshi and N. J. Halas, *ACS Nano*, 2009, **3**, 744–752.
575 S. Khatua, P. M. R. Paulo, H. F. Yuan, A. Gupta, P. Zijlstra and M. Orrit, *ACS Nano*, 2014, **8**, 4440–4449.
576 C. Y. Li, S. Duan, J. Yi, C. Wang, P. M. Radjenovic, Z. Q. Tian and J. F. Li, *Sci. Adv.*, 2020, **6**, eaba6012.
577 O. N. Assad, T. Gilboa, J. Spitzberg, M. Juhasz, E. Weinhold and A. Meller, *Adv. Mater.*, 2017, **29**, 1605442.
578 A. Kotnala, H. R. Ding and Y. B. Zheng, *ACS Photonics*, 2021, **8**, 1673–1682.
579 P. Bharadwaj, P. Anger and L. Novotny, *Nanotechnology*, 2007, **18**, 044017.
580 P. Anger, P. Bharadwaj and L. Novotny, *Phys. Rev. Lett.*, 2006, **96**, 113002.
581 K. Ray, R. Badugu and J. R. Lakowicz, *J. Phys. Chem. C*, 2007, **111**, 7091–7097.
582 M. H. Chowdhury, K. Ray, S. K. Gray, J. Pond and J. R. Lakowicz, *Anal. Chem.*, 2009, **81**, 1397–1403.
583 X. M. Yang, S. S. Zhu, Y. Dou, Y. Zhuo, Y. W. Luo and Y. J. Feng, *Talanta*, 2014, **122**, 36–42.
584 H. L. Tan and Y. Chen, *Sens. Actuators, B*, 2012, **173**, 262–267.
585 B. Tan, D. H. Wang, Z. J. Cai, X. Quan and H. M. Zhao, *Sens. Actuators, B*, 2020, **303**, 127230.
586 L. Yu, H. X. Chen, J. Yue, X. F. Chen, M. T. Sun, J. Hou, K. A. Alamry, H. M. Marwani, X. K. Wang and S. H. Wang, *Talanta*, 2020, **207**, 120297.
587 G. P. Acuna, F. M. Möller, P. Holzmeister, S. Beater, B. Lalkens and P. Tinnefeld, *Science*, 2012, **338**, 506–510.
588 H. P. Lu and X. S. Xie, *Nature*, 1997, **385**, 143–146.
589 F. Tenopala-Carmona, S. Fronk, G. C. Bazan, I. D. W. Samuel and J. C. Penedo, *Sci. Adv.*, 2018, **4**, eaao5786.
590 B. Commoner, *Nature*, 1964, **202**, 960–968.
591 J. D. Spitzberg, A. Zrehen, X. F. van Kooten and A. Meller, *Adv. Mater.*, 2019, **31**, e1900422.
592 M. Wanunu, W. Morrison, Y. Rabin, A. Y. Grosberg and A. Meller, *Nat. Nanotechnol.*, 2010, **5**, 160–165.
593 C. D. Geddes and J. R. Lakowicz, *J. Fluoresc.*, 2002, **12**, 121–129.
594 Z. Chen, H. Li, W. C. Jia, X. H. Liu, Z. M. Li, F. Wen, N. Zheng, J. D. Jiang and D. K. Xu, *Anal. Chem.*, 2017, **89**, 5901–5909.
595 I. Abdulhalim, A. Karabchevsky, C. Patzig, B. Rauschenbach, B. Fuhrmann, E. Eltzov, R. Marks, J. Xu, F. Zhang and A. Lakhtakia, *Appl. Phys. Lett.*, 2009, **94**, 063106.
596 C. J. Huang, J. Dostalek, A. Sessitsch and W. Knoll, *Anal. Chem.*, 2011, **83**, 674–677.
597 R. B. Hu, Y. Yang, Y. Liu, T. Liao, Y. Y. Liu, J. H. Tang, G. H. Wang, G. X. Wang, Y. Y. Liang, J. Yuan and B. Zhang, *J. Nanobiotechnol.*, 2022, **20**, 533.
598 J. L. Zhu, X. Zhao, J. Ouyang, N. Na and J. P. Mao, *Anal. Chem.*, 2023, **95**, 5267–5274.
599 S.-S. Li, Q.-Y. Kong, M. Zhang, F. Yang, B. Kang, J.-J. Xu and H.-Y. Chen, *Anal. Chem.*, 2018, **90**, 3833–3841.
600 G. L. Liu, Y.-T. Long, Y. Choi, T. Kang and L. P. Lee, *Nat. Methods*, 2007, **4**, 1015–1017.
601 Y. Choi, Y. Park, T. Kang and L. P. Lee, *Nat. Nanotechnol.*, 2009, **4**, 742–746.
602 Y. Choi, T. Kang and L. P. Lee, *Nano Lett.*, 2009, **9**, 85–90.
603 J. Park, S. Lee, J. Choi and I. Choi, *ACS Sens.*, 2021, **6**, 1823–1830.
604 I. Kim, H. Kim, S. Han, J. Kim, Y. Kim, S. Eom, A. Barulin, I. Choi, J. Rho and L. P. Lee, *Adv. Mater.*, 2023, **35**, 2300229.
605 M. K. Liu, K. B. Fan, W. Padilla, D. A. Powell, X. Zhang and I. V. Shadrivov, *Adv. Mater.*, 2016, **28**, 1553–1558.
606 T. Badloe, J. Kim, I. Kim, W. S. Kim, W. S. Kim, Y. K. Kim and J. Rho, *Light: Sci. Appl.*, 2022, **11**, 118.
607 M. Wuttig, H. Bhaskaran and T. Taubner, *Nat. Photonics*, 2017, **11**, 465–476.
608 Y. G. Jeong, Y. M. Bahk and D. S. Kim, *Adv. Opt. Mater.*, 2020, **8**, 1900548.
609 L. Sun, L. Xu, J. Y. Wang, Y. N. Jiao, Z. H. Ma, Z. F. Ma, C. Chang, X. Yang and R. D. Wang, *Nanoscale*, 2022, **14**, 9681–9685.
610 Y. S. Hu, Y. H. Bai, Q. Zhang and Y. J. Yang, *Appl. Phys. Lett.*, 2022, **121**, 141701.
611 H. Hu, X. Yang, F. Zhai, D. Hu, R. Liu, K. Liu, Z. Sun and Q. Dai, *Nat. Commun.*, 2016, **7**, 12334.
612 C. C. Wu, X. D. Guo, Y. Duan, W. Lyu, H. Hu, D. B. Hu, K. Chen, Z. P. Sun, T. Gao, X. X. Yang and Q. Dai, *Adv. Mater.*, 2022, **34**, e2110525.
613 Z. Chen, D. Li, H. Zhou, T. Liu and X. Mu, *Nanoscale*, 2023, **15**, 14100–14108.
614 Z. Y. Li, Y. B. Zhu, Y. F. Hao, M. Gao, M. Lu, A. Stein, A. H. A. Park, J. C. Hone, Q. Lin and N. F. Yu, *ACS Photonics*, 2019, **6**, 501–509.
615 G. Lee, E. S. Yu, Y. S. Ryu and M. Seo, *Nanophotonics*, 2022, **11**, 1783–1808.
616 A. Barik, L. M. Otto, D. Yoo, J. Jose, T. W. Johnson and S.-H. Oh, *Nano Lett.*, 2014, **14**, 2006–2012.
617 R. Salemmilani, B. D. Piorek, R. Y. Mirsafavi, A. W. Fountain, M. Moskovits and C. D. Meinhart, *Anal. Chem.*, 2018, **90**, 7930–7936.
618 G. Kelp, J. Li, J. Lu, N. DiNapoli, R. Delgado, C. Liu, D. Fan, S. Dutta-Gupta and G. Shvets, *Lab Chip*, 2020, **20**, 2136–2153.
619 H. Y. Lin, C. H. Huang, W. H. Hsieh, L. H. Liu, Y. C. Lin, C. C. Chu, S. T. Wang, I. T. Kuo, L. K. Chau and C. Y. Yang, *Small*, 2014, **10**, 4700–4710.
620 S. Cherukulappurath, S. H. Lee, A. Campos, C. L. Haynes and S. H. Oh, *Chem. Mater.*, 2014, **26**, 2445–2452.
621 Q. L. Tan, L. C. Tang, M. L. Yang, C. Y. Xue, W. D. Zhang, J. Liu and J. J. Xiong, *Opt. Lasers Eng.*, 2015, **74**, 103–108.
622 R. Rubio, J. Santander, L. Fonseca, N. Sabaté, I. Gràcia, C. Cané, S. Udina and S. Marco, *Sens. Actuators, B*, 2007, **127**, 69–73.
623 J. Fonollosa, M. Carmona, J. Santander, L. Fonseca, M. Moreno and S. Marco, *Sens. Actuators, A*, 2009, **149**, 65–73.

624 M. Dong, C. T. Zheng, S. Z. Miao, Y. Zhang, Q. L. Du, Y. D. Wang and F. K. Tittel, *Sensors*, 2017, **17**, 2221.
625 T. D. Dao, S. Ishii, A. T. Doan, Y. Wada, A. Ohi, T. Nabatame and T. Nagao, *Adv. Sci.*, 2019, **6**, 1900579.
626 J. W. Stewart, J. H. Vella, W. Li, S. H. Fan and M. H. Mikkelsen, *Nat. Mater.*, 2020, **19**, 158–162.
627 X. Tan, H. Zhang, J. Li, H. Wan, Q. Guo, H. Zhu, H. Liu and F. Yi, *Nat. Commun.*, 2020, **11**, 5245.
628 J. Xie, Z. Ren, J. Wei, W. Liu, J. Zhou and C. Lee, *Adv. Opt. Mater.*, 2023, **11**, 2202867.
629 F. Bonaccorso, Z. Sun, T. Hasan and A. C. Ferrari, *Nat. Photonics*, 2010, **4**, 611–622.
630 N. Liu, M. L. Tang, M. Hentschel, H. Giessen and A. P. Alivisatos, *Nat. Mater.*, 2011, **10**, 631–636.
631 S. K. Deng, J. E. Park, G. Kang, J. Guan, R. Li, G. C. Schatz and T. W. Odom, *Proc. Natl. Acad. Sci. U. S. A.*, 2022, **119**, e2202621119.
632 S. Castilla, I. Vangelidis, V. V. Pusapati, J. Goldstein, M. Autore, T. Slipchenko, K. Rajendran, S. Kim, K. Watanabe, T. Taniguchi, L. Martín-Moreno, D. Englund, K. J. Tielrooij, R. Hillenbrand, E. Lidorikis and F. H. L. Koppens, *Nat. Commun.*, 2020, **11**, 4872.
633 Y. Yao, R. Shankar, P. Rauter, Y. Song, J. Kong, M. Loncar and F. Capasso, *Nano Lett.*, 2014, **14**, 3749–3754.
634 J. Wei, Y. Li, L. Wang, W. Liao, B. Dong, C. Xu, C. Zhu, K. W. Ang, C. W. Qiu and C. Lee, *Nat. Commun.*, 2020, **11**, 6404.
635 H. Jiang, J. Fu, J. Wei, S. Li, C. Nie, F. Sun, Q. Y. S. Wu, M. Liu, Z. Dong, X. Wei, W. Gao and C. W. Qiu, *Nat. Commun.*, 2024, **15**, 1225.
636 J. Wei, Y. Chen, Y. Li, W. Li, J. Xie, C. Lee, K. S. Novoselov and C.-W. Qiu, *Nat. Photonics*, 2023, **17**, 171–178.
637 Q. R. Fu, R. Zhu, J. B. Song, H. H. Yang and X. Y. Chen, *Adv. Mater.*, 2019, **31**, e1805875.
638 Y. Mantri and J. V. Jokerst, *ACS Nano*, 2020, **14**, 9408–9422.
639 C. Kim, C. Favazza and L. H. V. Wang, *Chem. Rev.*, 2010, **110**, 2756–2782.
640 H. F. Zhang, K. Maslov, G. Stoica and L. H. V. Wang, *Nat. Biotechnol.*, 2006, **24**, 848–851.
641 S. Hu, K. Maslov and L. V. Wang, *Opt. Lett.*, 2011, **36**, 1134–1136.
642 Q. L. Fan, K. Cheng, X. Hu, X. W. Ma, R. P. Zhang, M. Yang, X. M. Lu, L. Xing, W. Huang, S. S. Gambhir and Z. Cheng, *J. Am. Chem. Soc.*, 2014, **136**, 15185–15194.
643 D. Cui, P. C. Li, X. Zhen, J. C. Li, Y. Y. Jiang, A. X. Yu, X. Hu and K. Pu, *Adv. Funct. Mater.*, 2019, **29**, 1903461.
644 T. Repenko, A. Rix, A. Nedilko, J. Rose, A. Hermann, R. Vinokur, S. Moli, R. Cao-Milàn, M. Mayer, G. von Plessen, A. Fery, L. De Laporte, W. Lederle, D. N. Chigrin and A. J. C. Kuehne, *Adv. Funct. Mater.*, 2018, **28**, 1705607.
645 L. Lin and L. H. V. Wang, *Nat. Rev. Clin. Oncol.*, 2022, **19**, 365–384.
646 K. S. Valluru, K. E. Wilson and J. K. Willmann, *Radiology*, 2016, **280**, 332–349.
647 S. V. Ovsepian, I. Olefir, G. Westmeyer, D. Razansky and V. Ntziachristos, *Neuron*, 2017, **96**, 966–988.
648 X. G. Liu, Y. K. Duan and B. Liu, *Aggregate*, 2021, **2**, 4–19.
649 C. Y. Zhou, L. Zhang, T. Sun, Y. Zhang, Y. D. Liu, M. F. Gong, Z. S. Xu, M. M. Du, Y. Liu, G. Liu and D. Zhang, *Adv. Mater.*, 2021, **33**, e2006532.
650 M. Hardy and P. Goldberg Oppenheimer, *Nanoscale*, 2024, **16**, 3293–3323.
651 W. Liu, K. Chung, S. Yua and L. P. Lee, *Chem. Soc. Rev.*, 2024, **53**, 10491–10522.
652 Y. Hang, A. Wang and N. Wu, *Chem. Soc. Rev.*, 2024, **53**, 2932–2971.
653 B. Wang, X. Zhu, S. Li, M. Chen, N. Liu, H. Yang, M. Ran, H. Lu and Y. Yang, *Nanomaterials*, 2019, **9**, 1263.
654 D. Mittal, M. Ahlawat and V. Govind Rao, *Adv. Mater. Interfaces*, 2022, **9**, 2102383.
655 K. Ćwieka, K. Czelej, J. C. Colmenares, K. Jabłczyńska, Ł. Werner and L. Gradoń, *ChemCatChem*, 2021, **13**, 4458–4496.
656 Z. Wang and P. Cheng, *Int. J. Heat Mass Transfer*, 2019, **140**, 453–482.
657 X. Chen, F. Wang, Y. Zhao, P. Wu, L. Gao, C. Ouyang, Y. Yang and X. Mu, *Research*, 2022, **2022**, 9765634.
658 I. Mora-Sero, S. Giménez, F. Fabregat-Santiago, R. Gómez, Q. Shen, T. Toyoda and J. Bisquert, *Acc. Chem. Res.*, 2009, **42**, 1848–1857.
659 H. Yuan, C. M. Wilson, J. Xia, S. L. Doyle, S. Li, A. M. Fales, Y. Liu, E. Ozaki, K. Mulfaul, G. Hanna and G. M. Palmer, *Nanoscale*, 2014, **6**, 4078–4082.
660 R. Xue, C. Huang, J. Deng, L. Yang, L. Li and X. Fan, *J. Mater. Chem. A*, 2022, **10**, 3771–3781.
661 W. Fan and M. Leung, *Molecules*, 2016, **21**, 180.
662 A. O. Govorov, H. Zhang and Y. K. Gun'ko, *J. Phys. Chem. C*, 2013, **117**, 16616–16631.
663 R. Sundararaman, P. Narang, A. S. Jermyn, W. A. Goddard, 3rd and H. A. Atwater, *Nat. Commun.*, 2014, **5**, 5788.
664 A. Manjavacas, J. G. Liu, V. Kulkarni and P. Nordlander, *ACS Nano*, 2014, **8**, 7630–7638.
665 M. Bernardi, J. Mustafa, J. B. Neaton and S. G. Louie, *Nat. Commun.*, 2015, **6**, 7044.
666 A. O. Govorov and H. Zhang, *J. Phys. Chem. C*, 2015, **119**, 6181–6194.
667 A. Primo, A. Corma and H. Garcia, *Phys. Chem. Chem. Phys.*, 2011, **13**, 886–910.
668 K. Wu, W. E. Rodriguez-Cordoba, Y. Yang and T. Lian, *Nano Lett.*, 2013, **13**, 5255–5263.
669 S. Mubeen, J. Lee, N. Singh, S. Kramer, G. D. Stucky and M. Moskovits, *Nat. Nanotechnol.*, 2013, **8**, 247–251.
670 Y. Zhong, K. Ueno, Y. Mori, X. Shi, T. Oshikiri, K. Murakoshi, H. Inoue and H. Misawa, *Angew. Chem., Int. Ed.*, 2014, **53**, 10350–10354.
671 K. Ueno and H. Misawa, *NPG Asia Mater.*, 2013, **5**, e61–e61.
672 J. Li, S. K. Cushing, P. Zheng, T. Senty, F. Meng, A. D. Bristow, A. Manivannan and N. Wu, *J. Am. Chem. Soc.*, 2014, **136**, 8438–8449.
673 M. W. Knight, H. Sobhani, P. Nordlander and N. J. Halas, *Science*, 2011, **332**, 702–704.
674 S. Linic, P. Christopher and D. B. Ingram, *Nat. Mater.*, 2011, **10**, 911–921.

675 Z. Liu, W. Hou, P. Pavaskar, M. Aykol and S. B. Cronin, *Nano Lett.*, 2011, **11**, 1111–1116.
676 D. B. Ingram and S. Linic, *J. Am. Chem. Soc.*, 2011, **133**, 5202–5205.
677 D. B. Ingram, P. Christopher, J. L. Bauer and S. Linic, *ACS Catal.*, 2011, **1**, 1441–1447.
678 X. Wu, X. Zhu, C. Kan and D. Shi, *CrystEngComm*, 2023, **25**, 1365–1373.
679 S. K. Cushing and N. Wu, *J. Phys. Chem. Lett.*, 2016, **7**, 666–675.
680 K. Awazu, M. Fujimaki, C. Rockstuhl, J. Tominaga, H. Murakami, Y. Ohki, N. Yoshida and T. Watanabe, *J. Am. Chem. Soc.*, 2008, **130**, 1676–1680.
681 E. Thimsen, F. Le Formal, M. Gratzel and S. C. Warren, *Nano Lett.*, 2011, **11**, 35–43.
682 I. Thomann, B. A. Pinaud, Z. Chen, B. M. Clemens, T. F. Jaramillo and M. L. Brongersma, *Nano Lett.*, 2011, **11**, 3440–3446.
683 Y. Wang, X. Sang, F. Wu, Y. Pang, G. Xu, Y. Yuan, H. Y. Hsu and W. Niu, *Nanoscale*, 2023, **15**, 18901–18909.
684 Z. Fusco, K. Catchpole and F. J. Beck, *J. Mater. Chem. C*, 2022, **10**, 7511–7524.
685 H. Tan, R. Santbergen, A. H. Smets and M. Zeman, *Nano Lett.*, 2012, **12**, 4070–4076.
686 J. A. Schuller, E. S. Barnard, W. Cai, Y. C. Jun, J. S. White and M. L. Brongersma, *Nat. Mater.*, 2010, **9**, 193–204.
687 K. R. C. A. Polman, *Opt. Express*, 2008, **16**, 21793.
688 R. A. Pala, J. S. Liu, E. S. Barnard, D. Askarov, E. C. Garnett, S. Fan and M. L. Brongersma, *Nat. Commun.*, 2013, **4**, 2095.
689 J. Li, S. K. Cushing, P. Zheng, F. Meng, D. Chu and N. Wu, *Nat. Commun.*, 2013, **4**, 2651.
690 V. E. Ferry, M. A. Verschuuren, H. B. Li, E. Verhagen, R. J. Walters, R. E. Schropp, H. A. Atwater and A. Polman, *Opt. Express*, 2010, **18**, A237–A245.
691 K. Aydin, V. E. Ferry, R. M. Briggs and H. A. Atwater, *Nat. Commun.*, 2011, **2**, 517.
692 N. Zhang, C. Han, X. Fu and Y.-J. Xu, *Chem*, 2018, **4**, 1832–1861.
693 F. Stete, M. Bargheer and W. Koopman, *Nanoscale*, 2023, **15**, 16307–16313.
694 K. Wang and T. He, *Nanoscale*, 2023, **15**, 12398–12405.
695 R. G. Ciocarlan, N. Blommaerts, S. Lenaerts, P. Cool and S. W. Verbruggen, *ChemSusChem*, 2023, **16**, e202201647.
696 P. Christopher, D. B. Ingram and S. Linic, *J. Phys. Chem. C*, 2010, **114**, 9173–9177.
697 L. Brus, *Acc. Chem. Res.*, 2008, **41**, 1742–1749.
698 P. K. Jain, X. Huang, I. H. El-Sayed and M. A. El-Sayed, *Acc. Chem. Res.*, 2008, **41**, 1578–1586.
699 P. Christopher, H. Xin and S. Linic, *Nat. Chem.*, 2011, **3**, 467–472.
700 O. Guselnikova, J. Vana, L. T. Phuong, I. Panov, L. Rulisek, A. Trelin, P. Postnikov, V. Svorcik, E. Andris and O. Lyutakov, *Chem. Sci.*, 2021, **12**, 5591–5598.
701 H. A. Atwater and A. Polman, *Nat. Mater.*, 2010, **9**, 865.
702 A. Polman, M. Knight, E. C. Garnett, B. Ehrler and W. C. Sinke, *Science*, 2016, **352**, aad4424.
703 Y. Kang, S. Najmaei, Z. Liu, Y. Bao, Y. Wang, X. Zhu, N. J. Halas, P. Nordlander, P. M. Ajayan, J. Lou and Z. Fang, *Adv. Mater.*, 2014, **26**, 6467–6471.
704 C. Ma, C. Liu, J. Huang, Y. Ma, Z. Liu, L.-J. Li, T. D. Anthopoulos, Y. Han, A. Fratalocchi and T. Wu, *Sol. RRL*, 2019, **3**, 1900138.
705 S. W. Baek, G. Park, J. Noh, C. Cho, C. H. Lee, M. K. Seo, H. Song and J. Y. Lee, *ACS Nano*, 2014, **8**, 3302–3312.
706 Y. Gao, Q. Zhu, S. He, S. Wang, W. Nie, K. Wu, F. Fan and C. Li, *Nano Lett.*, 2023, **23**, 3540–3548.
707 S. Cao, D. Yu, Y. Lin, C. Zhang, L. Lu, M. Yin, X. Zhu, X. Chen and D. Li, *ACS Appl. Mater. Interfaces*, 2020, **12**, 26184–26192.
708 G. Mokari and H. Heidarzadeh, *Plasmonics*, 2019, **14**, 1041–1049.
709 W.-Y. Rho, H.-S. Kim, W.-J. Chung, J. S. Suh, B.-H. Jun and Y.-B. Hahn, *Appl. Surf. Sci.*, 2018, **429**, 23–28.
710 N. K. Pathak, N. Chander, V. K. Komarala and R. P. Sharma, *Plasmonics*, 2016, **12**, 237–244.
711 O. A. M. Abdelraouf, A. Shaker and N. K. Allam, *Sol. Energy*, 2018, **174**, 803–814.
712 A. K. Ali, S. Erten-Ela, K. I. Hassoon and Ç. Ela, *Thin Solid Films*, 2019, **671**, 127–132.
713 M. A. Alkhalayfeh, A. A. Aziz and M. Z. Pakhuruddin, *Sol. Energy*, 2021, **214**, 565–574.
714 Y. Wang, Q. Zhang, F. Huang, Z. Li, Y.-Z. Zheng, X. Tao and G. Cao, *Nano Energy*, 2018, **44**, 135–143.
715 S. Chen, Y. j Wang, Q. Liu, G. Shi, Z. Liu, K. Lu, L. Han, X. Ling, H. Zhang, S. Cheng and W. Ma, *Adv. Energy Mater.*, 2017, **8**, 1701194.
716 Y. Zhao, Y. Luo, S. Wu, C. Wang, N. Ahmidayi, G. Lévêque, X. Portier and T. Xu, *Phys. E*, 2023, **146**, 115534.
717 A. Elrashidi, *Appl. Sci.*, 2022, **12**, 2519.
718 Y. A. Pritom, D. K. Sikder, S. Zaman and M. Hossain, *Nanoscale Adv.*, 2023, **5**, 4986–4995.
719 L.-C. Chen, C.-H. Tien, K.-L. Lee and Y.-T. Kao, *Energies*, 2020, **13**, 1471.
720 F. Juan, Y. Wu, B. Shi, M. Wang, M. Wang, F. Xu, J. Jia, H. Wei, T. Yang and B. Cao, *ACS Appl. Energy Mater.*, 2021, **4**, 3201–3209.
721 Z. Yuan, Z. Wu, S. Bai, Z. Xia, W. Xu, T. Song, H. Wu, L. Xu, J. Si, Y. Jin and B. Sun, *Adv. Energy Mater.*, 2015, **5**, 1500038.
722 Z. Samavati, A. Samavati, A. F. Ismail, A. Awang, E. S. Sazali, M. Velashjerdi and B. Eisaabadi, *Phys. Scr.*, 2023, **98**, 055506.
723 X. Meng, L. Liu, S. Ouyang, H. Xu, D. Wang, N. Zhao and J. Ye, *Adv. Mater.*, 2016, **28**, 6781–6803.
724 U. Aslam, V. G. Rao, S. Chavez and S. Linic, *Nat. Catal.*, 2018, **1**, 656–665.
725 G. Baffou and R. Quidant, *Chem. Soc. Rev.*, 2014, **43**, 3898–3907.
726 J. Zhao, S. Xue, R. Ji, B. Li and J. Li, *Chem. Soc. Rev.*, 2021, **50**, 12070–12097.
727 R. Kortlever, J. Shen, K. J. Schouten, F. Calle-Vallejo and M. T. Koper, *J. Phys. Chem. Lett.*, 2015, **6**, 4073–4082.
728 R. Kortlever, I. Peters, S. Koper and M. T. M. Koper, *ACS Catal.*, 2015, **5**, 3916–3923.

729 J. Zhang, B. Guan, X. Wu, Y. Chen, J. Guo, Z. Ma, S. Bao, X. Jiang, L. Chen, K. Shu, H. Dang, Z. Guo, Z. Li and Z. Huang, *Catal. Sci. Technol.*, 2023, **13**, 1932–1975.
730 H. Robatjazi, H. Zhao, D. F. Swearer, N. J. Hogan, L. Zhou, A. Alabastri, M. J. McClain, P. Nordlander and N. J. Halas, *Nat. Commun.*, 2017, **8**, 27.
731 W. Hou, W. H. Hung, P. Pavaskar, A. Goeppert, M. Aykol and S. B. Cronin, *ACS Catal.*, 2011, **1**, 929–936.
732 K. M. Choi, D. Kim, B. Rungtaweevoranit, C. A. Trickett, J. T. D. Barmanbek, A. S. Alshammari, P. Yang and O. M. Yaghi, *J. Am. Chem. Soc.*, 2016, **139**, 356–362.
733 J. Liu, C. Xia, S. Zaman, Y. Su, L. Tan and S. Chen, *J. Mater. Chem. A*, 2023, **11**, 16918–16932.
734 C. Wang, O. Ranasingha, S. Natesakhawat, P. R. Ohodnicki, M. Andio, J. P. Lewis and C. Matranga, *Nanoscale*, 2013, **5**, 6968–6974.
735 X. Guo, X. Li, S. Kou, X. Yang, X. Hu, D. Ling and J. Yang, *J. Mater. Chem. A*, 2018, **6**, 7364–7369.
736 P.-Y. Kung, F. Pan and Y.-H. Su, *J. Mater. Chem. A*, 2021, **9**, 24863–24873.
737 Y.-B. Sun, M. Ni, C. Chi, D.-R. Yang, X.-L. Chen, Q. Qi, J. Li and X.-H. Xia, *Chem. Eng. J.*, 2023, **467**, 143387.
738 M. P. D. S. Rodrigues, A. H. B. Dourado, L. D. O. Cutolo, L. S. Parreira, T. V. Alves, T. J. A. Slater, S. J. Haigh, P. H. C. Camargo and S. I. Cordoba de Torresi, *ACS Catal.*, 2021, **11**, 13543–13555.
739 R. Koutavarapu, C. Venkata Reddy, B. Babu, K. R. Reddy, M. Cho and J. Shim, *Int. J. Hydrogen Energy*, 2020, **45**, 7716–7740.
740 F. Dionigi and P. Strasser, *Adv. Energy Mater.*, 2016, **6**, 1600621.
741 J. Hu, H. Du, B. Qu, D. Jiang, C. Zhu and Y. Yuan, *Int. J. Hydrogen Energy*, 2021, **46**, 21433–21441.
742 J. Ding, F. Wang, F. Pan, P. Yu, N. Gao, R. H. Goldsmith, S. Cai, R. Yang and J. He, *ACS Catal.*, 2021, **11**, 13721–13732.
743 J. C. Colmenares and R. Luque, *Chem. Soc. Rev.*, 2014, **43**, 765–778.
744 K. Czelej, J. C. Colmenares, K. Jabłczyńska, K. Ćwieka, Ł. Werner and L. Gradoń, *Catal. Today*, 2021, **380**, 156–186.
745 A. Naldoni, M. D'Arienzo, M. Altomare, M. Marelli, R. Scotti, F. Morazzoni, E. Selli and V. Dal Santo, *Appl. Catal., B*, 2013, **130–131**, 239–248.
746 S. Murcia-López, M. González-Castaño, C. Flox, J. R. Morante and T. Andreu, *Mater. Sci. Semicond. Process.*, 2018, **73**, 30–34.
747 X. Wu, T. van der Heide, S. Wen, T. Frauenheim, S. Tretiak, C. Yam and Y. Zhang, *Chem. Sci.*, 2023, **14**, 4714–4723.
748 M. Tahir, M. Siraj, B. Tahir, M. Umer, H. Alias and N. Othman, *Appl. Surf. Sci.*, 2020, **503**, 144344.
749 Z. Zhang and G. W. Huber, *Chem. Soc. Rev.*, 2018, **47**, 1351–1390.
750 W. J. Liu, Z. Xu, D. Zhao, X. Q. Pan, H. C. Li, X. Hu, Z. Y. Fan, W. K. Wang, G. H. Zhao, S. Jin, G. W. Huber and H. Q. Yu, *Nat. Commun.*, 2020, **11**, 265.
751 P. Zhang, D. Sun, A. Cho, S. Weon, S. Lee, J. Lee, J. W. Han, D. P. Kim and W. Choi, *Nat. Commun.*, 2019, **10**, 940.
752 H. Zhao, P. Liu, X. Wu, A. Wang, D. Zheng, S. Wang, Z. Chen, S. Larter, Y. Li, B.-L. Su, M. G. Kibria and J. Hu, *Appl. Catal., B*, 2021, **291**, 120055.
753 M. Usman, W. M. A. Wan Daud and H. F. Abbas, *Renewable Sustainable Energy Rev.*, 2015, **45**, 710–744.
754 J. M. Lavoie, *Front. Chem.*, 2014, **2**, 81.
755 L. Zhou, J. M. P. Martirez, J. Finzel, C. Zhang, D. F. Swearer, S. Tian, H. Robatjazi, M. Lou, L. Dong, L. Henderson, P. Christopher, E. A. Carter, P. Nordlander and N. J. Halas, *Nat. Energy*, 2020, **5**, 61–70.
756 F. B. Hazim Mohameed Qiblawey, *Desalination*, 2008, **220**, 633–644.
757 M. Thirugnanasambandam, S. Iniyan and R. Goic, *Renewable Sustainable Energy Rev.*, 2010, **14**, 312–322.
758 J. Mandal, D. Wang, A. C. Overvig, N. N. Shi, D. Paley, A. Zangiabadi, Q. Cheng, K. Barmak, N. Yu and Y. Yang, *Adv. Mater.*, 2017, **29**, 1702156.
759 Z. Fang, Y.-R. Zhen, O. Neumann, A. Polman, F. J. García de Abajo, P. Nordlander and N. J. Halas, *Nano Lett.*, 2013, **13**, 1736–1742.
760 C. Fang, L. Shao, Y. Zhao, J. Wang and H. Wu, *Adv. Mater.*, 2011, **24**, 94–98.
761 E. C. Garnett, W. Cai, J. J. Cha, F. Mahmood, S. T. Connor, M. Greyson Christoforo, Y. Cui, M. D. McGehee and M. L. Brongersma, *Nat. Mater.*, 2012, **11**, 241–249.
762 Z. Wang, P. Tao, Y. Liu, H. Xu, Q. Ye, H. Hu, C. Song, Z. Chen, W. Shang and T. Deng, *Sci. Rep.*, 2014, **4**, 6246.
763 H. H. Richardson, M. T. Carlson, P. J. Tandler, P. Hernandez and A. O. Govorov, *Nano Lett.*, 2009, **9**, 1139–1146.
764 G. Baffou and R. Quidant, *Laser Photonics Rev.*, 2012, **7**, 171–187.
765 G. W. Crabtree and N. S. Lewis, *Phys. Today*, 2007, **60**, 37–42.
766 C. Chang, C. Yang, Y. Liu, P. Tao, C. Song, W. Shang, J. Wu and T. Deng, *ACS Appl. Mater. Interfaces*, 2016, **8**, 23412–23418.
767 E. M. Larsson, S. Syrenova and C. Langhammer, *Nanophotonics*, 2012, **1**, 249–266.
768 P. R. Ohodnicki, C. Wang, S. Natesakhawat, J. P. Baltrus and T. D. Brown, *J. Appl. Phys.*, 2012, **111**, 064320.
769 G. D. Nicholas Karker and M. A. Carpenter, *ACS Nano*, 2014, **8**, 10953–10962.
770 X. Zhang, Z.-g Zhang, Q. Wang, S.-n Zhu and H. Liu, *ACS Photonics*, 2019, **6**, 2671–2676.
771 K. Ikeda, H. T. Miyazaki, T. Kasaya, K. Yamamoto, Y. Inoue, K. Fujimura, T. Kanakugi, M. Okada, K. Hatade and S. Kitagawa, *Appl. Phys. Lett.*, 2008, **92**, 021117.
772 S. A. Dyakov, V. A. Semenenko, N. A. Gippius and S. G. Tikhodeev, *Phys. Rev. B*, 2018, **98**, 235416.
773 X. Huang, W. Zhang, G. Guan, G. Song, R. Zou and J. Hu, *Acc. Chem. Res.*, 2017, **50**, 2529–2538.
774 S. Mallidi, G. P. Luke and S. Emelianov, *Trends Biotechnol.*, 2011, **29**, 213–221.
775 D. M. Alshangiti, M. M. Ghobashy, H. A. Alqahtani, T. K. El-Damhougy and M. Madani, *RSC Adv.*, 2023, **13**, 32223–32265.

776 Q. Wang, H. Wang, Y. Yang, L. Jin, Y. Liu, Y. Wang, X. Yan, J. Xu, R. Gao, P. Lei, J. Zhu, Y. Wang, S. Song and H. Zhang, *Adv. Mater.*, 2019, **31**, e1904836.
777 H. Sun, Q. Zhang, J. Li, S. Peng, X. Wang and R. Cai, *Nano Today*, 2021, **37**, 101073.
778 P. C. Ray, S. A. Khan, A. K. Singh, D. Senapati and Z. Fan, *Chem. Soc. Rev.*, 2012, **41**, 3193–3209.
779 Y. Zhang, Q. Shen, Q. Li, P. He, J. Li, F. Huang, J. Wang, Y. Duan, C. Shen, F. Saleem, Z. Luo and L. Wang, *Adv. Sci.*, 2021, **8**, 2100386.
780 J. Song and W. Zhou, *Nano Lett.*, 2018, **18**, 4409–4416.
781 M. Goodarzi and T. Pakizeh, *Opt. Lett.*, 2019, **44**, 2212–2215.
782 R. Ma, D. Wu, Y. Liu, H. Ye and D. Sutherland, *Mater. Des.*, 2020, **188**, 108407.
783 S. Wang, L. Lin and Z. L. Wang, *Nano Lett.*, 2012, **12**, 6339–6346.
784 Q. Zhou, K. Lee, K. N. Kim, J. G. Park, J. Pan, J. Bae, J. M. Baik and T. Kim, *Nano Energy*, 2019, **57**, 903–910.
785 Y. Shao, C.-p Feng, B.-w Deng, B. Yin and M.-B. Yang, *Nano Energy*, 2019, **62**, 620–627.
786 J.-H. Zhang, Y. Li, J. Du, X. Hao and H. Huang, *J. Mater. Chem. A*, 2019, **7**, 11724–11733.
787 M. Kim, D. Park, M. M. Alam, S. Lee, P. Park and J. Nah, *ACS Nano*, 2019, **13**, 4640–4646.
788 D. Wang, Y. Lin, D. Hu, P. Jiang and X. Huang, *Composites, Part A*, 2020, **130**, 105754.
789 D.-L. Wen, X. Liu, H.-T. Deng, D.-H. Sun, H.-Y. Qian, J. Brugger and X.-S. Zhang, *Nano Energy*, 2019, **66**, 104123.
790 L. Gao, X. Chen, S. Lu, H. Zhou, W. Xie, J. Chen, M. Qi, H. Yu, X. Mu, Z. L. Wang and Y. Yang, *Adv. Energy Mater.*, 2019, **9**, 1902725.
791 X. Chen, Y. Zhao, F. Wang, D. Tong, L. Gao, D. Li, L. Wu, X. Mu and Y. Yang, *Adv. Sci.*, 2022, **9**, e2103957.
792 T. Y. Y. He, F. Wen, Y. Q. Yang, X. H. Le, W. X. Liu and C. K. Lee, *Anal. Chem.*, 2023, **95**, 490–514.
793 C. Wang, Q. F. Shi and C. K. Lee, *Nanomaterials*, 2022, **12**, 1366.
794 Y. Ma, W. Liu, X. Liu, N. Wang and H. Zhang, *Int. J. Optomechatronics*, 2024, **18**, 2342279.
795 V. J. Sorger, R. F. Oulton, R.-M. Ma and X. Zhang, *MRS Bull.*, 2012, **37**, 728–738.
796 A. S. Gritchenko, A. S. Kalmykov, B. A. Kulnitskiy, Y. G. Vainer, S. P. Wang, B. Kang, P. N. Melentiev and V. I. Balykin, *Nanoscale*, 2022, **14**, 9910–9917.
797 X. Liu, Q. Zhang, J. N. Yip, Q. Xiong and T. C. Sum, *Nano Lett.*, 2013, **13**, 5336–5343.
798 C. Huang, W. Sun, Y. Fan, Y. Wang, Y. Gao, N. Zhang, K. Wang, S. Liu, S. Wang, S. Xiao and Q. Song, *ACS Nano*, 2018, **12**, 3865–3874.
799 H. C. Lin, Y. C. Lee, C. C. Lin, Y. L. Ho, D. Xing, M. H. Chen, B. W. Lin, L. Y. Chen, C. W. Chen and J. J. Delaunay, *Nanoscale*, 2022, **14**, 10075–10081.
800 D. Wang, M. R. Bourgeois, W. K. Lee, R. Li, D. Trivedi, M. P. Knudson, W. Wang, G. C. Schatz and T. W. Odom, *Nano Lett.*, 2018, **18**, 4549–4555.
801 L. Rayleigh, Proc. R. Soc. London, Ser. A, 1907, **79**, 399–416.
802 G. Mie, *Ann. Phys.*, 1908, **330**, 377–445.
803 A. Yang, T. B. Hoang, M. Dridi, C. Deeb, M. H. Mikkelsen, G. C. Schatz and T. W. Odom, *Nat. Commun.*, 2015, **6**, 6939.
804 U. Fano, *J. Opt. Soc. Am.*, 1941, **31**, 213–222.
805 R. H. Ritchie, *Phys. Rev.*, 1957, **106**, 881.
806 A. Otto, *Z. Phys. A:Hadrons Nucl.*, 1968, **216**, 398–410.
807 L. Xie, H. Yang, Y. Yang, Z. Chen, H. Li, Z. Li and D. Liu, *Phys. Chem. Chem. Phys.*, 2024, **26**, 5607–5614.
808 F. Deng, J. Xiang, Z. Liu and T. Ding, *J. Mater. Chem. C*, 2021, **9**, 15927–15931.
809 A. Melikyan, L. Alloatti, A. Muslija, D. Hillerkuss, P. C. Schindler, J. Li, R. Palmer, D. Korn, S. Muehlbrandt, D. Van Thourhout, B. Chen, R. Dinu, M. Sommer, C. Koos, M. Kohl, W. Freude and J. Leuthold, *Nat. Photonics*, 2014, **8**, 229–233.
810 M. Eppenberger, A. Messner, B. I. Bitachon, W. Heni, T. Blatter, P. Habegger, M. Destraz, E. De Leo, N. Meier, N. Del Medico, C. Hoessbacher, B. Baeuerle and J. Leuthold, *Nat. Photonics*, 2023, **17**, 360–367.
811 R. R. Ghosh and A. Dhawan, *Sci. Rep.*, 2021, **11**, 18811.
812 H. Wei, Z. Wang, X. Tian, M. Kall and H. Xu, *Nat. Commun.*, 2011, **2**, 387.
813 Y. Yan, C. Zhang, J. Y. Zheng, J. Yao and Y. S. Zhao, *Adv. Mater.*, 2012, **24**, 5681–5686.
814 P. Neutens, P. Van Dorpe, I. De Vlaminck, L. Lagae and G. Borghs, *Nat. Photonics*, 2009, **3**, 283–286.
815 W. Du, T. Wang, H.-S. Chu and C. A. Nijhuis, *Nat. Photonics*, 2017, **11**, 623–627.
816 S. Ehtesabi, M. Richter, S. Kupfer and S. Grafe, *Nanoscale*, 2024, **16**, 15219–15229.
817 I. V. Doronin, A. A. Zyablovsky, E. S. Andrianov, A. S. Kalmykov, A. S. Gritchenko, B. N. Khlebtsov, S. P. Wang, B. Kang, V. I. Balykin and P. N. Melentiev, *Nanoscale*, 2024, **16**, 14899–14910.
818 P. A. D. Goncalves, T. Christensen, N. M. R. Peres, A. P. Jauho, I. Epstein, F. H. L. Koppens, M. Soljacic and N. A. Mortensen, *Nat. Commun.*, 2021, **12**, 3271.
819 M. S. Tame, K. R. McEnery, Ş. K. Özdemir, J. Lee, S. A. Maier and M. S. Kim, *Nat. Phys.*, 2013, **9**, 329–340.
820 H. Lu, Z. Yue, Y. Li, Y. Zhang, M. Zhang, W. Zeng, X. Gan, D. Mao, F. Xiao, T. Mei, W. Zhao, X. Wang, M. Gu and J. Zhao, *Light: Sci. Appl.*, 2020, **9**, 191.
821 X. Wang, K. Chang, W. Liu, H. Wang, J. Chen, K. Liu, J. Chen and K. Chen, *Nanoscale*, 2022, **14**, 7075–7082.
822 M. Honari-Latifpour and L. Yousefi, *Nanophotonics*, 2019, **8**, 799–806.
823 T. Ginley, Y. Wang, Z. Wang and S. Law, *MRS Commun.*, 2018, **8**, 782–794.
824 Q. N. Li, P. Vasilopoulos, F. M. Peeters, W. Xu, Y. M. Xiao and M. V. Milošević, *Phys. Rev. B*, 2024, **109**, 115123.
825 L. Wang, Y. Shi, G. Wang, X. Liang, T. Takarada and M. Maeda, *J. Mater. Chem. C*, 2021, **9**, 5105–5112.
826 J. Zhang, C. Song and L. Wang, *Phys. Chem. Chem. Phys.*, 2022, **24**, 23959–23979.
827 R. Zhu, J. Li, L. Lin, J. Song and H. Yang, *Adv. Funct. Mater.*, 2020, **31**, 2005709.

828 M. Dass, F. N. Gur, K. Kolataj, M. J. Urban and T. Liedl, *J. Phys. Chem. C*, 2021, **125**, 5969–5981.
829 A. M. Dallaire, S. Patskovsky, A. Vallee-Belisle and M. Meunier, *Biosens. Bioelectron.*, 2015, **71**, 75–81.
830 C. Wang, Y. Hu, Y. Liu, Y. Shan, X. Qu, J. Xue, T. He, S. Cheng, H. Zhou, W. Liu, Z. H. Guo, W. Hua, Z. Liu, Z. Li and C. Lee, *Adv. Funct. Mater.*, 2023, 2303696, DOI: 10.1002/adfm.202303696.
831 F. Diehl, S. Hageneder, S. Fossati, S. K. Auer, J. Dostalek and U. Jonas, *Chem. Soc. Rev.*, 2022, **51**, 3926–3963.
832 S. R. S. Veloso, V. Gomes, S. L. F. Mendes, L. Hilliou, R. B. Pereira, D. M. Pereira, P. J. G. Coutinho, P. M. T. Ferreira, M. A. Correa-Duarte and E. M. S. Castanheira, *Soft Matter*, 2022, **18**, 8384–8397.
833 G. Palermo, U. Cataldi, A. Condello, R. Caputo, T. Burgi, C. Umeton and A. De Luca, *Nanoscale*, 2018, **10**, 16556–16561.
834 Y. Yang, T. He, P. Ravindran, F. Wen, P. Krishnamurthy, L. Wang, Z. Zhang, P. P. Kumar, E. Chae and C. Lee, *Sci. Adv.*, 2024, **10**, eadk7488.
835 F. Wen and C. Lee, *Droplet*, 2024, **3**, e133.
836 F. Wen, C. Wang and C. Lee, *Nano Res.*, 2023, **16**, 11801–11821.
837 C. Wang, T. He, H. Zhou, Z. Zhang and C. Lee, *Bioelectron. Med.*, 2023, **9**, 17.
838 Z. Zhang, X. Liu, H. Zhou, S. Xu and C. Lee, *Small Struct.*, 2023, **5**, 2300325.
839 H. Zhou, L. Xu, Z. Ren, J. Zhu and C. Lee, *Nanoscale Adv.*, 2023, **5**, 538–570.
840 T. Zhu, Y. Zhou, Y. Lou, H. Ye, M. Qiu, Z. Ruan and S. Fan, *Nat. Commun.*, 2017, **8**, 15391.
841 A. Passian and N. Imam, *Sensors*, 2019, **19**, 4048.
842 S. Chen, *Methods Mol. Biol.*, 2020, **2173**, 71–82.
843 N. S. S. Mousavi, K. B. Ramadi, Y.-A. Song and S. Kumar, *Commun. Mater.*, 2023, **4**, 101.
844 J. L. Carvalho-de-Souza, J. S. Treger, B. Dang, S. B. Kent, D. R. Pepperberg and F. Bezanilla, *Neuron*, 2015, **86**, 207–217.
845 C. Xu, Z. Ren, J. Wei and C. Lee, *iScience*, 2022, **25**, 103799.
846 M. Shur, G. Aizin, T. Otsuji and V. Ryzhii, *Sensors*, 2021, **21**, 7907.
847 Z. Zhang, X. Guo and C. Lee, *Nat. Commun.*, 2024, **15**, 6465.
848 Z. Sun, Z. Zhang and C. Lee, *Nat. Electron.*, 2023, **6**, 941–942.
849 Z. X. Zhang, F. Wen, Z. D. Sun, X. G. Guo, T. Y. Y. He and C. K. Lee, *Adv. Intell. Syst.*, 2022, **4**, 2100228.
850 H. Bertin, Y. Brûlé, G. Magno, T. Lopez, P. Gogol, L. Pradere, B. Gralak, D. Barat, G. Demésy and B. Dagens, *ACS Photonics*, 2018, **5**, 2661–2668.
851 Z. Liu, D. Wang, H. Gao, M. Li, H. Zhou and C. Zhang, *Adv. Photonics*, 2023, **5**, 034001.
852 S. D. Bindesri, D. S. Alhatab and C. L. Brosseau, *Analyst*, 2018, **143**, 4128–4135.
853 Y. Hang, J. Boryczka and N. Wu, *Chem. Soc. Rev.*, 2022, **51**, 329–375.

